XNPIG 2024 X-ray and Neutron Phase Imaging with Gratings

X-ray and Neutron Phase Imaging with Gratings

Abstract

Invited

Sensitivity Enhancement in Grating-Based X-ray/Neutron Phase Imaging with Concave and Convex Parabolic Phase Gratings

Atsushi Momose[1], Pouria Zangi[2], Katsumasa Ikematsu[1], Pascal Meyer[2], Martin Börner[2], Hidekazu Takano[1], Yanlin Wu[1], Shinji Kobayashi[1], Yichen Fang[1], Ryosuke Ueda[1], Yoshichika Seki[1]

[1]*Institute of Multidisciplinary Research for Advanced Materials, Tohoku University, Japan*

[2]*Institute of Microstructure Technology, Karlsruhe Institute of Technology, Germany*

Email: *atsushi.momose.c2@tohoku.ac.jp*

Summary: The sensitivity to the beam deflection caused by refraction achieved by Talbot interferometry is normally proportional to the interferometer length (i.e. Talbot order) and inversely proportional to the period of grating. The attempt at increasing the sensitivity is hampered by the current technology of grating fabrication and/or the requirement of system compactness. In this study, the third approach for increasing the sensitivity is proposed and demonstrated by utilizing a pair of concave and convex parabolic gratings in place of the conventional rectangular phase grating.

X-ray and neutron phase imaging is established by the optical configuration for sensing slightly deflected beams caused by refraction and scattering by a sample. The sensitivity of a Talbot interferometer consisting of two gratings that are widely used for this purpose is determined by the period of gratings and the inter-grating distance. The smaller the grating period and the longer the inter-grating distance, the higher the sensitivity. The typical period of the gratings used for X-ray and neutron Talbot interferometry is on the order of a few microns. Since the gratings should have a high aspect ratio to ensure sufficient performance for X-rays or neutrons, it is not straightforward to further shorten the period with the current fabrication technology. The longer inter-grating distance (strictly speaking, the larger Talbot order) can also be selected if a long interferometer setting is allowed and the spatial coherence is sufficient. However, especially for the use in laboratory, compactness is an important property and a long inter-grating distance is not preferable.

In this study, we propose and demonstrate a new approach that requires neither a shorter grating period nor a longer interferometer length to increase the sensitivity. A phase grating with a rectangular structural profile fabricated by lithographic methods is widely used for Talbot interferometry. Here, we propose replacing such a phase grating with a pair of concave and convex parabolic phase gratings (L1 and L2), as shown in Fig. 1 [1]. This configuration is comparable to an array of Galilean telescopes, but here in this study the amplification function of the beam deflection is utilized.

In order to demonstrate this new approach experimentally, a pilot experiment was carried out using 17 keV X-rays on the beamline BL20XU, SPring-8, Japan. Concave and convex parabolic gratings made of nickel with a period of 10 μm were designed for this energy and fabricated by the X-ray LIGA technology at KIT. The focal length f_1 of L1 was 77 mm, and distance L between L1 and L2 was selected to be $f_1/2$. Figures 1(c) and 1(d) show a comparison of differential phase images obtained by the sensitivity-enhanced setup (Fig. 1(a)) and a conventional Talbot interferometer with a rectangular phase grating of the same period (Fig. 1(b)). The entire lengths of the both setups were almost the same but the differential phase signal was about twice, which was consistent with the theoretical

estimation, demonstrating the proof-of-concept of the signal enhancement successfully. In order to increase our understanding about optical design strategy, we also performed another experiment for surveying the enhancement effect regarding to the relation between f_1 and L. We found that the enhancement factor increases with L but $L < f_1$ (when L is close to f_1, the enhancement effect was unstable). We also found that the alignment between L1 and L2 in the lateral direction against the beam axis is not crucial, and the differential phase signal was almost constant within a certain range of misalignment. These details will also be described in the presentation.

In this study, the height of the Ni pattern limits the field of view, which corresponds to the vertical direction of Figs. 1(c) and 1(d) and was 60 μm. This constraint will be removed by tailoring parabolic profiles in the perpendicular direction against grating substrates. In addition, if a paraboloid two-dimensional array is formed, it would be possible to realize sensitivity enhancement in two directions. As a candidate technology for this purpose, two-photon lithography is attractive.

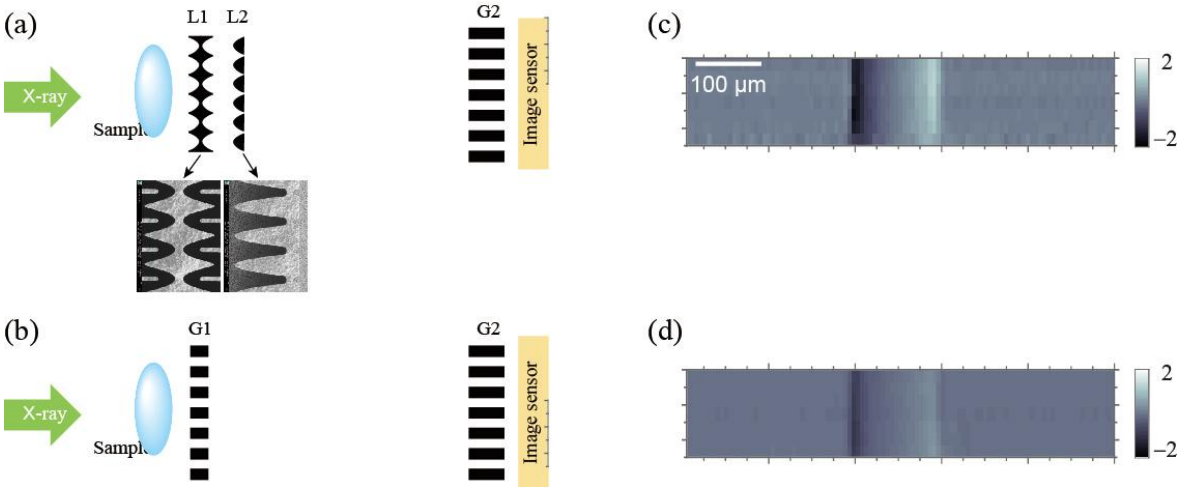

Figure 1: Sensitivity-enhanced Talbot interferometer with a pair of concave (L1) and convex (L2) parabolic phase gratings (a) and conventional Talbot interferometer with a rectangular phase grating (G1) (a). (c) and (d) are differential phase images measured by (a) and (b), respectively, with 17-keV synchrotron X-rays. The sample was a Nylon fiber 130 μm in diameter.

Acknowledgments

This work was financially supported by ERATO (Grant Number JPMJER1403) and SICORP (Grant Number JPMJSC1809), Japan Science and Technology Agency, and the BMBF via DLR under Contract No. 01DR18015A, Germany. The authors acknowledge the support of the Karlsruhe Nano Micro Facility (KNMFi), a Helmholtz Research Infrastructure at Karlsruhe Institute of Technology and furthermore M. Guttmann (KIT/IMT) for electroforming of lenses. The experiments were performed under the approval of the SPring-8 committee (2019B1321 and 2022B1356).

References

[1] P. Zangi, K. Ikematsu, P. Meyer, H. Takano, Y. Wu, J. Gutekunst, M. Börner, A. Last, J. G. Korvink, A. Momose, Sci. Rep. **13**, 9624 (2023).

Grating-Based X-ray Phase-Contrast and Dark-Field Imaging:

Recent Results from Basics Experimental Research, Algorithmic Developments and Clinical Translation from the Munich Lab

Franz Pfeiffer[1,2,3]

[1] *Chair of Biomedical Physics, School of Natural Sciences, Technical University of Munich, Germany*
[2] *Munich Institute of Biomedical Engineering, Technical University of Munich, 85748 Garching, Germany*
[3] *Department of Diagnostic and Interventional Radiology, Klinikum rechts der Isar, Munich, Germany*

Email: *franz.pfeiffer@tum.de*

The basic principles of X-ray image formation in radiography have remained essentially unchanged since Röntgen discovered X-rays over a hundred years ago. The conventional approach relies on X-ray attenuation as the sole source of contrast and uses only ray or geometric optics to describe and interpret image formation. This approach ignores another potentially more useful source of contrast, namely phase information. Phase-contrast (and Dark-Field) imaging techniques, which can be understood using wave optics rather than ray optics, offer opportunities to improve or complement standard attenuation contrast by incorporating phase information.

In this presentation, we will commence by briefly reviewing the basic physics that underpins grating-based phase-contrast and dark-field imaging [1,2]. We will then transition to highlighting some selected latest experimental advancements, focusing particularly on the cutting-edge techniques in grating fabrication. This includes the intricate process of fabricating X-ray absorption gratings by the centrifugal deposition of bimodal tungsten particles in high aspect ratio silicon templates [3], as well as the construction of X-ray absorption gratings using deep X-ray lithography with a conventional X-ray tube [4].

Further into the talk, we will delve into new algorithmic developments that are pushing the boundaries of imaging capabilities. An example of such innovation is the direct quantitative material decomposition employing grating-based X-ray phase-contrast CT [5].

Then, an overview of initial clinical results from patient studies will be presented, focusing on a range of lung diseases and the diagnostic enhancements provided by dark-field radiography [6,7]. We will explore the clinical value added, especially in the diagnosis and management of lung diseases such as COPD, lung emphysema, pulmonary fibrosis, lung cancer, and SARS-CoV-2.

Finally, the talk will provide an update on the current efforts and the achievements thus far in developing the first dark-field CT prototype suitable for human applications [8]. A novel dark-field Hounsfield scale will be introduced, aiming at the objective normalization of dark-field material parameters, with a particular focus on diagnosing lung diseases. The talk will also highlight the key algorithmic developments in CT reconstruction, which are essential for the advancement of this diagnostic technology [9,10].

The insights provided in this talk should be of great interest to anyone working in the fields of X-ray physics and biomedical imaging and diagnostics and will give an insight into the future of clinical imaging technologies. We conclude the lecture with an overview of the major challenges that still need to be overcome before this technology can be routinely used in clinical practice.

References

[1] Pfeiffer, F., Weitkamp, T., Bunk, O., & David, C. (2006). Phase retrieval and differential phase-contrast imaging with low-brilliance X-ray sources. Nature Physics, 2(4), 258-261.

[2] Pfeiffer, F., Bech, M., Bunk, O., Kraft, P., Eikenberry, E. F., Brönnimann, C., ... & David, C. (2008). Hard-X-ray dark-field imaging using a grating interferometer. Nature Materials, 7(2), 134-137.

[3] Pinzek, S., Gustschin, A., Gustschin, N., Viermetz, M., & Pfeiffer, F. (2022). Fabrication of X-ray absorption gratings by centrifugal deposition of bimodal tungsten particles in high aspect ratio silicon templates. *Scientific Reports*, *12*(1), 5405.

[4] Pinzek, S., Beckenbach, T., Viermetz, M., Meyer, P., Gustschin, A., Andrejewski, J., ... & Pfeiffer, F. (2021). Fabrication of x-ray absorption gratings via deep x-ray lithography using a conventional x-ray tube. *Journal of Micro/Nanopatterning, Materials, and Metrology*, *20*(4), 043801-043801.

[5] Braig, E., Böhm, J., Dierolf, M., Jud, C., Günther, B., Mechlem, K., ... & Pfeiffer, F. (2018). Direct quantitative material decomposition employing grating-based X-ray phase-contrast CT. *Scientific reports*, *8*(1), 16394.

[6] Willer, K., Fingerle, A. A., Noichl, W., De Marco, F., Frank, M., Urban, T., ... & Pfeiffer, F. (2021). X-ray dark-field chest imaging for detection and quantification of emphysema in patients with chronic obstructive pulmonary disease: a diagnostic accuracy study. *The Lancet Digital Health*, 3(11), e733-e744.

[7] Urban, T., Gassert, F. T., Frank, M., Willer, K., Noichl, W., Buchberger, P., ... & Pfeiffer, D. (2022). Qualitative and quantitative assessment of emphysema using dark-field chest radiography. *Radiology*, 303(1), 119-127.

[8] Viermetz, M., Gustschin, N., Schmid, C., Haeusele, J., von Teuffenbach, M., Meyer, P., ... & Pfeiffer, F. (2022). Dark-field computed tomography reaches the human scale. *Proceedings of the National Academy of Sciences*, 119(8), e2118799119.

[9] Schmid, C., Viermetz, M., Gustschin, N., Noichl, W., Haeusele, J., Lasser, T., ... & Pfeiffer, F. (2022). Modeling vibrations of a tiled Talbot-Lau interferometer on a clinical CT. *IEEE Transactions on Medical Imaging*, *42*(3), 774-784.

[10] Haeusele, J., Schmid, C., Viermetz, M., Gustschin, N., Lasser, T., Koehler, T., & Pfeiffer, F. (2023). Advanced Phase-Retrieval for Stepping-Free X-Ray Dark-Field Computed Tomography. *IEEE Transactions on Medical Imaging*.

Recent results and developments in edge-illumination x-ray phase contrast imaging

A. Olivo on behalf of the UCL Advanced X-Ray Imaging Group
Dept of Medical Physics and Biomedical Engineering, UCL, Gower St, London WC1E 6BT, UK

Edge-Illumination (EI) X-ray Phase Contrast Imaging (XPCI) was developed at the Elettra synchrotron in Italy in the late 90s [1], and translated for use with conventional x-ray sources at University College London in the mid-00s [2]. Since then, it has undergone significant development and new areas of application have constantly been targeted [3]. This talk will review a series of recent results of particular significance in specific areas of application (intra-operative imaging [4], digital histology [5], industrial [6] and security inspections [7]), introduce new technical developments especially in the areas of x-ray microscopy [8], high-energy [9] and dynamic imaging [10], and discuss underpinning principles related to e.g. what is effectively measured in scatter imaging scans [11] and how this differs from similar measurements performed with other techniques.

Acknowledgments
A. Olivo is supported by the Royal Academy of Engineering under their "Chairs in Emerging Technologies" scheme (CiET1819/2/78). Other relevant sources currently supporting the AXIm (Advanced X-ray Imaging) group includes a "Prosperity Partnership" EPSRC (part of UKRI) programme (grant EP/T005408/1), the National Institute of Biomedical Imaging and Bioengineering of the National Institutes of Health (Award No. R01EB028829), and the Innovative Research Call in Explosives and Weapons Detection, a Cross-Government programme sponsored by a number of Departments and Agencies under the UK Government's CONTEST strategy in partnership with the US Department of Homeland Security, Science and Technology Directorate.

Acknowledgments
[1] A. Olivo, PhD Dissertation, University of Trieste (Italy), Sept 1999
[2] A. Olivo and R. Speller, World Patent WO2008/029107, Priority Date 8 Sept 2006 (0617637.4)
[3] A. Olivo J. Phys.: Condens. Matter 33 (2021) 363002
[4] L. Massimi *et al*. Sci. Rep. 11 (2021) 3663
[5] L. Massimi *et al*. IEEE Trans. Med. Imaging 41 (2022) 1188-95
[6] D. Shoukroun *et al*. Compos. B Eng. 181 (2020) 107579
[7] T. Partridge *et al*. Nat. Commun. 13 (2022) 4651
[8] M. Esposito *et al*. Appl. Phys. Lett. 120 (2022) 234101
[9] A. Astolfo *et al*. Sci. Rep. 12 (2022) 3354
[10] L. Massimi *et al*. Phys. Rev. Lett. 127 (2021) 215503
[11] I. Buchanan *et al*. Appl. Phys. Rev. 10 (2023) 041406

The challenge of silicon-based manufacturing for high aspect ratio X-ray optics: a holistic approach

*L. ROMANO[1,2], Z. SHI[1,2], K. JEFIMOVS[2], D. JOSELL[3], A. PEREIRA[1,2], S. SPINDLER[1,2], Q. YU[1,2], L. CHEN[1,2], B. BENZ[2,4], M. RAWLIK[1,2], M. STAUBER[5], M. STAMPANONI[1,2]

[1]*Institute for Biomedical Engineering, University and ETH Zürich, 8092 Zürich, Switzerland*

[2]*Paul Scherrer Institut, 5232 Villigen PSI, Switzerland*

[3]*Materials Science and Engineering Division, NIST, USA*

[4]*Swiss Nanoscience Institute and Department of physics, University of Basel, Switzerland*

[5]*GratXray AG, Villigen, Switzerland*

Invited - Email: *lucia.romano@psi.ch*

Summary: Cutting edge micro- and nano-technologies for emerging applications in X-ray imaging and grating based X-ray interferometry from unique prototypes up to commercial devices are presented. Our microfabrication platform relies on silicon-based manufacturing technologies, which have been originally re-engineered to fulfil the high-quality requirements of X-ray Optics and to face up the main challenges of a unique fabrication technology. In view of a future realistic translation from a research-based to a real application, a holistic approach of defects engineering and device performances optimization is proposed.

X-ray Grating Interferometry (XGI) based imaging is a very promising, fast growing and competitive technique for medical [1], material science and security applications. The main bottleneck in X-ray Optics fabrication is the required high aspect ratio structure, whose quality and homogeneity strongly affect the performances of XGI. Our microfabrication platform relies on silicon-based manufacturing technologies, which have been originally re-engineered to fulfil the high-quality requirements of X-ray gratings. Our recent results including lithography [2], deep reactive ion etching (DRIE) [2,3], fan-shaped gratings [4,5], metal assisted chemical etching (MacEtch) [6-9], Au electroplating [10] with bottom-up gold feature filling [11,12] are reviewed, envisioning their advantages and drawbacks. The basic concept consists in creating a silicon template and filling it with highly X-ray absorbing metal (see Fig.1). With respect to LIGA-based approach, the silicon template fabrication requires two separate steps of patterning and pattern transfer in the substrate by highly anisotropic silicon etching. The advantage of this approach is the extremely high resolution of lithographic patterning techniques and the high precision of pattern transfer in silicon substrates, with demonstrated extreme high aspect ratio (up 10'000:1) at nanoscale [7]. The other side of the coin: being silicon a bulk crystal strongly limits the gold filling inside the template and the grating bending. Alternative solutions are bottom-up Au filling achieved using an accelerating electrolyte additive and fine electroplating potential tuning [11,12]. Grating bending can be addressed by reducing the substrate thickness and with a novel approach of fan-shape structure realized during the silicon etching step [4,5]. Etching defects might become relevant approaching trench depth in the range of 100 μm for aspect ratio higher than 50:1, several etching techniques have been explored in view of improving the quality control, new patterning strategies have been implemented to address the stability of high aspect ratio lamellas and the final performances in XGI.

Some examples (Fig. 1) are representative of our effective technological platform for X-ray optics fabrication with a large range of feature sizes and a sustainable manufacturing cost, useful for imaging systems with synchrotron [13] and tube [14] X-ray sources. Not only prototyping and large area scaling up of high aspect ratio gratings in gold, but also, we will discuss the main challenges in process engineering and reproducibility of the proposed protocols, the metrology issues associated with large area patterns, the reliability of XGI as

non-destructive characterization technique (scanning electron microscopy – SEM – requires cross sections with grating cleaving), the bending issues. In view of a future realistic translation from a research-based level to a real application, a new holistic approach of defects engineering in combination with XGI simulations promises an improved device fabrication by optimizing the performances as a function of the grating's fabrication offer and peculiarities.

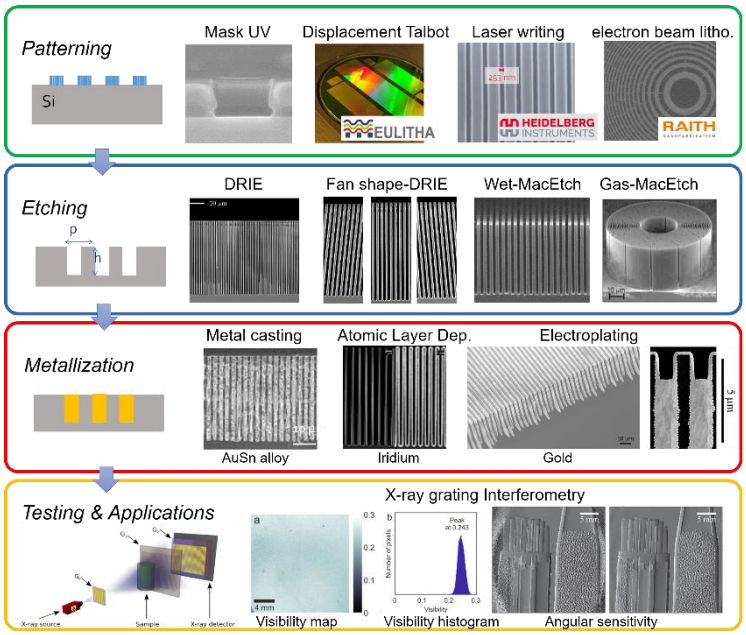

Figure 1: Conceptual map of silicon-based microfabrication: patterning, silicon etching and metallization steps (representative SEM images [3,4,6,7,10,12]). XGI assesses the grating quality, via visibility and angular sensitivity data [4,11,14].

Acknowledgments

We thank PSI clean room, coauthors [1-14], all former and current members of the grating fabrication team, the following funding agencies: SNF Sinergia Grant Nr. CRSII5 183568, PHRT-TT Project Nr. 2022-572 INTIMACY, SwissLOS Lottery Fund of Kanton Aargau, SNF R'Equip 189662 (SiDRY) and 177036 (DTL), PHRT-Pioneer Project Nr. 2021-612 CLARINET, Promedica Stiftung Chur - Project Nr. 1527, SNI PhDSchool Project Nr. P2205 MAGNET.

References

[1] M. Rawlik et al., Optica **10**, 938-943 (2023)
[2] Z. Shi et al., Japanese Journal of Applied Physics **60**, SCCA01 (2021)
[3] Z. Shi et al., Micromachines **11**, 864 (2020)
[4] Z. Shi et al., Opt. Lett. **46**, 3693-3696 (2021)
[5] Z. Shi et al., Applied Surface Science **588**, 152938 (2022)
[6] L. Romano et al., Advanced Engineering Materials **22**, 2000258 (2020)
[7] L. Romano et al., Nanoscale Horizons **5**, 869-879 (2020)
[8] Z. Shi et al., Materials Science in Semiconductor Processing **157**, 107311 (2023)
[9] M. M. Halvorsen et al., NIMA **1060**, 169046 (2024)
[10] K. Jefimovs et al., Micromachines **12**, 517 (2021)
[11] D. Josell et al., Journal of The Electrochemical Society **168**, 082508 (2021)
[12] D. Josell et al., Journal of The Electrochemical Society **167**, 132504 (2020)
[13] Z. Shi et al., Appl. Opt. **61**, 3850-3854 (2022)
[14] J. Vila-Comamala et al., Opt. Express **29**, 2049-2064 (2021)

Dark-field retrieval via the X-ray Fokker-Planck equation

Kaye S. Morgan[1],* Thomas Leatham[1], Jannis Ahlers[1], Mario Beltran[1], David Paganin[1]
[1]*School of Physics and Astronomy, Monash University, Australia*
Email: *kaye.morgan@monash.edu*

Summary: X-ray phase and dark-field imaging rely upon the use of either optics or mathematical models to make sense of variations in intensity. These models enable the retrieval or reconstruction of phase and dark-field images from the captured x-ray intensity image(s). One such model that is widely used in propagation-based phase contrast imaging is the Transport-of-Intensity Equation, which describes how x-ray intensity evolves as x-rays propagate, including phase effects. We have extended this model to incorporate dark-field effects, resulting in the X-ray Fokker-Planck equation [1, 2]. Here we present several novel dark-field retrieval approaches that arise from the FPE, for single-grid/speckle-based and propagation-based imaging set-ups [3-6].

X-ray phase contrast imaging has emerged in recent decades as a tool for capturing images of weakly-attenuating samples like the lungs, achieved by extracting how the x-ray wavefield changes in phase as it passes through the sample. A variety of set-ups have been employed, utilising gratings, the reflection of x-rays from crystals, or simply the self-interference of the x-ray wavefield with propagation, in what is known as a propagation-based set-up. One of the most widely-used approaches in propagation-based imaging for retrieving a phase image is based upon the Transport-of-Intensity Equation (TIE). Phase retrieval is achieved by inverting the TIE and inserting the observed x-ray image [7].

X-ray dark-field imaging has emerged more recently, able to map the presence of any microstructures within the sample that incoherently scatter the x-ray wavefield. X-ray dark-field imaging has primarily been achieved using crystal and grating-based set-ups. Because the Transport-of-Intensity Equation does not include dark-field effects, it cannot be used to retrieve a dark-field image from propagation-based images. In any case, dark-field effects have generally been assumed to be negligible in propagation-based set-ups. However, if there is sufficient local contrast in a propagation-based image, a local 'blurring-out' may indeed be observed, as seen in Fig. 1a. This effect can be more easily seen in a single-grid or speckle-based set-up, where a structured illumination is projected upon the sample, using a grid, or a piece of sandpaper to generate speckle. In these set-ups, local blurring or a reduction in the visibility of the illumination is seen some distance downstream (Fig. 1b) and extracted to form a dark-field image. In essence, the dark-field effects in propagation-based images are the same as those seen in single-grid/speckle-based set-ups, but now the sample is acting as the grid/sandpaper, creating its own 'structured illumination', which can be blurred out in the presence of dark-field effects.

To extract dark-field images from intensity data captured on a propagation-based set-up, we can use an extension to the Transport-of-Intensity Equation that does incorporate dark-field effects, the X-ray Fokker-Planck Equation [1, 2]. This equation describes how an x-ray beam can shift transversely due to phase effects and spread out or diffuse due to dark-field effects [8]. Effectively, it is the TIE, with an additional term for dark-field effects. To extract attenuation, phase and dark-field effects, three different measurements would typically be required, where some part of the system is changed between measurements, such as the x-ray energy or the sample-to-detector distance. This can be reduced to two measurements if we assume the sample is largely composed of a single material, so that

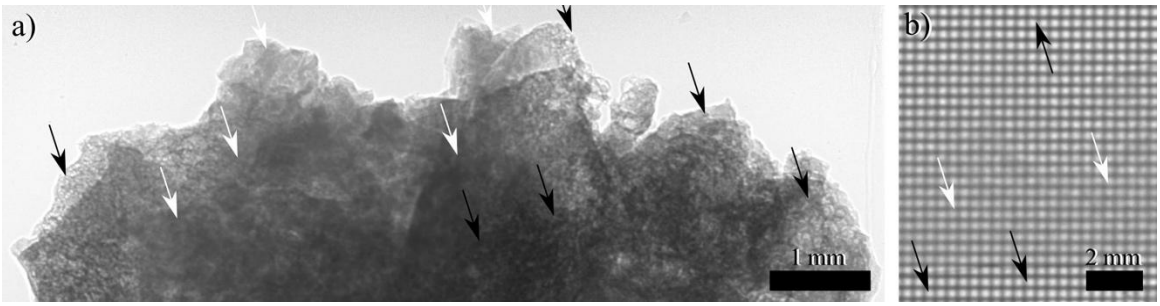

Figure 1: a) A propagation-based x-ray image of a piece of coal, captured at the Australian Synchrotron's MicroCT beamline by Benedicta Arhatari and Andrew Stevenson, using a white beam, 1.5m propagation. The black arrows indicate areas of the image where dark-field effects are weak, and fine details are observed. The white arrows indicate areas where dark-field effects are visible, with the image detail appearing blurred, with less contrast and broader features. Dark-field effects are generated by micropores in the piece of coal. b) A single-grid-based x-ray image of 6 micron spheres behind a 151 micron period grid, 25keV, captured at the Australian Synchrotron's Imaging and Medical beamline, showing similar dark-field effects [6].

attenuation and phase are linked to the thickness of the sample.

Here we present the results of retrieving sample thickness and a dark-field image using propagation-based x-ray images at two different sample-to-detector distances [3, 4]. At the shorter distance, phase and attenuation effects are most visible, allowing a high-resolution retrieval of the sample thickness. At the larger distance dark-field effects become evident (e.g. as seen in Fig. 1a), and can be retrieved by inverting the Fokker-Planck Equation.

As an alternative, we present how sample thickness and dark-field images can be retrieved by capturing propagation-based images at two different x-ray energies [5]. In this case, the dark-field effects are more visible at the lower x-ray energy. This approach presents advantages in the case of using an energy-resolving detector, since both images can be captured with the same magnification and position within the one exposure.

Finally, we show how a Fokker-Planck approach can be used in single-grid/speckle-based imaging (e.g. Fig. 1b) to retrieve a dark-field image, an approach which has been seen to be robust to noise in the raw intensity image [6].

Acknowledgments

This research was undertaken on the Imaging and Medical Beamline, and MicroCT Beamline, both at the Australian Synchrotron, part of ANSTO, and was supported by the Australian Research Council (FT180100374, DP230101327). Many thanks to Benedicta Arhatari and Andrew Stevenson for Fig. 1a.

References

[1] Morgan, K.S. and Paganin, D.M., Applying the Fokker–Planck equation to grating-based x-ray phase and dark-field imaging. *Scientific Reports*, 9(1), 17465 (2019).

[2] Paganin, D.M. and Morgan, K.S., X-ray Fokker–Planck equation for paraxial imaging. *Scientific Reports*, 9(1), 17537 (2019).

[3] Leatham, T.A., Paganin, D.M. and Morgan, K.S., X-ray dark-field and phase retrieval without optics, via the Fokker–Planck equation. *IEEE Transactions on Medical Imaging,* 42(6), p.1681-1695 (2023).

[4] Leatham, T.A., Paganin, D.M. and Morgan, K.S., X-ray phase and dark-field computed tomography without optical elements. *arXiv:2310.09496,* Accepted, *Optics Express* (2023).

[5] Ahlers, J.N., Pavlov, K.M., Kitchen, M.J. and Morgan, K.S., X-ray dark-field via spectral propagation-based imaging. *arXiv preprint arXiv:2309.15874* (2023).

[6] Beltran, M.A., Paganin, D.M., Croughan, M.K. and Morgan, K.S., Fast implicit diffusive dark-field retrieval for single-exposure, single-mask x-ray imaging. *Optica*, 10(4), p.422-429 (2023).

[7] Paganin, D., Mayo, S.C., Gureyev, T.E., Miller, P.R. and Wilkins, S.W., Simultaneous phase and amplitude extraction from a single defocused image of a homogeneous object. *Journal of Microscopy*, 206(1), p.33-40 (2002).

[8] Paganin, D.M., Pelliccia, D. and Morgan, K.S., 2023. Paraxial diffusion-field retrieval. *Physical Review A*, 108, 013517 (2023).

Multi-directional neutron dark-field imaging with single absorption grating

MATTEO BUSI[1], *MARKUS STROBL[1]
[1]*Applied Materials Group, Paul Scherrer Institute, 5232 Villigen, Switzerland*
Email: *markus.strobl@psi.ch*

Summary: Neutron dark-field imaging is a valuable technique for exploring material microstructures, offering high-resolution mapping through small-angle scattering. Conventional methods using Talbot-Lau interferometers are limited to probing one scattering direction at a time. A new approach is introduced, employing a single absorption grating with a two-dimensional pattern to simultaneously capture multiple scattering directions. This technique was successfully used to resolve fiber orientations in carbon compound materials and to reveal the complex morphology of transformed martensitic phases in additively manufactured stainless steel samples.

Neutron dark-field imaging is a potent technique for investigating into the microstructural characteristics of materials by employing high-resolution full-field mapping of ultra small-angle scattering [1]. However, the conventional approach, utilizing Talbot-Lau interferometers, faces a constraint in its ability to probe only one scattering direction at a time due to the line grating utilized. In this contribution, we introduce a multi-directional neutron dark-field imaging approach, employing a single absorption grating with a two-dimensional pattern [2]. This innovative technique allows for the simultaneous probing of multiple scattering directions, alongside conventional attenuation and differential phase contrast. Furthermore, we show that the autocorrelation probed by using this approach, which is primarily limited by high L/D collimation ratio, can be dramatically increased by taking advantage of the inverse-pattern regime [3].

The efficacy of this method is demonstrated through successful applications, including the resolution of fiber orientations in a carbon compound material (see Fig. 1). Additionally, the approach proves instrumental in unraveling the complex morphology of the transformed martensitic phase in additively manufactured stainless steel dogbone samples following mechanical deformation. Notably, the results unveil a preferential alignment of transformed domains parallel to the load direction, a finding validated by electron backscatter diffraction (EBSD). Real-space correlation functions derived from our method exhibit excellent agreement with those extracted from the EBSD map.

The presented results underscore the capability of multi-directional neutron dark-field imaging to overcome significant limitations of conventional techniques, particularly in assessing complex, heterogeneous, and anisotropic microstructures. Importantly, this approach provides quantitative structural information across multiple length scales. Moreover, its seamless integration with a time-of-flight approach is facilitated by the grating's constant visibility across different wavelengths, rendering it achromatic. This integration enhances the versatility of the method and expands its applicability in the investigation of materials with diverse properties and behaviors, further solidifying its standing as a robust tool in the realm of materials science and imaging technologies.

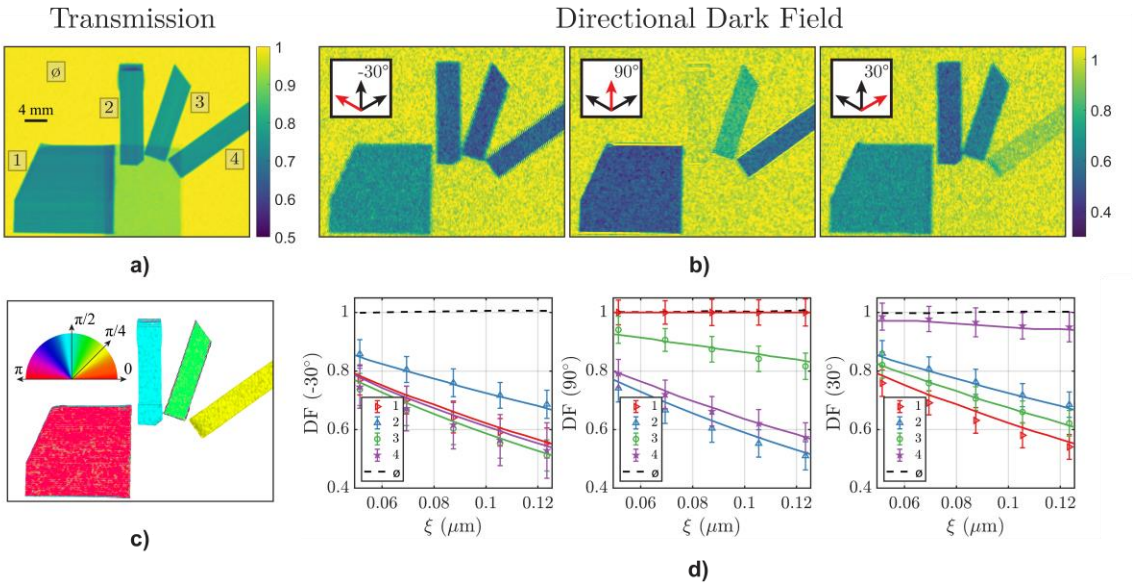

Figure 1. *a) Attenuation contrast image of the carbon fiber samples (attached to an aluminum plate). b) Directional dark-field contrast images of the carbon fibers samples using an hexagonal pattern grating. The scattering direction probed in the corresponding graphs is shown as red arrow in the insets. c) Microstructural orientation map of the carbon fibers. d) Autocorrelation length curves of the four carbon fiber samples and the background (black-dashed line), for the three probed scattering directions. The solid lines are the theoretical curves, obtained from calculations with the known structural parameters, whereas the markers are the measured values in the respective regions-of-interest with corresponding error bars.*

Acknowledgments

The authors acknowledge grant of internal beamtime at the ICON beamline of Paul Scherrer Institute.

References

[1] Strobl, Markus. "General solution for quantitative dark-field contrast imaging with grating interferometers." *Scientific reports* 4.1 (2014): 7243.

[2] Busi, Matteo, et al. "Multi-directional neutron dark-field imaging with single absorption grating." *Scientific Reports* 13.1 (2023): 15274.

[3] Busi, Matteo, et al. "Cold and thermal neutron single grating dark-field imaging extended to an inverse pattern regime." *Applied Sciences* 12.6 (2022): 2798.

The neutron grating imaging system and its progress at CSNS

Jie Chen[1,2], Shengxiang Wang[1,2]

[1]*Institute of High Energy Physics, Chinese Academy of Sciences; Beijing, 100049, China.*

[2]*Spallation Neutron Source Science Center, Dongguan 523803, China*

Neutron grating interferometry imaging offers unique capabilities in studying the internal structures and properties of materials by providing scattering images, making it an invaluable tool for scientific research and industrial applications. In the scattering zoom of the energy-resolved neutron imaging instrument (ERNI) at the China Spallation Neutron Source (CSNS), a traditional Talbot-Lau grating interferometery with a designed length of two meters has been installed, along with a symmetric interferometry setup. The adjustment platforms for the G1 and G2 gratings are installed on the guide rails on different sides of the system, to facilitate the transition from the traditional Talbot-Lau setup to the symmetric setup. The field of view for the system is about 60mm ×60mm. Neutron has high penetration and a magnetic moment. The potential applications of neutron grating interferometry imaging include metals and alloys3, magnetic domain visualization and so on.

Neutron Phase Imaging of Additively Manufactured Metallic Materials at Kyoto University Reactor

Yoshichika Seki[1], Takenao Shinohara[2], Masahiro Hino[3], Mugeng Li[3], Riichiro Nakamura[2]
Tetsuo Samoto[1], Yoshiki Terakawa[1], Atsushi Momose[1]
[1]*Institute of Multidisciplinary Research for Advanced Materials, Tohoku University, Japan*
[2]*J-PARC Center, Japan Atomic Energy Agency, Japan*
[3]*Institute for integrated Radiation and Nuclear Science, Kyoto University, Japan*
Email: *yoshichika.seki.e6@tohoku.ac.jp*

Summary: Metal additive manufacturing technology has rapidly advanced in recent years, bringing innovation for the manufacturing industry. One of its quality issues is the presence of microvoids within fabricated objects. At the Kyoto University Research Reactor, we are developing a non-destructive observation method for the microvoids using visibility imaging of neutron Talbot-Lau interferometry. We successfully examined variations in the size of defects caused by hot isostatic pressing process. Ongoing research extends this method to metal samples with various process parameters, attempting a quantitative analysis of defect characteristics.

Metal additive manufacturing, a process involving the melting and solidification of metallic material using laser or electron beams to make three-dimensional objects layer on layer, is a promising process method, and vigorous research is being carried out to improve its quality. In particular, laser powder bed fusion method (L-PBF) can provide superior dimensional accuracy and surface roughness compared to other methods, making it suitable for components for space and aviation that require durability. However, depending on the fabrication conditions, defects (mainly microvoids ranging in size from a few micrometers to several hundred micrometers) can be formed in the fabricated objects, resulting in a decrease of their fatigue strength. These defects are usually detected through destructive observation using optical microscopes within a limited field of view. While the X-ray CT technique is occasionally employed as a non-destructive method, it is unsuitable for thick metals and is incapable of detecting defects smaller than a few micrometers.

We have been developing a non-destructive observation method for microvoids in metallic objects by L-PBF, using visibility (dark-field) imaging of neutron Talbot-Lau (TL) interferometry. The visibility imaging is sensitive to the small-angle scattering intensity caused by microvoids, and can visualize it a relatively large area (~ several hundred m^2) of gratings. The development has been conducted at the CN-3 port of the Kyoto University Research Reactor (KUR). At this port, a neutron phase imaging system with a TL interferometer has been installed for regular use. Due to 20 μm-thick gadolinium absorbers on absorption gratings, clear moiré fringes with a visibility of 55% were observed for neutron beams with a peak wavelength of 2.0 Å.

We first observed rods of nickel-based alloy Inconel 718 with a diameter of 12 mm made by L-PBF. Since the as-made sample by additive manufacturing typically exhibits internal microvoids of the order of micrometers, post-processing with hot isostatic pressing (HIP) is often employed to mitigate these defects. To investigate the effect of the HIP process, the measurements were performed on rods with and without HIP treatment, respectively. For visibility imaging, each sample were observed at two different positions in the interferometer, corresponding to the size scale of microvoids (i.e., auto-correlation length

of visibility imaging) ξ = 0.3 μm and 4 μm. Figure 1 displays the absorption, the differential-phase, and the visibility images of the two rods obtained at a sample position of ξ = 4 μm. The average differential-phase profile of the two rods, as shown in Fig. 2(a), were almost consistent with each other, demonstrating that the HIP process did not induce microscopic density change in the rods. On the contrary, the average visibility profiles plotted in Fig. 2(b) and (c) show clear differences between the two rods. At ξ = 4 μm (Fig. 2(b)), the visibility recovered significantly after the HIP process while at ξ = 0.3 μm (Fig. 2(c)) this relation is reversed. These results indicate that HIP process diminished microvoids in the rod to sub-micrometers scale from its original size of the order of micrometers. In addition, we performed a computed tomography (CT) of the HIP treated rod with visibility images at ξ = 0.3 μm. The resultant contrast in Fig. 3 visualized the three-dimensional distribution of miniaturized defects that remain even after the HIP process.

Furthermore, we have recently started visibility imaging of 1 cm^3 cubic samples of AlSi10Mg, Ti6Al4V, SUS316L, and Inconel 718, fabricated with varying process parameters of L-PBF, specifically laser power and scanning speed. The obtained visibility contrasts were in agreement with the relative density differences evaluated by the Archimedean method. For a quantitative analysis of visibility signals, theoretical models considering void shape, fraction, and their anisotropy were attempted. These results will also be presented.

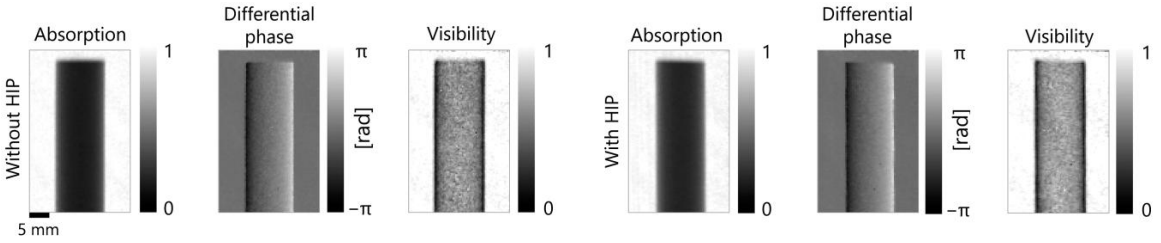

Figure 1: Absorption, differential-phase, and visibility images of Inconel 718 rods with/without HIP process at a sample position of ξ = 4 μm.

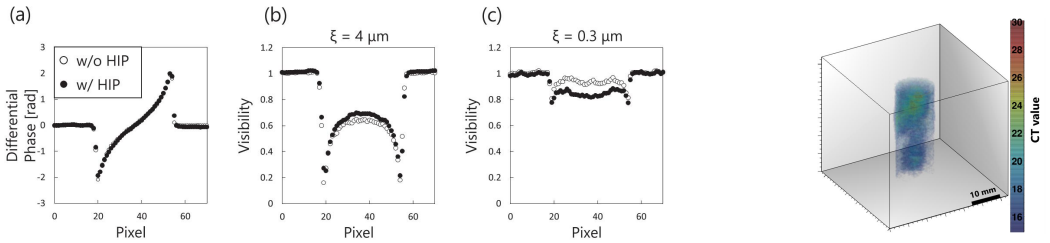

Figure 2 (Left): Average horizontal profiles of (a) differential-phase imagese; (b) visibility images at ξ = 4 μm; and (c) visibility images at ξ = 0.3 μm. Figure 3 (Right): Visibility CT of Inconel 718 rod with the HIP process at ξ = 0.3 μm.

Acknowledgments
This work was supported by JST ERATO (Grant Number JPMJER1403) and JSPS KAKENHI (Grant Number 20H00215). The development was further facilitated by Tohoku University nanofabrication platform in the nanotechnology platform project sponsored by the Ministry of Education, Culture, Sports, Science and Technology (MEXT). The experiments were performed under the Visiting Researcher's Program of the Institute for Integrated Radiation and Nuclear Science, Kyoto University.

References

[1] Y. Seki, T. Shinohara, M. Hino, R. Nakamura, T. Samoto, and A. Momose, Rev. Sci. Instrum. **94**, 103701 (2023).

Quantitative modeling of dark-field image formation

* Fabio DE MARCO[1,2]
[1]*Department of Physics, University of Trieste, Italy*
[2]*Elettra Synchrotron, Basovizza, Italy*
Email: *fabiodomenico.demarco@units.it*

Summary: The dark-field modality represents the amount of visibility reduction in a grating-based or wavefront-marking imaging setup by a sample. It is usually related to small-angle scatter generated by the sample, and thus encodes information similar to that retrieved by the USAXS/USANS technique. However, retrieving comparably quantitative information in a dark-field imaging experiment can be difficult.
We here present two aspects that aim to describe the imaging process quantitatively: a generalization of the Yashiro-Lynch model for arbitrary wavefront markers, and "visibility-hardening", an effect similar to beam-hardening that affects the dark-field signal magnitude in polychromatic illumination.

A model relating microstructural parameters to the dark-field modality has previously been developed for grating-based imaging [1–3]. For a sample downstream of the modulation grating, the monochromatic dark-field signal (using 1D gratings) is related to the z-projected autocorrelation function $G(\boldsymbol{\xi})$ of the object's electron density in a single point

$$\boldsymbol{\xi} = [\xi_x, \xi_y] = [0, \lambda L/p], \quad (1)$$

with L the sample-detector distance, and p the pitch of the detected grating self-image.
By considering scatter as a convolution of intensities with a (slowly varying) blur kernel, and interpreting the effect on measured intensities in Fourier space, we derived an equivalent model applicable to measurements with arbitrary wavefront markers, such as sandpaper. If no analyzer grating is used, we can generalize visibility at a spatial frequency $\mathbf{f} = [f_x, f_y]$ as the magnitude of the 2D Fourier transform of the measured intensity pattern, normalized by the mean. We then find that the reduction factor of this visibility $V(\mathbf{f})$ is determined by $G(\boldsymbol{\xi})$ at

$$\boldsymbol{\xi}(\mathbf{f}) = \lambda L \mathbf{f}. \quad (2)$$

Thus, when a non-periodic wavefront marker is used, a wide range of $\boldsymbol{\xi}$ values is being sampled, and a greater amount of scattering information is retrievable. In a given two- or three-grating interferometer configuration, only a single value of $\boldsymbol{\xi}$ contributes, so either λ or L must be varied to achieve comparable information [1, 2, 4].
We validate our approach with speckle-based measurements of microsphere suspensions performed at the SYRMEP beamline of the Elettra synchrotron. At a photon energy of about 24 keV, three microsphere diameters (0.17 / 0.26 / 0.51 μm), three propagation distances (0.69 / 1.21 / 1.68 m), and two sample depths (4 / 10 mm) were tested. By numerically solving $G(\boldsymbol{\xi})$ for concentrated solutions [5], particle size, scatter strength, and volume fraction of the scatterers could be retrieved by regression of our model to the data. Measured particle sizes are in good agreement with the listed microsphere diameters. However, since the beam was only roughly monochromatized by a filter, we observe some deviations due to the remaining polychromaticity.

Secondly, we present the "visibility-hardening" effect [5]. Like beam-hardening, it appears in setups with polychromatic sources, where it leads to a deviation of the exponential Beer-Lambert relationship between signal strength and sample thickness, and can thus induce "cupping" artifacts in tomographic measurements. We note that this effect is distinct from

the (already known) effect of beam-hardening on visibility—visibility-hardening can be observed even if attenuation is negligible.
This phenomenon obviously affects the interpretation of dark-field signal values in polychromatic illumination, and is thus relevant for lab-based dark-field applications, especially when a very strong dark-field signal is generated. We provide a comprehensive mathematical description, which allows estimating the impact of the effect for a given setup and sample, and validate it with experiments of a phantom consisting of attenuating and scattering materials (aluminum and EPDM foam) in a lab-based, three-grating X-ray dark-field imaging setup operated at 60 kV.

Both effects are "forward models," i.e., they predict measurement results from not directly observable quantities. For practical use in imaging, these need to be solved in the opposite direction, i.e., be treated as inverse problems. This requires precise knowledge of experimental parameters (such as the X-ray spectrum), and certain assumptions about experimentally inaccessible parameters (e.g., the shape of the scattering particles). We discuss these limitations and some possible approaches for solving these inverse problems.

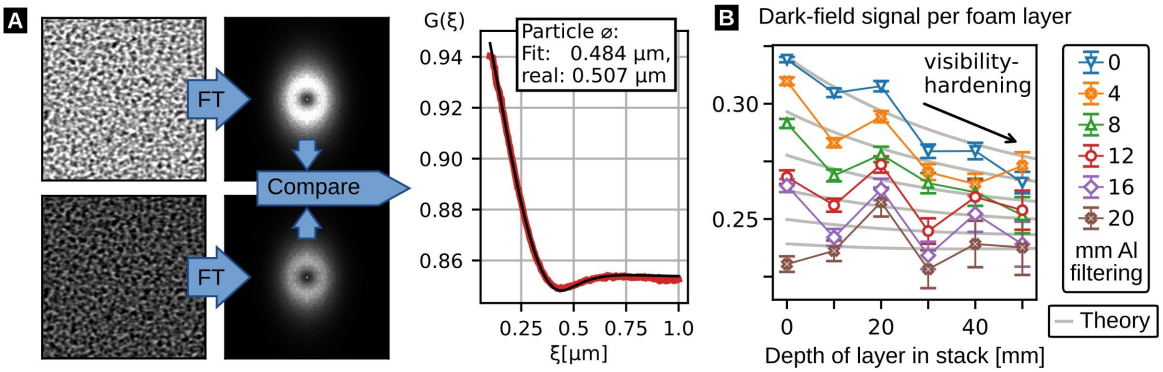

Figure 1: (a) Comparing the Fourier magnitudes of speckle patterns recorded with and without sample allows extraction of quantitative structural parameters. (b) Under polychromatic illumination, visibility-hardening decreases an object's dark-field when preceded by other dark-field-active objects.

Acknowledgments
The shown work was partly performed in the group of Prof. Franz Pfeiffer (Chair of Biomedical Physics, Technical University of Munich), and partly in the group of Prof. Pierre Thibault (Department of Physics, University of Trieste). I acknowledge my colleagues J. Andrejewski, T. Urban, K. Willer, L. Gromann, T. Koehler, H.-I. Maack, J. Herzen, S. Savatović, V. Di Trapani, M. Margini, G. Lautizi, and thank them for their contributions. I acknowledge Elettra Sincrotrone Trieste for providing access to its synchrotron radiation facilities and thank Dr. Giuliana Tromba and Dr. Adriano Contillo for assistance in using the SYRMEP beamline. Beamtime was allocated for proposal 20215615. This work is part of a project that has received funding from the European Research Council (ERC) under the European Union's Horizon 2020 research and innovation program (Grant agreement No. 866026). This work was carried out with the support of the Karlsruhe Nano Micro Facility (KNMF, www.kit.edu/knmf), a Helmholtz Research Infrastructure at Karlsruhe Institute of Technology (KIT).

References

[1] S. K. Lynch *et al.*, *Appl. Opt.* **50**, 4310–4319 (2011).
[2] W. Yashiro, Y. Terui, K. Kawabata, A. Momose, *Opt. Express*. **18**, 16890–16901 (2010).
[3] M. Strobl, *Sci. Rep.* **4**, 7243 (2014).
[4] F. Prade, A. Yaroshenko, J. Herzen, F. Pfeiffer, *EPL*. **112**, 68002 (2015).
[5] S. Gkoumas *et al.*, *Sci. Rep.* **6**, 35259 (2016).
[6] F. De Marco *et al.*, *IEEE Trans. Med. Imaging* (2023).

Dual phase grating interferometry theory and applications

Yongshuai Ge[1,2], Peiping Zhu[3], Yuhang Tan[1,2]

[1]*Research Center for Medical Artificial Intelligence, Shenzhen Institute of Advanced Technology, Chinese Academy of Sciences, Shenzhen, 518055, China*
[2]*Paul C Lauterbur Research Center for Biomedical Imaging, Shenzhen Institute of Advanced Technology, Chinese Academy of Sciences, Shenzhen 518055, China*
[3]*Institute of High Energy Physics, Chinese Academy of Sciences, Beijing 100049, China*

Email: ys.ge@siat.ac.cn

Summary: As a new type of X-ray grating interferometer, dual phase grating interferometer systems [1-3] potentially have higher radiation dose efficiency for differential phase contrast (DPC) imaging than the conventional Talbot-Lau interferometer by replacing the absorption analyzer grating with phase grating.

In this talk, a rigorous theoretical framework [4] using wave optics will be presented to explain the working mechanism of the grating based X-ray differential phase contrast imaging (XPCI) interferometer systems consist of more than one phase grating. Under the optical reversibility principle, the wave optics interpretation was simplified into the geometrical optics interpretation, in which the phase grating was treated as a thin lens. Namely,

$$\frac{1}{d_i}+\frac{1}{r_i}=\frac{1}{f_i}$$

where f_i is expressed as:

$$f_i=\frac{2l_i+1}{8}\frac{p_i^2}{\lambda}, l_i \in Z$$

It is found that the optical reversibility and symmetry are mainly for the source grating period p_0 and diffraction fringe period p_f. In other words, if the arrayed source has a period of p_0, the forward imaging procedure would generate diffraction fringe with period of p_f. As a contrary, when the arrayed source has a period of p_f, the backward imaging procedure would generate diffraction fringe with period of p_0. This is to say p_f is equal to the period of the formed image of the source on the detector plane, and p_0 is equal to the period of the formed fringe on the source plane. Moreover, the theory indicates that it is better to keep the periods of the two phase gratings different to generate large period diffraction fringes when a source grating is utilized. Experimental results will be presented to validate these theoretical findings.

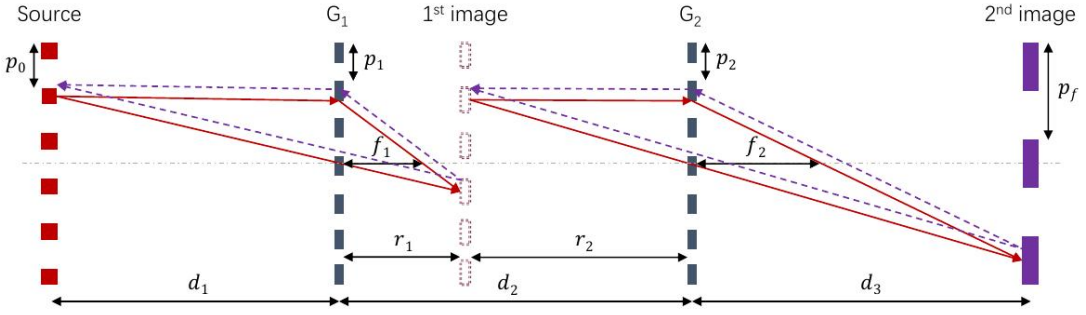

Figure 2: Illustration of the thin lens interpretation of a dual phase grating setup. G_1 and G_2 are phase gratings. Herein, the solid arrows represent the forward imaging procedure, in which an arrayed source (in red color)

positioned on the left hand side is assumed. Additionally, the backward imaging procedure is schemed by the dashed arrows, in which the arrayed source (in purple color) is assumed on the right hand side.

To predict the angular sensitivity responses of the dual phase grating differential phase contrast (DPC) interferometers, an alternative approach is proposed to estimate the sensitivity [5] of a dual phase grating X-ray interferometer, which is assumed working at the optimal visibility responses. Specifically, the sensitivity response of every phase grating is determined independently, and the global sensitivity responses of the dual phase grating imaging systems are obtained by jointing the two cascaded individual responses together, namely,

$$S: \begin{cases} S_1 = 4 \times \begin{cases} \dfrac{|f_1|(l_1 + z_1)}{p_1 l_1}, & \text{if } -l_1 \le z_1 < 0, \\ \dfrac{|f_1|(|r_1| - z_1)}{p_1 |r_1|}, & \text{if } \min(r_1, 0) \le z_1 \le \max(r_1, 0), \end{cases} \\ S_2 = 4 \times \begin{cases} \dfrac{|f_2|(|l_2| + z_2)}{p_2 l_2}, & \text{if } -|l_2| \le z_2 < 0, \\ \dfrac{|f_2|(r_2 - z_2)}{p_2 r_2}, & \text{if } 0 \le z_2 \le r_2. \end{cases} \end{cases}$$

where S_1 denotes the sensitivity response of the first phase grating, and S_2 denotes the sensitivity response of the second phase grating. In addition, the sensitivity responses (particularly the magnitude) of two distinct imaging scenarios, i.e., real and virtual source images, are determined and validated. Compared to the real source setup, the virtual source setup could help to avoid the zero (or very low) sensitivity response located between G1 and G2. However, the periods of G1 and G2 have to be slightly varied to generate the virtual source image. Using this new sensitivity prediction method, the DPC imaging performance of a dual-phase grating system could be further optimized.

Based on a dual phase grating interferometer, its energy resolving capability is explored [6] with the aim to accelerate the data acquisition speed of dark-filed imaging when quantifying the dimension of micro-structures inside an object. To do so, both theoretical analyses and numerical simulations are investigated. Specifically, the responses of the dual phase grating interferometer at varied X-ray beam energies are studied. Results show that the fringes generated from dual $1.5\,\pi$ phase grating interferometer outperform the ones generated from dual $0.5\,\pi$ phase grating system with higher fringe visibility and signal uniformity. Results demonstrate that the micro-bubble size can be accurately predicted from the energy resolved dark-filed projections that are acquired with only half number of mechanical movements. Compared with the mechanical position translation approach, thereby, the combination of such energy resolving capability helps to greatly shorten the total dark-field imaging time in dual phase grating interferometer.

References

[1] M. Kagias, Z. Wang, K. Jefimovs, and M. Stampanoni, “Dual phase grating interferometer for tunable dark-field sensitivity,” Appl. Phys. Lett. 110, 014105 (2017).

[2] A. Yan, X. Wu, and H. Liu, “Quantitative theory of x-ray interferometers based on dual phase grating: fringe period and visibility,” Opt. Express 26, 23142–23155 (2018).

[3] A. Yan, X. Wu, and H. Liu, “Clarification on generalized lau condition for x-ray interferometers based on dual phase gratings,” Opt. Express 27, 22727–22736 (2019).

[4] Ge, Yongshuai, Jianwei Chen, Peiping Zhu, Jun Yang, Shiwo Deng, Wei Shi, Kai Zhang et al. "Dual phase grating based X-ray differential phase contrast imaging with source grating: theory and validation." Optics Express 28, no. 7 (2020): 9786-9801.

[5] Ge, Yongshuai, Jianwei Chen, Jiecheng Yang, Peiping Zhu, Huitao Zhang, Hairong Zheng, and Dong Liang. "Angular sensitivity of an x-ray differential phase contrast imaging system with real and virtual source images." Optics Letters 46, no. 11 (2021): 2791-2794.

[6] Cai, Xuebao, Yuhang Tan, Xin Zhang, Jiecheng Yang, Jinyou Xu, Hairong Zheng, Dong Liang, and Yongshuai Ge. "Energy resolving dark-field imaging with dual phase grating interferometer." Optics Express 31, no. 26 (2023): 44273-44282.

Clinical Dark-Field Radiography of the Human Lungs

Henriette Bast[1,2,3],Rafael Schick[1,2,3],Theresa Urban[1,2,3],Manuela Frank[1,2,3],Konstantin Willer[1,2,3],Thomas Koehler[4,5],Florian T. Gassert[3],Daniela Pfeiffer[3,5],Franz Pfeiffer[1,2,3,5]

1. Technical University of Munich

2. Munich Institute of Biomedical Engineering, Technical University of Munich, Germany

3. Department of Diagnostic and Interventional Radiology, Klinikum rechts der Isar, Munich, Germany

4. Philips Innovative Technologies, Hamburg, Germany

5. Munich Institute for Advanced Study, Technical University of Munich, Germany

Summary: Dark-field chest radiography is an emerging X-ray imaging technology that provides information about the structural integrity of human lungs using small-angle scattering. Our prototype system for dark-field radiography of the human chest enables clinical studies to investigate the influence of different pulmonary conditions on dark-field radiographs. This presentation will give an overview of our latest results, demonstrating the diagnostic value of dark-field radiography.

Background: X-ray imaging is an essential tool in daily clinical routine. While conventional X-ray imaging is based on the attenuation properties of different materials, X-ray dark-field imaging forms an image contrast based on small-angle scattering. This complementary image information can provide additional information about the imaged structure.

Methods: One possible method to obtain dark-field images is grating-based interferometry. A three-grating setup enables dark-field imaging using commercially available X-ray sources (1,2). Our prototype system for clinical dark-field radiography of the human chest, which uses such a three-grating setup, allows the simultaneous acquisition of both a dark-field image and an attenuation-based image of the human lungs during a 7s-long scan (3). In several clinical studies, the dark-field signal of study participants with healthy lungs and with various lung diseases have been assessed (3–8). Reader studies by radiologists were performed and the so-called dark-field coefficient (4), which is the total dark-field signal of the lung divided by the lung volume, was used as a quantitative measure of the structural integrity of the human lung.

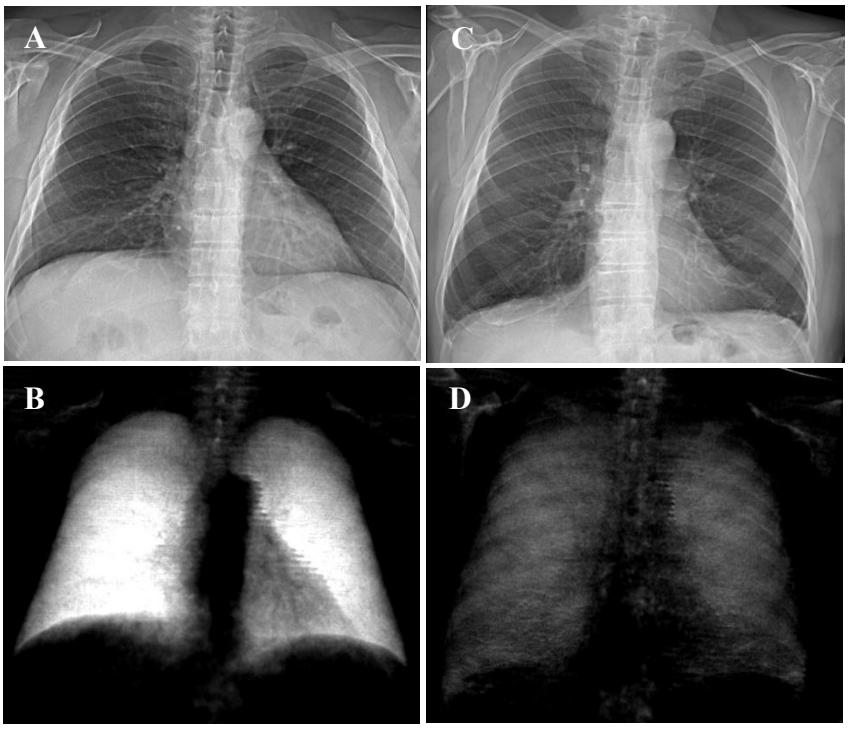

Figure 1: Attenuation-based (A, C) and dark-field radiographs (B, D) of a healthy study participant (A, B) and a patient with emphysema (C, D). For both study participants, the same respective image windows were applied. While the dark-field signal of the healthy lung (B) is strong and homogeneous, an emphysematous lung exhibits a low and patchy dark-field signal (D).

Results: The many intact alveoli of healthy lungs lead to a high amount of small-angle scattering, thus exhibiting a strong and homogeneous signal in the dark-field image (4). If the lung alveoli are impaired, less small-angle scattering occurs, resulting in a decreased and inhomogeneous dark-field signal. Hence, dark-field imaging allows conclusions about the structural integrity of the lung alveoli (3,5–8). First results of our clinical studies show that providing the dark-field images in addition to the conventional radiographs can improve the diagnostic capabilities of radiologists (5,6,9).

Conclusion: As microstructural changes in the human lungs can be difficult to see in conventional attenuation-based images, dark-field radiography has potential for improved diagnostics of different lung diseases.

Acknowledgments

We acknowledge the help of Philips Medical Systems DMC during the hardware and software development for the prototype system for dark-field radiography of the human chest. We also acknowledge the support of Felix T. Gassert, Alexander Fingerle and Andreas Sauter for conducting our clinical studies.

References

[1] Pfeiffer F et al. Phase retrieval and differential phase-contrast imaging with low-brilliance X-ray sources. Nature Phys. 2006.

[2] Pfeiffer F et al. Hard-X-ray dark-field imaging using a grating interferometer. Nature Mater. 2008.

[3] Willer K, Fingerle AA et al. X-ray dark-field chest imaging for detection and quantification of emphysema in patients with chronic obstructive pulmonary disease: a diagnostic accuracy study. The Lancet Digital Health.2021.

[4] Gassert FT, Urban T et al. X-ray Dark-Field Chest Imaging: Qualitative and Quantitative Results in Healthy Humans. Radiology. 2021.

[5] Frank M, Gassert FT et al. Dark-field chest X-ray imaging for the assessment of COVID-19-pneumonia. Commun Med. 2022.

[6] Urban T, Gassert FT et al. Qualitative and Quantitative Assessment of Emphysema Using Dark-Field Chest Radiography. Radiology. 2022.

[7] Gassert FT et al. Dark-Field Chest Radiography of Combined Pulmonary Fibrosis and Emphysema. Radiol Cardiothorac Imaging. 2022.

[8] Gassert FT et al. X-ray Dark-field Chest Radiography of Lymphangioleiomyomatosis. Radiology. 2022.

[9] Urban T, Sauter AP et al. Dark-Field Chest Radiography Outperforms Conventional Chest Radiography for the Diagnosis and Staging of Pulmonary Emphysema. Invest Radiol. 2023.

X-ray Dark-Field Computed Tomography at the Human-Scale: Challenges and Implementation of a First Prototype

* Jakob Haeusele[1], Manuel Viermetz[1], Nikolai Gustschin[1], Clemens Schmid[1], Tobias Lasser[1,2], Thomas Koehler[3,4], Franz Pfeiffer[1,4]

[1]*Munich Institute of Biomedical Engineering, Technical University of Munich, 85748 Garching, Germany*

[2]*Computational Imaging and Inverse Problems, Technical University of Munich, 85748 Garching, Germany*

[3]*Philips Innovative Technologies, 22335 Hamburg, Germany*

[4]*Institute for Advanced Studies, Technical University of Munich, 85748 Garching, Germany*

Email: *jakob.haeusele@tum.de*

Summary: Grating-based X-ray dark-field imaging is an interferometric technique that enables visualization of the alveolar structures in lungs. In the clinical context, the technique has been successfully tested with radiographic applications, but has not yet been transferred to computed tomography (CT) imaging. Recently, we presented a first human-scale prototype that overcomes previous roadblocks with novel design and data processing approaches. Here, we report on the main challenges during development and how we addressed them.

While initial studies have already demonstrated that dark-field imaging complements and improves conventional radiography of the thorax, dark-field CT, which is capable of yielding unobstructed 3D views, has only recently been brought to the human scale: With a first prototype system, we demonstrated the feasibility to implement a Talbot-Lau interferometer on a clinical CT system (Philips iCT, Philips Healthcare, Cleveland, USA) to perform dark-field imaging with clinical acquisition time and field of view [1].

So far, a major hinderance for this was the susceptibility of Talbot-Lau interferometers to mechanical vibrations coupled with a need to minimize data acquisition time for clinical routine. A proper mechanical system design ensuring relative stability against vibrations and a sophisticated data processing scheme to remove remaining perturbation-based artifacts is therefore vital to achieve good image quality. To model and predict the occurring system fluctuations we employ an approach that is based on principle component analysis. It allows us to learn the system's perturbation characteristics by first processing an air reference scan and then applying the learned prior information to sample scans of arbitrary samples. This approach allows for an unambiguous decomposition of sample information and interferometer perturbations due to, e.g., vibrations [2,3,4].

Furthermore, to address the need for fast acquisition times in full-body medical CT, a departure from conventional step-and-shoot acquisitions as used in most laboratory environments to a mode where the gantry and detector operate continuously is necessary. Therefore, we developed a novel phase-sampling scheme capable of handling continuous rotation and arbitrary phase-steps: In our approach, we create a spatio-temporal modulation of the interferometer fringe pattern by harnessing the inherent system vibrations that move the gratings. Additionally, we fine-tune a Moiré fringe pattern on the detector, resulting in a spatial gradient in the interferometer phase.
To accommodate for this during the central phase-retrieval step, we additionally contrived of an advanced sliding-window-based demodulation scheme to minimize the impact of artifacts due to the simultaneous movement of interferometer gratings and sample projections. With this approach we significantly reduce streaking artifacts and improve the

resulting reconstruction quality while still allowing for fast acquisition and data processing times [5].

The developed prototype can perform measurements on the second scale and can perform all three acquisition modes of CT imaging, namely axial, surview, and helical scanning. Fig. 1 depicts example measurements acquired by the system using an anthropomorphic thorax phantom. To simulate the porous lung parenchyma, we use a custom neoprene insert. While the neoprene shows a very small signal strength in the attenuation channel, it exhibits a strong dark-field signal due to its fine small-angle scattering micro-structure. This demonstrates the system's capability to exploit a material's porosity for contrast generation.

The developed prototype brings dark-field CT an important step closer to clinical usage as it demonstrates as a first proof-of-concept the viability of the technique at human-scales.

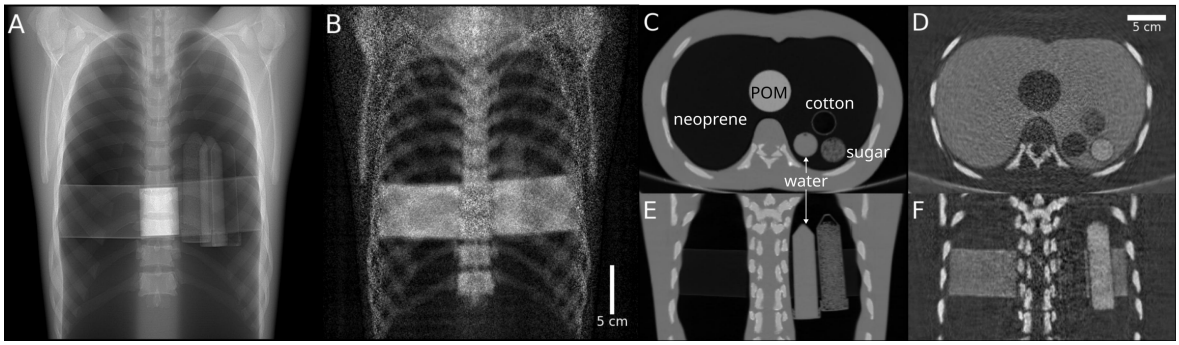

Figure 1: **Left:** Surview scan of an anthropomorphic thorax phantom acquired with the dark-field CT prototype. **A:** conventional attenuation-based surview. **B:** dark-field surview. **Right:** Corresponding helical CT scan. **C:** conventional attenuation-based axial slice. **D:** dark-field channel. **E** and **F** show correspondig coronal slices at height of the spine.

Acknowledgments

This work was supported by the Karlsruhe Nano Micro Facility, a Helmholtz Research Infrastructure at Karlsruhe Institute of Technology.

We acknowledge support of the TUM Institute for Advanced Study, funded by the German Excellence Initiative, the ERC (H2020, AdG 695045) and Philips GmbH Market DACH.

References

[1] Viermetz, M., Gustschin, N., Schmid, C., Haeusele, J., von Teuffenbach, M., Meyer, P., Bergner, F., Lasser, T., Proksa, R., Koehler, T., and Pfeiffer, F., "Dark-field computed tomography reaches the human scale" Proceedings of the National Academy of Sciences **119**(8), e2118799119 (2022).

[2] Haeusele, J., Schmid, C., Viermetz, M., Gustschin, N., Lasser, T., Koehler, T., and Pfeiffer, F., "Robust Sample Information Retrieval in Dark-Field Computed Tomography with a Vibrating Talbot-Lau Interferometer," TechRxiv (2023).

[3] Schmid, C., Viermetz, M., Gustschin, N., Noichl, W., Haeusele, J., Lasser, T., Koehler, T., and Pfeiffer, F., "Modeling vibrations of a tiled Talbot-Lau interferometer on a clinical CT", IEEE Transactions on Medical Imaging **42**(3), 774-784 (2023).

[4] Viermetz, M., Gustschin, N., Schmid, C., Haeusele, J., Noel, P., Proksa, R., Löscher, S., Koehler, T., and Pfeiffer, F., "Technical design considerations of a human-scale Talbot-Lau interferometer for Dark-Field CT," IEEE Transactions on Medical Imaging **42**(1), 220–232 (2023).

[5] Haeusele, J., Schmid, C., Viermetz, M., Gustschin, N., Lasser, T., Koehler, T., and Pfeiffer, F., "Advanced phase-retrieval for stepping-free x-ray dark-field CT" IEEE Transactions on Medical Imaging **42**(10), 2876-2885 (2023).

Opportunities in dark-field imaging for characterizing novel materials systems

*MATIAS KAGIAS[1,2,3,4,5], SEOLA LEE[4], DILWORTH Y. PARKINSON[6,7],

JULIA R. GREER[4,5]

[1]*Division of Synchrotron Radiation Research, Lund University, Lund, Sweden*

[2]*NanoLund, Lund University, Lund, Sweden*

[3]*Wallenberg Initiative Materials Science for Sustainability, Lund University, Lund, Sweden*

[4]*Division of Engineering and Applied Science, California Institute of Technology, Pasadena CA, USA*

[5]*Kavli Nanoscience Institute, California Institute of Technology, Pasadena CA, USA*

[6]*Center for Advanced Mathematics for Energy Research Applications, Lawrence Berkeley National Laboratory, Berkeley CA, USA*

[7]*Advanced Light Source, Lawrence Berkeley National Laboratory, Berkeley CA, USA*

Email: *matias.kagias@sljus.lu.se*

Summary: The dark-field (or visibility reduction) signal can be accessed with a wide range of approaches, from conventional Talbot grating interferometers and random speckle patterns, to arrays of focusing lenses generating structured X-ray illumination. Each of them with unique advantages and limitations. In this talk, I will present recent developments in terms of X-ray dark-field sensitive instrumentation with a focus on materials science based applications. Specifically, I will discuss the application and potential of dark-field imaging for characterizing novel complex material systems such as nano-architected metamaterials.

The X-ray dark-field signal [1] has opened many possibilities for investigating structures smaller than the resolution limit of the imaging system. This has enabled a multitude of applications and opportunities both in medical and materials science research. Noteworthy examples from each domain include breast [2] and lung imaging [3], and carbon fibre reinforced polymers [4]. Typically, the dark-field signal is quantified by the visibility reduction (blurring) of a modulation that is introduced in the X-ray beam. The specific system design i.e length, energy and modulator design are critical for the strength and information content of the retrieved dark-field signals. Both experimental and theoretical advancements have allowed for a quantitative understanding of the dark-field signal in connection to the underlying structure. This synergy is crucial for characterizing novel complex materials.

One material class where dark-field imaging can greatly impact are nanolattices. Nanolattices are a new class of structural materials that can achieve ultra-high strength to weight ratios [5] and are highly resilient to supersonic impact [6]. A great challenge for wide adoption of such materials is scalable fabrication and characterization. The latest progress in fabrication methods has enabled the production of centimetre wide nanoarchitected sheets with feature sizes in the range of a few hundred nanometres [7]. Characterization of the overall architecture and uniformity of such sheets can be challenging, time consuming, and destructive with conventional microscopy methods such Scanning Electron Microscopy (SEM) due to the broad range of length scales involved.

In this presentation, I will discuss the applicability and opportunities of recently developed dark-field based imaging methods [8] for characterizing scalable nanoarchitected materials such as nanolattices. Finally, I will showcase the latest experimental results highlighting the direct correlation of the dark-field signal with macroscopic mechanical properties of nanoarchitected sheets with features in the 500 nm range [9].

Acknowledgments
M.K. acknowledges financial support the Swiss National Science Foundation (grant Nr P400P2_194371). Part of this work was supported by the Wallenberg Initiative Materials Science for Sustainability funded by the Knut and Alice Wallenberg Foundation. The Kavli Nanoscience Institute is acknowledged for cleanroom facilities and access to nanofabrication tools. This research used resources of the Advanced Light Source, which is a DOE Office of Science User Facility under contract no. DE-AC02-05CH11231.

References
[1] Pfeiffer F, Bech M, Bunk O, Kraft P, Eikenberry EF, Brönnimann Ch, Grünzweig C & David C. Hard-X-ray dark-field imaging using a grating interferometer. Nat Mater. 2008 Feb;7(2):134-7. doi: 10.1038/nmat2096.
[2] Wang, Z., Hauser, N., Singer, G. *et al.* Non-invasive classification of microcalcifications with phase-contrast X-ray mammography. *Nat Commun* **5**, 3797 (2014). doi:10.1038/ncomms4797
[3] Gassert, F. T., Urban, T., Frank, M., Willer, K., Noichl, W., Buchberger, P., Schick, R., Koehler, T., Jens von Berg, Fingerle, A. A., Sauter, A. P., Makowski, M. R., Pfeiffer, D., & Pfeiffer, F. X-ray Dark-Field Chest Imaging: Qualitative and Quantitative Results in Healthy Humans Radiology 2021 301:2, 389-395 doi:10.1148/radiol.2021210963
[4] Kagias, M., Wang, Z., Birkbak, M.E., Lauridsen, E., Abbis, M., Lovric, G., Jefimovs, K. & Stampanoni, M. Diffractive small angle X-ray scattering imaging for anisotropic structures. *Nat Commun* **10**, 5130 (2019). doi: 10.1038/s41467-019-12635-2
[5] Meza, L. R., Das, S. & Greer, J. R. Strong, lightweight, and recoverable three-dimensional ceramic nanolattices. Science (80-.). 345, 1322–1326 (2014) doi: 10.1126/science.1255908.
[6] Portela, C. M., Edwards, W. B., Veysset. D., Sun, Y., Nelson, K., A., Kochmann, D., M. & Greer, J. R. Supersonic impact resilience of nanoarchitected carbon. Nat. Mater. 292, 6294 (2021) doi:10.1038/s41563-021-01033-z
[7] Kagias, M., Lee, S., Friedman, A. C., Zheng, T., Veysset, D., Faraon, A. & Greer, J. R. Metasurface-Enabled Holographic Lithography for Impact-Absorbing Nanoarchitected Sheets. *Adv. Mater.* 2023, 35, 2209153. doi:10.1002/adma.202209153
[8] Kagias, M., Wang, Z., Lovric, G., Jefimovs., K. & Stampanoni, M. Simultaneous reciprocal and real space imaging of time evolving systems. Phys. Rev. Applied 15, 044038 (2021) doi: 10.1103/PhysRevApplied.15.044038
[9] Kagias, M. et al. 2024 (In Submission)

Oral

Toward forward-model-based dark-field material decomposition

K. TAPHORN[1,2*], L. KASTER[2], T. SELLERER[2], J. HERZEN[1,2]

[1]*Research Group Biomedical Imaging Physics, Department of Physics, TUM School of Natural Sciences, Technical University of Munich, Germany*

[2]*Chair of Biomedical Physics, Department of Physics, TUM School of Natural Sciences and Munich Institute of Biomedical Engineering, Technical University of Munich, Germany*

Email: *kirsten.taphorn@tum.de*

Summary: Spectral X-ray imaging enables the retrieval of material-selective information based on material decomposition algorithms. Forward-model-based approaches rely on the quantitative attenuation coefficients of the desired basis materials. Because a similar coefficient can be derived for the dark-field signal, spectral X-ray dark-field imaging is generally possible. However, assessing the linear diffusion coefficient of complex scatterer is challenging. We present an optimization approach to retrieve the linear diffusion coefficient from simple phase-stepping data. The method is shown on multiple materials, and the results are validated with spectrometer measurements. By that, we pave the way for model-based material decomposition in the dark-field channel.

Spectral X-ray imaging has gained high research interest in the last decade and has become widely available in clinical routine. The advantages over conventional X-ray imaging are a potential reduction of noise, or equivalently, a reduction of dose at constant image quality, the material separation, which is especially interesting for applications of contrast agents, the suppression of beam-hardening artifacts, and the possibility to calculate virtual-mono energetic and non-contrasted images.

Grating-based phase-contrast and dark-field imaging with a three-grating Talbot-Lau interferometer provides two additional and complementary contrast channels to the conventional attenuation [1]. While the phase contrast is related to the electron density of the observed object, the dark-field image visualizes ultra-small angle X-ray scattering based on the sample's microstructure on a length scale far below the image resolution.

The dark-field signal can be quantitatively derived from scatter theory, and a coefficient is defined [2] similarly to the attenuation coefficient in the attenuation channel. The so-called linear diffusion coefficient has a distinct dependence on the X-ray's energy based on the structure of the material and the setup geometry, which makes spectral dark-field imaging generally a tool to provide a differentiation of different microstructures. Using a calibration-based approach, dark-field material decomposition was recently demonstrated in projection [3]. An alternative to the calibration known from the attenuation channel is forward-model-based material decomposition that utilizes a model for the measured intensity based on the theoretical attenuation coefficient of the desired basis materials. To transfer this approach to the dark-field channel, the quantitative linear diffusion coefficient of the basis materials must be known. However, the coefficient is difficult to assess for scattering materials with a complex micro structure, which usually requires sophisticated hardware and measurements.

We present an experimental approach to retrieve the linear diffusion coefficient of a scatterer from simple phase-stepping projection data [4]. The proposed approach is demonstrated experimentally, and the results are validated with spectrometer measurements.

Closed-cell structural foams (Evonik Industries AG, Essen, Germany) made from polymethacrylimide were used as scattering materials. A microscopy image (Helium-Ion microscope, Zeiss, Oberkochen) of one of the foams is shown in Figure 1 A.
A set of dual-energy X-ray dark-field projections of the material is acquired at a conventional three-grating Talbot-Lau interferometer without additional hardware. The measured visibilities for different sample thicknesses are shown in Figure 1 B. The measurements are then compared to a model function for the expected visibility. Thereby, the expected visibility $\hat{V}_i^s$ depends on the X-ray spectrum $D^s(E)$, the visibility spectrum visibility $V(E)$, and the linear diffusion coefficient $-a/E^b$ and thickness t_i of the material of interest:

$$\hat{V}_i^s = \int D^s(E) \cdot V(E) \cdot exp\left(-t_i \cdot a/E^b\right) dE. \quad (1)$$

Via a least-squares optimization, the parameters a and b, which define the linear diffusion coefficient's signal strength and energy dependence, are retrieved.
Calculating the expected visibility with the optimized parameters fits well to with the measured visibility (cf., Figure 1 B). We validated the results by measuring the energy-dependent dark-field signal with a single-pixel spectrometer (Amptek, Inc., Bedford, Massachusetts). For different setup geometries, the results from the optimization for the linear diffusion coefficient agree well with the ground truth of the energy-dependent dark-field signal. Conclusively, the proposed approach provides the quantitative linear diffusion coefficient, which paves the way for quantitative X-ray dark-field imaging in general and forward-model-based material decomposition in the dark-field channel in particular.

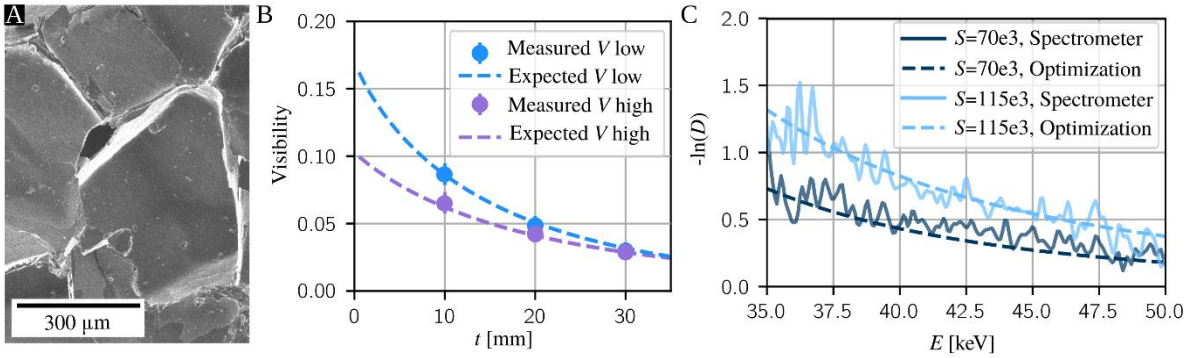

Figure 1: A microscopy image of the material's micro structure is depicted in A. The visibility measured with two different X-ray spectra is depicted in B, depending on the sample thickness. The expected visibility (dashed lines) calculated from the optimized linear diffusion coefficient fits well the measured visibility. The results from the optimization are validated with spectrometer measurements for different setup geometries (different sensitivities *S*) in C, which agree well with the calculated spectral dark-field signal.

Acknowledgments
We acknowledge Evonik Industries AG (Essen, Germany) who kindly provided the sample materials. We acknowledge Alexander Hötger and Alexander Holleitner (Walter Schottky Institute, TUM) for providing and assisting the helium-ion microscope.

References

[1] F. Pfeiffer, M. Bech, O. Bunk, P. Kraft, E. F. Eikenberry, C. Brönnimann, C. Grünzweig, C. David, Hard X-ray dark-field imaging using a grating interferometer. *Nat. Mater.,* 7, 134–137 (2008)

[2] F. Prade, A. Yaroshenko, J. Herzen, F. Pfeiffer, Short-range order in mesoscale systems probed by X-ray grating interferometry. *EPL,* 112, 68002 (2015)

[3] T. Sellerer, K. Mechlem, R. Tang, K. Taphorn, F. Pfeiffer, J. Herzen, Dual-Energy X-Ray Dark-Field Material Decomposition. *IEEE Transactions on Med. Imaging* 40, 974-985 (2021)

[4] K. Taphorn, L. Kaster, T. Sellerer, A. Hötger, J. Herzen, Spectral X-ray dark-field signal characterization from dual-energy projection phase-stepping data with a Talbot-Lau interferometer. *Sci Rep,* 13, 767 (2023)

Single-mask X-ray multimodal imaging for the investigation of dynamic processes across the life and physical sciences

L.Massimi[1,*] Adele de Ninno[2], Samuel J.Clark[3], Sebastian Marussi[4], Adam Doherty[5], Joachim Schulz[6,7] Shashidhara Marathe[8], Christoph Rau[8], Marco Endrizzi[5], Peter D. Lee[4], Alessandro Olivo[5], Luca Businaro[2] and Alessia Cedola[1]

[1]*CNR-Nanotec (Rome Unit),National Research Council of Italy, Rome, Italy*
[2]*CNR-IFN (Institute of Photonics and Nanotechnologies), Rome, Italy.*
[3]*X-ray Science Division, Argonne National Laboratory, Lemont, Illinois, USA*
[4]*Department of Mechanical Engineering, University College London, London, UK*
[5]*Department of Medical Physics and Biomedical Engineering, University College London, London, UK*
[6]*MicroWorks GmbH, Karlsruhe, Germany*
[7]*Institute of Microstructure Technology, Karlsruhe Institute of Technology, Karlsruhe, Germany*
[8]*Diamond Light Source, Harwell Oxford Campus, UK*

Email: *l.massimiphd@gmail.com*

Summary: we present the application of a time-resolved implementation of the single mask beam-tracking (BT) X-ray imaging method to different dynamic processes, spanning across the life and physical sciences. Specifically, we targeted additive manufacturing and fluid dynamics. Our results show the ability of this approach to quantitatively capture high and low contrast dynamic processes with milliseconds time resolution at micron spatial resolution using the three contrast channels, transmission, phase and dark-field.

X-ray multimodal imaging is based on the retrieval of phase changes and ultra-small angle scattering (or dark-field) in addition to conventional transmission. The availability of these additional contrast channels has already proven to be valuable in many research fields, including medicine and materials sciences, thanks to the ability to provide superior contrast for soft tissues as well as to highlight the internal microscopic structures of objects below the system's resolution [1,2]. The availability of high flux synchrotron radiation beamlines has recently opened the way to dynamic X-ray imaging with impressive time resolution [3] allowing the investigation of rapidly changing processes. However, dynamic imaging has mainly been limited to conventional absorption or free-space propagation phase imaging. Free-space propagation is not quantitative in single-shot mode unless the sample is homogeneous, which is often a condition not satisfied when investigating the dynamics of a process. On the other hand, the use of quantitative imaging approaches based on gratings or masks poses challenges to a dynamic implementation. This is mainly due to the requirement acquiring frames while displacing one or more optical elements, which may not be compatible with the speed requirements of dynamic imaging. While single-shot methods exist, they typically impose a compromise between time and spatial resolution. To overcome these limitations, we propose a dynamic implementation of the beam tracking imaging method [4]. BT uses a single absorption mask that shapes the beam into a series of beamlets, which are then individually resolved by a detector with a sufficiently small pixel. When a sample is introduced into the beam path, the profile of each beamlet modified by the sample is compared to that obtained without the sample in place to retrieve transmission, refraction and dark-field. The main advantage of BT over other grating and mask-based techniques is the requirement of a single absorption mask, which greatly simplifies the experimental setup. However, when BT is used as a single-shot method, the spatial resolution will be limited by the period of the mask in use, since the separation between adjacent beamlets determines the sampling rate. The way to overcome this limitation is the acquisition of images where the sample is translated by sub-period steps which are subsequently recombined into an image

with spatial resolution determined by the mask aperture size. Since only a single movement is required, a dynamic implementation of this method is relatively straightforward and does not pose any demanding hardware requirement [5]. Dynamic BT is based on the continuous translation of the mask in front of the sample, while the detector acquires a sequence of images. The speed of the mask has to be adjusted to match the final required time resolution, considering that to achieve an aperture-limited spatial resolution, the recombination of a number of images equal to ratio between mask period and aperture is required. To investigate the capabilities and the experimental challenges of this approach, we targeted additive manufacturing and fluid dynamics in two different experiments performed at Diamond and ESRF synchrotron facilities, respectively, where we obtained multi-modal images with micrometric spatial resolution and a time resolution of milliseconds. In the first case, we imaged the melting of aluminium powder and titanium slabs, both providing a very high contrast, by a high-power laser beam, demonstrating that the availability of the additional contrast channels can provide otherwise unavailable insights on the process [5, 6]. Specifically, thanks to the higher sensitivity of the phase channel to density variations, we

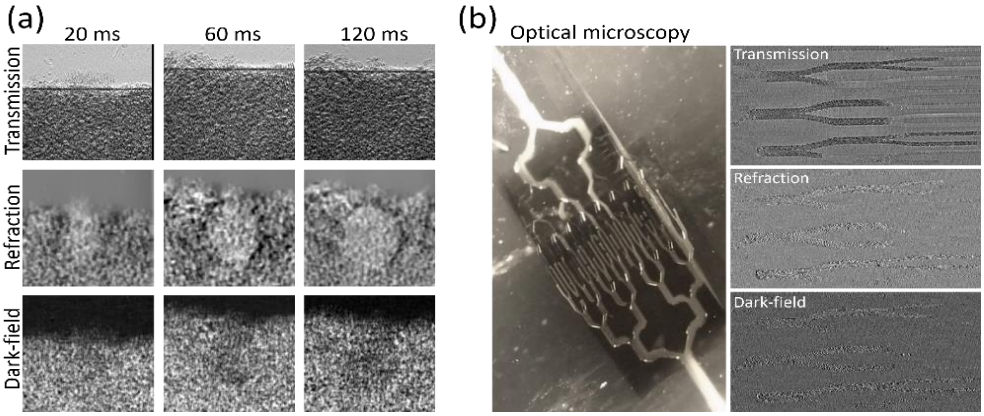

Figure 1(a) Multimodal X-ray imaging of melting of aluminium powder. (b) Dynamic X-ray multimodal images from a microfluidic laboratory-on-chip device combined with optical microscopy

have been able to detect the formation of melted features before they become visible in the transmission as well as to trace the dynamic of the power identifying the accumulation points before the start of the actual melting process (see Fig.1a). In the second experiment, we combined our BT dynamic approach with microfluidic laboratory-on-chip devices, to image the flow of the liquid in an in-vitro model of vascular network by means of a solution of water and glass microspheres acting as contrast agent for refraction and dark-field. We found that the additional contrast channels allowed visualizing and quantifying fluid parameters even for low sphere concentrations, at which the fluid becomes invisible in the conventional transmission images, opening to multimodal contrast-enhanced X-ray angiography (see Fig.2b).

References

[1] Savvidis, Savvas, et al. Acta Biomaterialia 141 (2022): 290-299.

[2] Shoukroun, D., et al. Materials Today Communications 31 (2022): 103279.

[3] Olbinado, Margie P., et al. Journal of Physics D: Applied Physics 51.5 (2018): 055601.

[4] Vittoria, Fabio A., et al. Applied Physics Letters 106.22 (2015).

[5] Massimi, Lorenzo, et al. Physical Review Letters 127.21 (2021): 215503.

[6] Massimi, Lorenzo, et al. Scientific Reports 12.1 (2022): 12136.

Energy resolving dark-field imaging with dual phase grating interferometer

Yuhang Tan[1], Xuebao Cai[1], Yongshuai Ge[1,2]
[1]*Research Center for Medical Artificial Intelligence, Shenzhen Institute of Advanced Technology, Chinese Academy of Sciences, Shenzhen, 518055, China*
[2]*Paul C Lauterbur Research Center for Biomedical Imaging, Shenzhen Institute of Advanced Technology, Chinese Academy of Sciences, Shenzhen, 518055, China*
Email: ys.ge@siat.ac.cn

Summary: In this study, the feasibility of performing energy resolving dark-filed imaging is investigated for dual phase grating interferometer system. Numerical simulations are carried out under two conditions to study the period and the visibility of the diffraction fringes. Results show that the fringes generated from dual 1.5π phase grating interferometer outperform the ones generated from dual 0.67π phase grating system with higher fringe visibility and signal uniformity. Physical experiments are carried out to demonstrate the capability of performing energy resolving dark-filed imaging with accelerated data acquisition speed for dual phase grating interferometer system. Results demonstrate that the micro-bubble size can be accurately predicted from the energy resolved dark-filed projections that are acquired with only half number of mechanical movements. Thereby, the entire data acquisition period of dark-field imaging could be significantly reduced in dual phase grating interferometer.

X-ray dark-filed imaging is a powerful approach to quantify the dimension of micro-structures of the object. Often, a series of dark-filed signals have to be measured under various correlation lengths. For instance, this is often achieved by adjusting the sample positions by multiple times in Talbot-Lau interferometer. Moreover, such multiple measurements can also be collected via adjustments of the inter-space between the phase gratings in dual phase grating interferometer. As expected, the multiple mechanical translations would prolong the entire data acquisition time of dark-filed imaging. Moreover, the radiation dose efficiency of dark-field imaging with Talbot-Lau interferometer gets reduced as the analyzer grating stops more than half amount of the incident X-ray photons. In this study, the energy resolving capability of the dual phase grating interferometer, which having higher radiation dose efficiency, is explored with the aim to accelerate the data acquisition speed of dark-filed imaging. To do so, both theoretical analyses and numerical simulations are investigated.

By default, the X-ray wave emitted from a single slit source is assumed to be polychromatic. With the standard Kirchhoff's diffraction theory, the final X-ray intensity can be approximated as follows:

$$\mathrm{I}_d(x_d) \approx \frac{\mathrm{U}_0^2}{(d_1+d_2+d_3)^2} \cdot \left(1 + \mathrm{A}_1(\lambda)\cos\left(\frac{2\pi f_2}{d_3 p_2} x_d\right) + \mathrm{A}_2(\lambda)\cos\left(\frac{4\pi f_2}{d_3 p_2} x_d\right)\right), \qquad (1)$$

in which U_0 denotes the amplitude of the initial disturbance, λ denotes the X-ray wavelength, d_1, d_2, and d_3 denotes the distance between the source and G_1, G_1 and G_2, and G_2 and the detector, respectively. Eq.1 demonstrates that the visibility of a dual phase grating interferometer system depends on the X-ray beam energy *E*. Indeed, such energy dependent responses provide an important opportunity to acquire multiple energy resolving dark-filed images at a fixed sample position in dual phase grating interferometer system.
The quantitative dark-field imaging model for dual phase grating interferometer is primarily inherited from Strobl. Assuming the radius of the hard microsphere sample is *r*, and the real-space autocorrelation function can be expressed as follows:

$$G\left(\frac{\xi_E}{r}\right)=\left[1-\left(\frac{\xi_E}{2r}\right)^2\right]^{\frac{1}{2}}\left(1+\frac{\xi_E^2}{8r^2}\right)+\frac{1}{2}\frac{\xi_E^2}{r^2}\left[1-\left(\frac{\xi_E}{4r}\right)^2\right]\ln\left[\frac{\xi_E}{2r+\left(4r^2-\xi_E^2\right)^{\frac{1}{2}}}\right], \qquad (2)$$

where ξ_E denotes the correlation length of the system. For a given beam spectra with mean energy of $\overline{E}$, the dark-field signal can be expressed as:

$$DF(\overline{E})=\sigma_{DF}^2\left[1-G\left(\frac{\xi_{\overline{E}}}{r}\right)\right]. \qquad (3)$$

Herein, σ_{DF}^2 represents the scattering cross-section of the microsphere and is numerically equal to the maximum dark-field signal of the given particle. Essentially, multiple sets of dark-field signals can be simultaneously obtained by varying the mean beam energy $\overline{E}$ (corresponds to different correlation lengths) in dual phase grating system.

The numerical diffraction fringes and energy responses of the dual phase grating interferometer under different monochromatic X-ray beams are shown in Fig.2a. As depicted in Fig.2a-1, the period of fringes obtained at 20.0 keV (1.5π phase grating) is two times larger than the ones obtained at 60 keV (π phase). At 45 keV (0.67π phase), the generated diffraction fringes look less uniform. Results plotted in Fig.2a-2 demonstrate that the dual phase grating and the Talbot-Lau interferometer have comparable energy responses at low working energies, e.g., 30 keV. However, the dual phase grating interferometer has superior energy responses than the Talbot-Lau interferometer at high working energies, e.g., 60 keV, see the results in Fig.2a-3.

The diffraction fringes acquired at low energy and high energy are depicted in Fig.2b-1 along with their line profiles. Moreover, the extracted dark-field projection is shown in Fig.2b-2, and the vertically averaged profile is plotted below. Finally, regression analysis is performed with respect to the acquired eight dark-field signals to estimate the particle size *r*. Specifically, the solid fitting curve plotted in Fig.2b-3 is defined by Eq.3. The fitting results show that the scanned silicon dioxide microsphere has a diameter of $0.54 \pm 0.06\mu m$, which is in good agreement with the actual particle size.

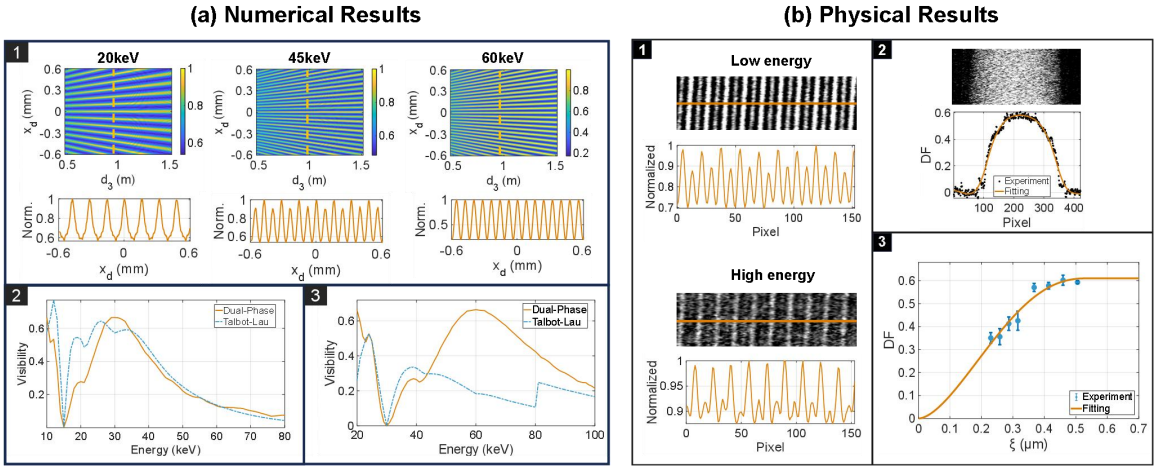

Figure 2: (a) Numerical diffraction fringes and energy responses of the dual phase grating interferometer under different monochromatic X-ray beams. (b) The physical experimental dark-field imaging results.

References

[1] M. Strobl, Sci. reports 4, 7243 (2014).

[2] A. Yan, X. Wu, and H. Liu, Sci. Technol. 28, 1055–1067 (2020).

[3] M. Kagias, Z. Wang, K. Jefimovs, and M. Stampanoni, Appl. Phys. Lett. 110, 014105 (2017).

Bottom-up Au electroplating of high-aspect-ratio Si-based X-ray micrograting

L. Chen[1,2], * D. Josell[3], Q. Yu[1,2], K. Jefimovs[2], M. Stauber[4], M. Stampanoni[1,2], L. Romano[1,2]

[1]*Institute for Biomedical Engineering, University and ETH Zürich, 8092 Zürich, Switzerland*

[2]*Paul Scherrer Institut, 5232 Villigen PSI, Switzerland*

[3]*Materials Science and Engineering Division, National Institute of Standards and Technology, United States of America*

[4]*GratXray AG, Villigen, Switzerland*

Email: *liyang.chen@psi.ch*

Summary: Au micro-gratings with small pitch and high aspect ratio are desired for high sensitivity and dose efficient X-ray interferometry imaging. We use Au bottom-up filling (BUF) in etched Si templates to realize high-aspect-ratio Au micro-gratings. Void-free Au-BUF is demonstrated in shallow trenches, where clear BUF progression is observed. Fine tuning of the process parameters is needed as a function of grating feature size and aspect ratio. Void-free BUF becomes more challenging when the aspect ratio increases as truncated BUF can occur. Progress to nearly-void-free filling of gratings with 2.1-µm-wide and 150-µm-deep trenches (i.e., aspect ratio exceeding 70) as a function of the plating potential is reported.

High-aspect-ratio Au micro-gratings are critical optical components for X-ray grating interferometry imaging [1-3]. The electroplating technique of Au-BUF developed at NIST [1,4] has been reproduced, and is now being scaled-up at PSI. The electrolytes used for BUF of Au gratings are simple and nontoxic, containing $Na_3Au(SO_3)_2$, Na_2SO_3, and micromolar concentrations of Bi^{3+} additive. A typical BUF process goes through an incubation period, Bi-activated local deposition at the bottom, sustained bottom-up filling, and self-passivation [5] that are well explained and visualized by a recent model [6]. High-aspect-ratio void-free Au BUF can be realized by controlling the solution concentration and pH, as well as the plating potential.

Figure 1(a) illustrates our micro-grating fabrication process: i) the Si template is patterned with a micro-grating structure by photolithography and deep reactive-ion etching, ii) a uniformly conductive Pt/Al_2O_3 bilayer (40-nm-thick Pt on 10-nm-thick Al_2O_3 on Si) seed layer for Au electroplating is formed by atomic layer deposition, iii) Au is electroplated in the BUF modality. We achieved void-free Au BUF of 2.1-µm-wide and 12-µm-deep gratings at the potential of -0.80 V. We terminated the deposition process for different time periods after the activation of BUF to capture the filling evolution of the gratings with scanning electron microscopy (SEM) characterization. Figure 1(b) and 1(c) show the deposited Au gratings at 80 min and 150 min after activation of the BUF, respectively. Figure 1(c) shows the Au grating at 800 min, following self-passivation of the BUF process.

We systematically investigated the process reproducibility and the filling quality as a function of the grating area. For example, void-free BUF of high-aspect-ratio gratings is more challenging because deposition on the sidewall can happen during active filling, causing truncated BUF depicted in Figure 2(a). Electroplating parameters need to be adjusted in accord with the feature dimensions. For grating depth increased from 12 µm to 150 µm and the linewidth remaining unchanged at 2.1 µm, electrolyte and additive concentrations were doubled and the potential shifted positive (i.e., the overpotential

driving deposition reduced). Figure 2(b), 2(c), and 2(d) capture the Au filling of 2.1-µm-wide and 150-µm-deep micro-gratings at potentials of -0.73 V, -0.70 V, and -0.69 V, respectively. The gratings filled at -0.69 V are nearly void-free, the plating parameters requiring only some additional fine tuning to achieve completely void-free filling.

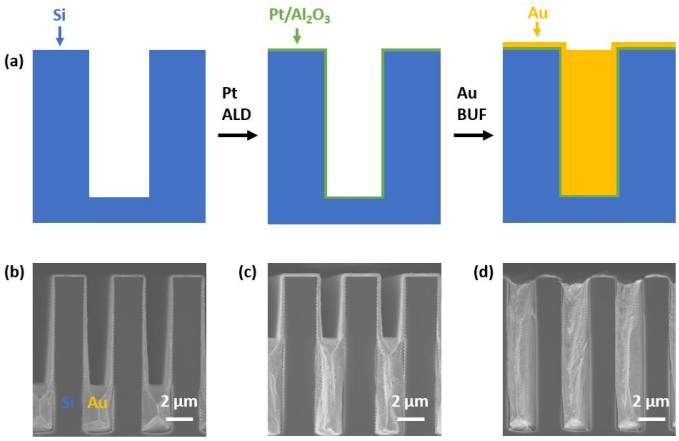

Figure 1: (a) Schematic of BUF Au process in micro-gratings. SEM images in cleaved cross section of Au BUF in 2.1-µm-wide and 12-µm-deep Si gratings with trenches filled by (b) 1/3, (c) 3/5, and (d) fully filled.

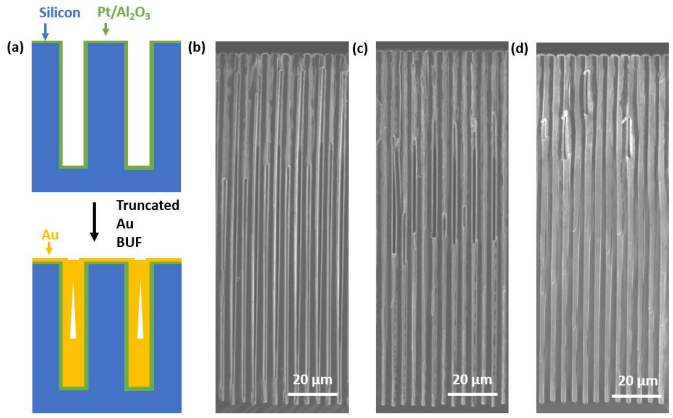

Figure 2: (a) Schematic of truncated Au-BUF in Si micro-gratings. SEM images of cleaved 2.1-µm-wide and 150-µm-deep micro-gratings filled at potentials of (b) -0.73 V, (c) -0.70 V, and (d) -0.69 V, showing a decreasing void volume with a more positive potential.

Acknowledgments

We thank the clean room operation team as well as the technical staff of PSI, Craig Lawley for setting up the Au BUF at PSI and the following funding agencies: SNF Sinergia Grant Nr. CRSII5 183568, PHRT-TT Project Nr. 2022-572 INTIMACY, SwissLOS Lottery Fund of Kanton Aargau, SNF R'Equip 189662 (SiDRY), SNF R'Equip 177036 (DTL).

References

[1] D. Josell et al., Pushing the Limits of Bottom-Up Gold Filling for X-ray Grating Interferometry, *J Electrochem Soc*, **167**, 132504, (2020)

[2] D. Josell et al., Bottom-Up Gold Filling in New Geometries and Yet Higher Aspect Ratio Gratings for Hard X-ray Interferometry, *J Electrochem Soc*, **168**, 082508, (2021)

[3] Z. Shi et al., Fabrication of a fractal pattern device for focus characterizations of X-ray imaging systems by Si deep reactive ion etching and bottom-up Au electroplating, *Appl Opt*, **61**, 3850, (2022)

[4] D. Josell and T. P. Moffat, Bottom-up Filling of Damascene Trenches with Gold in a Sulfite Electrolyte, *J Electrochem Soc*, **166**, D3022, (2019)

[5] D. Josell and T. P. Moffat, Extreme Bottom-up Gold Filling of High Aspect Ratio Features, *Acc Chem Res*, **56**, 677, (2023)

[6] D. Josell, T. M. Braun, and T. P. Moffat, Mechanism of Bismuth Stimulated Bottom-up Gold Feature Filling, *J Electrochem Soc*, **169**, 122507, (2022)

Patterning methods for MacEtch of high aspect ratio X-ray optics.

B. BENZ[1,2,3],* M. POGGIO[1,2], M. STAMPANONI[3,4], L. ROMANO[3,4]

[1]*Department of physics, University of Basel, Switzerland*

[2]*Swiss Nanoscience Institute, University of Basel, Switzerland*

[3]*Paul Scherrer Institute, Switzerland*

[4]*Institute for Biomedical Engineering, University and ETH Zürich, Switzerland*

Email: *bryan.benz@psi.ch*

Summary: In this work we present the use of MacEtch (metal assisted chemical etching) as a tool to fabricate ultra- high aspect ratio gratings in the micro- and nanoscale. A focus on the fabrication process is given, especially the patterning of the used platinum catalyst.

What would be the specifications for an ideal grating for your application? Current manufacturing methods struggle with providing gratings of submicron feature size and ultra-high aspect ratios. For this, a new method of manufacturing needs to be used. MacEtch [1] with its ability to etch feature sizes down to 10nm and aspect ratios up to 10'000 [2] is an ideal candidate. The technology is very promising in enabling a higher resolution and sensitivity for grating based interferometry. It consists of a local electrochemical reaction happening at room temperature, which can use O_2 or H_2O_2 as the oxidizer, HF as the etchant and a noble metal as the catalyst [1]. This reaction happens on the catalyst surface, removing the silicon surrounding it, leaving a path of removed material as the catalyst sinks into the substrate. This process can happen in liquid [3] or gas phase [2,4] and has already been successfully demonstrated for simple small-scale patterns and structures, providing gratings with straight sidewalls. The transition to more complex and larger area struggles, largely due to the non-uniform moving of the catalyst during the etching. This limiting problem has not been understood completely and there is still disagreement in the literature on how to control it. This is the focus of our project, which aims to investigate and push what is achievable with MacEtch. For this, systematic studies on the etching behaviour are performed, including different conditions and patterns.

Previous work in grating fabrication with MacEtch in liquids showed that another limit is the stability of the grating lamellas [5]. This can be addressed in two ways: using gas-MacEtch, which removes the capillary forces as the reactants and products are all in gas phase (vapor HF and gas O_2, see Fig.1a), and including bridges between the silicon lamellas. Both methods require special patterning strategies of the metal catalyst, since MacEtch requires interconnected metal structures and periodic structures in X-ray optics can produce undesired interferometric patterns. For the gas phase the best etching results were achieved with platinum [4], however patterning at the nanoscale isn't trivial. The standard lift-off technique struggles with achieving a good yield due to the thermal requirement of platinum deposition by physical evaporation, which causes thermal reflow of the patterned resist (see Fig1.c). Here, we will address the patterning strategies and the optimization of the actual methods for high aspect ratio X-ray optics. We will present some alternative methods for pattern transfer in Pt catalyst layer using electron-beam lithography and reactive ion etching with a multilayer metal break approach. First etching results already indicate the ability to realize patterned nanostructures with the desired ultra-high aspect ratios (see Fig.1d).

Gratings microfabrication by displacement Talbot lithography and deep reactive ion etching

Q. YU[1,2], * K. JEFIMOVS[2], C.K.YEH[3], L. WANG[3], H. SOLAK[3], L. CHEN[1,2], M. STAUBER[4], M. STAMPANONI[1,2], L. ROMANO[1,2]

[1]*Institute for Biomedical Engineering, University and ETH Zürich, 8092 Zürich, Switzerland*

[2]*Paul Scherrer Institut, 5232 Villigen PSI, Switzerland*

[3]*Eulitha AG, Grosszelgstrasse 21, 5436 Würenlos, Switzerland*

[4]*GratXray AG, Villigen, Switzerland*

Email: *qihui.yu@psi.ch*

Summary: Displacement Talbot Lithography in combination with deep reactive ion etching allows large area rapid patterning of submicron pitch periodic gratings with high aspect ratio. A patterning approach to introduce non-periodic features, such as cross-bars, needed to limit the line distortions during Au electroplating process for absorption gratings is presented.

High quality gratings are among the key elements for successful imaging with X-ray grating interferometry. Grating fabrication, specifically of absorption gratings, with small pitch, high aspect ratio and large area, is a great challenge from a microfabrication point of view. For the source and analyzer gratings, it is crucial to achieve a high attenuation in the range of 90% through the grating lines of the incoming X-rays, for this reason highly absorbing materials such as Au are utilized. For high energies the required Au thickness increases leading to the need of high aspect ratio metal structures. Fabrication of such structures uniformly over large areas is still an active field of research.

Silicon based manufacturing of X-ray diffractive gratings allows high precision pattern definition by lithographic techniques and high aspect ratio silicon templates by pattern transfer methods, such as Si deep reactive ion etching (DRIE). In the range of submicron pitch size, the patterning technique becomes very demanding in terms of fabrication cost. Despite the fact that the resolution of conventional contact/proximity lithography can reach feature sizes down to ~0.5 μm, the accurate control of the linewidth and uniformity becomes already very challenging for gratings with periods in the range of 1-2 μm [1]. Electron-beam lithography are then required to improve the resolution [2] with expensive long patterning time for gratings area on full wafers at 4-8 inch wafer scale. In this respect, Displacement Talbot Lithography (DTL) allows rapid patterning of periodic structures with features down to about 100 nm [3]. In combination [1,4,5] with Si deep reactive ion etching (DRIE), DTL has been used to fabricate high aspect ratio small pitch Si gratings for X-ray imaging applications [1,5]. The use of periodic patterns is the main limitation of DTL, which strongly restrict the application when more exotic X-ray Optics are needed [6]. In particular, for the fabrication of high aspect ratio absorption gratings [7,8] the grating structure requires transversal cross-bars in the silicon etched templates to reduce the line distortions during the following Au electroplating step.

In this work, we propose a patterning approach with two subsequent exposures in a negative photoresist. The first mask exposure (Fig.1a) forms the periodic pattern with small pitch for the X-ray diffractive grating by DTL. Conventional UV-mask lithography is used to create the transversal cross-bar pattern (Fig.1b), which resolution and uniformity is less critical in the X-ray interferometer setup. Since the photoresist is negative, only the un-exposed areas are dissolved during the final development process (Fig.1.c). Then, the final photoresist pattern can be directly pattern-transferred in Si by DRIE or into an intermediate hardmask material, for example SiO_2, (Fig.1d-e) for high aspect ratio gratings.

A negative resist with good adhesion properties, uniformity and resolution for both techniques is presented. First promising DRIE etching results observed by scanning electron microscopy (SEM) are shown in Fig.1f-g for grating with pitch size of 1.2 µm.

The presented technology enables rapid, scalable, high throughput, large area, small pitch grating production, which has potential impact for industrially compatible production and immediate applications of large field of view, compact, highly sensitive X-ray grating interferometry in the fields of medical diagnostic, pathology and material inspection.

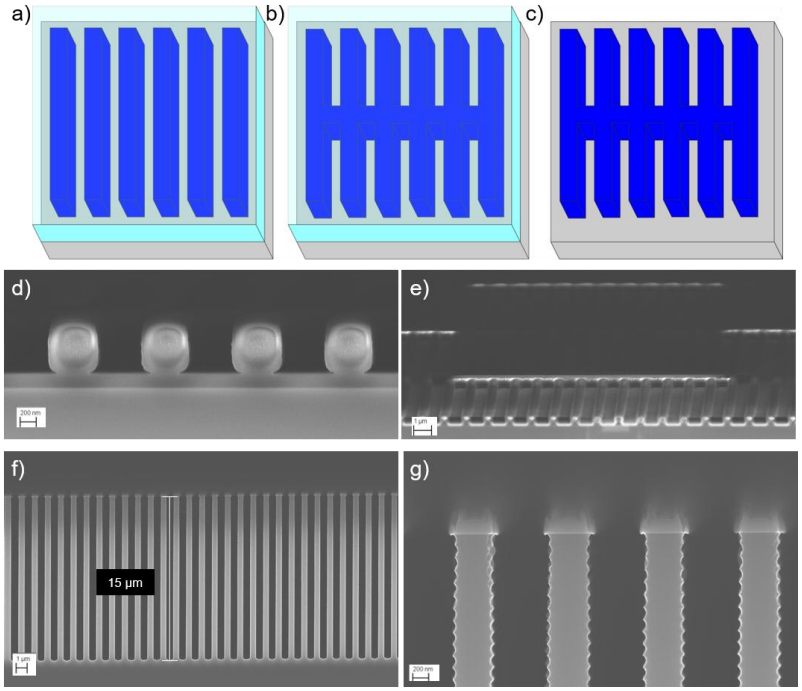

Figure 1: Schematics of the double exposure (dark blue) in negative photoresist (light blue) to enable the patterning of periodic grating lines by DTL (a) in addition to transversal cross-bar pattern (b). Since the used photoresist is negative, only un-exposed areas are dissolved during the final development process (c). SEM images in cross section of a grating with a pitch size of 1.2 µm and a duty cycle of 0.5: the DLT pattern of negative photoresist on top of the silicon substrate coated with an antireflective layer (d); the final pattern with gratings lines and cross-bar etched in SiO_2 layer (e); the etching of Si grating to a depth of 15 µm by DRIE using SiO_2 as hardmask (f); details of the top part of the grating (g) showing the typical scallops of the DRIE process and the residual of SiO_2 hardmask, indicating the DRIE process can be continued to etch additional 20 µm.

Acknowledgments

We thank the clean room facilities of PSI and the following funding agencies: SNF Sinergia Grant Nr. CRSII5 183568, SNF_R'Equip grants 206021_177036/1 and 206021_189662 (SiDRY), PHRT-TT Project Nr. 2022-572 INTIMACY, SwissLOS Lottery Fund of Kanton Aargau.

References

[1] K. Jefimovs et al., Advances in Patterning Materials and Processes XXXIV (March 27, 2017) **10146**, 101460L-101460L-101467, (2017)
[2] M. Kagias et al., Materials Science in Semiconductor Processing **92**, 73-79, (2019)
[3] H. H. Solak et al., Opt. Express **19**, 10686-10691, (2011)
[4] Z. Shi et al., Japanese Journal of Applied Physics(submitted), (2020)
[5] R. Tang et al., Opt. Express **31**, 40450-40468, (2023)
[6] A. Pandeshwar et al., Applied Physics Letters **120**, 193701, (2022)
[7] D. Josell et al., Journal of The Electrochemical Society **167**, 132504, (2020)
[8] K. Jefimovs et al., Micromachines **12**, 517, (2021)

Fabrication of 500µm deep masks for higher energy X-ray Phase Contrast Imaging

Alessandro Rossi[1]*, Daniel Josell[2], Sandro Olivo[3],
Ioannis Papakonstantinou[1]

[1]*Department of Electronic & Electrical Engineering, University College London, UK*

[2]*Material and Measurement Laboratory, National Institute of Standards and Technology, United States*

[3]*Department of Medical Physics and Biomedical Engineering, University College London, UK*

Summary: Fabrication of high aspect ratio (A.R.>10) masks has boosted X-ray phase contrast imaging (XPCI) potential enabling its usage with conventional sources. Among the several approaches to exploit phase contrast in X-ray imaging, Edge Illumination (EI) showed higher contrast compared to conventional attenuation-based X-ray imaging, maintaining its performance at relatively high energy too (>100 keV). EI uses two masks selectively absorbing and analysing the beam. To exploit EI at higher energies (160kVp), commonly used in industry, a pair of 500µm tall Si/Au gratings (A.R.>25) has been fabricated, showing superior contrast and therefore better suitability for industrial applications.

X-ray Phase Contrast imaging (XPCI) has attracted great interest over the last three decades thanks to its inherent sensitivity to hard-to-detect low-Z objects in conventional attenuation-based X-ray Imaging, due to significantly higher δ than β for most materials hard X-ray regime. This means in turn that, for an X-ray beam travelling through a sample, phase shift effects can be more evident than attenuation ones, leading to higher contrast images when objects' phase shift are detected instead of (or in combination with) their attenuation. Over the years, researchers have established several different approaches to exploit phase contrast in X-ray Imaging, firstly using synchrotron radiations and, also thanks to the advances in fabrication of gratings, conventional lab sources. [1,2,3] XPCI with conventional sources is indeed often implemented using a combination of high aspect ratio (HAR) phase and absorption or absorption-only gratings to selectively absorb and modulate the beam, as is the case in Edge Illumination (EI). [4-7]

EI employs a set of matching HAR absorption gratings, often referred to as masks. The first mask splits the beam into an array of well separated beamlets and the second, placed against the detector, selectively masks part of the pixels leaving only a smaller area exposed to the beamlets. [8,9,10] This arrangement makes the system sensitive to small beamlets' angular deviations due to refraction induced by the sample placed in between the masks, preserved also under more relaxed spatial and temporal coherence conditions, and at higher energies (>100keV). [11,12]

Interest in an effective lab translation of XPCI arises from prospective applications in a plethora of industry sectors, on top of the medical field where it has already been used for mammographic and chest scans among others.[11-18] In industrial applications, however, the common need to image denser and higher-Z objects requires higher X-ray energies: X-ray tube voltages in the range 160-225 kVp and occasionally up to 450 kVp are regularly used for industrial non-destructive testing (NDT). High-energy XPCI however introduces a series of complications due to the high photons' penetration depths resulting in a low detecting efficiency for most detectors, lower phase shifts induced by the samples, and a need for deeper gratings able to selectively absorb and/or retard the beam. [19]

High quality deeper gratings are however complicated to fabricate as the physical and chemical processes involved can fail at the bottom of very HAR structures due to a

hindered diffusion of reactants and byproducts and the optimisation of new strategies for successful vertical etching are still of great interest. [20,21]

In this work, we show a micro-fabrication process for Si and Au ≈500µm deep masks for EI at high energies and its performances. Firstly, Si wafers are patterned with a 6µm thick SPR Megaposit photoresist using Direct Writing Lithography (DWL). This combination enables a homogeneous photoresist coating of up to 4" wafers with very little substrate preparation and fully patterns it in 1-2h without the need for lithographic masks. The obtained photoresist thickness is needed to fully resist the following, 2.5h long, 'ramped' multi-step Deep Reactive Ion Etching (DRIE). DRIE, in the form of Bosch method, is based on a cycle of protecting and etching steps of the exposed Si substrate by means of, respectively, C_4F_8 and SF_6 gases repeated over time. [21] With the increase of the lamellae's aspect ratio, the sluggish migration of the gases into the Si trenches can fail to maintain the desired anisotropic etching, key for good quality gratings, especially for long etchings like ours when overheating and photoresist dissolution are significant. This problem is overcome by a ramped increase in vertical bias and cycles duration, optimised to dynamically maintain a vertical etching, as shown in Image 1a, keeping particular care on the Si surface cleanliness by means of repeated and thorough plasma oxidation. To ensure mechanical stability at cost of linear artifacts in the images, low frequency transversal Si buttresses are included in the design, while further transversal gaps are included for the same reason as well as to improve electrical conductivity across the sample. To improve gases' diffusion during DRIE and the following metallisation, the area around the gratings pattern has been etched too resulting in protruding lamellae. [22]

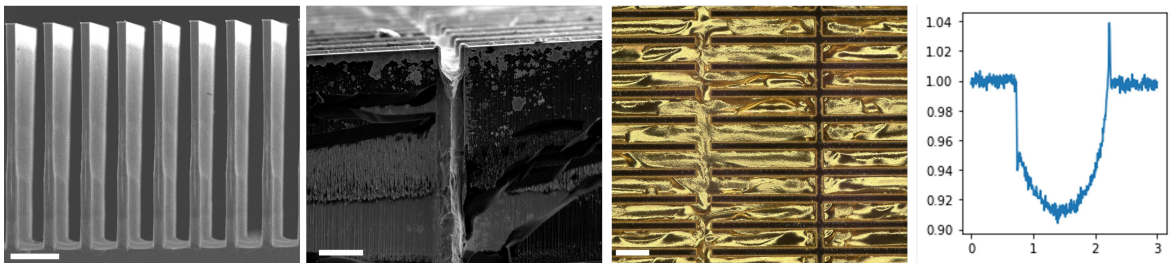

Figure 1.. a) Front-view SEM image of the edge of a mask fully etched, b) side-view SEM of the post-plating mask, showing a void-free Au filling, c) top-view optical image of fully plated mask. Scale bar = 100µm. d) Radiography of 1.5 mm thick Al rod using ≈500µm thick masks (x-axis scale is in mm)

The gratings are then coated with a Cr/Au seed layer to ensure conductivity for the final Au plating inside the trenches. Using a common sulphide-based Au plating solution resulted in a preferential plating at the top of the lamellae, which eventually clogged the apertures and prevented a full filling of the trenches. Therefore, Bi-mediated Au 'superconformal' bottom-up electroplating is used for a highly dense and homogeneous filling of more than 90% than the ≈500µm apertures, for the first time for structures of such height. The addition of Bi^{3+} to Au plating solution, combined with the appropriate applied voltages, results in a void-free Au plating, as shown in the SEM micrograph in Image 1b and the optical top-view Image 1c (where the transversal gaps and Si bridges are visible), and previously proved to be comparable to bulk density. [23, 24]

The obtained gratings are experimentally compared to a previously available set of ≈300µm deep pair of gratings commercially available with radiographs at different energies, showing an increased potential for industrial XPCI for the ≈500µm thanks to their lower X-ray transmission and improved contrasts gratings, especially at higher energies. Preliminary results on the thicker masks' performances show a good show excellent sensitivity to phase shift also at high energies. Phase-induced edge enhancement is clearly visible in Image 1d using a conventional source at 160kVp, filtering energies up to 45keV.

Acknowledgments

This work was funded by EPSRC (grant EP/T005408/1). A.O. was supported by the Royal Academy of Engineering under the "Chairs in Emerging Technologies" scheme (grant CiET1819/2/78). The authors acknowledge the assistance of the technical team in the London Centre for Nanotechnology (LCN): Steve Etienne, Vijayalakashmi Krishnan, Lorella Rossi, Rohit Khanna, and Suguo Huo, as well as the assistance of Anton Charman, Daniel Briglin, and David Bates at Nikon-XTek.

References

[1] M. Endrizzi, *X-ray Phase Contrast Imaging*, Nucl. Instrum. Methods Phys. Res. A **878**, 88-98 (2018)

[2] A. Snigirev et al., *On the possibilities of x-ray phase contrast microimaging by coherent high-energy synchrotron radiation*, Rev. Sci. Instrum. **66**, 5486–5492 (1995)

[3] D. Chapman et al., *Diffraction enhanced x-ray imaging,* Phys. Med. Biol. **42**, 2015 (1997)

[4] A. Olivo J. Phys., *Edge-illumination x-ray phase contrast* imaging, Condens. Matter **33**, 363002 (2021)

[5] A. Momose et al., *Demonstration of X-ray Talbot Interferometry,* Japan. J. Appl. Phys. **42**, L866 (2003)

[6] F. Pfeiffer et al., *Hard-X-ray dark-field imaging using a grating interferometer,* Nat. Mater. **7**, 134 (2008)

[7] D. Noda et al., *Fabrication of Diffraction Grating with High Aspect Ratio Using X-ray Lithography Technique for X-ray Phase Imaging*, Jpn. J. Appl. Phys. **46**, 849 (2007)

[8] A. Olivo & R. Speller, *Modelling of a novel x-ray phase contrast imaging technique based on coded apertures*, Phys. Med. Biol. **52**, 6555 (2007)

[9] P.C. Diemoz et al., Appl. *Sensitivity of laboratory based implementations of edge illumination X-ray phase contrast imaging*, Phys. Lett. **103**, 244104 (2013)

[10] P.C. Diemoz et al. (2014). In : *22nd International Congress on X-Ray Optics and Microanalysis*, Hamburg 2–6 September 2013. J. Phys.: Conf. Ser. **499** 012006

[11] T. Partridge et al., *Enhanced detection of threat materials by dark-field x-ray imaging combined with deep neural networks,* Nat. Comm. **13**, 4561 (2022)

[12] T. Partridge et al., *Reliable extraction of x-ray refraction and dark-field signals with a large field of view, multi-modal scanning system at spectral energies up to 150 kVp*, J. Phys. D, Accepted Manuscript

[13] G. Tromba et al., *The SYRMEP Beamline of Elettra: Clinical Mammography and Bio-medical applications,* AIP Conf. Proc. **1266**, 18–23 (2010)

[14] E. Castelli et al., *Mammography with Synchrotron Radiation: First Clinical Experience with Phase-Detection Technique***,** Radiology **259**, 684–694 (2011)

[15] M. Stampanoni et al., *The first analysis and clinical evaluation of native breast tissue using differential phase-contrast mammography*, Investigative Radiology **46**, 801-806 (2011)

[16] K. Willer et al, *X-ray dark-field chest imaging for detection and quantification of emphysema in patients with chronic obstructive pulmonary disease : a diagnostic accuracy study,* Lancet Digi. Health **3**, e733–e744 (2021)

[17] H. Rougé-Labriet et al., *X-ray Phase Contrast osteo-articular imaging: a pilot study on cadaveric human hands*, Sci. Rep. **10,** 1911 (2020)

[18] S. Mayo et al., *In-Line Phase-Contrast X-ray Imaging and Tomography for Materials Science,* Materials ***5*(5)**, 937-965 (2012)

[19] T. Thüring et al, *X-ray phase-contrast imaging at 100 keV on a conventional source*, Sci Rep **4**, 5198 (2014)

[20] I. Buchanan et al., *Effective modelling of high-energy laboratory-based X-ray phase contrast imaging utilizing absorption masks or gratings*, J. Appl. Phys. **128**, 214503 (2020)

[21] M.S. Gerlt et al., *Reduced Etch Lag and High Aspect Ratios by Deep Reactive Ion Etching (DRIE)*, Micromachines, **12(5)**, 542 (2021)

[22] F. Laermer, S. Franssila, L. Sainiemi, and K. Kolari, *Handbook of Silicon Based MEMS Materials and Technologies (Third edition).* Elsevier. 417-446 (2020)

[23] M.Michalska et al., *Fabrication of High-Aspect-Ratio Nanogratings for Phase-based X-ray imaging*, Adv. Funct. Mat. **33**, 2212660 (2023)

[24] D. Josell et al., *Pushing the Limits of Bottom-Up Gold Filling for X-ray Grating Interferometry*, J. Electrochem. Soc. **167**, 132504 (2020)

[25] D. Josell et al., *Robust Bottom-Up Gold Filling of Deep Trenches and Gratings*, J. Electrochem. Soc. **169,** 032509 (2022)

A simulation study of optimized-aperture gratings for edge illumination cone-beam phase contrast x-ray imaging

* P.-J. VANTIENEN[1,2], J. SIJBERS[1,2],J. DE BEENHOUWER[1,2]
[1]*imec-Vision Lab, University of Antwerp, Belgium*
[2]*DynXlab: Center for 4D Quantitative X-ray Imaging and Analysis, Antwerp, Belgium*
Email: *pieter-jan.vanthienen@uantwerpen.be*

Summary: Edge illumination (EI) is an established x-ray phase-contrast imaging method that relies on gratings to obtain attenuation, phase and dark field contrast. Despite the successful transition from synchrotron to lab sources, the cone-beam geometry of lab systems limits the effectiveness of conventional gratings. The non-parallel incidence of X-rays on planar gratings with equally sized apertures introduces unwanted shadowing effects. In this paper, a grating design with optimized position-dependent apertures is introduced and compared to a conventional grating and a grating with fan-beam shaped gratings bars. Numerical simulations show that this optimized-aperture design must be considered when constructing an EI setup.

Introduction

Edge-illumination (EI) is an x-ray phase-contrast imaging method that relies on gratings to obtain attenuation, phase and dark field contrast. EI finds its origin in synchrotron radiation experiments with parallel beam sources [1], but has gradually evolved towards lab systems [2]. However, the cone beam geometry of lab systems limits the effectiveness of using conventional planar gratings with equal apertures. Indeed, while the grating apertures are designed for parallel-beam imaging, cone beam X-rays might deviate significantly from such a geometry, resulting in an intensity decrease towards the detector edge, known as the shadow effect [3,4]. Besides a loss of flux, shadowing also reduces contrast and restricts the field of view and the design parameters of the grating [4,5]. In this paper, we study optimized-aperture (OA) gratings and compare them to conventional gratings and gratings with fan-beam shaped grating bars (sheared gratings), of which the latter was the optimal choice according to our previous study [4].

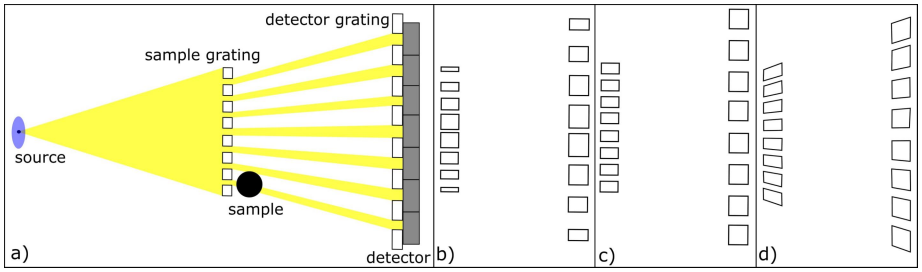

Figure 1: a) An EI setup. b) OA gratings. c) Conventional gratings. d) sheared gratings.

Method

The gratings are evaluated using the Monte-Carlo software GATE. The simulation setup contains a source, sample, detector, and two gold-plated gratings, as shown in Fig.1a. A source-to-detector distance of 1800 mm and a grating magnification factor of 3/2 is used in the simulations. The source is a polychromatic (60kV) cone-beam source with a finite spot-size of 34×10 μm^2. For a line-detector consisting of 3201 pixels of 150 µm, this geometry results in a cone angle of 15.2◦. Each Monte-Carlo simulation in GATE uses $2 \cdot 10^8$ photons and the illumination curve is sampled at 5 phase-steps for every flat field and projection.

The phantom is an aluminum cylinder, positioned at the edge of the field of view. The OA grating is shown in Fig 1b). While the grating period stays constant, the size of the apertures linearly increases towards the edge of the field of view, hereby compensating the flux loss by broadening the beamlets. The OA grating is compared to a conventional grating (Fig. 1c) and a sheared grating (Fig 1d).

Experiments & results

The effectiveness of the gratings is evaluated based on four experiments, of which the results are shown in Table 1. In the first experiment, the gratings are compared based on the intensity of the flat field. The flat field intensity of OA gratings is comparable to sheared gratings: slightly lower at perfect alignment, slightly higher at the outer phase-step. The second experiment evaluates the loss in attenuation contrast due to beam hardening, by comparing the maximal attenuation contrast of the phantom. While a loss is observed compared to sheared gratings, the loss in attenuation contrast of OA gratings is significantly lower compared to conventional gratings. The third experiment compares the peak-to-peak contrast-to-noise ratio (p2pCNR)[5], which is obtained by dividing the difference between the phase contrast peaks of the phantom by the phase contrast variance. The OA gratings have a lower p2pCNR than sheared gratings, but higher than conventional gratings. The fourth experiment compares the gratings on contrast precision, by calculating the standard deviation of the phase and attenuation contrast in the centre of the phantom over 50 simulations. The contrast precision of OA gratings is significantly better than conventional gratings and comparable to sheared gratings: the attenuation contrast standard deviation is slightly lower but the phase contrast standard deviation is slightly higher.

	Intensity[photons/pixel]		attenuation contrast	p2pCNR [10^6]	Contrast standard deviation	
	Phase-step	Aligned			Attenuation	Phase [µrad]
conventional	468	2461	0,65±0,08	5,7±1	0,080	0,690
sheared	1811	**5862**	**1,85±0,02**	**50±4**	0,016	**0,134**
OA	**1939**	5649	1,35±0,02	42±4	**0,014**	0,145

Table 1: Results of the four experiments: flatfield intensity, attenuation contrast, peak-to-peak contrast-to-noise ratio and contrast precision.

Conclusion

Conventional EI setups suffer from shadowing, which causes a reduction in detected flux, lower contrast, and setup parameter restrictions. This paper studies an OA grating, that significantly reduces the shadow effect, while retaining the ease-of-use of conventional gratings. A comparative study of the flux, attenuation contrast, p2pCNR, and contrast precision shows that the grating outperforms conventional gratings. Although sheared gratings still perform better, the benefits of ease-of-use of OA gratings will outweigh in certain cases the limited differences in performance.

Acknowledgments

This research was supported by Research Foundation - Flanders (FWO) (G094320N, G090020N, S003421N)

References

[1] A. Olivo, et al., Med. Phys. 28(8), 1610–1619 (2001)

[2] A. Olivo and R. Speller, Appl. Phys. Lett. 91(7), 074106 (2007)

[3] P.-J. Vanthienen, et al., Opt. Express 31, 28051-28064 (2023)

[4] B. Huyge, et al., IEEE 18th International Symposium on Biomedical Imaging, pp. 1310-1313 (2021)

[5] J. Sanctorum, et al., Proc. SPIE 12242, 1224218 (2022)

Single-exposure x-ray dark-field imaging: on the quantification of sample microstructure using a single-grid setup

*YING YING HOW, DAVID M. PAGANIN, KAYE S. MORGAN
School of Physics and Astronomy, Monash University, Australia
Email: ying.how1@monash.edu

Summary: Small or ultra-small angle x-ray scattering (SAXS or USAXS) from unresolved sample microstructures contributes to contrast in x-ray dark-field imaging. Here we present a novel method for quantitative single-exposure grid-based x-ray dark-field imaging. By illuminating the sample with a resolved grid pattern, we extracted the scattering angle via the retrieved dark-field signal and related the angle to the sample microstructure size for a selection of microspheres. We are now quantitatively comparing the extracted scattering angle to the SAXS distribution via simulation and experimental data to explore the possibility of parallel SAXS measurements from a single sample exposure.

The size of the smallest detectable sample feature in an imaging system is usually restricted by the spatial resolution of the system. This limitation can now be overcome by x-ray dark-field imaging, where the dark-field signals are generated by the small or ultra-small angle x-ray scattering (SAXS or USAXS) from otherwise-unresolved sample features, such as fibres, powders or bubbles. A quantitative dark-field signal is useful since it can provide information about the size, packing density, and/or material of unresolved sample microstructure, information that is inaccessible from the conventional or phase-contrast x-ray images. However, many of the dark-field imaging techniques require multiple exposures and well-aligned optics.

Single-grid imaging is an emerging x-ray imaging technique that has a relatively simple setup. It only requires one optical element to provide a reference pattern - typically a grid [1, 2], but alternatively a piece of sandpaper [3,4], in which case the technique is known as speckle-based imaging. The attenuation, phase shift and dark-field signals can be extracted simultaneously from a single sample exposure by observing how the reference pattern is reduced in intensity, locally shifted, and blurred out, due to the presence of the sample. The sample-induced changes in the reference pattern can be extracted by performing a local cross-correlation between grid-only and grid-and-sample images. By performing a model-informed curve-fitting analysis on the cross-correlation results, we can extract the change in amplitude and the mean of the reference pattern, which then gives us the dark-field signal [5]. This technique is therefore feasible for dynamic imaging, where a short data acquisition time can minimise motion blurring and the radiation dose delivered to the sample.

Recently, we have described how a local cross-correlation approach can extract a scattering angle to quantify the dark-field signal from single-grid imaging [5] and have related the signal to the sample microstructure size [6]. In this setup, the sensitivity to weak scattering can be increased by extending the sample-to-detector distance, but at the risk of saturating the dark-field signal. We have investigated the consistency of the extracted scattering angle as the sample-to-detector distance is varied and hence at what distance quantitative dark-field imaging should be performed using a single sample exposure. We have applied our algorithm to images of polystyrene microspheres of 5 different diameters to evaluate how our measurements align with theoretical predictions. Our results show that the extracted dark-field scattering angle is inversely proportional to $\sqrt{T}$, where T represents

the sample thickness, which was consistent with our theoretical model for multiple refraction through these microspheres.

We are now quantitatively relating the dark-field scattering angle to the SAXS angle, which is conventionally measured using a specialised SAXS setup that uses a single pinhole. We model the scattering from randomly-packed polystyrene microspheres using the angular spectrum method and projection approximation in our simulation and verify our model using the single-grid dark-field and SAXS data collected from a synchrotron. Understanding this quantitative relationship could be useful in diagnosing or tracking lung diseases such as emphysema and cystic fibrosis, where there is a change in alveoli size which alters the x-ray dark-field signal [7,8], and in airport screening, where such a technique could be used to identify powder-like goods [9].

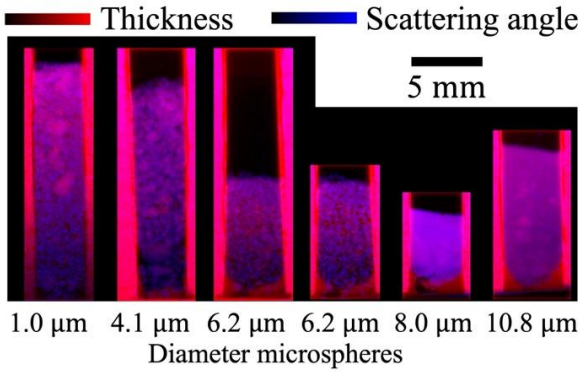

Figure 1: Colour image of the wedge-shaped polystyrene microsphere samples, separated by rubber walls, showing the complementarity of the attenuation and dark-field signals (normalised between 0 and 1 individually), here both extracted from a single sample exposure using the algorithm described in How *et al*., 2022, 2023 [5,6].

Acknowledgements
This research was undertaken on the Imaging and Medical Beamline at the Australian Synchrotron, part of ANSTO. The project is supported by the Australian Research Council (FT180100374).

References
[1] H. H. Wen *et al.*, Single-shot x-ray differential phase-contrast and diffraction imaging using two-dimensional transmission gratings, *Opt. Lett.* **35**, 1932-1934, (2010).
[2] K. S. Morgan *et al.*, Quantitative single-exposure x-ray phase contrast imaging using a single attenuation grid, *Opt. Express* **19**, 19781-19789, (2011).
[3] K. S. Morgan *et al.*, X-ray phase imaging with a paper analyzer, *Appl. Phys. Lett.* **100**, 124102, (2012).
[4] S. Berujon *et al.*, X-ray multimodal imaging using a random-phase object, *Phys. Rev. A* **86**, 063813, (2012).
[5] Y. Y. How *et al.*, Quantifying the x-ray dark-field signal in single-grid imaging, *Opt. Express* **30**, 10899-10918, (2022).
[6] Y. Y. How *et al.*, On the quantification of sample microstructure using single-exposure x-ray dark-field imaging via a single-grid setup, *Sci. Rep.* **13**, 11001, (2023).
[7] M. J. Kitchen *et al.*, Emphysema quantified: mapping regional airway dimensions using 2D phase contrast X-ray imaging, *Biomed. Opt. Express* **11**, 4176-4190, (2020).
[8] K. Willer *et al.*, X-ray dark-field chest imaging for detection and quantification of emphysema in patients with chronic obstructive pulmonary disease: a diagnostic accuracy study, *The Lancet Digit. Heal.* **3**, e733–e744, (2021).
[9] E. A. Miller *et al.*, Phase contrast x-ray imaging signatures for security applications, *IEEE Trans. Nucl. Sci.* **60**, 416-422, (2013).

Implementation of hard x-ray dual-phase grating interferometer at UGCT

*Ruizhi Tang[1,2], Caori Organista[1,2,3,4], Jan Aelterman[1,2,5], Marco Stampanoni[3,4], Matthieu N. Boone[1,2]

[1]*Centre for X-Ray Tomography (UGCT), Ghent University, Belgium*

[2]*Department of Physics and Astronomy, Ghent University, Belgium*

[3]*Swiss Light Source, Paul Scherrer Institute, Switzerland*

[4]*Institute for Biomedical Engineering, ETH Zurich, Switzerland*

[5]*IPI-TELIN-IMEC, Ghent University, Belgium*

Email: *ruizhi.tang@ugent.be*

Summary: A dual-phase x-ray grating interferometer (DP-XGI) is implemented at UGCT to quantitatively investigate the submicron-structural information of samples from the relationship between the dark-field signal and correlation length. To allow quantitatively interpretation of this tunable dark-field imaging, accurate geometrical parameters of the interferometer are needed. These are accurately retrieved through a parameter space determination algorithm, and two gratings are automatically aligned with high precision. Moreover, a correction algorithm has been developed to cope with the excess dark-field signal resulting from a beam hardening effect. Different types of samples have been imaged by our set-up, such as nano-spheres, mineral materials and woods.

In DP-XGI, Moiré patterns generated by the superposition of the modulation pattern of two phase-grating are directly resolved by the detector [1]. A typical configuration of the set-up is shown in Figure 1 [2]. One of advantages provided by DP-XGI is that it is tunable, meaning that the correlation length can be adjusted by changing the inter-grating distance (R_g) without influencing the sample's magnification. Therefore, DP-XGI provides a straightforward way to measure the pixel-wise relationship between the correlation length and dark-field signal [1], from which the quantitative small-angle scattering information can be retrieved [3].

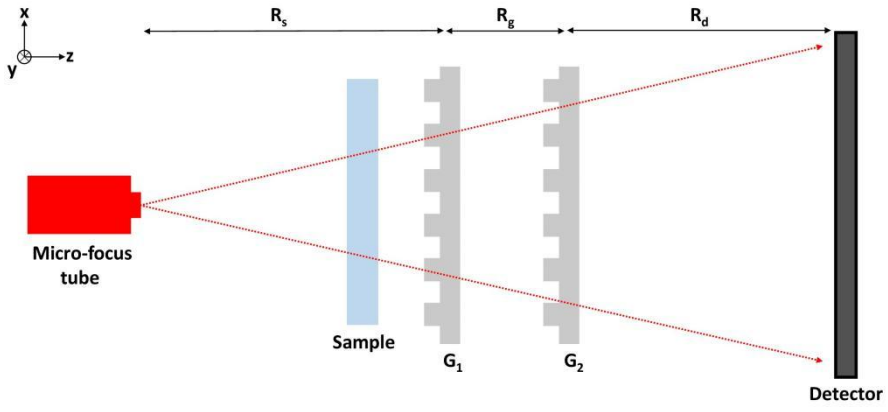

Figure 1: Schematic of dual-phase x-ray grating interferometry.

Since the correlation length is a parameter that is a function of the geometrical parameters of the set-up, a precise calculation requires accurate determination of the geometrical distances [4]. Based on the properties of the Moiré fringe, a parameter space determination algorithm is developed to precisely retrieve three distances (R_s, R_g and R_d) and rotational

Gratings for X-ray and neutron DPCI: what's new?

* R. FETTIG[1], T. BECKENBACH[1], J. GUTEKUNST[1], K. KAISER[1], P. MEYER[2]
[1]*microworks GmbH, Schnetzlerstr.9, 76137 Karlsruhe, Germany*
[2]*Karlsruhe Institute of Technology, Institute of Microstructure Technology, 76344 Eggenstein-Leopoldshafen, Germany*
E-Mail: *rainer.fettig@microworks.de*

X-ray Lithography [1] is a versatile tool for microstructure fabrication with many applications. Its potential to create high aspect ratio microstructures in radiation resistant polymer and filling them by electroplatable metals makes it ideal for producing the fine, high structures required for Grating Based X-ray Imaging (GBXI). While the Edge Illumination approach [2] usually poses no challenge in grating fabrication using the LIGA-Technique due to its larger periods which need to match the detector pixel size, gratings for the Talbot-Lau [3] approach are more challenging.
We are constantly improving the process, and these are the areas we will focus on in the talk:

✓**small period:** Scientists have shown a diverse interest in small periods around 1µm and smaller, which improves the contrast-to-noise ratio and generates complex patterns of diffraction intensities. X-ray LIGA has the potential to make high aspect ratio structures, which can be described on a logarithmic scale for 1µm linewidth or above. An aspect ratio (AR) of 10 and 20 is considered routine, while 50 usually requires process tuning. However, an AR of around 100 still poses challenges.

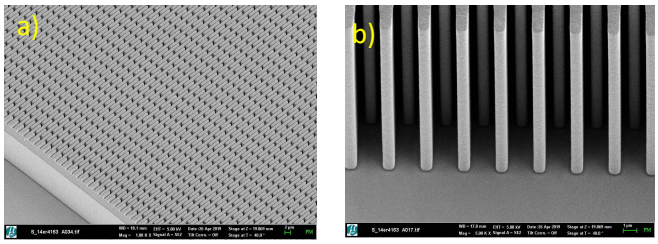

Figure 1 a and b: SEM picture of a 1.4 µm period gratings (bridge design) with 16 µm thick Au lamellae (a-top view, b-sideview)

✓**inclined bridge:** Long, high, and narrow polymer lines in grating layouts are typically unstable. To address this, bridges that are 2µm wide are used, with the distance between them adapted based on height requirements. However, the bridge regions are transparent to X-rays, which is highly unwanted when used as a G0 grating since the magnification of the bridges onto the detector is undesirable. To solve this issue, the bridges are inclined to decrease unwanted transmission; the irradiation are performed by tilting mask and sample with the desired angle (5 to 10 deg.).

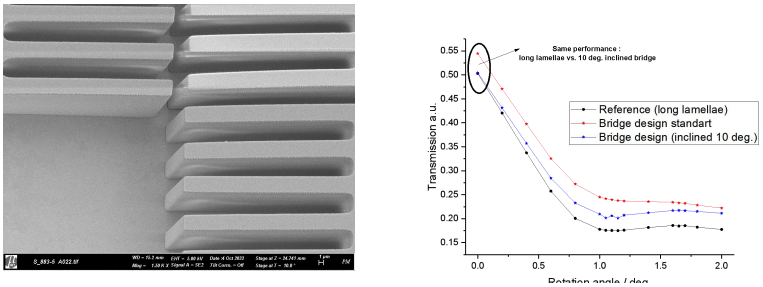

Figure 2: By inclining the bridge, the performance is similar to long lamellae design

✓**substrate:** The use of different substrates, such as graphite, silicon, vitreous carbon and polyimide, allows for customization to suit various applications. As an example, to increase transmission of a phase grating G1 used at a back lighter experiment (designed

energy: 10keV), we have considerably reduced the thickness of the polyimide substrate from 500µm to 10µm.

✓**removing the resist/stabilisation :** When the source grating, whose resist is still present, is placed only a few centimeters away from high power rotating anode sources, a loss in visibility and therefore a loss in image quality is observed after several months of use. This effect is attributed to the aging of the resist under irradiation. Solution: stripping the resist but the problem is the collapse of the metallic structure when the resist is removed. A new method, which consists of positioning perpendicular arranged metal bridges on top of the grating (roof bridges), is tested as a solution.

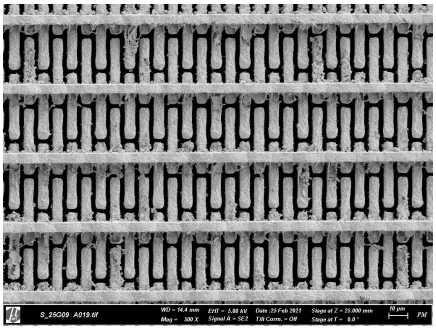

Figure 3: A 7.72µm period grating with fully removed resist and 10µm nickel top bridges

All of these latest developments are used in our standardized Talbot-Lau setup with three LIGA gratings (TALINT EDU interferometer) [4].

We will also look at Microworks' current grating standards (periods, aspect ratios, duty cycle and grating size) as we believe that standardization is the first step towards reducing the cost of grating sets.

The metals commonly used in the X-ray LIGA process do not provide sufficient absorption for gratings used in neutron imaging. Gadolinium (Gd) is the best choice for such gratings, but no process exists for its electrodeposition.

Triggered by an approach described by Gustschin [5] we adopted the method using gadolinium oxide powder. Starting with anisotropically etched silicon, it was possible to uniformly fill areas of 90mm diameter of Si structures with 56µm pitch, 30µm gap 60µm deep, giving a filling equivalent to 18µm pure Gd. Based on some preliminary tests, gap widths down to 4µm appear feasible.

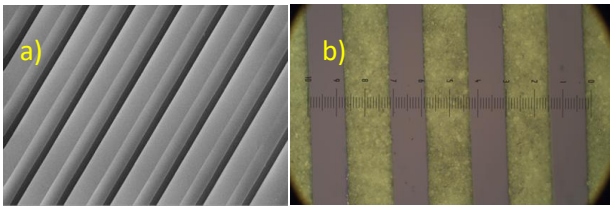

Figure 4: A grating etch in a silicon wafer, pitch 56µm, gap 30µm, depth 60µm a) as etched, b) filled with GdO_2 powder.

Acknowledgments

The authors acknowledge the support of the Karlsruhe Nano Micro Facility (KNMF) and the ANKA synchrotron light source facility at the Karlsruhe Institute of Technology (KIT).

References

[1] P. Meyer and J. Schulz "Deep X-ray Lithography" Micromanufacturing Engineering and Technology, 2nd edition, pp.365-391, 2015 - DOI: 10.1016/B978-0-323-31149-6.00016-5

[2] Alessandro Olivo 2021, Edge-illumination x-ray phase-contrast imaging, J. Phys.: Condens. Matter **33** 363002, DOI: 10.1088/1361-648X/ac0e6e

[3] Birnbacher, Lorenz et. al. (2021). Quantitative X-ray phase contrast computed tomography with grating interferometry: Biomedical applications of quantitative X-ray grating-based phase contrast computed tomography. European Journal of Nuclear Medicine and Molecular Imaging. 48. 10.1007/s00259-021-05259-6.

[4] J. Gutekunst et. al. Advancing research and education with simple setup Talbot-Lau-Interferometers NDT.net Issue: 2023-03, 12th Conference on Industrial Computed Tomography (iCT) 2023, 27 February - 2 March 2023 Fürth, Germany (iCT 2023) | Vol. 28(3) DOI: 10.58286/27750

[5] A. Gustschin, T. Neuwirth, A. Backs, et al., Rev. Sci. Instrum. **89**, 103702 (2018); DOI:10.1063/1.5047055

On spaces of scattering functions in AXDT reconstruction

Ruifeng Liu[1], Li Zhang[1] and Zhentian Wang[1,*]
[1]*Department of Engineering Physics, Tsinghua University, Beijing, China*
Email: *wangzhentian@tsinghua.edu.cn*

Summary: In the forward model of anisotropic X-ray dark-field tomography (AXDT), the scattering function for every voxel is equivalently defined as a real function on unit sphere, and all their linear combinations forms an inner space of functions, called *space of scattering functions*. As the space is infinite dimensional in principle, appropriate discretization should be adopted in numerical reconstruction, i.e., the scattering function should be parameterized by a finite number of parameters. Here, we prove that, the choice of the number of parameters for scattering functions is not arbitrary and has an upper limit, or it will cause ill-conditioned problems in reconstruction.

The techniques of tensor tomography extended the concept of conventional computed tomography by reconstructing, instead of a scalar field, a tensor field carrying information of local anisotropic structures within every voxel of the sample. The reconstruction processes of tensor tomography techniques are mathematically based on the forward models, in which the tensor model for every voxel plays a key role. As the tensor is in an infinite dimensional space in principle, it is necessary to discretize it for numerical reconstruction. There are many ways to construct a discretized model for scattering tensor in the infinite dimensional space $\mathrm{C}(\mathrm{S}_2, \mathrm{R})$, and they share the same idea with function approximation methods, which is to approximate complicated functions by linear combinations of a series of linearly independent simple functions. By function approximation, a function can be decomposed into the sum of a series of products of simple functions and corresponding coefficients. Thus, the decomposition process let a function be represented by a series of parameters.

In literature, researchers may use different family of functions and different number of parameters. In 2014, Malecki et al. [1] used seven parameters, which corresponds to three orthogonal edge directions and four body diagonal directions of unit cube, to represent a scattering tensor. In 2016, Wieczorek et al. [2] used three parameters, corresponding to three spherical-harmonics functions degree four. In 2019, Gao et al. [3] used a 3-by-3 symmetric matrix with six degrees of freedom to approximate a scattering tensor.

As a limited number of parameters is used to approximate the scattering function, one may make a general conjecture by intuition, that as the number of parameters increases, the quality of reconstructed image should be improved. However, this is not the truth, because in the linear problem of reconstruction, redundant parameters lead to ill-conditioned problems. We prove a general proposition, that the choice of the number of parameters for approximating scattering functions is not arbitrary and has an upper limit, or it will cause ill-conditioned problems. In the proposition, the upper limit of parameters depends on the imaging system and image acquisition sequence, which corresponds with the manner of the sample's rotation, and do NOT depend on the family of functions nor the sample. We then discuss the upper limits under different conditions, and find out a particular upper limit of 15 for the imaging system and data acquisition sequence proposed by Malecki et al. [1]

The proof is carried out by three main steps. First, we deduced a uniform form of the discretized forward models in previous works, based on the closed-form continuous model for AXDT, given as follows by Wieczorek et al. (see Fig. 1).

$$d_j = \exp\left(- \int_{L_j} \int_{S_2} h(u, t_j, l_j)\eta(u, x) \frac{d\Omega(u)}{4\pi} dx \right) \#(1)$$

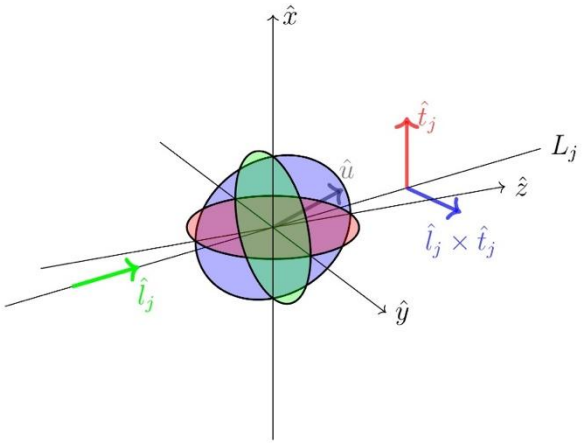

Figure 1: Geometric diagram of variables in AXDT model.

We then prove that one of the factors of the ill-conditioned problems in reconstruction process is an unequal condition, that the number of parameters for function approximation exceeds the rank of a certain matrix concerned with a factor called *weighting function* or *weight factor* in literature, which depends on the imaging system. Finally, we prove that, the rank of the mentioned matrix equals to the dimensionality of a specific subspace (called *weighting space*) of the space of continuous real functions on unit sphere, and the subspace is expanded by the weighting function after different rotation operations, which correspond with the ones of the sample. In the calculation of the dimensionality of the weighting space under the specific condition, we adopt spherical-harmonics decomposition and exploit the rotational invariance of spherical harmonics [4].

To summarize our work, we prove that the number of parameters to approximate scattering functions in AXDT has an upper limit which equals to the dimensionality of a specific subspace of $C(S_2, R)$. Our work implies a new metric for X-ray tensor tomography systems, which indicate the capability of a tensor tomography system to accommodate valid parameters for tensor reconstruction, and may enable optimization of the choice of family of functions and corresponding parameters.

References

[1] A. Malecki, G. Potdevin, T. Biernath, E. Eggl, K. Willer, T. Lasser, J. Maisenbacher, J. Gibmeier, A. Wanner, and F. Pfeiffer, X-ray tensor tomography, *Europhysics Letters*, **105**(3), 38002, (2014)

[2] M. Wieczorek, F. Schaff, F. Pfeiffer, and T. Lasser, Anisotropic x-ray dark-field tomography: A continuous model and its discretization, *Physical Review Letters*, **117**, 158101, (2016)

[3] Z. Gao, M. Guizar-Sicairos, V. Lutz-Bueno, A. Schröter, M. Liebi, M. Rudin, and M. Georgiadis, High-speed tensor tomography: Iterative reconstruction tensor tomography (IRTT) algorithm, *Acta Crystallographica A,* **75**, 223–238, (2019)

[4] R. Richtmyer et al. *Principles of advanced mathematical physics: Volume II*. New York: Springer-Verlag Inc. 323 (1981)

Assessing Image Quality in Grating Interferometry Breast CT: A Qualitative Study with Fresh Tumorectomy Scans

*S. KASER[1,2], M. RAWLIK[1,2], C. ORGANISTA[1,2] A. PEREIRA[1,2], S. SPINDLER[1,2], M. STAUBER[3], S. VAN GOGH[1,2], M.-C. ZDORA[1,2], M. POLIKARPOV[1,2], Z. WANG[1,4], J. XU[1,2], E. G. YUKIHARA[2], K. JEFIMOVS[2], Z. SHI[1,2], L. ROMANO[1,2], J. B. CHRISTENSEN[2], R. A. KUBIK-HUCH[5], T. NIEMANN[5], C. LEO[6], Z. VARGA[7], M. MARCON[8], J. WEBER[8], K. OCHS[8], M. STAMPANONI[1,2]

[1]*Institute for Biomedical Engineering, ETH Zürich and University of Zürich, Zürich, Switzerland*
[2]*Paul Scherrer Institute, Villigen, Switzerland*
[3]*GratXray AG, Villigen, Switzerland*
[4]*Department of Engineering Physics, Tsinghua University, Haidian District, 100080 Beijing, China*
[5]*Department of Radiology, Kantonsspital Baden, Baden, Switzerland*
[6]*Interdisciplinary Breast Center, Kantonsspital Baden, Baden, Switzerland*
[7]*Department of Pathology and Molecular Pathology, University Hospital Zürich, Zürich, Switzerland*
[8]*Institute for Diagnostic and Interventional Radiology, University Hospital Zürich, Zürich, Switzerland*
skaser@ethz.ch

Summary: Grating-Interferometry Breast CT (GI-BCT) shows potential to improve early cancer detection as compared to state-of-the-art imaging techniques. In this study, we conducted an experiment employing our static GI-BCT system, capturing images of fresh tumorectomy samples (scanned directly post-removal from patients). The reconstructed images were presented to experienced radiologists for the assessment of perceived image quality. By focusing on the subjective evaluation by radiologists, we aim to provide understanding of GI-BCT's diagnostic potential in breast cancer.

For breast cancer detection, various state-of-the-art imaging modalities can be used. Mammography and breast tomosynthesis images are sometimes difficult to interpret in women with dense breast due to limited contrast and (partial) tissue overlap [1]. Three-dimensional imaging techniques like MRI or full-body CT have the shortcoming of requiring contrast medium administration and/or lower image resolution. Dedicated breast CT, which has been recently introduced to clinical practice [2], combines full volumetric information with high resolution. Here, grating interferometry [3] has been shown to increase dose efficiency (lower contrast-to-noise ratio at the same dose level).

In our study at the Paul Scherrer Institute, Switzerland, we imaged five fresh tumorectomy samples on a GI-BCT system equipped with a tungsten-anode X-ray source operated at 70kVp, a Talbot-Lau interferometer (symmetric geometry, grating pitches of 4.2µm, 46keV design energy, 5th order) and a 100µm-pixel-size photon-counting detector. With a geometric magnification of 1.75, the field-of-view was 10 cm wide.

The tumorectomy samples were delivered by Kantonsspital Baden (KSB) directly after being removed from the patient. Each specimen underwent measurements at various absorbed dose levels, ranging between 22 mGy and 176 mGy. Three distinct images – attenuation, phase contrast, and dark field – were obtained from each measurement. Furthermore, a fused image [3] was calculated from the attenuation and phase reconstructions.

Following image reconstruction, the images were presented to experienced radiologists for qualitative evaluation, assessing perceived image sharpness, noise, overall image quality, tumor margins and calcification visibility. To further assess diagnostic potential of GI-BCT,

our measurements were compared with images from KSB's in-house devices – post-operative full-body CT of the specimen and pre-operative mammography scans. Additionally, findings underwent cross-referencing with histopathology and pre-operative mammography reports.

Our study aims to answer key questions in the diagnostic potential of GI-BCT, such as providing information on how and if subjectively perceived image quality correlates with quantitative assessments and dose, how our system compares to state-of-the-art hospital techniques, and how effectively it can depict calcifications. Our objective is to complement studies focusing exclusively on quantitative image quality assessment in GI-BCT [3] and to give first insights how this already demonstrated quantitative gain in image quality could potentially contribute to a future diagnostic improvement due to a gain in perceived image quality.

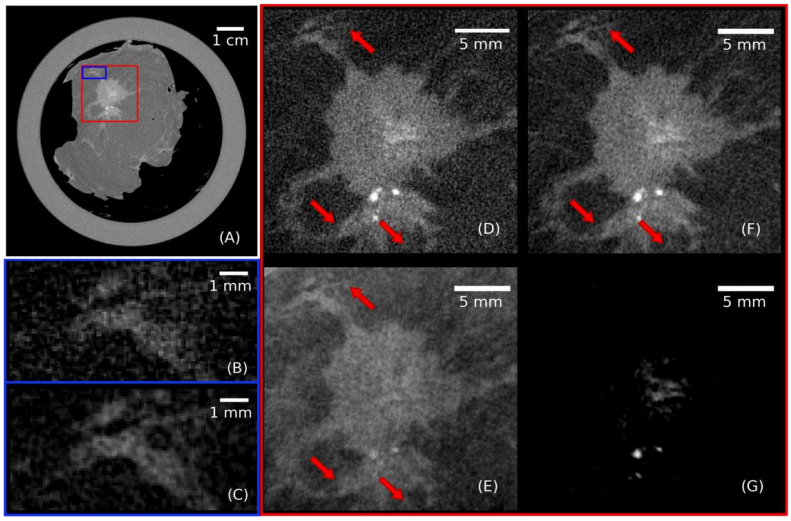

Figure 1: (A) Example reconstruction (attenuation image) of a tumorectomy sample measured with the static setup at approximately 66 mGy. Two regions of interest (ROI) were marked and zoomed in. ROI blue: (B) attenuation, (C) fused image. ROI red: (D) attenuation, (E) phase, (F) fused (attenuation and phase), (G) dark-field image.

Acknowledgments
The authors are grateful to Gordan Mikuljan and Philipp Zuppiger of PSI for their fantastic technical expertise and support. The authors acknowledge the clean room facilities of PSI and the technical staff for the support in gratings fabrication. We want to thank Andreas Boss for contributing with his clinical expertise to this work. This work has been funded by the SNF R'Equip grant 189662 (SiDRY) and 177036 (DTL), the ETH-Research Commission Grant Nr. ETH-12 20-2, ETH Doc.Mobility Fellowship, the Promedica Stiftung Chur Project 1527, the SNF Sinergia Grant Nr. CRSII5 183568, the PHRT-Pioneer Project Nr. 2021-612 CLARINET, PHRT-TT Project 2022-572 INTIMACY, PHRT-SC Project 2024-985 NAVIGATOR as well as the SwissLOS Lottery Fund of Kanton Aargau.

References

[1] Skaane et al., Performance of breast cancer screening using digital breast tomosynthesis: results from the prospective population-based Oslo Tomosynthesis Screening Trial. *Breast Cancer Research and Treatment* 169, 489–496 (2018).

[2] Zhu et al., Dedicated breast CT: state of the art-Part II. Clinical application and future outlook. *European radiology* 32, 2286–2300 (2022).

[3] Rawlik et al., Increased dose efficiency of breast CT with grating interferometry. *Optica* 10.7, 938-943 (2023).

Adaptation of a single 2D grating phase contrast technique on laser-based Kα X-ray source

*A. STOLIDI[1], G. GIAKOUMAKIS[1,2], J. PRIMOT[2], R. CLADY[3], D. GUDZ[3], O. UTÉZA[3] and A. FERRÉ[3]

[1]*Université Paris-Saclay, CEA, List F-91120, Palaiseau, France*
[2]*Université Paris-Saclay, ONERA, DOTA, F-91123 Palaiseau, France*
[3]*Aix-Marseille Université, CNRS, LP3 UMR 7341, 13288, Marseille, France*
Email: adrien.stolidi@cea.fr

Summary: The emergence of advanced laser technologies has led to more accessible and cost-effective X-ray sources through laser plasma interaction. These sources deliver ultrashort X-ray pulses, synchronized with driving lasers, serving as high-resolution diagnostic tools. Notably, laser-based Kα X-ray sources, with stable shot-to-shot flux, present promising assets for X-ray imaging. This communication presents the adaptation and benefits of a phase contrast method called multilateral shearing interferometry (MLSI) on such X-ray source.

The advent of innovative laser technologies with high power and repetition rates has given rise to new facilities that offer alternative sources of X-rays through laser plasma interaction [1]. These facilities are more compact and cost-effective compared to large-scale options such as synchrotrons and XFEL. Additionally, they are more widely accessible. By delivering ultrashort X-ray pulse durations – which are inherited from the duration of the driving laser pulse and intrinsically synchronized between the optical driver laser and the generated X-ray pulses – these facilities can serve as high-resolution diagnostic tools for both spatial and temporal aspects.

One such example is the laser-based Kα X-ray source, which is generated when an ultrashort and intense laser is focused on a high atomic number Z solid target. This source provides a stable shot-to-shot X-ray flux at a high repetition rate, consisting of a broad spectrum of Bremsstrahlung emission surrounded by large-amplitude monochromatic Kα and Kβ lines, specific to the chosen target material.

X-ray phase contrast imaging methods have already been adapted on such source [2-3]. Here we present an adaptation of multilateral shearing interferometry (MLSI) technique – a single 2D grating technique – on a laser-based Kα X-ray source (see Figure 1 (a)). Phase contrast measurement of a known canonical physical object will be shown (see Figure 1 (b)), as well as its retrieved projected thickness with an average Pearson correlation score up to 0.98 between simulated and experimental phase images.

Discussions on the motivations to adapt MLSI technique on such source will be addressed. For instance, the deal with the choice of a single 2D grating device; the ability of the MLSI technique to be sensitive to the characteristics of the X-ray sources, which are themselves linked to the management of laser intensity; or the use of the phase gradient measurement redundancy [4] to improve the quality of the phase image retrieved. All these developments rely on a global objective of moving towards a single shot acquisition configuration, and therefore, target laboratory X-ray dynamic imaging dedicated to fast transient phenomena.

Single 2D-grating X-ray phase contrast imaging dedicated to quantitative characterisation of Carbon material damaged by induced lightning

L. GUITARD[1,2], *A. STOLIDI[1], G. GIAKOUMAKIS[3], R. SOUSA MARTINS[4], A. JARNAC[4] and J. PRIMOT[2]

[1]*Université Paris-Saclay, CEA, List F-91120, Palaiseau, France*
[2]*Université Paris-Saclay, ONERA, DOTA, F-91123 Palaiseau, France*
[3] *Université Paris-Saclay, ONERA, DMAS, F-92322, Chatillon, France*
[4] *Université Paris-Saclay, ONERA, DPHY, F-91123 Palaiseau, France*

Email: adrien.stolidi@*cea.fr*

Summary: In aircraft production, the aerospace industry increasingly integrates carbon fibre reinforced polymers (CFRP), which may develop defects from operational wear, like lightning strikes. This study employs multilateral shearing interferometry (MLSI) on a micro focus X-ray tube with a high-resolution detector to robustly characterize density changes resulting from induced lightning damage in CFRP.

In the production of aircraft, the aerospace industry increasingly incorporates carbon fibre reinforced polymers (CFRP). These materials may have defects arising from manufacturing processes or operational wear, such as lightning strikes. To examine thoroughly these defects, it is wise to employ a technique that can assess the material's physical properties comprehensively. Numerous non-destructive evaluation (NDE) methods are employed for studying CFRP [1] and X-ray imaging stands out as it enables thorough volume inspection with exceptional spatial resolution. In particular, these carbon-based materials and their structures (successive oriented plys of align carbon fibres) are well adapted to X-ray phase contrast imaging.
In this study, multilateral shearing interferometry (MLSI) technique – a single 2D grating technique – have been adapted on a micro focus X-ray tube with a very high resolution detector (measured spatial resolution of 5 µm) in order to achieve a robust and quantified characterization of density changes resulting from lightning damage in CFRP (see Figure 1). The sample considered in this study is a laboratory manufactured CFRP with the carbon ply arrangement at ± 45°. This orientation guaranties that, through the whole thickness, all plies contribute equally to the transport of current between the entry and exit points. Then the sample was subjected to a transient electrical discharge delivered by a current generator in accordance with the lightning test standards. The specimen is passed on a dedicated X-ray phase contrast-imaging bench. The MLSI technique measures in one acquisition phase gradients in multiple directions. This asset will fit well with the considered CFRP sample ply arrangement.
Here, specific treatments in the Fourier domain [2] are performed to extract phase gradients and then retrieve the phase image, in addition to the classical attenuation (see Figure 2). Complementary qualitative information on the different modalities can be seen on a zoomed region. The visuals display imperfections aligned with the carbon fibre orientation, delineating the current path within the CFRP. Larger areas have been investigated.

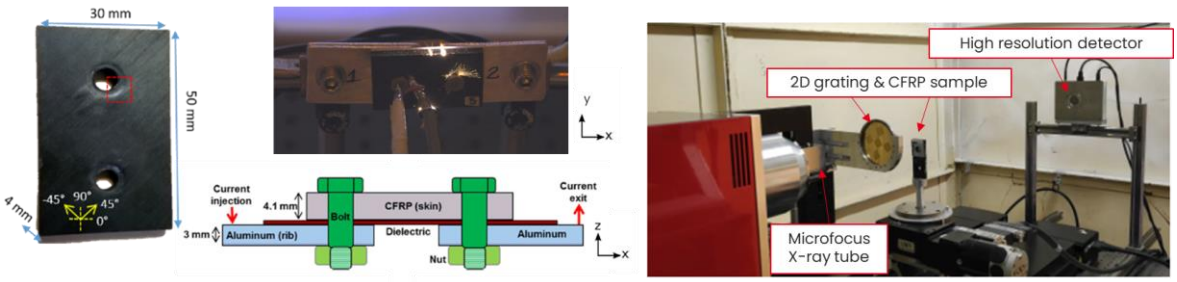

Figure 1: CFRP tested sample (left) with a lightning induced strike (midde) and the laboratory X-ray phase contrast bench (right).

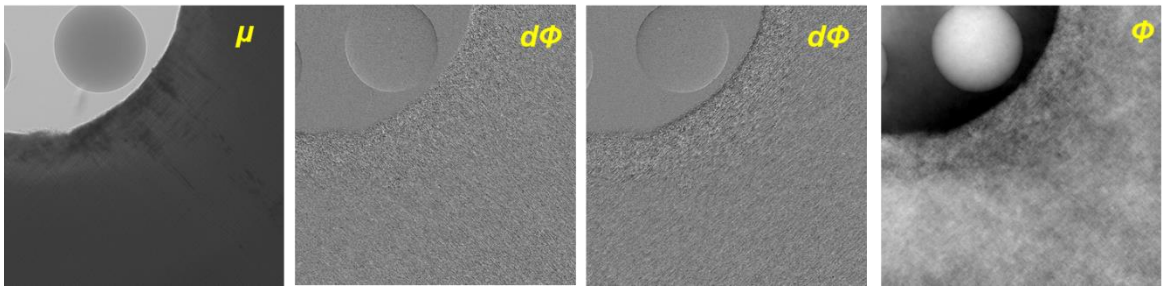

Figure 2: CFRP and PMMA ball X-ray images. From left to right : Attenuation (μ), Phase gradients ($d\Phi$) along (x+y) and (x-y), Phase (Φ)

The next step is to quantitatively retrieved the phase Φ. Therefore, a reference material has been added and density map ρ have been produced following the relations

$$\Phi = x\,\frac{2\pi\delta}{\lambda} \qquad (1)$$

with

$$\delta = \frac{r_e N_a \lambda^2 \rho}{2\pi} \sum_j q_j \frac{Z_j}{A_j} \qquad (2)$$

where x is the thickness of the sample, λ is the wavelength, δ is the decrement of the refractive index, r_e is the classical electron radius, N_a is the Avogadro's number, q_j is the mass fraction, Z_j is the atomic number and A_j is the atomic mass. Equation (2) assumes that the X-ray photon energies are away from absorption edges.

Measurement reveals significant density fluctuations, uncovering regions with decreased density attributed to damage-induced porosity and areas with heightened density due to internal residual stress. These findings are systematically compared and validated against conventional X-ray attenuation tomography and thermography imaging.

References

[1] Gholizadeh, Samira. "A review of non-destructive testing methods of composite materials." *Procedia structural integrity* 1 (2016): 50-57.

[2] Giakoumakis, G., Primot, J., Jarnac, A., Guitard, L., & Stolidi, A. Artifacts reduction in high-acutance phase images for X-ray grating interferometry. *Optics Express*, 30(23), 41147-41156. (2022).

Recent development in X-ray phase contrast imaging at NSRL

*Zhao Wu[1], Qisi Lin[1], Dongliang Guo[1], Meng Huang[1], Gang Liu[1], Yalin Lu[2],
* Yangchao Tian[1]

[1] *NSRL, University of Science and Technology of China, Hefei, China*

[2] *HFNL, University of Science and Technology of China, Hefei, China*

Email: *wuzhao@ustc.edu.cn, ychtian@ustc.edu.cn*

Summary: In recent years, we devoted to new X-ray phase contrast imaging techniques and their implementations. In this paper, two imaging systems, including a non-interferometric grating-based X-ray phase contrast imaging system and an X-ray Talbot-Lau interferometer, are reported. These systems are characterised by alterable energy, large field of view, fast CT acquisition or high visibility, which are pursued in real applications. Furthermore, we also carried out some biological imaging researches and methodological researches.

X-ray phase contrast imaging (XPCI) has gained significant attention for its ability to enhance the contrast of soft tissues in X-ray radiography and computed tomography (CT). Grating-based XPCI method holds significant potential for advancing its practical applications due to its compatibility with conventional X-ray tubes. However, most grating-based XPCI systems cost a long time to perform CT scan under fixed X-ray energy with small field of view. These shortcomings limit its real application, especially in pre-clinical or clinical imaging.

In recent years, we devoted to new X-ray phase contrast imaging techniques and their implementations to explore its practical applications. At first, we established a non-interferometric grating-based XPCI setup, which realized variable energy, large field of view and fast phase contrast imaging based on medical imaging components [1]. Comparison between the previously reported prototype systems is performed below.

TABLE I. Comparison between the previously reported prototype systems. [1]

Parameters	NSRL system	Tapfer *et al.*	Hauke *et al.*	Zhang *et al.*	Astolfo *et al.*		Li *et al.*
Mode	CT	CT	Radiography	Radiography	Radiography		Radiography
Energy (kV)	50–90	40	100	36	56	80	60 kV
Power (kW)	12	0.03	10	—	0.112	0.16	0.6
Coherence	Incoherence	Partial	Partial	Partial	Coherence		Incoherence
Monochromatic	Polychromatic	Polychromatic	Polychromatic	Polychromatic	Polychromatic		Polychromatic
FOV(mm^3/mm^2)	160×160×6.4	25×25×35	280×1160	200×100	200×500		222×500
Grating periods (μm)	30 (G_0) 24 (G_1) 120 (G_2)	10 (G_0) 3.24(G_1) 4.8 (G_2)	11.54 (G_0) 3.39 (G_1) 4.8 (G_2)	—	75 (G_1) 97.5 (G_2)		15.75 (G_0) 7 (G_1) 12.6 (G_2)
Grating duty cycle	0.6 (G_0) 0.56 (G_1) 0.59 (G_2)	—*	0.5 (G_0) 0.6 (G_1) 0.5 (G_2)	—	0.71 (G_1) 0.71 (G_2)		0.7 (G_0) 0.5 (G_1) 0.5 (G_2)
Max. scan time	7 min	28 h	60 min	—	12 min		--

* Not reported in the literature.

In addition, we also installed an X-ray Talbot-Lau interferometer (XTLI) utilizing a microarray anode structured target (MAAST) source. The adoption of this special source eliminated source grating, and increased photon utilization efficiency. Furthermore, it achieved an extended field of view with inverse geometry illumination [2]. The critical parameters of this imaging system are listed in Table II.

TABLE II. The critical parameters of the X-ray Talbot-Lau interferometer. [2]

Energy	Length	Target	Grating G1	Grating G2	Visibility	Resolution	Field of view
40 keV	0.8 m	Period 3 μm	Period 5.08 μm π phase shift	Period 16.6μm Amplitude	32.0% @65kV	100 μm	Φ35 mm

Based on the XTLI, we have carried out some biological imaging researches and methodological researches. Figure 1 displays the obvious contrast enhancement in phase mode compared with the attenuation mode. Furthermore, we tried to detect early emphysema of mice by quantitative analysis. Figure 1(c&f) shows the phase mode achieves better detectability [3]. Meantime, a flexible Talbot-Lau interferometer was discussed, where the visibility remained high in a certain range [4]. By further theoretical deduction, we find this flexible system owns the merit of tunable structure scattering sensitivity with constant phase contrast sensitivity, field of view and spatial resolution [5].

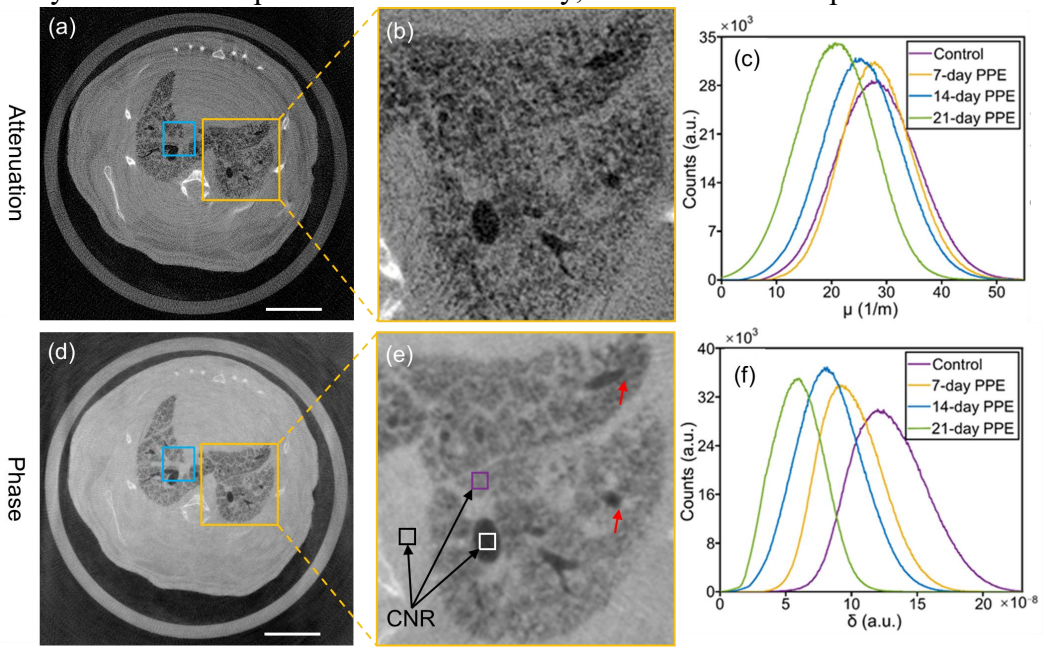

Figure 1: Imaging of mice by the XTLI equipped with MAAST and detection of early emphysema. [2,3]

Acknowledgments

This work was supported in part by the USTC Research Funds of the Double First-Class Initiative under Grant YD2310002008; the National Key Scientific Instruments and Equipment Development Projects of China under Grant CZBZDYZ20140002 and CZYQYX20210015; the National Natural Science Foundation of China under Grant NSFC U2032148; the Youth Innovation Promotion Association of the Chinese Academy of Sciences under Grant 2020457.

References

[1] Z. Wu, W. B. Wei, K. Gao, et al., Prototype system of noninterferometric phase-contrast computed tomography utilizing medical imaging components, *J. Appl. Phys.*, **129**, 074901, (2021)

[2] Q. Lin, Z. Wu, G. Zan, et al., High energy x-ray Talbot-Lau interferometer employing a microarray anode-structured target source to extend the field of view, *Phys. Med. Biol.*, **68**, 21NT01, (2023)

[3] Q. Lin, Z. Wu, M. Huang, et al., Detection of early pulmonary emphysema by multi-contrast X-ray Talbot-Lau interferometer, *Med. Phys.* (under review)

[4] Q. Lin, Z. Wu, Y. Lu, et al., (2021) In: *IEEE International Conference on Medical Imaging Physics and Engineering*, 2021, Flexible X-ray Talbot-Lau grating interferometer, p. 1

[5] Z. Wu, G. B. Zan, Q. S. Lin, et al. Flexible X-ray Talbot-Lau interferometer with tunable structure scattering sensitivity, (unpublished).

Variance of refraction as a signal and the absolute nature of scattering measurements not based on fringe visibility reduction

[*]I. Buchanan[1], S. Cipiccia[1], C. Navarrete[1], C. Peiffer[1], L. Fardin[2,1], A. Astolfo[1], T. Partridge[1], M. Esposito[1], M. Endrizzi[1], C.K. Hagen[1], P.R.T. Munro[1], A. Bravin[2], D. Bate[3], A. Olivo[1]

[1]*Department of Medical Physics and Biomedical Engineering, UCL, WC1E 6BT, UK*

[2]*European Synchrotron Radiation Facility, 38043 Grenoble, France*

[2]*Nikon X-Tek Systems Ltd., Tring Business Centre, Tring, Herefordshire, UK*

[*]Email: ian.buchanan.15@ucl.ac.uk

Summary [99/100 words]: We report on the potential of a new signal in x-ray phase contrast imaging (XPCi), the variance of the refraction channel, that increases linearly with thickness and average feature size, with the latter being anti-correlated with the so-called 'dark field' channel. This new channel may provide an additional quantitative dimension to the imaged samples, as experimentally measured signals match model predictions. Furthermore, we discuss the direct measurement of scattering signals via non-interferometric methods, and how these are unaffected by system-specific parameters such as the auto-correlation length, which significantly affects the measured signal in methods relying on fringe visibility reduction.

X-ray dark-field or ultra-small angle scatter imaging has become increasingly important since the introduction of phase-based x-ray imaging and is having transformative impact in fields such as *in vivo* lung imaging and explosives detection. In a range of applications such as industrial testing, scanning of large and thick samples, or those whose shape is not well-suited for computed tomography (CT), fast planar imaging scans may be desirable. These objects typically contain features that would be resolvable in CT, but their overlapping makes it impossible to do so in a 2D scan. We show that the variance of refraction can still yield a degree of quantitative information on these features, that complements that provided by the dark-field channel. As proof of concept, we provide experimental and matching simulated data of this signal acquired at beamline ID17 of the European Synchrotron Radiation Facility (ESRF), showing that it also increases linearly with thickness and may thus be suitable for CT applications, and additional simulated results which probe the potential of this new contrast channel [1].

As part of the introduction of this new contrast channel, we illustrate its variability against system parameters such as aperture size, feature size, and X-ray energy in Edge Illumination [2], and compare these dependencies to those of dark field. Furthermore, we demonstrate how, in non-interferometric XPCi methods that do not use fringe visibility reduction to extract the dark field signal, this does not depend on the system's auto-

correlation length, unlike other approaches [3]; instead, it depends only on feature size and x-ray energy.

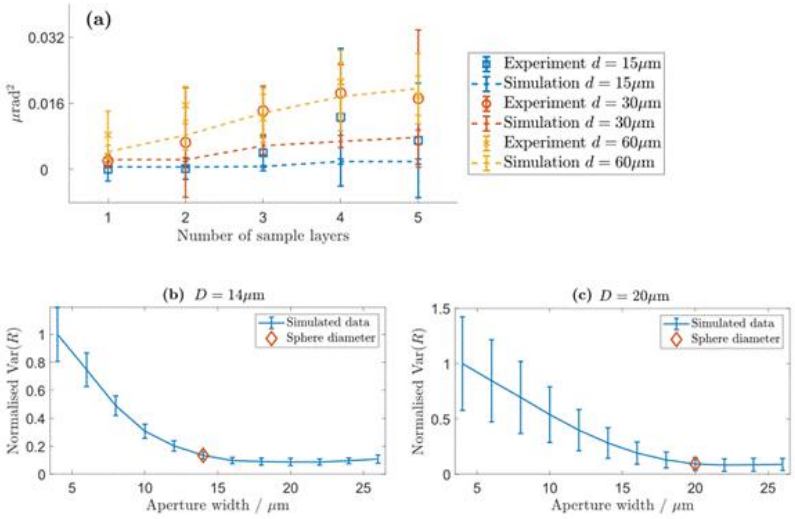

Figure 1: Variance of refraction (VR). (a) Shows comparisons between model (dashed lines) and experiment (dots) for a single, 40 µm wide beamlet in a scanning configuration with a 60 keV beam, where the samples consist of increasing slabs of calibrated microspheres. (b) and (c) show simulated data vs. beamlet size for scatterers of different diameters, showing how the plots plateau when the size of the scatterer matches that of the beamlet used to probe the sample, in analogy with the behaviour of DF as a function of auto-correlation length in grating-based methods.

Acknowledgments

This work was supported by the EPSRC (Grant EP/T005408/1). AO and CKH are supported by the Royal Academy of Engineering under the "Chairs in Emerging Technologies" and "Research Fellowships" schemes, respectively. PRTM is supported by the Royal Society under the "University Research Fellowships" scheme.

References

[1] I. Buchanan "Direct x-ray scattering signal measurements in edge-illumination/beam-tracking imaging and their interplay with the variance of the refraction signals," *Appl. Phys. Rev.* 1 (2023).

[2] A. Olivo, "Edge-illumination x-ray phase-contrast imaging," Journal of Physics: Condensed Matter 33, 363002 (2021).

[3] M., Strobl, "General solution for quantitative dark-field contrast imaging with grating interferometers" *Sci. Rep.*, 4 (2014) 1.

Inline edge illumination through sample mask misalignment: a proof of concept

* NICHOLAS FRANCKEN[1], JAN DE BEENHOUWER[1], JAN SIJBERS[1]
[1]*imec-Vision Lab, Department of Physics, University of Antwerp, Belgium*
Email: *nicholas.francken@uantwerpen.be*

Summary: Edge illumination (EI) is an X-ray phase contrast imaging setup that allows measuring two additional complimentary contrasts. The setup consists of two absorbing masks with slit shaped apertures. Typically, one of the masks is stepped during scans, complicating the application of EI in inline settings. Current solutions exist, but require either limiting the number of retrieved contrasts or fabricating specialized masks. In this work, an EI scanning method with purposely misaligned conventional EI masks is proposed to enable inline EI. Good agreement is found between conventional and inline EI flatfield parameters, and first inline scan results are presented.

Abstract: Edge illumination (EI) is an X-ray phase contrast imaging setup that allows, apart from the conventional attenuation contrast, retrieval of both the phase and dark field contrasts, the former providing enhanced contrast for low absorbing materials compared to attenuation contrast and the latter providing information on the material microstructure distribution [1]. The EI setup employs two absorbing masks with slit shaped apertures, placed in front of the sample and detector. During an EI scan, so-called illumination curves (ICs) are sampled by laterally stepping the sample mask, hence changing the alignment between sample and detector mask apertures. Comparing sample and flatfield IC fit parameters allows retrieving the attenuation, phase, and dark field contrasts [2].

Current inline EI solutions consist of either performing single-shot acquisitions [3] or using an asymmetric sample mask [4]. The downside of the former is that it only allows for two of the three contrasts to be retrieved, while the latter requires installing new hardware.
The asymmetry of these EI masks refers to the aperture pitch, which is symmetric for a conventional EI mask but changes over consecutive detector columns for an asymmetric mask. This changing sample mask aperture pitch modifies the aperture alignment with the (regularly spaced) detector mask apertures and hence also the measured pixel intensities. Asymmetric sample masks thus allow ICs to be measured directly on the detector, instead of having to step the mask.
The same principle can be applied to conventional EI masks, which are designed to be used at a specific geometric magnification (typically between 1.5 and 2). The projected sample and detector mask aperture pitch only match when the source, masks and detector are placed at positions satisfying the mask design magnification.
Misaligning the sample mask along the optical axis will cause its projected pitch to deviate from that of the detector mask, with the resulting shift in aperture alignment causing an IC profile over the detector columns, as in the asymmetric mask EI setup. Scanning a sample inline across this IC allows retrieving the three EI contrasts through the same means as in conventional EI. This approach to inline EI, while mentioned in [5], has to the best of our knowledge never been validated experimentally.

In this work, a proof of concept for inline EI scans based on sample mask misalignment is demonstrated. The ICs of a conventional and inline EI setup are compared, and the first results of all three contrasts for an inline scanned test sample are presented.

All scans were performed using the EI setup detailed in [6]. Two experiments were performed. First, a conventional EI IC was compared to an IC of the inline EI setup. The conventional EI IC consisted of 11 projections, taken at equally spaced sample mask steps in the [-50 μm, 50 μm] interval (relative to perfect mask alignment). For the inline EI IC, the sample mask was misaligned 25 mm along the optical axis, resulting in an IC profile stretched out over 48 detector columns.
For the second experiment, an inline EI scan was performed for a test sample that consisted of a plexiglass cylinder wrapped in a rubber band and mounted on a wooden stick (see Figure 2). The sample mask was misaligned 10 mm along the optical axis and the sample was stepped across an inline EI IC in 251 steps of one (demagnified) pixel width.

The resulting IC profiles of the first experiment are shown in Figure 1, where the intensity is plotted in function of the sample mask aperture shift, relative to perfect aperture alignment. Good agreement is found between the two IC profiles.

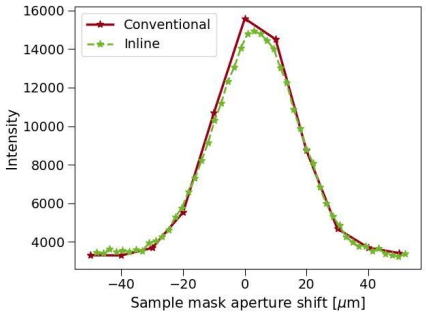

Figure 1: Comparison between an IC of a conventional and misalignment-based inline EI setup.

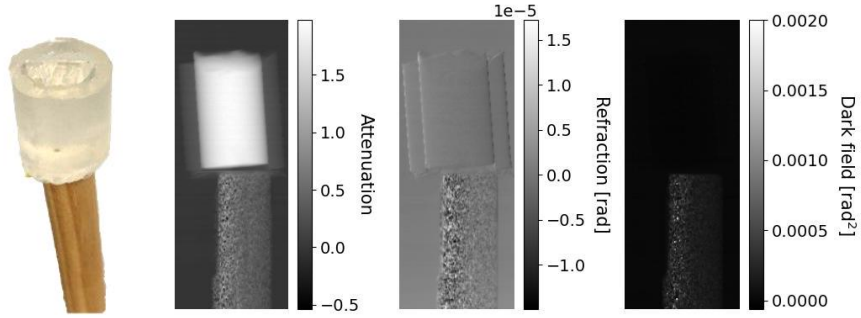

Figure 2: From left to right: test sample and retrieved attenuation, refraction and dark field contrasts.

The retrieved contrasts of the inline EI scan are shown in Figure 2, with the rubber band edges clearly visible in the refraction contrast and the fiber structure of the wood showing up in the dark field contrast.

In conclusion, these results show the potential of performing inline EI scans by purposefully misaligning the sample mask of a conventional EI setup.

Acknowledgments
This research is funded by the Research Foundation Flanders (FWO) project FoodPhase (S003421N).

References

[1] A. Olivo, *Physics: Condens. Matter*, **33**, 363002 (2021)
[2] M. Endrizzi and A. Olivo, *J. Phys. D: Appl. Phys*, **47**, 505102 (2014)
[3] P.C. Diemoz, F. A. Vittoria, C. K. Hagen, et al., *J Synchrotron Radiat.*, **22(4)**, 1072-1077 (2015)
[4] M. Endrizzi, A. Astolfo, F. Vittoria, et al., *Sci Reports*, **6**, 25466 (2016)
[5] A. Astolfo, I. Buchanan, T. Partridge, et al., *Sci Reports*, **12**, 3354 (2022)
[6] B. Huyge, P. Vanthienen, N. Six, et al., *e-Journal of Nondestructive Testing*, **28(3)**, 1435-4934 (2023)

Artifacts and corrective strategies in X-ray phase imaging using 2D gratings

*G. GIAKOUMAKIS[1,2], A. STOLIDI[2], A. JARNAC[3], L. GUITARD[1,2] and J. PRIMOT[1]

[1]*Université Paris-Saclay, ONERA, DOTA, F-91123, Palaiseau, France*
[2]*Université Paris-Saclay, CEA, List F-91120, Palaiseau, France*
[3]*Université Paris-Saclay, ONERA, DPHY, F-91123 Palaiseau, France*

Email: georges.giakoumakis@onera.fr

Summary:
X-ray phase contrast imaging using multilateral shearing interferometry (MLSI) offers the benefit of measuring the phase shift in multiple orientations with a single interferogram. However, extracting this quantity requires experimental conditions of the imaging system and algorithmic strategies, which can lead to artifacts in phase images. This communication presents the source of these artifacts in the context of MLSI in X-ray phase imaging, as well as recently developed tracking methods and corrective strategies. An application of these methods on lightning-strike composite panels for aeronautical application is given.

Among all modulators commonly used in X-ray phase imaging, multi-lateral shearing interferometry (MLSI) technique – a single 2D grating technique – benefit of simultaneously measuring the wavefront phase shift in multiple orientations and thus retrieve the phase information in a single interferogram [1]. However, objects with abrupt intensity transitions such as edges or splits, can be strenuous to be phase sampled by the grating. In particular, under-sampling artifacts arise in the phase image as soon as the transitions of the object evolve faster than the period of the interferogram.
Classically, apodization techniques could be performed in order to reduce artifacts however by lowering the spatial resolution of the phase image [2]. To preserve the spatial resolution while reducing artifacts, a preventive approach has been recently developed that we called “Method of Artifacts Reduction from the Intensity of the Object” (MARIO) [3]. This method is based on the construction of a new interferogram that does not hold any intensity information from the sample, the main cause of under-sampling artifacts in high-acutance phase images.
The gain of MARIO on experimental data can be evaluated by performing the "Confidence Map" [4], a graphical tool that has been recently developed in the context of MLSI in X-ray phase imaging. This method gives an estimation of the experimental errors for any phase image retrieved from a gradient-based device, taking advantage of the MLSI to measure at least two orthogonal gradients simultaneously. It is primarily used to alert the observer to the presence of artifacts that could affect his interpretation of the image by associating a cause with the creation of each artifact: dislocation, under-sampling and noise.
We present an experimental application of a carbon fibre reinforced polymers (CFRP) specimen passed on a dedicated X-ray phase contrast-imaging bench (see Figure 1). The raw interferogram and phase image are presented in Figure 2. Strong under-sampling artifacts and dislocation artifacts arise inside and at the edge of the sample, as it can be seen using the Confidence Map (see Figure 3 – left). The proposed MARIO (see Figure 2 – right and Figure 3 – right) is efficiently removing these artifacts. Indeed, in this example, the under-sampling alerts are decreased by a factor of 44.0 and the dislocation alerts by a factor 16.0, thus purifying the phase information of the sample.

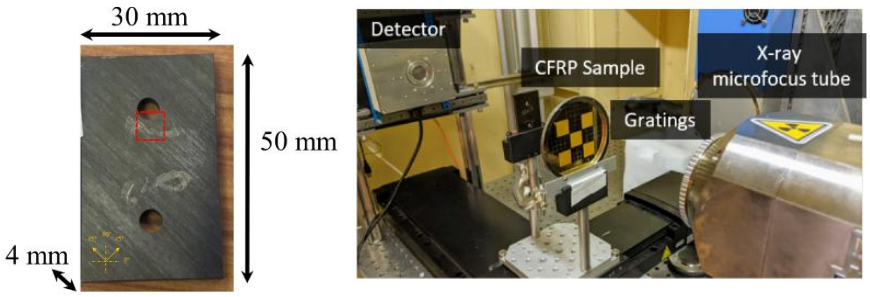

Figure 1: CFRP tested sample (left) and the laboratory X-ray phase contrast bench (right).

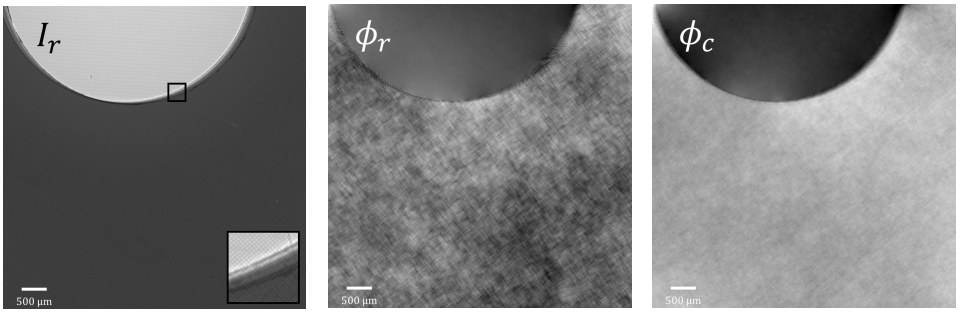

Figure 2: From left to right : raw interferogram (µ) ; raw phase image (ϕ_r) ; corrected phase image (ϕ_c).

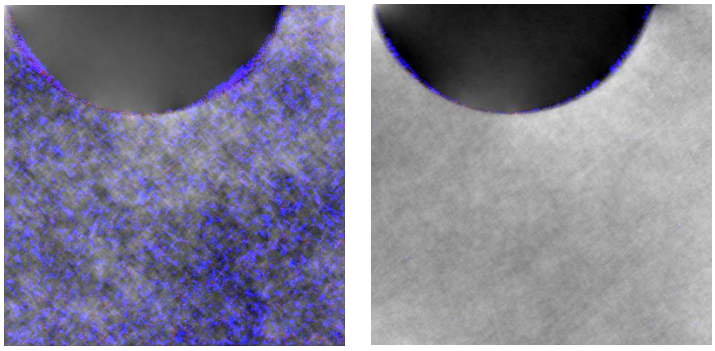

Figure 3: (left) CFRP raw phase image superimposed to its associated Confidence Map. The under-sampling alerts are displayed in blue and phase dislocation alerts are displayed in red. (right) CFRP phase image processed by MARIO superimposed to its associated Confidence Map. A clear reduction of the alerts is noticeable inside and at the edge of the sample.

Acknowledgments
The authors thanks the Department of Physics Instrumentation Environment Space (DPHY) and the Department of Materials And Structures (DMAS) from ONERA for the availability of the CFRP-test piece.

References

[1] J. Rizzi, T. Weitkamp, N. Guérineauu, M. Idir, P. Mercère, G. Druart, G. Vincent, P. da Silva, and J. Primot, "Quadriwave lateral shearing interferometry in an achromatic and continuously self-imaging regime for future x-ray phase imaging," *Optics Letters* (2011).
[2] P. Podder, T. Z. Khan, M. H. Khan, and M. M. Rahman, "Comparative performance analysis of hamming, hanning and blackman window," *International Journal of Computer and Applications*, **96** (2014).
[3] Giakoumakis, G., Primot, J., Jarnac, A., Guitard, L., & Stolidi, A. Artifacts reduction in high-acutance phase images for X-ray grating interferometry. *Optics Express*, 30(23), 41147-41156. (2022).
[4] Stolidi, A., Giakoumakis, G., Primot, J., Jarnac, A., & Tisseur, D. Confidence map tool for gradient-based X-ray phase contrast imaging. *Optics Express*, 30(3), 4302-4311. (2022).

Hybrid tomographic reconstruction in grating interferometry breast CT: physics-based likelihood meets data-driven prior

*S. VAN GOGH[1,2,3], S. MUKHERJEE[4], M. RAWLIK[1,2], A. PEREIRA[1,2], S. SPINDLER[1,2], M.-C. ZDORA[1,2], M. STAUBER[5], Z. WANG[1,2,6], J. XU[1,2], Z. VARGA[7], M. STAMPANONI[1,2]

[1]*Institute for Biomedical Engineering, ETH Zurich, Switzerland*
[2]*SLS, Paul Scherrer Institute, Villigen, Switzerland*
[3]*Istituto Dalle Molle di studi sull'intelligenza artificiale (IDSIA USI-SUPSI), Lugano, Switzerland*
[4]*Dept. of Electronics and Electrical Communication Engineering, IIT-Kharagpur, Kharagpur, India*
[5]*GratXray AG, Villigen, Switzerland*
[6]*Department of Engineering Physics, Tsinghua University, Haidian District, Beijing, China*
[7]*Department of Pathology and Molecular Pathology, University Hospital Zürich, Zürich, Switzerland*
Email: *stefano.vangogh@idsia.ch*

Summary: Breast cancer's early detection is currently hindered by limitations in available imaging technologies. Grating Interferometry Breast CT (GI-BCT) shows promise in addressing these limitations as it could potentially offer fast, painless scans with superior resolution. In this work, a hybrid reconstruction framework that synergistically combines tomographic modelling with machine learning priors addresses the challenges in GI-BCT, by mitigating noise and ill-conditioning of the reconstruction problem. We show that with the developed framework GI-BCT can surpass conventional CT in clinically compatible scenarios, enabling dose reduction and improved spatial resolution, thereby bringing the technology close to first *in-vivo* studies.

Breast cancer is the most common malignancy in women. Unfortunately, currently used breast imaging technologies are limited, most importantly by low soft-tissue contrast and insufficient spatial resolution. This limits the achievable sensitivity and specificity of these methods. X-ray phase contrast CT holds the potential to overcome these limitations, offering the prospect of painless and rapid scans with superior three-dimensional resolution. Despite its successful use on synchrotrons for over two decades, its adaptation into a clinically compatible device has yet to happen. Grating Interferometry CT (GI-CT) is widely considered as the phase-contrast method with the best chance of making this transition. Its modest requirements in terms of beam coherence, notable mechanical robustness, and capability to scan with a large field-of-view (FOV) make it in fact compatible with clinical X-ray tubes and human-sized subjects. To assess the compatibility of Grating Interferometry Breast CT (GI-BCT) with clinical demands such as a large FOV and low radiation doses and to explore the additional benefits that phase contrast may bring to breast CT, our team has developed a prototype scanner [1]. However, phase contrast CT reconstruction in the low-dose regime is challenging due to the unique signal acquisition scheme in GI-CT and to the existing constraints in terms of hardware fabrication.

The objective of this work was to address these challenges, related to high problem ill-conditioning, as well as to high and heterogeneous noise amplitudes. This was achieved by integrating cutting-edge data-driven regularization with classical iterative reconstruction algorithms. A hybrid reconstruction framework was thus developed which alternates between physics-based image updates that optimize the likelihood and data-driven regularization steps which optimize the prior.

The high problem ill-conditioning was addressed in two steps. First, we optimized the conditioning of the tomographic operators by developing parallelizable analytically differentiable basis functions [2]. Second, we imposed prior knowledge on the relation

between the absorption and phase-contrast channels which allows to iteratively fuse the two into a single image and leverage the strengths of each channel [3]. We found that within this algorithm, called fused intensity-based iterative reconstruction (FIBIR), phase contributes mostly with high spatial frequency content to the final fused image, whereas absorption has a predominant role in the formation of low spatial frequency content. Deep learning algorithms were employed to address the noise issue, effectively eliminating undesired noise and artifacts introduced by the physics-based likelihood. Specifically, we developed a new regularization paradigm called GradReg which, contrary to existing regularization techniques, removes noise and artefacts in the gradient space rather than in the image space [4]. This allows a seamless integration with quasi-Newton optimization algorithms during reconstruction, which in turn greatly accelerates convergence.

Our preliminary *ex-vivo* studies have shown the feasibility of reducing the dose and/or improving spatial resolution with GI-BCT compared to clinical breast CT (see Fig. 1). Specifically, the developed reconstruction framework allows to increase the dose efficiency of GI-BCT compared to conventional CT thanks to the synergistic effect of the FIBIR parameterization and the GradReg regularization by effectively using the higher spatial frequency information available in GI-BCT.

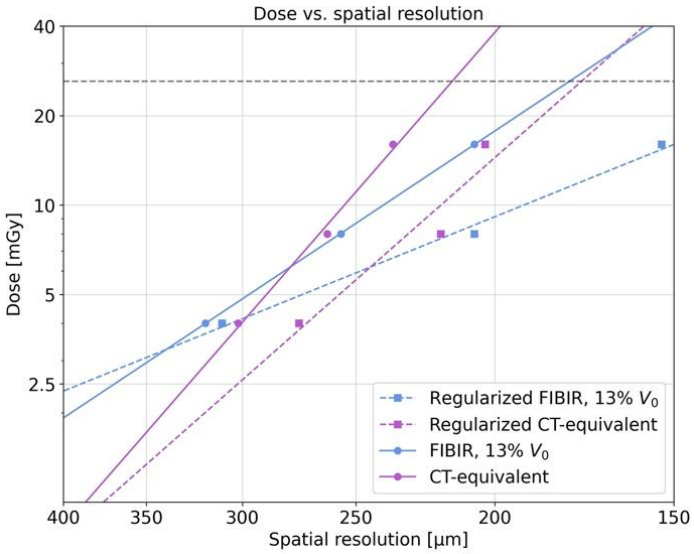

Figure 1: Higher dose efficiency in GI-BCT compared to conventional CT. Conventional CT with iterative reconstruction is shown in purple, GI-BCT with the proposed FIBIR algorithm [3] in blue. Continuous lines indicate unregularized reconstructions, dashed lines reconstructions regularized with GradReg [4]. The dashed grey horizontal line indicates the upper dose limit of clinical breast CT. Figure taken from [4].

Acknowledgments

This work has been funded by the ETH-Research Commission Grant Nr. ETH-12 20-2, an ETH Doc.Mobility Fellowship, the Promedica Stiftung Chur, the SNF Sinergia Grant Nr. CRSII5 183568, SNF Sinergia Grant Nr. CRSII5 183568, PHRT-TT Project Nr. 2022-572 INTIMACY as well as the Swisslos Lottery Fund of Kanton Aargau.

References

[1] Rawlik et al., Increased dose efficiency of breast CT with grating interferometry. *Optica* 10.7, 938-943 (2023).

[2] van Gogh et al., Iterative phase contrast CT reconstruction with novel tomographic operator and data-driven prior, *PLoS ONE* 17(9) (2022)

[3] van Gogh et al., Towards clinical-dose Grating Interferometry Breast CT with Fused Intensity-based Iterative Reconstruction, *Opt. Express* 31, 9052-9071 (2023)

[4] van Gogh et al., Data-driven gradient regularization for quasi-Newton optimization in iterative grating interferometry CT reconstruction, *IEEE Transactions on Medical Imaging* (2023)

Enhanced detection of threats in a single scan utilizing phase-based X-ray imaging techniques and deep neural networks

T. Partridge[1]*, S.S. Shankar[2], I. Buchanan[1], P. Modregger[3], A. Astolfo[1,4], D. Bate[4,1], A. Olivo[1]

[1]*Department of Medical Physics and Biomedical Engineering, UCL, UK*
[2]*Nylers Ltd, UK*
[3]*Depatment of Physics, University of Siegen, Germany*
[4]*Nikon X-Tek Systems Ltd, UK*
Email : tom.partridge@ucl.ac.uk

Summary: Advances in phase-based and energy resolving x-ray technology offer new opportunities for materials discrimination. Despite this, they are frequently applied in isolation. This study starts exploring the potential of their combined use and assesses what sort of advantages this could have compared to dual-energy x-ray imaging alone. Moreover, we consider the joint application of off-the-shelf machine learning approaches and how they can effectively discriminate and, in some cases, identify various materials in complex imaging scenarios, offering potential applications across the life and physical sciences.

The field of x-ray imaging has seen significant advances over recent years, notably through the introduction of new contrast mechanisms, often based on different physical principles. Specific examples include x-ray phase contrast imaging, which led to the first in vivo study on humans at synchrotrons [1] and is currently being translated for use in extremities [2], as well as intra-operative imaging [3]. Another area of interest is that of x-ray dark-field imaging, used for the first in vivo clinical study outside a synchrotron [4] and undergoing adaptation for implementation in clinical CT [5]. Alongside these, another line of development which is gaining significant momentum is energy-resolved x-ray imaging [6], implemented through new-generation photon counting detectors.

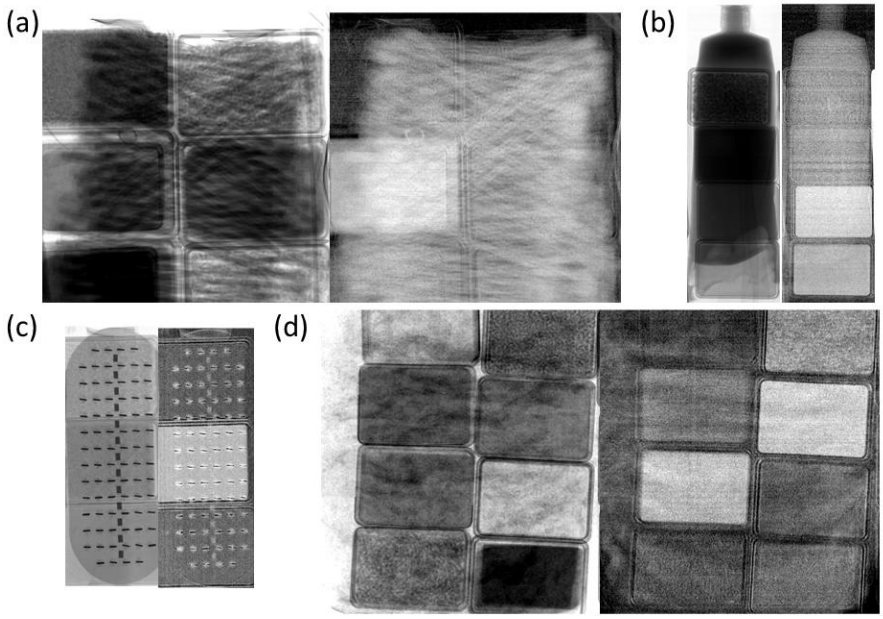

Figure 1. Example images from the trial, in each case showing an attenuation (left) and dark-field image (right) side by side.: their complementarity is apparent, with the different materials often standing out much more clearly against the cluttering objects in the dark field images, and contrast often switching polarity from one modality to the other (materials that look dark in attenuation turning bright in dark field and vice-versa). Panel s (a-d) show boxes containing various materials being obscured by a cotton buds, toothpaste, a nailbrush and nappies, respectively.

So far, these new channels of information have largely been used independently from one another, which limits their prospective impact. A key strength of our approach is its capability to provide attenuation, phase, and dark field images in a single scan [7], examples of attenuation and dark field images are shown in figure 1. When coupled with an energy-resolving detector, this yields seven separate contrast channels: high and low energy images of attenuation, differential phase, and dark field, along with an attenuation image at a much higher energy arising from the beam transmitted through the mask septa. This study starts exploring the potential of their combined use and assesses what sort of advantages this could have in terms of material discrimination. We also look at the match between this "multi-contrast" x-ray approach and machine learning methods, showing that use of the latter can significantly enhance performance. In a previous study we looked at matching machine learning with x-ray dark field imaging to detect a specific threat material (C4) obscured by electrical items [8], here we expand on the x-ray contrast channels used, and especially on the range of investigated materials and thicknesses. Specifically, we show that analysing the signals from a combination of x-ray contrasts with deep learning can lead to extremely promising results, just a single miss out of 313 cases, in an extremely complex dataset consisting of 19 threat materials combined with 56 non-threat ones, all at three thicknesses (12, 18 and 30mm), and obscured by a plethora of cluttering objects [9]. While the method has been tested on this larger material and image dataset, the methodology extends beyond threat detection, and could be applied across the life and physical sciences, encompassing distinctions like diseased vs. healthy tissues or degraded vs. pristine materials.

Acknowledgments

This work was supported by the Innovative Research Call in explosives and weapons detection. This is a cross-government programme sponsored by several departments and agencies under the UK government's CONTEST strategy in partnership with the US Department of Homeland Security, Science and Technology Directorate. Additional support was obtained from HMG's Defence and Security Accelerator (DASA) under the Future Aviation Security Solutions (FASS) programme (grants ACC101705 and ACC106964) and from the Engineering and Physical Sciences Research Council (EPSRC) (grant EP/T005408/1). AO was supported by the Royal Academy of Engineering under the Chairs in Emerging Technologies scheme.

References

[1] Castelli et al. Radiology **259**, 684-94, (2011)
[2] Yoshioka et al. Sci. Rep. **10**, 6561, (2020)
[3] Massimi et al. Sci. Rep. **11**, 3663, (2021)
[4] Willer et al. Lancet Dig. Health 3, e733-44, (2021)
[5] Viermetz et al. PNAS **119,** e2118799119, (2022)
[6] Danielsson et al. Phys. Med. Biol. **66**, 03TR01, (2021)
[7] A. Astolfo et al. Sci. Rep. **7**, 2187, (2017)
[8] T. Partridge et al. Nat Commun., **13**, 4651 (2022)
[9] T. Partridge et al. *(under revision)*. arXiv:2309.11943

Source Phase Stepping for grating interferometry using Addressable Cold-Cathode Flat-Panel X-ray Source

Guocong Shao[1†], Qing Li[1†], Qi Liu[2], Jun Chen[2], Linghong Zhou[1], Wangjiang Wu[1*], Yuan Xu[1*]

[1]*School of Biomedical Engineering, Southern Medical University, China*

[2]*State Key Laboratory of Optoelectronic Materials and Technologies, Guangdong Province Key Laboratory of Display Material and Technology, School of Electronics and Information Technology, Sun Yat-sen University, China*

† Guocong Shao and Qing Li contributed equally

* Corresponding authors. Email: wwj12110303@i.smu.edu.cn *and* yuanxu@smu.edu.cn

Summary: X-ray grating interferometry can provide three valuable contrast information: absorption, differential phase contrast, and dark-field signal. However, it requires high-precision mechanical movement of one of the gratings to obtain the phase stepping curve (PSC). In this study, we propose a novel addressable cold-cathode flat-panel X-ray source to achieve fast source phase stepping. The cathode of the source is composed of millions of ZnO nanowires, which can be selectively controlled to emit electrons by the gate voltage through field emission effect. After the electrons striking on the structured anode target, addressable region-specific X-ray luminescence and thus the PSC can be obtained.

1. Introduction

The basic principle of grating interferometry for phase contrast imaging is the fractional Talbot effect, which consists of a coherent X-ray source, a phase grating G1, an absorption grating G2, and a detector. The method for extracting the phase usually involves mechanically stepping the grating G2 over one period along the perpendicular direction of the grating's lines. However, this mechanical phase stepping suffers from the drawback of system instability. To overcome this limitation, we proposed a novel addressable cold-cathode flat-panel source capable of emitting structured coherent X-rays [1]. This source employs electrons field emission and features an array of gate structure, which enables region-specific X-ray emission and potentially replacing the grating phase stepping with source stepping.

2. Method

The schematic diagram of our proposed addressable flat-panel X-ray source grating interferometry was shown in Figure 1, which consists of an addressable cold-cathode flat-panel X-ray source, a π -phase-shifting grating G1, an absorption grating G2, and a detector. The cathode of the source is composed of densely arranged ZnO nanowires (NWs), which can be divided into several groups as indicated by the yellow, red, purple, and blue strips in Figure 1. Each group of ZnO NWs can independently emit electrons by applying the gate voltage via field emission effect. The anode consists of an array of micro-periodically distributed anode strips that are connected to a high voltage generator. After sequentially applying the gate voltage to each group of ZnO NWs, structured X-ray illumination can be obtained and the source stepping can be achieved.

In the current simulation, the source stepping curve of structured point sources grating interferometry was obtained. X-ray propagation starts with spherical waves and undergoes Fresnel near-field diffraction between G1 and G2, forming self-imaging of the G1 grating at the fractional Talbot distances. Due to the small period of the self-imaging of G1, an absorption grating G2 was utilized. The performance of the source stepping curve was compared with the grating phase stepping methods where grating G2 was stepped over one period.

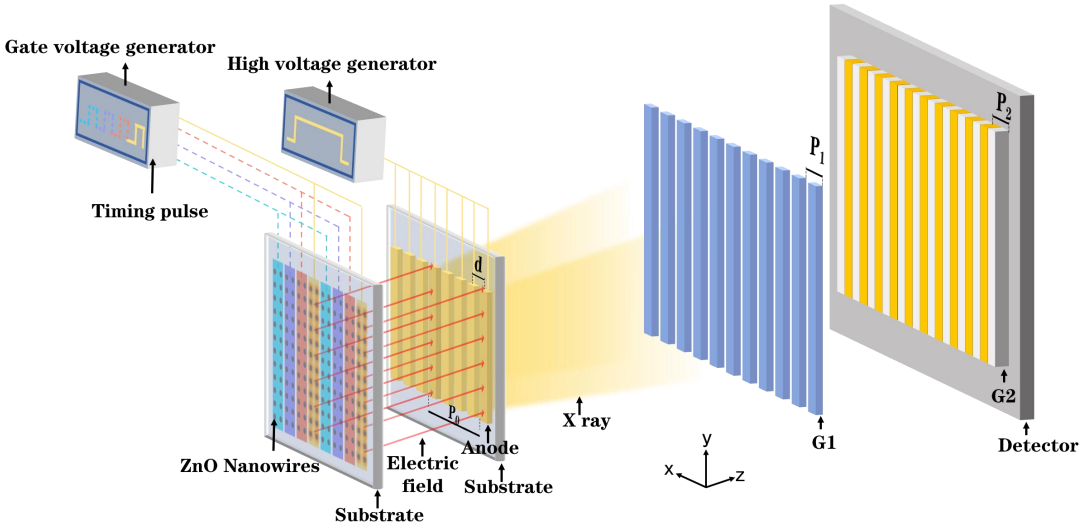

Figure 1. Schematic diagram of the addressable flat-panel X-ray source grating interferometry.

3. Results

The parameters for the simulation are described as follows. The grating G1 and G2 had period of 4 μm and 2 μm, respectively. Source to grating G1 distance and G1 to G2 distance were 2.16 m and 3.6 cm, respectively. The detector pixel size was 50 μm. For source stepping simulation, the source period (P_0) was 120 μm and the stepping size (d) was set as 15 μm, which resulted in stepping number of 8. For comparison, grating phase stepping was also simulated by moving G2 with stepping size of $P_2/8$.

The phase stepping curves obtained by the two methods are shown in Figure 2. According to the calculations, the visibility obtained by the two methods are comparable. Thus, the source phase stepping achieved by the proposed addressable cold-cathode flat-panel X-ray source has the potential to replace grating phase stepping. However, the high visibility obtained in the simulation and the slight deviation of the curve are probably due to the usage of a perfectly coherent light source and the use of an ideal rectangular grating. The current simulation has certain limitations. First, it did not yet consider the beam characteristics of the anode strips. Second, the change of grating effective thickness within the X-ray cone beam was not considered. In future, we will optimize and improve the simulation to better match the practical application scenarios of the flat panel source.

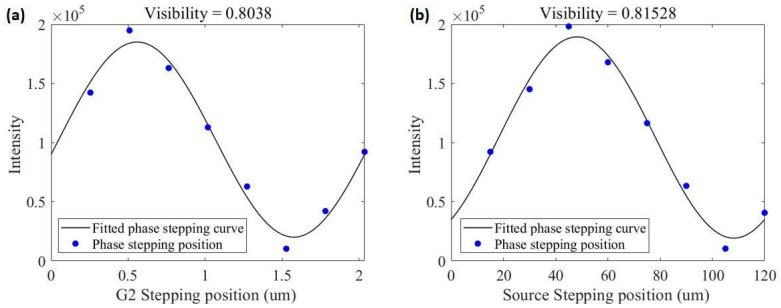

Figure 2. Phase stepping curve of (a) grating phase stepping and (b) source phase stepping.

References

[1] Wu, Wangjiang, et al. "Feasibility Study of a Cold-cathode Flat-panel X-ray Source with Micro-array Anode Target for Grating Interferometer Computed Tomography." *IEEE Transactions on Nuclear Science,* 70(12), 2553 – 2560, (2023).

Quantification of grating defects using simulation and measurements on the visibility of a Talbot-Lau interferometer

A. PEREIRA[1,2]*, S. SPINDLER[1,2], P. SOMMER[1,2], M. RAWLIK[1,2], L. ROMANO[1,2], D. JOSELL[3], M. STAUBER[4], M. STAMPANONI[1,2]

[1]*Intsitute for Biomedical Engineering, ETH Zürich, Switzerland*

[2]*Swiss Light Source, Paul Scherrer Institute, Switzerland*

[3]*Materials Science and Engineering Division, NIST, Maryland, United States of America*

[4]*GratXray AG, Villigen, Switzerland*

Email: *vieirapa@ethz.ch*

Summary: The quality of gratings in X-ray grating interferometry (XGI) is decisive for the image quality of the refraction and scattering signal. Understanding the impact of grating imperfections on the signal is thus important for the design and optimization of XGI systems. To understand and quantify these effects, we have developed a wave propagation simulation that considers source and geometric properties to simulate grating imperfections as well as allow modelling and optimization of systems with different source sizes and spectra.

The performance of XGI is heavily dependent on the geometry, source size, spectrum, and gratings used. One performance metric for XGI is the so-called "angular sensitivity", which can be increased by using gratings with small pitch [1]. However, ensuring accurate measurement of the refraction angle requires a sufficiently strong signal-to-noise ratio (SNR), which in turn depends on the visibility of the interference pattern [2]. To reach high visibility, gratings must be manufactured using heavily X-ray absorbing material, such as Au, of height sufficient to effectively attenuate high-energy photons. The fabrication of high aspect-ratio (HAR) gratings is thus pillar to bringing XGI devices into clinical environments. Despite progress in fabrication technology, manufacturing of HAR gratings remains challenging and subject to imperfections that reduce visibility and decrease signal. Grating imperfections are intimately related to the manufacturing process and can include non-uniformity of line width and duty cycle in 3D, which can be visualized with line distortions and gaps on the grating surface, as well as variations of lamella height and width perpendicular to the surface. Quantification of the influence of such imperfections in specific grating geometries is key to imposing tolerances on fabrication artifacts in order to guide manufacturing processes and design XGI systems.

In Fig 1. we compare the performance of 4.2µm pitch gratings manufactured in polymer by X-LIGA [3] versus gratings fabricated in silicon by DRIE [4] followed by Au bottom-up electroplating [5] in a symmetric Talbot-Lau setup operated at the 3rd Talbot order and designed for 46keV. The X-LIGA gratings exhibit only slightly higher average visibility (Fig. 1b) despite their much taller Au-filled grating structure (180 µm versus 145 µm for the DRIE gratings), their performance being impacted by a high density of low visibility lines (Fig. 1a). The impact of such defects increases with larger source size as seen in Fig. 2a. In contrast, the DRIE gratings provide a defect-free, uniform visibility profile (Fig. 1a).

We developed a full resolved free space propagation simulation framework without magnification rescaling. To counteract the increase in grid points from not using a divergent beam to plane wave transformation, we accelerated the computation using Graphical Processing Units (GPU). The source is modelled as a composition of multiple individual point sources with different energies and positions [6], each leading to a single

simulation. Propagation through gratings and samples is based on a multi-slice scalar wave approach [7], enabling the modelling of any system and object in 2D. This allows us to quantify the impact of any grating's geometry and imperfections on XGI.

In Fig. 2c we simulate the effect of grating defects, such as cracks and poor Au filling of the polymer template (schematically in Fig. 2b), on the visibility as a function of the source size and lateral shift of the grating features. The simulated visibility decrease caused by such defects in the G0 grating is in accord with the experimental results in Fig. 1a. Notably, a larger source size spreads the influence of a single defect across a wider area on the detector plane. This leads to poor SNR and uncertainty in the retrieved refraction angle. As the DRIE manufactured gratings have lower height than the X-LIGA gratings, we trace the similarity of their median visibilities with substantial reduction in counts for DRIE (Fig. 1b) to tapering artifacts in the DRIE gratings that lower the mean duty cycle (35% compared to 50%).

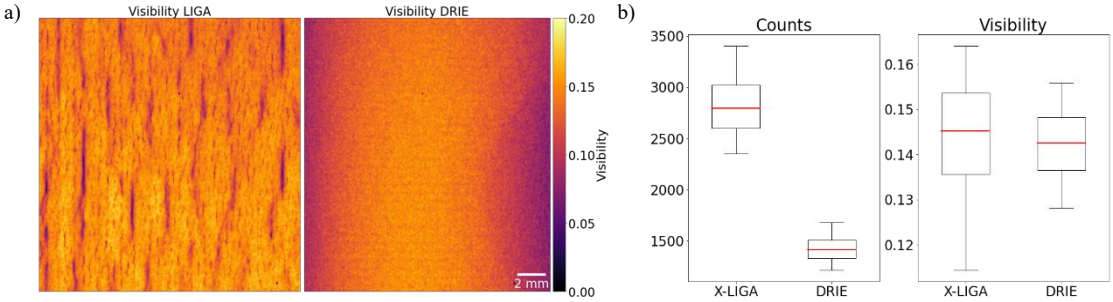

Figure 1: a) The visibility achieved using X-LIGA or DRIE manufactured gratings used in a 3rd Talbot-Order symmetric setup designed for 46keV and operated with a Hamamatsu L10101 with 70kVp and 200µA. The spectrum was additionally filtered using a 3mm Aluminum filter. b) Transmission and visibility distribution over a central region in Fig 1a).

Figure 2: a) Measured visibility from X-LIGA gratings with cracks and poor Au filling of the polymer template with two different source sizes b) Schematic and binary model for a half period shift in G0 as input for the simulation. The shift models a crack in the grating structure. C) Simulations of the visibility of a single crack leading to a half-period lateral shift in the G0 grating for different source sizes. The larger the source size the wider the effect of the crack on the visibility.

Acknowledges

The authors thank SwissLOS Lottery Fund of Kanton Aargau, the Promedica Stiftung Chur - Project Nr. 1527, SNF Sinergia Grant Nr. CRSII5 183568, PHRT-TT Project Nr. 2022-572 INTIMACY, PHRT-Pioneer Project Nr. 2021-612 CLARINET, SNF R'Equip 189662 (SiDRY) and SNF R'Equip 177036 (DTL).

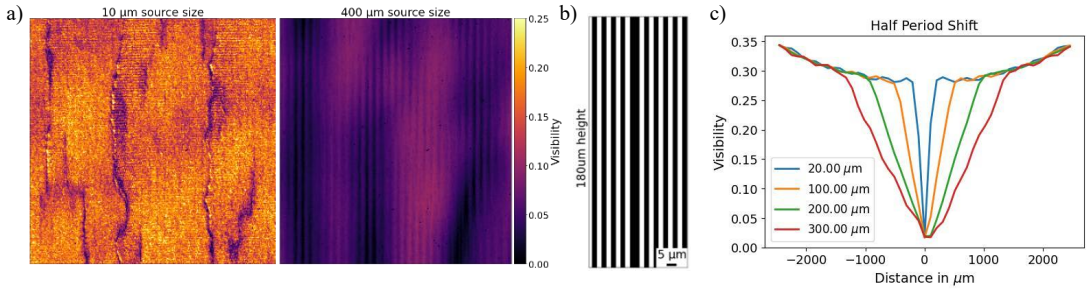

References

[1] T. Donath et al., J. Appl. Phys. 106, 054703 (2009).
[2] V. Revol et al., Rev. Sci. Instrum. 81, 073709 (2010).
[3] P. Meyer et al., XNPIG Conference Proceedings, 110 (2017).
[4] Z. Shi et al., Micromachines, 11(9), 864 (2020).
[5] D. Josell et al., J. Electrochem. Soc. 167, 132504 (2020).
[6] B. Saleh, M. Teich., Fundamentenls of photonics. John Wiley & Sons, (2019)

[7] L, Kenan et al., Opt. Express 25(3), 1831-1846 (2017).

X-ray Dark-field Computed Tomography for Monitoring of Tissue Freezing

Dominik John[1,2,3,4,*], Wolfgang Gottwald[1,2,3], Daniel Berthe[1,2,3], Sami Wirtensohn[1,2,3,4], Julia Hickler[1,2,3], Lisa Heck[1,2,3], and Julia Herzen[1,2,3]

[1]*Research Group Biomedical Imaging Physics, Department of Physics, TUM School of Natural Sciences, Technical University of Munich, 85748 Garching, Germany*

[2]*Chair of Biomedical Physics, Department of Physics, TUM School of Natural Sciences, Technical University of Munich, 85748 Garching, Germany*

[3]*Munich Institute of Biomedical Engineering, Technical University of Munich, 85748 Garching, Germany*

[4]*Institute of Materials Physics, Helmholtz-Zentrum Hereon, Outstation at DESY, 21502 Geesthacht, Germany*

Email: *dominik.john@tum.de*

Summary: Cryoablation, a minimally invasive cancer treatment, requires precise monitoring of tissue freezing to avoid damaging healthy tissue and ensure complete tumor encapsulation. Traditional CT monitoring using the hypoattenuating properties of ice offers low contrast between frozen and unfrozen tissue. We demonstrate that X-ray dark-field imaging, capturing small-angle scattering from ice crystals, significantly enhances this contrast in a porcine phantom experiment. Dark-field radiographs and CT scans show better detection of frozen regions compared to X-ray attenuation alone. This suggests X-ray dark-field imaging as a promising tool for improved monitoring of tissue freezing.

Cryoablation, a technique in interventional oncology for treating liver, kidney, prostate, lung, and breast malignancies, is gaining popularity [1]. This minimally invasive method involves freezing tumor tissues using a cryoprobe and offers advantages over surgical resection such as less pain, reduced scarring, and same-day discharge of the patient [2]. However, careful monitoring of the process is crucial to protect healthy tissues and maintain an adequate safety margin around the tumor [3]. The most frequently used monitoring approaches, ultrasound imaging (US) and computed tomography (CT), each have their drawbacks: US fails to visualize the posterior margin of the tumor due to acoustic shadowing caused by the ice ball [4] and CT only shows the slight difference in contrast due to the lower ice density.

To overcome the limitations in CT attenuation contrast, the X-ray dark-field signal is a promising candidate. It is very sensitive to scattering structures on a length scale smaller than the resolution of the imaging system, which may include, for example, ice crystals present in the sample. Thus, frozen tissue can be distinctly distinguished from unfrozen soft tissue, which usually shows little scattering. This effect has previously been demonstrated for distinguishing radiographs of frozen and unfrozen fruit [5] but has not yet been examined for tissue models either in radiography or computed tomography.

In our work, we actively freeze a porcine phantom designed to mimic the tissue composition of a human breast using a liquid nitrogen reservoir connected to a rod inside the sample. Using a conventional rotating anode source and a Talbot-Lau interferometer, we track the extent of the frozen region over time both in attenuation and dark-field using a photon-counting detector. Initially, we perform the experiment using radiographs taken at regular intervals, followed by a transition to a CT setup for three-dimensional and time-resolved imaging. We demonstrate that the frozen region in the tissue is significantly easier

to track in the dark-field compared to attenuation alone, both in radiographs and CT images [6]. Figure 1 (a) shows an axial CT slice of the sample at three points in time: While the border of the frozen region is barely visible as a slight grey shadow in the attenuation (top row, orange arrow), it is easy to recognize as a bright region in the dark-field image (bottom row, orange arrow). Further examination of the two signals in our work shows that this effect is independent of the chosen image windowing and that the dark-field signal is better suited for tracking of the freezing.

Utilizing the dark-field signal, we create a fusion image with a color overlay marking frozen pixels, set by a dark-field threshold, and the anatomical details from attenuation data. The result is shown in Figure 1 (b). A similar visualization may later assist interventional radiologists in cryoablation procedures by enabling precise cryoprobe maneuvering using anatomical information, while providing essential data on freezing extent to determine the required duration of the freezing protocol.

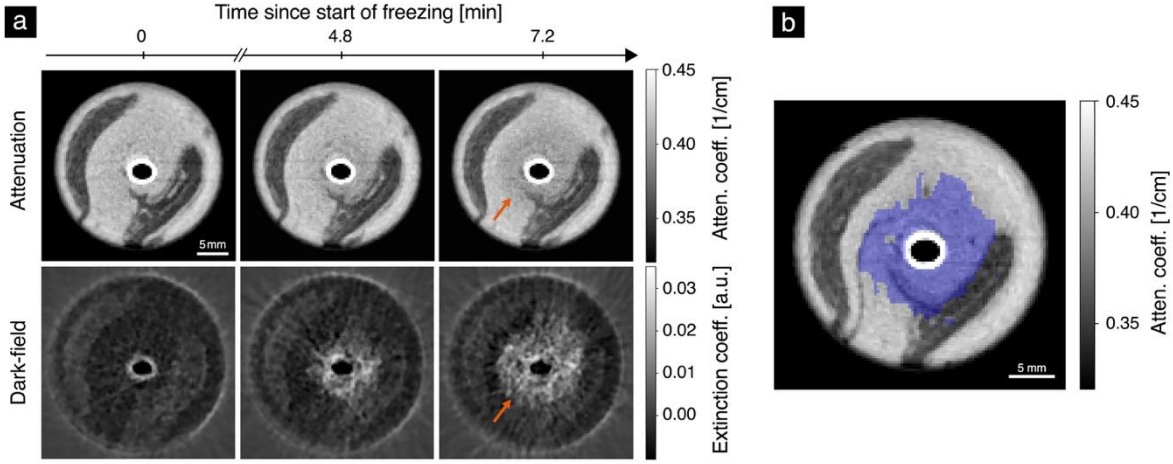

Figure 1: (a) CT image slices of porcine phantom at different time points of the freezing process. The top row shows the attenuation, the bottom channel the dark-field. While the freezing is only visible as a slight dark shadow in attenuation, it is clearly visible as a bright region in dark-field. (b) Fusion image of freezing information from the dark-field overlayed onto the corresponding attenuation image.

In summary, we show that dark-field imaging is not only relevant for diagnostics, but also a promising candidate for improved monitoring of tissue freezing. Therefore, it warrants further investigation for its potential in enhancing cryoablation monitoring.

References

[1] Mahnken, A. H., König, A. M. & Figiel, J. H. Current technique and application of percutaneous cryotherapy. In RöFo-Fortschritte auf dem Gebiet der Röntgenstrahlen und der bildgebenden Verfahren, vol. 190, 836–846 (© Georg Thieme Verlag KG, 2018)
[2] Pusceddu, C., Paliogiannis, P., Nigri, G. & Fancellu, A. Cryoablation in the management of breast cancer: Evidence to date. Breast Cancer: Targets Ther. 283–292 (2019).
[3] Rewcastle, J. C., Sandison, G. A., Muldrew, K., Saliken, J. C. & Donnelly, B. J. A model for the time dependent three-dimensional thermal distribution within iceballs surrounding multiple cryoprobes. Med. Phys. 28, 1125–1137 (2001).
[4] Pfleiderer, S. O. et al. Cryotherapy of breast cancer under ultrasound guidance: initial results and limitations. Eur. Radiol. 12, 3009–3014 (2002)
[5] Nielsen, M. S., Christensen, L. B. & Feidenhans, R. Frozen and defrosted fruit revealed with x-ray dark-field radiography. Food Control. 39, 222–226 (2014).
[6] John, D. et al. X-ray Dark-field Computed Tomography for Monitoring of Cryoablation Procedures: A Phantom Study, 13 September 2023, PREPRINT (Version 1), Research Square [https://doi.org/10.21203/rs.3.rs-3345993/v1]

Laboratory-based x-ray microscopy for three-dimensional soft tissue imaging using intensity-modulation masks

*M. Esposito[1], A. Astolfo[1], A. Teplov[2], Y. Yagi[2], I. Buchanan[1], M. Endrizzi[1,3], O.V.Makarova[4], C.-M. Tang[5], J.D. Ferrara[6], A. Olivo[1]

[1]*Department of Medical Physics and Biomedical Engineering, University College London, , London WC1E 6BT, United Kingdom*

[2]*Department of Pathology, Memorial Sloan Kettering Cancer Center, New York, New York, USA*

[3]*X-ray microscopy and tomography lab, The Francis Crick Institute, London, NW1 1AT, United Kingdom*

[4]*Creatv MicroTech Inc., Chicago IL 60612, United States of America*

[5]*Creatv MicroTech Inc., Potomac MD 20854, United States of America*

[6]*Rigaku Americas Corporation, 9009 New Trails Drive, The Woodlands, Texas 77381, USA*

Email: *michela.esposito@ucl.ac.uk*

Summary: We report the first proof of concept for three-dimensional soft tissue imaging with a laboratory-based x-ray microscope based on intensity-modulation masks, allowing for multi-modal retrieval of transmission, refraction and scattering signals. The newly developed microscope offers micron resolution in the resolved channels (transmission and refraction), while it can reach submicron resolution in the scattering channel. The combination of micron-level spatial resolution, fixed by using intensity modulation masks, and the enhanced contrast, arising from phase-based imaging, allows for the differentiation of fine details in liver and oesophageal samples.

Volumetric imaging of mm-sized soft tissue samples with micron resolution opens new possibilities in functional biology and clinical practice (e.g., histopathology), driven by the growing need for studying microscale structures in a three-dimensional context at the mesoscale. To answer these needs, we have developed a laboratory-based x-ray microscope for volumetric imaging of soft tissue samples using intensity modulation masks. Masks shape an x-ray beam into an array of beamlets. Changes in the shaped beamlets allow for the co-registered and quantitative retrieval of transmission, refraction, and scattering signals [1].

The microscope consists of a rotating anode (Cu) x-ray source, monochromatized to select the Cu K lines (~8 keV). The beam is shaped by a free-standing Au membrane [2] (10 μm thick) with vertical slits (1 μm width and 7.5 μm periodicity), placed at a distance of 67 cm from the source focal spot. An indirect detector, with an effective pixel size of 0.75 μm, was placed 25 mm downstream of the sample. For an imaging system based on intensity-modulation masks, the spatial resolution in the resolved channels (refraction and transmission) is fully determined by the mask aperture width [3], without adverse effects due to source and detector. With an aperture width (and thus a resolution limit) of 1 μm the scattering channel allows for imaging of ensembles of sample features in the nanoscale [4]. We demonstrated how the combination of micron-level spatial resolution, enhanced contrast arising from phase-based imaging and sub-micron ensemble visualisation from the scattering channel, allows for sub-cellular resolution in soft tissue samples [5].

Here, for the first time, we demonstrate the capabilities of the microscope for soft tissue imaging in tomographic mode. Two biological samples were used for this study: a Formalin-Fixed Paraffin-Embedded (FFPE) liver specimen and a decellularized piglet oesophagus (a scaffold for regenerative medicine). Computed Tomography (CT) scans over 360 degree (0.5-degree step) were acquired with the samples translated orthogonally to the mask slits (dithering) in 5 steps of 1.5 μm each to provide full sample illumination.

Acquired data were retrieved at each dithering step, recombined and reconstructed using a standard Filtered Back Projection Algorithm.

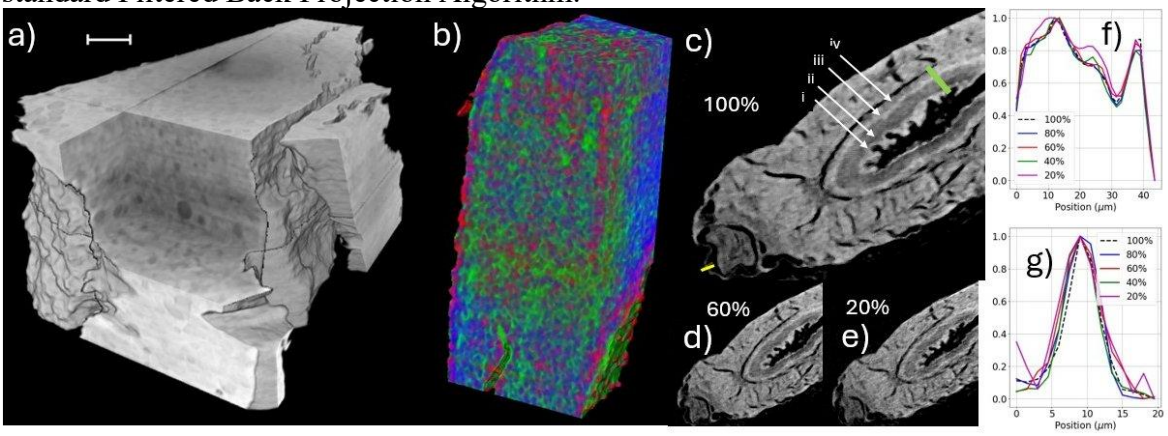

Figure 1: a) Volumetric rendering of the phase CT of FFPE liver sample. Scale bar is 100 μm. Sample micro-structures, including liver and fat cells, are visible. b) Multi-channel 3D rendering of a liver sample with transmission in green, phase in blue and scattering in red. Cells' nuclei appear in red due to their sub-micron inner structure. c) Phase CT of a decellularized piglet oesophagus. Oesophageal layers are visible: i. lamina propria and muscularis mucosae; ii. Submucosa; iii. submucosa - inner circular muscular layer transition; iv. inner circular muscular layer. Panels d) and e) show the same slice reconstructed using a cycloidal CT approach, obtained with only a fraction of the acquired data: 60% and 20%, respectively (~1.7 and 5-times reduction in exposure time). Panel f) and g) show intensity profiles across the green and yellow line, respectively, shown in c).

Figure 1 shows the first results obtained with the microscope. Microscale structures, including liver cells and fat cells, are visible (panel a), while the complementarity of the retrieved contrast channels is shown in panel b. In particular, the scattering channel, shown in red, highlights the presence of liver cell nuclei that light up in this channel due to their sub-micron inner structure. The full paper will report the histological validation of these findings, which is currently in progress. Panel c shows a reconstructed slice for the decellularized oesophagus, showing how the microscope allows for differential of faint density changes in soft tissue through the visualisation of oesophageal layers. The effect of reducing the exposure time using a cycloidal CT approach [6] is also shown in panel d-g, demonstrating how acquisition time can be reduced without loss of contrast or resolution.

Acknowledgments

Research reported in this publication was supported by the National Institute of Biomedical Imaging and Bioengineering of the National Institutes of Health under Award No. R01EB028829. The content is solely the responsibility of the authors and does not necessarily represent the official views of the National Institutes of Health. Additional support was received from the EPSRC (Grants No. EP/T005408/1, No. EP/P023231/1, and No. EP/M028100/1). A.O. was supported by the Royal Academy of Engineering under their "Chairs in Emerging Technologies" scheme (CiET1819/2/78).

References

[1] F. Vittoria et al., Beam tracking approach for single–shot retrieval of absorption, refraction, and dark–field signals with laboratory x–ray sources, Appl. Phys. Lett. **106**, 224102, 2015

[2] O. Makarova et al., Freestanding high-aspect-ratio gold masks for low-energy, phase-based x-ray microscopy, Nanotechnology **34**, 045301, (2022)

[3] M. Esposito et al., A laboratory-based, low-energy, multi-modal x-ray microscope with user-defined resolution, Appl. Phys. Lett.**102**, 234101, (2022)

[4] M. Esposito et al., Laboratory-based x-ray dark-field microscopy, Phys. Rev. Appl. **20**, 064039, (2023)

[5] M. Esposito et al., Technical note: Cartilage imaging with sub-cellular resolution using a laboratory-based phase-contrast x-ray microscope, Med. Phys. **50**, 6130, (2023)

[6] C.K. Hagen et al., A. Cycloidal computed tomography, Phys Rev Appl. 14, 014069, (2020)

Dark-field lung imaging without an analyser grating

S. SPINDLER[1,2]*, A. PEREIRA[1,2], C. ORGANISTA[1,2], M.-C. ZDORA[1,2], G. LOVRIC[2], G. LAUTIZI[3,4], C. DULLIN[5], A. CONTILLO[3], E. LONGO[3], N. SODINI[3], L. D'AMICO[3,4], K. JEFIMOVS[1,2], D. JOSELL[6], L. ROMANO[1,2], G. TROMBA[3], M. RAWLIK[1,2], M. STAMPANONI[1,2]

[1]*Institute for Biomedical Engineering, ETH Zurich, Switzerland*
[2]*Swiss Light Source, Paul Scherrer Institute, Switzerland*
[3]*Elettra-Sincrotrone Trieste S. C. p. A., Italy*
[4]*Department of Physics, University of Trieste, Via Valerio 2, 34127 Trieste, Italy*
[5]*Department for Diagnostic and Interventional Radiology, University Goettingen, Germany*
[6]*Materials Science and Engineering Division, NIST, USA*
Email: *simon.spindler@psi.ch*

Summary: Lung diseases like the chronic obstructive pulmonary disease are a major health burden to society [1]. Dark-field lung imaging is a promising tool to detect gradual and irreversible damage of the lung's microstructures in early stages. We present an analyser-free lung imaging system based on a dual-phase interferometer which allows to tune and directly resolve the fringe. It provides the classical absorption chest image with additional dark-field information without the dose impairment of other shown approaches for lung radiography and CT [2,3]. This setup achieves a relevant autocorrelation length (ACL) range with feasible visibilities.

X-ray grating interferometry (GI) is sensitive to the dark-field signal induced by sub-pixel structures and provides an imaging modality suitable for objects like the lung. GI systems induce periodic interference patterns which allow to measure refraction properties with a purely intensity-sensitive detector. Refracting objects cause this pattern to distort and shift (differential phase-contrast) while unresolvable structures cause an overall reduction of the pattern's intensity difference (dark-field). The periodicity of the interference patterns is often too small to be measured with a detector directly which makes absorption gratings (analyser gratings) in front of the detector necessary in order to decouple the fringe size from the detector pixel size. This grating absorbs roughly half of the photons that were exposed to the patient and makes the attenuation image half as dose efficient as classical imaging modalities. Dual-phase interferometers allow to generate tuneable Moiré-fringes by superimposing the Talbot carpet from two phase gratings. The Moiré-fringes can be set large enough to be resolved directly by changing the distance between the two gratings, making analyser gratings unnecessary. The amount of diffusion on the interference pattern depends on the ACL and determines the dose efficiency of the system. The diffusion is maximal when the ACL and the micro-structure sizes are approximately equal. Due to the nature of the dark-field contrast, the signal can saturate and yields a lower bound on the actual signal present. To obtain quantitative information and be sensitive to small changes, ACLs for lung imaging are orders of magnitude smaller than the structure size [4].

We present first results of dark-field imaging of porcine lungs without the need for analyser gratings. The data were acquired at the SYRMEP beamline at ELETTRA with a monochromatic 40 keV dual-phase system consisting of two 1 μm-pitch phase gratings [5] only and an ACL range from 0.29 to 0.6 μm. Notably, there were no X-ray optics behind the lungs. From the analysis of the directly resolved fringe, we obtained the dark-field image which shows the systems sensitivity to the micro-structures of the lung. We

demonstrate the feasibility of the method, estimate the dark-field signal over the achieved ACL range which was not reported previously [4]. The porcine lungs were passively inflated by connecting the trachea to ambient pressure and applying a negative pressure by continuously evacuating the surrounding chamber as seen in Fig. 1. This allowed to obtain radiography as well as CT data as a proof of concept.

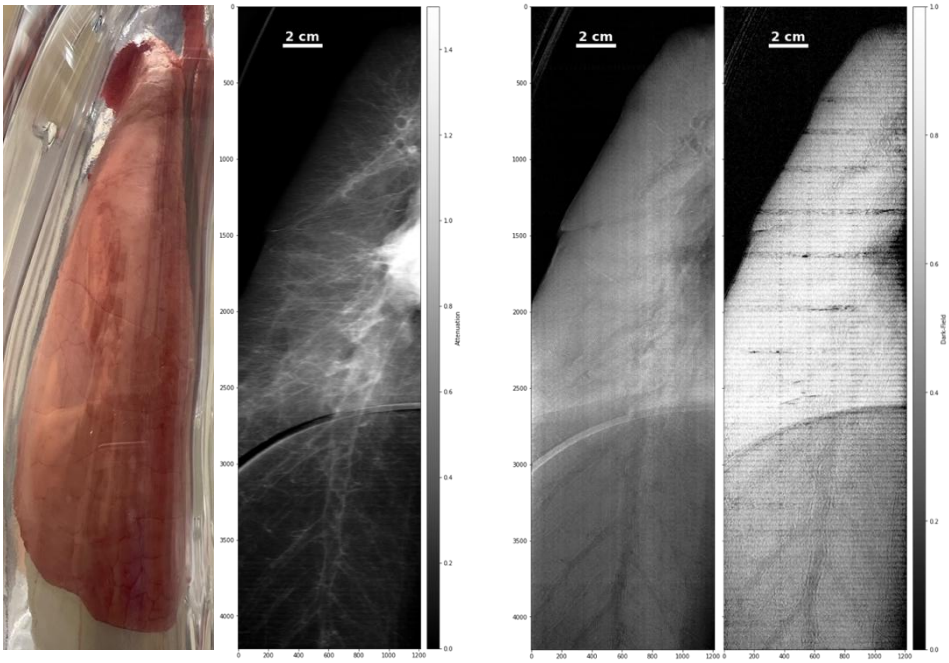

Figure 1: From left to right an image of sample in the inflation chamber is shown, radiography images of the attenuation contrast and the dark field for 0.36 µm as well as 0.54 µm ACL. The images are 8 cm wide, 30 cm high and were stitched out of 120 images vertically.

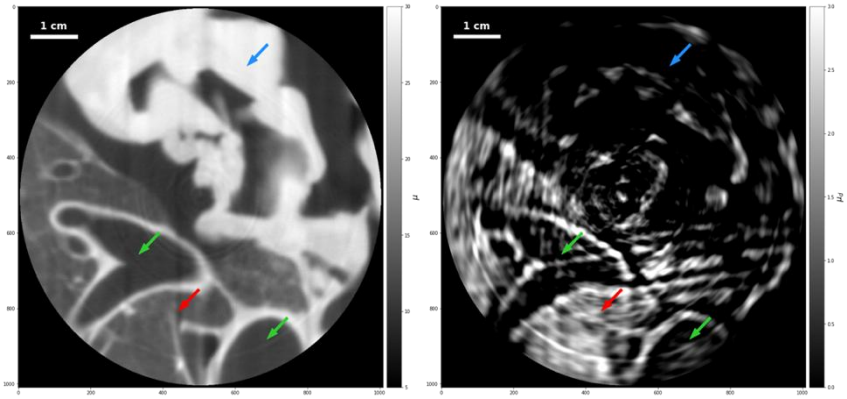

Figure 2: On the *left*: Reconstruction of the attenuation data, on the *right*: Reconstruction of the dark-field data. The dark-field CT clearly shows signal for lung tissue (red arrow) while it does not for the heart (blue arrow) and air spaces (green arrows).

Acknowledgements
The authors thank SwissLOS Lottery Fund of Kanton Aargau, SNF R'Equip 189662 (SiDRY), SNF R'Equip 177036 (DLT), PHRT-Pioneer Project Nr. 2021-612 CLARINET, SNF Sinergia Grant Nr. CRSII5, PHRT-TT Project Nr. 2022-572 INTIMACY and Promedica Stiftung Chur – Project Nr. 1572 for supporting this work.

References

[1] A.S. Buist *et al.*, Int J Tuberc Lung Dis. 12(7), 703-708 (2008)
[2] K. Willer *et al.*, The Lancet Digital Health 3(11), 733-744 (2021)
[3] M. Viermetz *et al.*, PNAS 119(8) (2022)
[4] S. Spindler *et al.*, SciRep 13, 2731 (2023)
[5] C. Organista *et al.*, SciRep 14, 384 (2024)

Optimization of Dark-field CT for Lung Imaging

P. GUO[1,2], S. SPINDLER[3], M. RAWLIK[3], X. LI[4], L. ZHANG[1,2], * Z. WANG[1,2],

[1]*Department of Engineering Physics, Tsinghua University, China*

[2] *Key Laboratory of Particle & Radiation Imaging (Tsinghua University) of Ministry of Education, Beijing, China*

[3] *Institute for Biomedical Engineering, ETH Zürich and University of Zürich, Zürich, Switzerland*

[4] *Nuctech Company Limited, Beijing, China*

Email: *wangzhentian@tsinghua.edu.cn*

Summary: The dark-field CT is a novel CT method based on grating interferometer, and it is sensitive in lung imaging. In current design of dark-field CT prototype, the visibility was chosen as the metric to evaluate system's performance and guide the optimization. Here we proposed a metric in the form of contrast-to-noise ratio (CNR) to better fit the purpose of lung imaging. We designed a concentric-circle-shaped phantom containing PMMA spheres with different diameters representing healthy and lesioned alveoli. CNR was calculated on this phantom with different combination of system parameters. A negative correlation between CNR and system total length was observed, and the maximum CNR could be acquired within a certain range of grating period.

Introduction

Dark-field imaging using a grating interferometer is sensitive to porous structure like alveoli. A prototype of dark-field CT with a scale of humans has been recently developed [1], advancing this novel imaging method to clinical application. In the design of this prototype, system parameters like grating periods and duty-cycles were optimized using system visibility as the metric.

Here we proposed a detailed optimization method for dark-field lung CT. We focused on the design using projective fringe approach with three absorption gratings [2], however the method can be generalised to other grating-based dark-field imaging modalities [1,3]. We selected the CNR between healthy and lesioned alveoli as the optimization metric to guide our system design and preliminary design conclusions were drawn.

Methods

In the design of the prototype in [1], system parameters, like grating periods and duty-cycles were evaluated with the metric of visibility. Since visibility is negatively correlated to dark-field noise [4], it's reasonable to pursue a high visibility. However, since the dark-field CT was designed with the purpose of lung imaging, it is more appropriate to optimize based on the ability to differentiate structural changes of alveoli. Here we propose a metric to distinguish healthy and lesioned alveoli in the form of CNR, which is also a form of detectability index [5]:

$$d' = \frac{\langle S \rangle_2 - \langle S \rangle_1}{\sqrt{\frac{1}{2}\sigma_1^2 + \frac{1}{2}\sigma_2^2}} \quad \#(1)$$

where $\langle S \rangle_1$ and σ_1 denotes the mean value and the standard deviation of class 1 and the same for subscript 2 and class 2. In our study, the class 1 and 2 represent the healthy and lesioned alveoli's reconstructed linear diffusion coefficient (LDC) of dark-field signal, respectively.

To calculate the system's dark-field CNR, we designed a concentric-circle-shaped phantom, whose inner and outer ring contain lesioned and healthy alveoli. We here use

PMMA spheres with different diameters to simulate healthy and lesioned alveoli's dark-field signal [6].

To evaluate each combination of system parameters, the dark-field CNR is calculated as follows. The LDC of two groups of PMMA spheres were measured at different autocorrelation length in advance. For a given designed autocorrection length, the LDC was calculated from the fitting of the measured data and used to calculate the line integrals through forward fan-beam projection. The contrast and noise were obtained after a fan-beam FBP reconstruction to calculate the CNR. The noise in the line integral is estimated using the analytical model in [4], in which the background visibility is calculated through wave-optical simulation.

Results

PMMA spheres' LDC at different autocorrelation length measured in [6] was used to fit. As for the optimization, there are five degrees of freedom, including the position of the three gratings, the period of one of the gratings, and the duty-cycle of G0. The optimized CNR at different system total length (distance between X-ray source and G2) is shown in Figure 1 (a). It can be observed that the optimized CNR went down as the total length increased, which could be attributed to the fact that increased quantum noise due to the decrement of intensity is dominating the optimization.

Besides, at the total length of 1.05 m, the optimized CNR is shown in Figure 1 (b). It can be observed that the optimized CNR first increased and decreased with the grating period, and remains constant within a certain range of G1 period. This could be explained that the system had an optimal autocorrelation length for the maximum CNR. In that range of grating period, the grating positions could be adjusted to meet the optimal autocorrelation length, while the autocorrelation length would be either larger or smaller than the optimal value due to the constraints on grating positions.

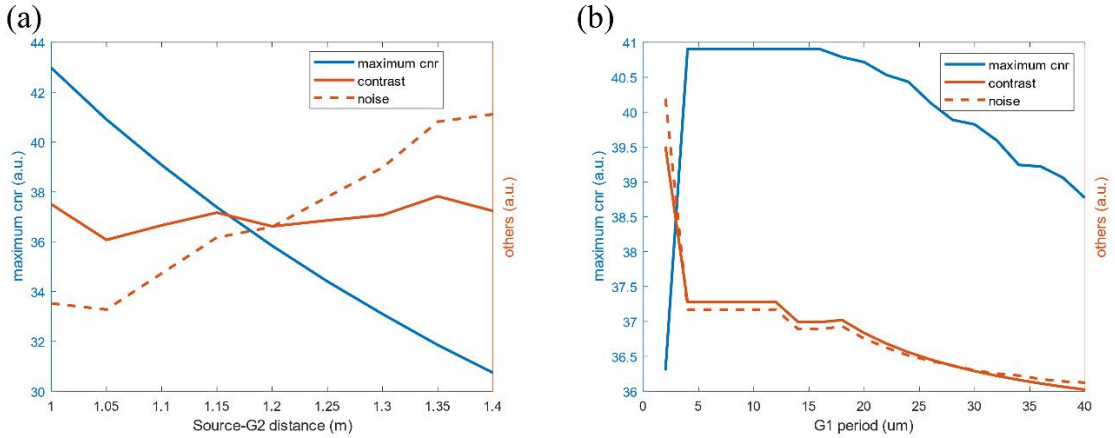

Figure 1: (a) The maximum CNR and normalized dark-field contrast and noise at each system total length. (b) The maximum CNR, dark-field contrast, and noise at each G1 period with the total length of 1.05 m.

Conclusion

In this study, we proposed a new metric to optimize the design of lung dark-field CT based on the form of CNR and developed an optimization workflow. We applied the optimization process to our dark-field CT design, and studied the dependence of CNR on system parameters. We observed that the CNR was negatively correlated to the system total length, and the maximum CNR could be acquired within a certain range of grating period. Our further plan is to consider more factors, like a more realistic human chest model.

References

[1] M. Viermetz et al., *Dark-Field Computed Tomography Reaches the Human Scale*, PNAS **119**, (2022).

[2] Z. Huang, K. Kang, L. Zhang, et al., *Alternative Method for Differential Phase-Contrast Imaging with Weakly Coherent Hard x Rays*, Phys. Rev. A **79**, 013815 (2009).

[3] M. Kagias, Z. Wang, K. Jefimovs, and M. Stampanoni, *Dual Phase Grating Interferometer for Tunable Dark-Field Sensitivity*, Applied Physics Letters **110**, 014105 (2017).
[4] V. Revol, C. Kottler, R. Kaufmann et al., *Noise Analysis of Grating-Based x-Ray Differential Phase Contrast Imaging*, Review of Scientific Instruments **81**, 073709 (2010).
[5] H. H. Barrett and K. J. Myers, *Foundations of Image Science* (John Wiley & Sons, New York, 2013).
[6] S. Spindler, D. Etter, M. Rawlik, et al., *The Choice of an Autocorrelation Length in Dark-Field Lung Imaging*, Sci Rep **13**, 1 (2023).

Sensitivity calculation for the dual phase grating interferometer by Lau condition

Jun yang[1], Fangke Zong[1], Chenggong Zhang[1], Haoqi Tang[1], Jinchuan Guo[2] and *Rongchang Chen[1]

[1]*Institute of Advanced Science Facilities, Shenzhen, China*
[2]*College of physics and Optoelectronic Engineering, Shenzhen University, China*
E-mail: chenrc@mail.iasf.ac.cn

Summary: A new sensitivity method is proposed for the sensitivity analysis of Talbot-Lau interferometer and dual-phase grating interferometer. The method can make full use of the Lau condition of the system, and skillfully relate the movement of the X-ray source with the movement of the imaging fringes, thus simplifying the derivation process of the system sensitivity. It has important theoretical value and practical significance for the design of the sensitivity of the dual-phase grating interferometer.

Abstract: For the sensitivity of the dual-phase grating interferometer, there are different methods[1-2] to address the problem. However, these methods are all based on the Talbot-Lau interferometer sensitivity established by Tilman Donath[3], and the Talbot-Lau interferometer sensitivity was obtained by two implicit unreasonable assumptions. The first assumption was that the X-rays propagating along the optical axis weren't refracted after passing through the object. This assumption could only be valid when X-rays were normally incident on a uniform object. The second assumption was that the angles between the X-rays and the optical axis were very small, and these paraxial X-rays could intersect with the optical axis after being refracted by the object, and the intersection point happened to fall on the plane where the analysis grating was located. For X-rays, the refractive index of air was slightly larger than the refractive index of the object, so X-rays generally propagated in the direction away from the optical axis after passing through objects such as spheres, rather than in the direction close to the optical axis. Even if the X-ray could intersect with the optical axis after passing through the object, the intersection point may not fall on the plane where the analysis grating was located.
Firstly,we introduce a new method for the calculation of period and visibility of dual phase grating interferometer, which indicates that when the positions of phase gratings are far away from the positions where the fringe visibility is optimal, the fringe period of the dual π-phase grating interferometer is twice the theoretical results under the illumination of polychromatic x-ray. Secondly, a new sensitivity model, shown in Fig. 1, for the dual phase grating interferometer is proposed here: the transverse fringe shift produced by the object is equivalent to that produced by the position change of the X-ray source. The new sensitivity model converts the X-ray refraction by an object into the position change of the X-ray source. In addition, the another key procedure for calculating the sensitivity

of the interferometer is to use the Lau condition to connect the position change of the X-ray source with the transverse shift of the fringe. Using the new sensitivity model above, the sensitivity of the dual phase grating interferometer and Talbot-Lau interferometer are successfully obtained, which provides theoretical support for the optimization of the dual phase grating interferometer. Finally, we will briefly introduce the fast CT imaging based on liquid-jet source.

Key words: X-ray phase-contrast imaging; Talbot-Lau interferometer; dual phase grating interferometer; sensitivity; Lau condition

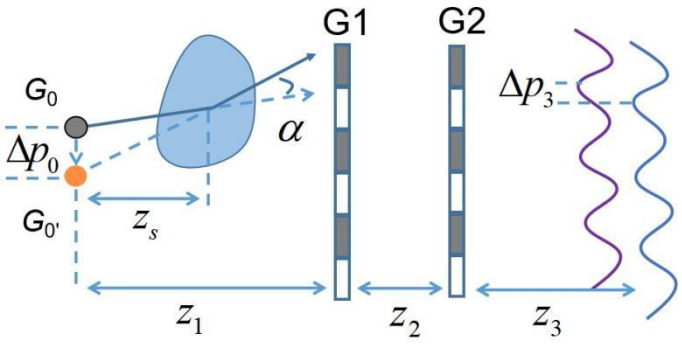

Figure 1: Schemetics of refraction back projection

References

[1] Y. Aimin, W. Xizeng, L. Hong. Sample phase gradient and fringe phase shift in dual phase grating X-ray interferometry[J]. Opt. Express, 2019, 27(24): 35437-35447.

[2]GE Yongshuai, CHEN Jianwei, YANG Jiecheng, et al. Angular sensitivity of an x-ray differential phase contrast imaging system with real and virtual source images[J]. Opt. Lett., 2021, 46(11): 2791-2794.

[3] DONATH T, PFEIFFER F, BUNK O, et al. Phase-contrast imaging and tomography at 60 keV using a conventional X-ray tube source[J]. Rev. Sci. Instrum., 2009, 80(5)：053701.

High-Resolution Multi-Contrast Tomography with an X-ray Micro Array Anode Structured Target Source

G. B. ZAN[1], S. GUL[1], S. LEWIS[1], W. B. YUN[1], P. PIANETTA[2], Y. J. Liu[3]

[1] *Sigray, Inc. 5750 Imhoff Drive, Concord, CA 94520, USA*

[2] *Stanford Synchrotron Radiation Lightsource, SLAC National Accelerator Laboratory, Menlo Park, CA 94025, USA*

[3] *Walker Department of Mechanical Engineering, The University of Texas at Austin, Austin, TX, 78712, USA*

Email: gbzan@sigray.com

Summary: A Talbot-Lau interferometry (TLI) system with a micro array anode structured target (MAAST) X-ray source offers advantages for many important applications. We will present the design of a MAAST based TLI system and its applications in biology and energy materials. The results highlight the exceptional capability of high-resolution multi-contrast X-ray tomography. Our design addresses some long-standing challenges in X-ray TLI phase contrast imaging and enables compact system designs that can potentially be made broadly available to academia research and industrial applications.

Multi-contrast X-ray imaging with high resolution and sensitivity using Talbot-Lau interferometry (TLI) offers unique imaging capabilities that are important to a wide range of applications, including exciting biomedical possibilities for imaging diseases that cannot be detected using existing X-ray imaging approaches [1-3]. A major advantage of TLI is the ability to use high power, low coherence X-rays through an absorption grating (G0) to perform XPCI with high throughput [4]. Over the past few years, most of the TLI systems used X-ray energies below 30 keV due to the difficulty of fabricating high aspect ratio absorption gratings. The reliance on G0 to enhance the spatial coherence also reduces the available photon flux by 50% or more. Most importantly, the challenge of fabricating suitable high aspect ratio (AR) gratings cannot be overstated, because the AR required for a given operating energy E is proportion X-ray energy ($\propto E^{7/2}$) [5]. At the same time, a G0 with large AR limits the field of view ($\propto AR^{-1}$) because the fringe visibility decreases due to the collimation effect [6]. Despite the novelty of this technology, these restrictions are the main reasons why TLI is not yet very commonly used in high energy applications.

To tackle these challenges, a novel MAAST X-ray source was developed, as shown in fig 1. The MAAST features an array of precisely controlled micro structured metal inserts (MMIs) embedded in a diamond substrate (see inset in fig 1B)[7]. This design overcomes the limitations of the conventional TLI configuration, which comprises an extended source and a G0 grating, by designing and incorporating the illumination pattern into the MAAST source as a built-in feature. The feasibility of MAAST source was established for high energy TLI with the Monte Carlo simulations. The performance of the MAAST can be optimized with respect to areal density, dimensions, and material for the MMIs and their substrate [8-10]. Based on our MAAST source, we designed a TLI system for X-ray imaging and tomography with high spatial resolution and sensitivity (fig. 1D) [7, 8, 11].

To demonstrate the capability of MAAST-based TLI in the applications of biology and energy materials, a tomography of a Drum fish tooth (see fig. 2) [7] and a Lithium battery [12] have been investigated with high resolution and tri-contrast (absorption, phase, and scattering), respectively. The correlative tri-contrast dataset facilitates a correlation analysis that provides useful complementary structural information that is otherwise inaccessible. The results from both examples highlight the exceptional capability of high-

resolution multi-contrast X-ray tomography empowered by the MAAST-based TLI method in the field of biomedicine and renewable energy. Furthermore, studies of the Chronic obstructive pulmonary disease and lung cancer are ongoing to explore the whole range of possibilities using higher X-ray energies (60 keV) and larger field of view (30 cm). Such studies have conventionally been considered extremely challenging because they require X-ray energies that are sufficiently high to penetrate through the human chest cavity. Our design opens up a wide new range of academia research and industrial applications.

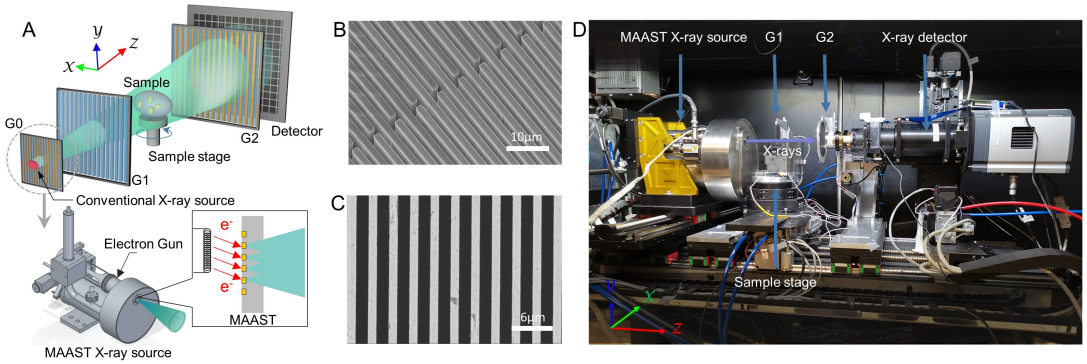

Figure 1: Schematic comparison of the conventional TLI setup and our approach with a MAAST source is shown in (A). SEM images of the MAAST pattern with etched grooves (B) and with W-MMIs embedded in the polycrystalline diamond substrate (C). Photographic image of MAAST-based X-ray interferometry (D).

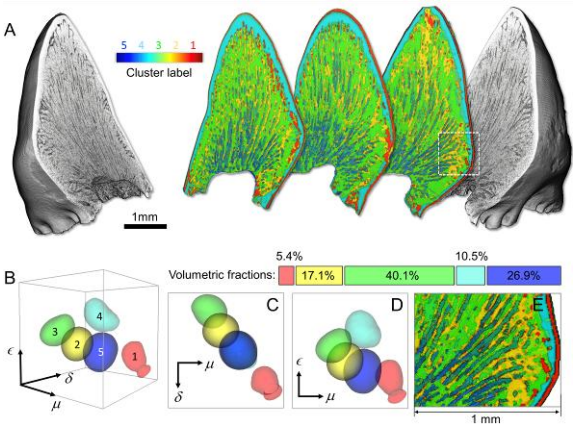

Figure 2: Tri-contrast tomography facilitated data clustering and segmentation. (A) The 3D rendering of the tomographic result (grayscale in the left and right), with a few virtual slices color coded to the data classification results. (B–D) illustrate the different properties of the five different data clusters. (E) A magnified view of the white rectangle in (A).

Acknowledgments

The authors acknowledge the funding from the National Institute of Biomedical Imaging and Bioengineering of the National Institutes of Health under Award Number R44EB023284 and R44HL154950.

References

1. Momose, A., *Phys. Med.*, 2020. **79**: p. 93-102.
2. Birnbacher, L., et al., *Eur. J. Nucl. Med. Mol. Imaging.*, 2021: p. 1-18.
3. Wang, Z., et al., *Nat. Commun.*, 2014. **5**: p. 3797.
4. Pfeiffer, F., et al., *Nat. Phys.*, 2006. **2**(4): p. 258-261.
5. Thüring, T., et al., *Sci. Rep.*, 2014. **4**: p. 5198.
6. Thüring, T., et al., *Appl. Phys. Lett.*, 2011. **99**(4): p. 041111.
7. Zan, G., et al., *Proc. Natl. Acad. Sci. U.S.A.*, 2021. **118**(25): p. e2103126118.
8. Zan, G., et al., *Phys. Med. Biol.*, 2019. **64**(14): p. 12.
9. Zan, G., et al., *Phys. Med. Biol.*, 2020. **65**(3): p. 035008.
10. Zan, G., et al., *Proc. of SPIE*, 2019. **11113**: p. 111130H.
11. Zan, G., et al., *J. Appl. Phys.*, 2019. **126**(16): p. 164901.
12. Zan, G., et al., *ACS Mater. Lett.*, 2021. **3**(12): p. 1786-1792.

Poster

Simulation of the interference pattern in a laboratory-based dual phase grating interferometer

ROBIN KRÜGER[1], TILL DREIER[2], * MARTIN BECH[1]
[1]*Medical Radiation Physics, Lund University, Sweden*
[2]*Excillum AB, Sweden*
Email: *martin.bech@med.lu.se*

Summary: We hereby present a study focused on the manifestation of the interference pattern within a laboratory-based dual phase grating interferometer featuring geometric magnification. A wave-propagation simulation for curved wave-fronts in the x-ray regime was developed taking transversal and longitudinal incoherence of the laboratory setup into account. We measured the interference pattern of two phase gratings in the laboratory using a micro-focus x-ray source. The comparison of measurements and simulations shows concurrence in interference pattern characteristics, such as variations in visibility.

Using two binary phase gratings, an interference pattern can be created that is directly resolvable by common x-ray detectors, even hybrid pixel detectors (Figure 1). Thus, eliminating the need for an absorbing detector mask increasing the efficiency of the interferometer, which is particularly relevant in laboratory experiments.

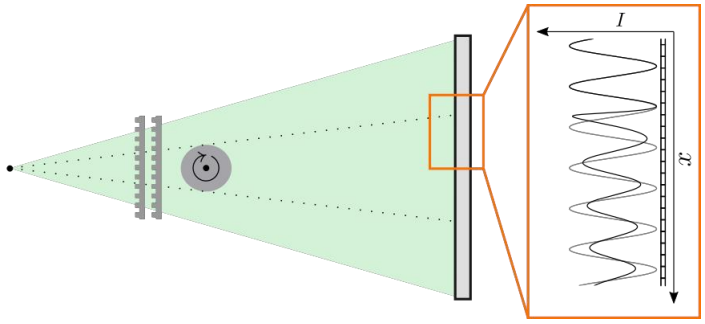

Figure 1: Schematic drawing of the experimental setup. Two binary phase gratings producing an interference pattern which is directly resolvable with the x-ray detector.

The large period of the interference pattern emerges due to slightly different periods of the gratings. The resulting Moiré frequency beating translates into an intensity modulation on the detector [1]. In a magnifying setup the locations of the gratings are relevant as well, and the beating period of the interference pattern equals the beating period of the magnified periods of both gratings.

To get a better understanding of the emergence of the interference pattern and to explain the measured interference patterns, we have developed a wave propagation simulation that takes the special properties of the laboratory setup into account, such as the size of the x-ray spot, the spectral behaviour of the system and the magnification.

Due to geometric magnification, a curved wave-front has to be simulated. The high aspect ratio of the gratings results in different phase shifts depending on the position and angle of incidence, which has a significant effect on the interference pattern and is therefore taken into account. This effect was also shown by Tang et al. [2].

The simulation framework is written in python which makes it accessible and easy to adapt to other geometries. Almost all parameters of the simulation can be varied making it possible to test various settings without the need to program.

The longitudinal incoherence of the system is taken into account by carrying out simulations for different energies and weighting them with the spectral behaviour of the system, where the x-ray source was modelled with the help of the SpekPy library [3] and then combined with absorption in gratings, air, and the detector efficiency. To include the transversal incoherence of the laboratory setup into the simulation, a theoretical model for the shift of the interference pattern based on the x-ray spot position was developed and verified by experiments and simulations.

The simulation itself was verified by experimental data of a dual phase grating setup as shown in Figure 1. We used two binary phase gratings made of silicon with a structure height of 36 µm and the periods 3.50 µm and 3.89 µm. The high aspect ratio gratings were manufactured at the Paul Scherrer Institute using a wet etching process described by David et al. [4]. Furthermore, we used an Eiger2 R 500K photon counting detector manufactured by Dectris Ltd. and a prototype micro-focus source from Excillum AB. The x-ray source allows to vary the size and position of the x-ray spot, which also allowed us to examine the dependence of the interference pattern on these parameters.

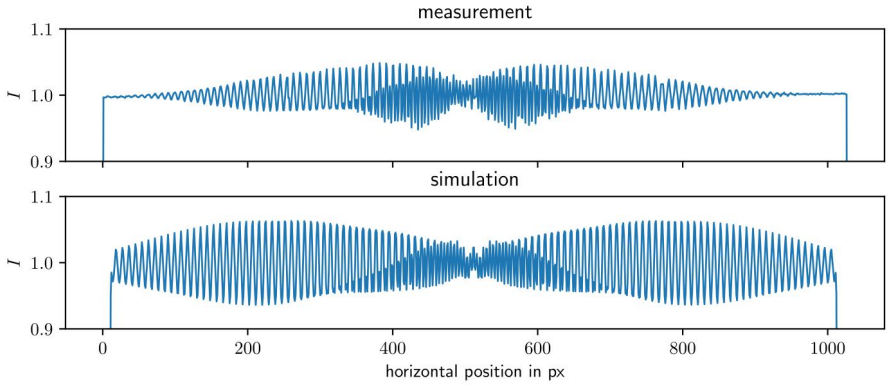

Figure 2: Comparison between measurement and corresponding simulation.

Comparison between measurement and simulation shows good agreement. In particular, a decrease in visibility in the centre of the interference pattern (Figure 2) could be reproduced, which has its origins in a combination of the system's spectral behaviour and the different trajectories through the gratings due to the cone beam geometry. Our simulation toolbox can be used for the further optimization of grating-based experiments, especially useful in polychromatic, cone-beam conditions such as in the laboratory setup.

Acknowledgments
This project is financially supported by the European Research Council (ERC) grant number 101089334.

References

[1] M. Bech (2022) In: Proceedings of SPIE **12242**, Developments in X-Ray Tomography XIV, San Diego, 2022. San Diego: SPIE, 1224211.
[2] R. Tang, C. Organista, W. Goethals, W. Stolp, M. Stampanoni, J. Aelterman, and M.N. Boone, *Optics Express*, **31(2)**, 1677–1691, (2023) .
[3] G. Poludniowski, A. Omar, R. Bujila, and P. Andreo , *Medical Physics,* **48(7)**, 3630–3637, (2021).
[4] C. David, J. Bruder, T. Rohbeck, C. Grünzweig, C. Kottler, A. Diaz, O. Bunk, and F. Pfeiffer, *Microelectronic Engineering*, **84(5)**, 1172–1177, (2007).

Performance Evaluation of Differential Phase Contrast CT and Dual-Energy CT for Quantitative Imaging

Xin Zhang[1], Ting Su[1], Yongshuai Ge[1,2]

[1]*Research Center for Medical Artificial Intelligence, Shenzhen Institute of Advanced Technology, Chinese Academy of Sciences, Shenzhen, 518055, China*
[2]*Paul C Lauterbur Research Center for Biomedical Imaging, Shenzhen Institute of Advanced Technology, Chinese Academy of Sciences, Shenzhen 518055, China*

Email: ys.ge@siat.ac.cn

Summary: This study aims to evaluate the performance of differential phase contrast CT (DPCT) and dual-energy CT (DECT) for quantitative imaging. The selected comparison criteria are electron density (ρ_e) and effective atomic number (Z_{eff}). Utilizing numerically simulated data, image domain-based decomposition algorithms are employed to extract ρ_e and Z_{eff} information across three distinct spatial resolution levels. Results show that DPCT is recommended for ultra-high spatial resolution (0.03 mm) imaging tasks, such as micro-CT imaging. On the other hand, DECT is preferable for applications requiring low spatial resolution (0.3 mm), such as diagnostic imaging tasks. At a spatial resolution of 0.1 mm, DECT and DPCT exhibit similar quantitative imaging performance.

X-ray attenuation-based DECT and DPCT imaging are two approaches to derive quantitative information of the scanned object [1][2]. In absorption CT, only μ of the object is measured, whereas in DPCT, both δ and μ can be obtained. In DECT, dual-energy imaging data is assumed to be acquired by scanning the object twice with different beam spectra (low-energy and high-energy), and the measured μ in each scan can be expressed as

$$\mu = \rho_e \left[\tau_{PE} \frac{Z_{eff}^{m-1}}{E^3} + \tau_{KN}(E) \right] \quad (1)$$

where τ_{PE} is an energy-independent constant, $\tau_{KN}(E)$ is the energy-dependent Klein-Nishina coefficient, and m is a constant. The ρ_e and Z_{eff} of DECT can be obtained by solving these two equations about μ_{LE} and μ_{HE} obtained from the two scans. For DPCT, the imaging data is assumed to be acquired from the Talbot-Lau interferometer system working with the low-energy X-ray beam and the measured δ is expressed as

$$\delta = \frac{\rho_e r_0 h^2 c^2}{2\pi E^2} \quad (2)$$

where r_0 is the classical radius of the electron, h is the Planck constant, and c is the speed of light in vacuum. It is easy to get the ρ_e map of DPCT through this equation and Z_{eff} can be obtained by substituting this ρ_e into Eq. (1). In this study, the simulated physical phantom incorporates nine materials and soft tissues: water, PMMA, PTFE, PS (polystyrene), adipose, blood, brain, breast, and lung. Numerical simulations of DECT and DPCT imaging are conducted by assuming a fan-beam imaging geometry. For DECT, the low-energy X-ray beam is generated with a 80 kVp tube potential, and the high-energy X-ray beam is generated with a 140 kVp tube potential. In DPCT imaging, the system is assumed to have the same geometry as the DECT imaging system. Additionally, 2-alternative forced choice (2AFC) tasks [3], based on Channelized Hotelling Observer (CHO) [4], are employed to simulate human observer performance.

The ρ_e and Z_{eff} decomposition results and the corresponding CHO analysis results are shown in Fig.1. When Δx = 0.3 mm, the decomposed quantitative ρ_e and Z_{eff} maps from DECT show better overall visual performance than the ones generated from the DPCT.

The CHO scores of DPCT are also much lower than that of DECT and all around 50% (for both ρ_e and Z_{eff} images) which means that the inserts are almost indistinguishable from the DPCT image. As the image spatial resolution increases, for example, $\Delta x = 0.1$ mm, the quality of DPCT images has been greatly improved. The obtained quantitative ρ_e and Z_{eff} maps from DPCT show close visual performance to the ones generated from DECT. If keep increasing the spatial resolution from sub-millimeter down to micrometer, for example, $\Delta x = 0.03$ mm, the DPCT imaging shows a superior capability in generating better quantitative images than the DECT imaging method. The imaging quality of DECT deteriorated and the noise increased significantly. At this micrometer spatial resolution scenario, the CHO results show that the DPCT outperforms the DECT by approximately 1.5 times for both ρ_e and Z_{eff} maps.

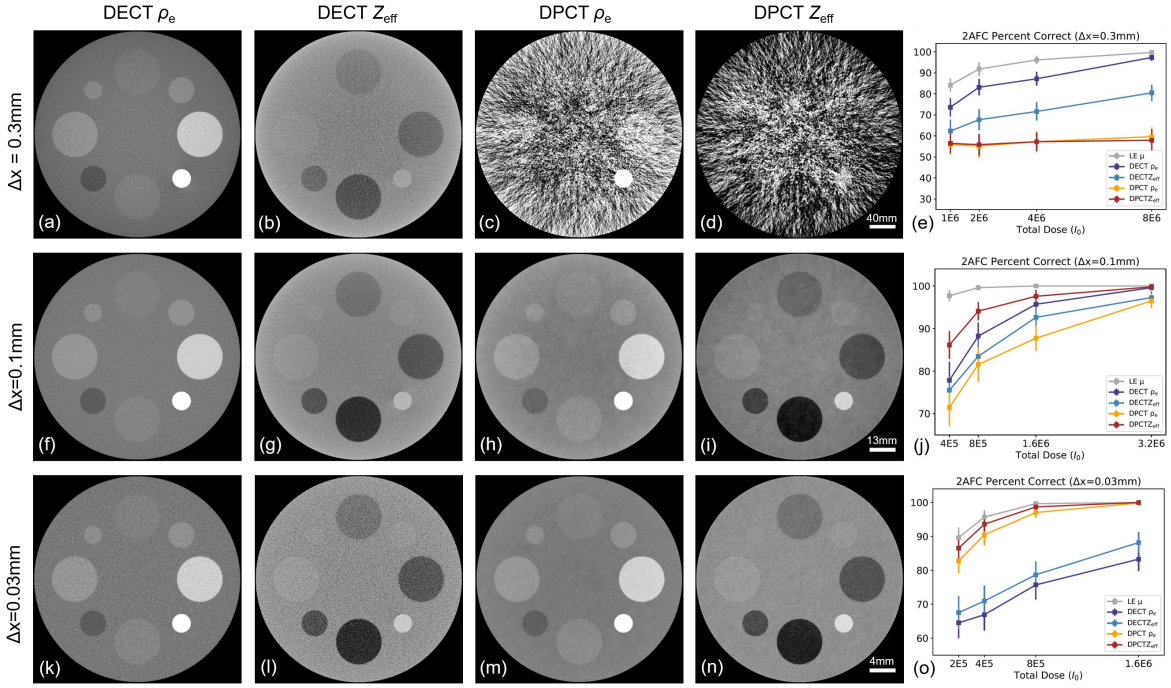

Figure 1: Images in the first and fourth columns show the quantitative decomposition results of DECT and DPCT. The CHO analysis results are presented in the fifth column. From top to bottom, they correspond to spatial resolution of $\Delta x = 0.3$ mm, $\Delta x = 0.1$ mm, and $\Delta x = 0.03$ mm. The ρ_e map and ρ_{eff} map display windows are $[2.61, 4.15] \times 10^{23}\text{cm}^{-3}$ and $[4.29, 10.63]$ when $\Delta x = 0.3$ mm, $[2.61, 4.15] \times 10^{23}\text{cm}^{-3}$ and $[5.53, 9.47]$ when $\Delta x = 0.1$ mm, and $[2.61, 4.15] \times 10^{23}\text{cm}^{-3}$ and $[5.53, 9.47]$ when $\Delta x = 0.03$ mm, respectively.

In conclusion, DPCT is recommended for ultra-high spatial resolution (0.03 mm) imaging tasks, such as micro-CT imaging. On the other hand, DECT is preferable for applications requiring low spatial resolution (0.3 mm), such as diagnostic imaging tasks. At a spatial resolution of 0.1 mm, DECT and DPCT exhibit similar quantitative imaging performance.

References

[1] Dual energy CT in clinical practice[M]. Berlin: Springer, 2011.

[2] Qi Z, Zambelli J, Bevins N, et al. Physics in Medicine & Biology, 2010, 55(9): 2669.

[3] Yu L, Leng S, Chen L, et al. Medical physics, 2013, 40(4): 041908.

[4] Yao J, Barrett H H. Mathematical Methods in Medical Imaging. SPIE, 1992, 1768: 161-168.

Modulated Talbot-Lau interferometer

S. SPINDLER[1,2] *, M. RAWLIK[1,2], L. ROMANO[1,2], B. BENZ[2,3], Q. YU[2], L. CHEN[1,2], A. PEREIRA[1,2], C. ORGANISTA[1,2], P. GUO[4,5], Z. WANG, M[4,5]. STAMPANONI[1,2]

[1]*Institure for Biomedical Engineering, ETH Zurich, Switzerland*
[2]*Swiss Light Source, Paul Scherrer Institute, Switzerland*
[3]*Swiss Nanoscience Institute and Department of physics, University of Basel, Switzerland*
[4]*Department of Engineering Physics, Tsinghua University, China*
[5]*Key Laboratory of Particle & Radiation Imaging (Tsinghua University) of Ministry of Education, Beijing, China*
Email: *simon.spindler@psi.ch*

Summary: X-ray grating interferometers provide the diagnostically valuable refraction and diffusion properties of objects. Recent advances showed first breakthroughs towards clinical applications in breast and lung imaging [1,2]. A commonly used system type is the Talbot-Lau interferometer (TLI). Manufacturing capabilities, high signal intensity and geometric constraints are convoluted competing parameters for system designs due to the intrinsic connection between grating pitches, signal and system length. We present a modulated Talbot-Lau interferometer (MTLI) that separates these requirements through modulated envelope gratings. This enables to select the fractional Talbot distance independently from the system geometry.

Since its discovery, X-ray imaging has become one of the most important widely available diagnostic tools. Besides the advancement to computed tomography (CT) and the detector technology, the method so far only utilized the attenuation of materials. Grating interferometry allowed for the first time to make phase and diffusion properties accessible with clinically relevant imaging times and widely available X-ray sources. Tabletop X-ray systems generally require three gratings to obtain the phase information; an absorption source grating (G_0) to obtain spatial coherence, a phase grating (G_1) to induce an intensity fringe and an absorption analyser grating (G_2) to measure small scale fringes with larger detector pixels. These widely used TLIs provided first medically relevant results for breast and lung imaging [1,2].

TLI are designed for a particular application. The angular sensitivity, the autocorrelation length (ACL), the total systems length and the design energy confine the design parameters. The chosen pitch of the G_2 in combination with the system length and sample position define the systems sensitivity. The resulting position and pitch of G_1 should have the fractional Talbot distance close to the position of G_2 [3] in order to have a high signal visibility. Many systems must compromise at this point already as the optimal parameters would lower the pitch of G_0 below feasible periods. Therefore, the pitch of G_0 is often set to the lowest achievable pitch and the remaining parameters are set to be as close to the intended optimum as possible. Particularly large focal spots, necessary for fast acquisition, make the system sensitive to defects in the G_0 grating leading to a reduction in visibility and lower dose efficiency. Further issues may arise if G_1 must be placed at inconvenient positions.

We propose the use of MTLI to place G_1 more freely, have shorter fractional Talbot distances, increasing the pitch of the G_0 and/or increasing the absorption grating structure height (increase design energy). MTLIs utilize Moiré fringes (Fig. 1) generated by a

structured array of phase-shifting gratings [4] (Fig. 2). The fringe's periodicity is governed by the large structure pitch *P*, while the fractional Talbot distance is defined by the fine structure *p*. This decouples the geometry from the interferometric requirements of G_1 and enables a significantly freed up parameter space.

One application which might significantly benefit from MTLI is dark-field lung CT. The size of a gantry, target ACL range of the system and high photon energies make the sensitivity of a TLI system limited by the fabrication of small-pitch G_0, typically around 4.8 µm. With MTLI, however, the geometry is the limiting factor. A 1.1 m long, 0.7 m bore system with the design energy of 60 keV and ACL around 0.2 µm can have the G_0 pitch larger than 10 µm. The simulated polychromatic visibility of a phase-stepping curve at the detector is above 30%. A modulated envelope grating can be fabricated with a combination of advanced lithography and dry etch [5] for the silicon template and bottom up electroplating [6] for the Au filling.

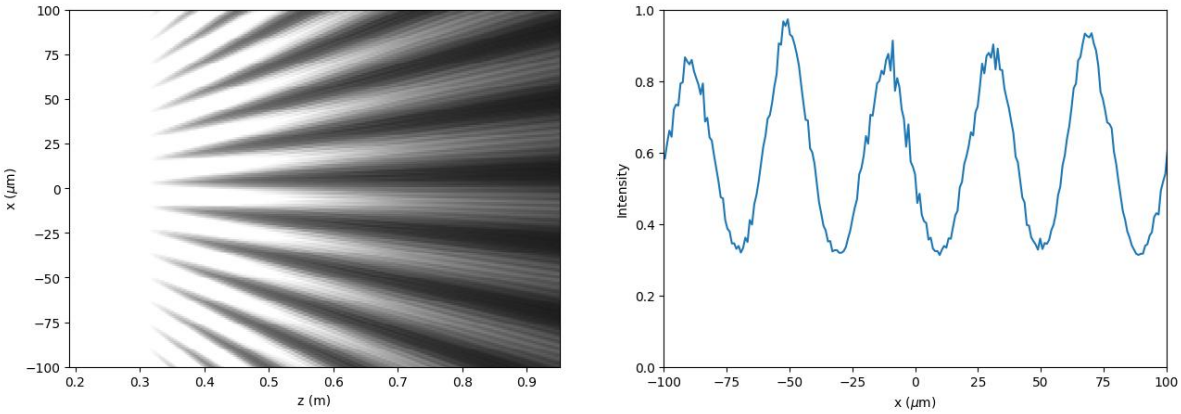

Figure 1: *Left:* Simulated Talbot carpet of the modulated envelope grating, inducing a Moiré fringe of about 40 µm pitch at the analyser grating plane. *Right:* Simulated polychromatic intensity profile of the fringe before the analyser grating with a visibility of 50 %.

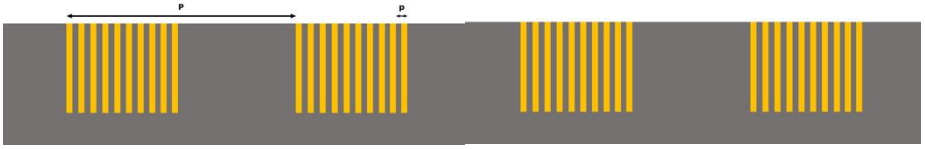

Figure 2: Cross-section of a gold-filled silicon modulated envelop grating with structure pitch *P* and modulation pitch *p*.

Acknowledgements
The authors thank SwissLOS Lottery Fund of Kanton Aargau, SNF R'Equip 189662 (SiDRY), SNF R'Equip 177036 (DLT), PHRT-Pioneer Project Nr. 2021-612 CLARINET, SNF Sinergia Grant Nr. CRSII5, PHRT-TT Project Nr. 2022-572 INTIMACY, Promedica Stiftung Chur – Project Nr. 1572 and SNI PhDSchool Project Nr. P2205 MAGNET for supporting this work.

References
[1] M. Rawlik *et al.,* Optica, 10(7), 938-943 (2023)
[2] K. Willer *et al.,* Lancet Digital Health, 3(11), 733-744 (2021)
[3] T. Donath *et al.,* Journal of Applied Physics, 106 (2009)
[4] A. Pandeshwar *et al.,* Applied Physics Letters, 120 (2022)
[5] Z. Shi *et al.*, Japanese Journal of Applied Physics 60, SCCA01 (2021)
[6] D. Josell *et al.*, Journal of The Electrochemical Society 167, 132504 (2020)

Quantitative Phase-contrast Microtomography using Talbot Array Illuminators at PETRA III Beamlines P05 & P07

Dominik John[1,2,3,4,*], Mirko Riedel[1,2,3,4], Alex Gustschin[1,2,3], Pidassa Bidola[4], Madleen Busse[1,2], Lisa Marie Petzold[1,2,3], Fabio De Marco[5,6], Natalia Pellegata[7], Pierre Thibault[5,6], Felix Beckmann[4], Julian Moosmann[4], Jörg U. Hammel[4] and Julia Herzen[1,2,3]

[1]*Research Group Biomedical Imaging Physics, Department of Physics, TUM School of Natural Sciences, Technical University of Munich, 85748 Garching, Germany*

[2]*Chair of Biomedical Physics, Department of Physics, TUM School of Natural Sciences, Technical University of Munich, 85748 Garching, Germany*

[3]*Munich Institute of Biomedical Engineering, Technical University of Munich, 85748 Garching, Germany*

[4]*Institute of Materials Physics, Helmholtz-Zentrum Hereon, Outstation at DESY, 21502 Geesthacht, Germany*

[5]*Department of Physics, University of Trieste, 34127 Trieste, Italy*

[6]*Elettra-Sincrotrone Trieste, 34149 Basovizza, Italy*

[6]*Institute of Diabetes and Cancer at the Helmholtz Center Munich, Ingolstaedter Landstr. 1, 85764, Neuherberg, Germany*

Email: *dominik.john@tum.de*

Summary: In this work, we demonstrate the potential of an advanced method for three-dimensional analysis of biomedical and material science specimens at the micrometer scale using Talbot Array Illuminators (TAI) combined with Unified Modulated Pattern Analysis (UMPA). This technique allows efficient and precise phase retrieval, yielding high sensitivity, and is applicable to a wide range of sample classes with varying material compositions.

For the three-dimensional analysis of specimens in material science and biomedicine in the micrometer range, quantitative methods of retrieving the phase information of the sample are highly beneficial: In virtual histology, they allow gaining valuable insights into the mechanisms of disease while in material science, slight changes in the sample composition undetectable with traditional methods may be visualized. One such method, speckle-based imaging, uses diffractive and absorptive beam modulators to create a defined intensity pattern in space, which is then modified by the sample [1]. The changed pattern is then compared with the reference pattern to retrieve information about the attenuation, phase shift and small-angle scattering produced. Typically used modulators such as sandpaper create random speckle patterns, which require a large number of frames for accurate phase retrieval and generally provide low visibility. In order to circumvent these shortcomings and increase the sensitivity of the method, we have implemented a beam modulator in the form of a 2D periodic phase-shifting grating called a Talbot array illuminator (TAI) [2,3] at the beamlines P05 and P07 of PETRA III (*DESY,* Hamburg) [4] and combined it with Unified Modulated Pattern Analysis (UMPA) as a phase-retrieval algorithm [5,6]. Unlike absorptive elements, the TAI modulates the entire incoming radiation to create a Talbot carpet and allows to quantitatively retrieve the electron density of the sample with high sensitivity and lower measurement time.

In our ongoing research, we apply the method to a wide range of samples in the fields of material science and biomedicine. Figure 1 shows a scan of a sandstone sample that was first saturated with brine and then flooded with oil (n-Decane), conducted at beamline P07 using a peak energy of 57 keV. Due to the quantitative nature of our method, the three materials are well distinguishable using thresholds set for the electron density.

The method is also used at beamline P05 to compare the composition of healthy tissue with that of tumor invaded tissue for different organ systems and for the quantification of different contrast media [7]. Due to the higher sensitivity and therefore higher contrast, the method will also be used to analyze the vascular structure of diseased tissue, thereby contributing to advancements in biomedical research and diagnosis.

Our findings demonstrate the efficacy of the TAI-based approach in accurately quantifying sample composition and allowing a high throughput of samples at the beamline.

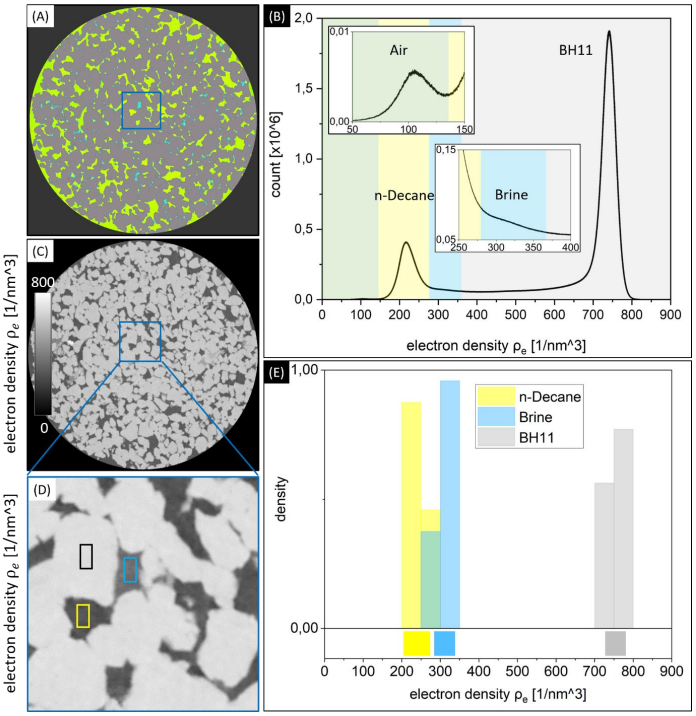

Figure 1: Quantitative analysis of a sandstone sample containing brine and oil (n-Decane) reconstructed using UMPA. (A) Slice through the electron density of the reconstructed volume. The density variation between n-Decane (yellow) and Brine (blue) is visible in the labeled ROI. (B) Histogram of the electron density volume. The segmentation handles used to represent the material boundaries in panel (A) are shown. (C) Tomogram corresponding to panel (A) in gray. (D) Enlarged area in panel (C). ROIs of 20x30 pixels representative for the two-liquid phases and the solid Bentheimer rock are featured. (E) Rug distribution of the electron density of the materials as marked in panel (D) and in agreement with the handles set in the histogram in panel (B).

References

[1] M.-C. Zdora. State of the art of X-ray speckle-based phase- contrast and dark-field imaging. Journal of Imaging 4.5 (2018):60.

[2] A. Gutschin et al. High-resolution and sensitivity bi-directional x-ray phase contrast imaging using 2d talbot array illuminators. Optica 8.12 (2021): 1588-1595.

[3] M. Riedel et al. Comparing x-ray phase-contrast imaging using a Talbot array illuminator to propagation-based imaging for non-homogeneous biomedical samples. Scientific Reports 13.1 (2023):6996

[4] F. Wilde et al. Micro-CT at the imaging beamline P05 at PETRA III. AIP conference Proceedings 1741 (2016), 030035.

[5] F. De Marco et al. High-speed processing of X-ray wavefront marking data with the Unified Modulated Pattern Analysis (UMPA) model. Optics Express 31.1 (2023): 635-650

[6] M.-C. Zdora et al. X-ray phase-contrast imaging and metrology through Unified Modulated Pattern Analysis. Physical Review Letters 118.20 (2017): 203903.

[7] Pellegata N. S. MENX and MEN4. Clinics (Sao Paulo, Brazil) (2012), 67 Suppl 1, 13–18.

Low Dose Grating-based Phase Contrast Computed Tomography via Improved Grating Structure

Changsheng Zhang[1,3], * Jian Fu[1,2,3]

[1] *School of Mechanical Engineering and Automation, Beihang University, Beijing*

[2] *Jiangxi Research Institute, Beihang University, Nanchang*

[3] *Ningbo Institute of Technology, Beihang University, Ningbo*

Email: *by1807136@buaa.edu.cn, fujian706@buaa.edu.cn*

Summary: Grating-based phase contrast computed tomography (GB-PCCT) offers excellent imaging contrast on weak absorption objects. Limited by the absorption of gratings and the phase retrieval principle, it leads high radiation dose. In this paper, we report a low-dose GB-PCCT method. It optimizes the duty cycle of the G2 grating and integrates a bidirectional misalignment structure within the G2 grating, thereby permitting one-shot scans and enhancing x-ray utilization. The proposed method is validated with experimental data and results in a significant reduction in radiation dose. This study demostrates potential of GB-PCCT techniques in future clinical applications.

Observation of Laser Welding of Dissimilar Materials using X-ray 4D Phase CT

Ryosuke Ueda[1], Yuzo Nagatomo[1], Yichen Fang[1], Shinji Kobayashi[1], Masato Hoshino[2], Yoshichika Seki[1], Atsushi Momose[1]

[1]*Institute of Multidisciplinary Research for Advanced Materials, Tohoku University, Japan*

[2]*JASRI/Spring-8, Japan*

Email: *ryosuke.ueda.a7@tohoku.ac.jp*

Summary: X-ray phase imaging is suitable for observation of polymer materials because of its high sensitivity even for materials with light element. 4D X-ray phase CT (Computed Tomography) has been studied using white synchrotron radiation and pink beam to observe the temporal changes inside the sample. This study focuses on the use of 4D phase CT to observe laser welding of dissimilar materials, especially polymers and metals. 4D X-ray phase CT can visualize the inside of polymer materials with high contrast and allow us to observe the temporal changes in melting and welding occurring inside the materials.

X-ray imaging is widely used in the medical and materials fields because it allows non-destructive observation of the inside of an object. Conventional X-ray imaging visualizes the amount of X-rays absorption as X-rays pass through an object and is called absorption contrast imaging. However, absorption contrast is not so sensitive to materials made of light elements. On the other hand, X-ray also induces a phase shift when they pass through an object. Phase contrast is more sensitive to light elements than absorption contrast.

A Talbot interferometer with diffraction gratings is known as one of the X-ray phase imaging techniques [1]. The Talbot interferometer has been used in various fields because it does not require a high-resolution image detector and can provide a large field of view using a large area grating. Three images mapping absorption, refraction (or differential phase), and scattering) are available. Polychromatic beams can also be used in the interferometers, and the performance with a beam of 10 % energy bandwidth is almost comparable to that of a monochromatic beam. Therefore, high-speed imaging and four-dimensional X-ray phase computed tomography (4D phase CT) with white synchrotron light, or a pink beam extracted from white synchrotron light have been demonstrated [2].

As an application of 4D phase CT, we have studied the observation of materials during laser processing. Laser is used in a variety of precision material processing applications, such as welding, brazing, cutting, drilling, marking, and cleaning. However, methods for observing the internal behaviour of materials during processing are still limited. X-ray absorption imaging is used to observe the inside of materials, but it does not provide a clear image of light-element materials such as polymers. On the other hand, X-ray phase CT can visualize the inside of polymer materials with high contrast, which is expected to contribute to the optimization and improvement of the laser processing described above.

This study focused on the observation of laser welding of dissimilar materials. The sample consists of two materials, i.e., polymer and metal. The upper part is a laser-transparent polymer, while the lower part is a metal. By irradiating the laser from top of the sample toward the bottom, the lower metal is heated, and the polymer in contact with the metal is

melted. After the laser irradiation is stopped, the melted polymer solidifies, and the polymer and metal are joined.

The experiment was performed at BL28B2, SPring-8, Japan. Figure 1(a) shows the constructed experimental layout. A pink beam of 25 keV central energy with 10 % bandwidth is generated from white light using a multilayer mirror. The beam passes through the sample, the π/2-type G1 phase grating, and the G2 absorption grating, and is captured by an X-ray beam monitor. The period of both G1 and G2 is 5.3 μm. The beam monitor consists of a phosphor screen (LuAG 200 μm thickness) and a CMOS high-speed camera. The number of pixels is 2048 × 2048 and the pixel size is 10 μm. Note that the image height and width is limited to 352 × 768 to obtain a high frame rate. The sample is rotated at 32 ms/rotation, during which 320 images are measured. For the fringe scanning method, the G1 grating moves one period during five sample rotations. Therefore, the number of phase steps is five and the absorption, the phase and the scattering image are obtained every 160 ms. A infrared Nd:YAG fiber laser with wavelength of 1064 nm was introduced downward on the sample. The laser was operated with continuous wave (c.w.) mode. The sample was made of the polymer (polycarbonate, PMMA, etc.) that easily transmits laser in the upper part and the aluminum in the lower part as shown in Fig. 1(b). The upper and lower parts of the sample rotate in unison for CT measurement.
Figure 2 shows an example of 4D-CT experiment of PMMA and Al in laser welding. The results are shown here for every 800 ms. More detailed image results and prospects for further time resolution improvements will be presented in the presentation.

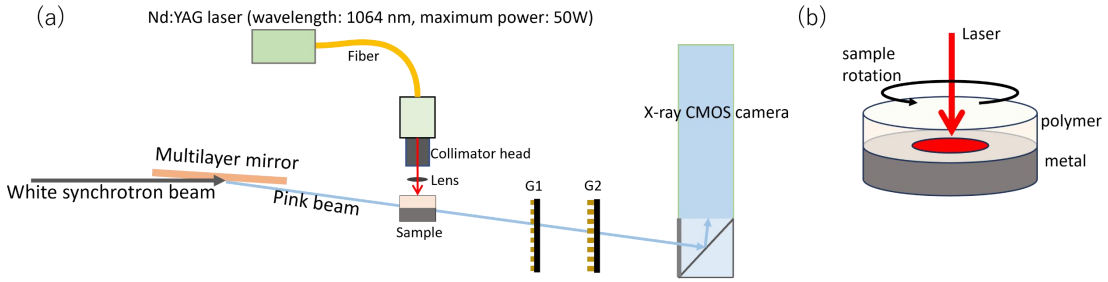

Figure 1: (a) Experimental layout at Spring-8 beamline BL28B2. (b) Sample configuration (laser-transparent polymer at the top and metal at the bottom).

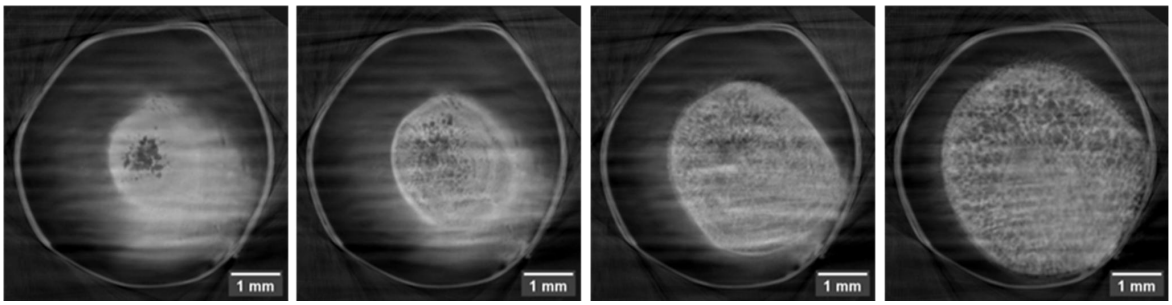

Figure 2: Results of 4D phase CT measurement of PMMA and Al in laser welding. From left to right, the time series of the PMMA sample cross section near the welding interface are shown for every 800 ms.

Acknowledgments
This work was supported by JSPS KAKENHI Grant Number JP23K11700. The experiments using synchrotron radiation were approved by SPring-8 committee (2021B1341, 2022B1533 and 2023A1810).

References

[1] A. Momose, S. Kawamoto, I. Koyoma, et al., Jpn. J. Appl. Phys., 42 (2003), L866.
[2] K. Vegso, Y. Wu, H. Takano, M. Hoshino, and A. Momose, Sci. Rep. 9, 7404 (2019).

Fabrication of large-area and fan-shaped gratings with high aspect ratio by bonding hot melt adhesive film with metal foil

Runtao Deng[1,2], Yufeng Li[1,2], Jincheng Lu[1,2], Peiyuan Guo[1,2], Li Zhang[1,2], Zhentian Wang[1,2,*]

[1]*Department of Engineering Physics, Tsinghua University, Haidian District, Beijing, China*

[2]*Key Laboratory of Particle & Radiation Imaging (Tsinghua University) of Ministry of Education, Beijing, China*

Email: *wangzhentian@tsinghua.edu.cn*

Summary: One of the main bottlenecks of X-ray grating interferometry (XGI) is the fabrication of high aspect ratio, large area and high-quality phase and absorption gratings. In this work, we utilize organic adhesive film and metal foil to fabricate absorption grating with pitch of tens of micrometers, which features ultra high aspect ratio and can be fabricated into fan-shape to cope with beam divergence. This fabrication method is complementary to LIGA and silicon-based process for XGI applications such as security inspection and medical imaging.

In grating fabrication of XGI, two major approaches remain dominant: the so-called LIGA process (from German acronym Lithographie, Galvanoformung, Abformung) and the silicon-based micro-fabrication method which mainly uses lithography, etching and metallization. State of art LIGA grating fabrication can achieve gold structures as high as 180μm at a pitch of 4.2μm [1]. For silicon-based process the substrate can be etched to a depth of 100μm with 2μm pitch [2]. Both of these two methods are suitable for fabricating gratings with small pitches (2-10μm) and high aspect ratio.

In applications of XGI for large objects such as security inspection and medical imaging, not all the gratings' pitches are required to be smaller than 10μm, and the pitch of G_2 can be set to tens of microns to meet requirements [3]. Still, there are two main challenges for grating fabrication in these applications. First the gratings with a large area are required to provide sufficient field of view. Second, since the X-ray source is operated at high voltage up to 160 kVp, the gratings with high metallization are required to block X-rays in order to get high visibility. Both requirements remain challenging for LIGA and silicon-based process. Additionally, these processes are expensive and time consuming therefore are not ready for mass production at this stage. It is necessary and preferable to find an alternative, cheap method for at least fabricating large pitch of gratings for applications such as homeland security and medical imaging.

The stack&slice method [4] and thermal composite method [5] of bonding different metal foils is a potential method to fabricate large-area and cheap absorption gratings with almost "unlimited'' high aspect ratio. The thermal composite method is operated as follows: two different metals such as silver and aluminum are put layer by layer alternately and then pressed for a long time in high temperature, and the two different metals are closely bonded by molecular diffusion. Because the absorption coefficients of silver and aluminum are different, the absorption grating is formed. The heating temperature is 520 °C and the time is 2 hours in that work.

We proposed a similar method by bonding hot melt adhesive film with tungsten metal foil. The tungsten foil is chosen due to its high X-ray absorption coefficient. Besides it has

relatively high hardness and melting point which means the grating is more durable and stable in fabrication as well as it is cheaper than gold. The thicknesses of organic adhesive film and tungsten metal foil are both 20μm which means the pitch of grating is 40μm. Our fabrication process is as follows, first, we cut the adhesive film and tungsten foil into 140 × 1 mm^2 (length × thickness), and then we put the two foils layer by layer alternately in a mould. Finally, the temperature is raised to about 100 °C and pressed with a device for about 30 seconds which is suitable for mass production, and the organic adhesive film is closely bonded with tungsten foil. A sample fabricated by this method is shown in Figure 1.

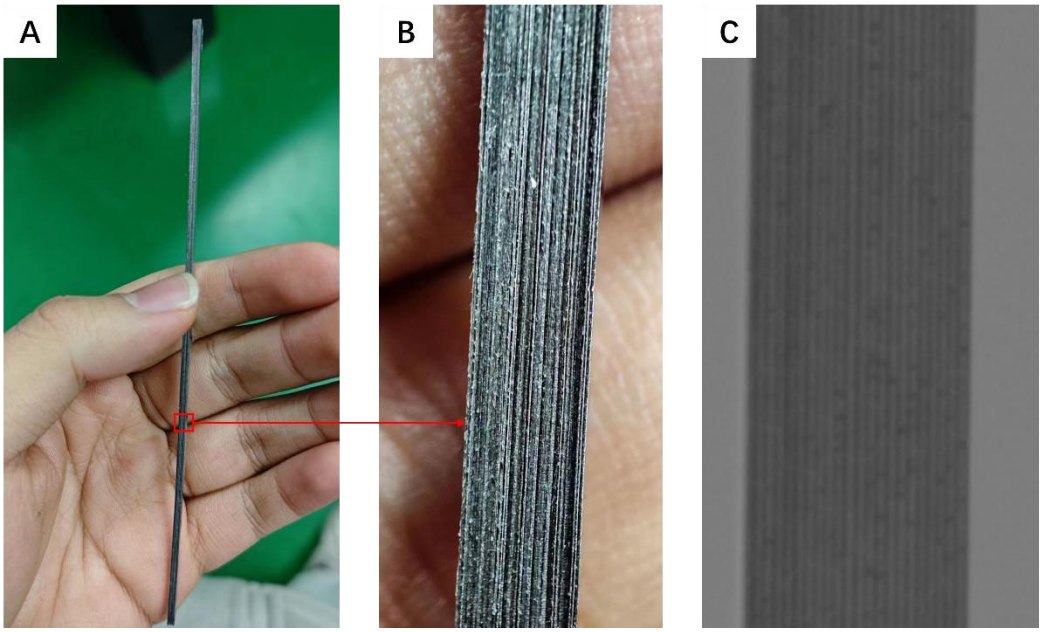

Figure 1: (A) The photo of the sample, (B) Partial magnification of the sample, (C) The sample's absorption image by X-ray.

There are some advantages in this method. Firstly, the area of grating can be large. The length of the grating is given by the length of the foil which is 140mm, the width of the grating depends on the number of layers stacked. Secondly the thickness of tungsten is 1mm which means that more than 90% X-ray can be absorbed for a photon average energy of 57keV, and the hot melt adhesive film is made of organic matter, so the X-ray absorption coefficient is very low which reduces the loss of the visibility. Thirdly, because of the good ductility of the adhesive film, it has the potential to be fabricated into fan-shape to cope with beam divergence, which is important for gratings with high aspect ratio. In our future plan, a sample which has more layers is going to be fabricated, and we will explore the method to fabricate fan-shape gratings.

References

[1] A. Faisal *et al.*, J. Micro/Nanolith. MEMS MOEMS **18**, 1 (2019).
[2] M. Kagias *et al.*, Materials Science in Semiconductor Processing **92**, 73 (2019).
[3] M. Viermetz *et al.*, Proc. Natl. Acad. Sci. U.S.A. **119**, e2118799119 (2022).
[4] K. Wan *et al.*, jjap **47**, 7412 (2008).
[5] H. Wu *et al.*, Jpn. J. Appl. Phys. **60**, 076506 (2021).

Longchao Men,Peiyuan Guo,Jincheng Lu,Li Zhang,Zhentian Wang
Tsinghua University

Please check the attachment

Summary: Conventional dual-energy X-ray imaging is a clinically well-established technology that is used in various imaging applications to improve clinical diagnosis. The properties of dark-field signals and attenuation signals are similar in some aspects. In this work, we experimentally validated the applicability of dual-energy dark-field imaging. We found that the power exponential model of linear diffusion coefficient is satisfied, which lays the foundation for the realization of quantitative identification of material microstructure by dual-energy dark-field imaging.

Introduction: Chronic obstructive pulmonary disease (COPD) is one of the leading causes of death worldwide. In recent years, dark-field imaging has been demonstrated to enable the detection of early-stage lung diseases. By combining spectral and dark-field imaging to take advantage of the energy-dependent scattering properties of the sample, additional information about its subpixel microstructure can be accessed. Kirsten et al. approximated the dark-field linear diffusion coefficient using a power-law and showed the potential of spectral dark-field imaging to differentiate lung pathologies based on simulations[1]. Thorsten et al. considered a diluted suspension of monodisperse microspheres and decomposed samples into two different microstructure materials[2]. Presently, the investigation of spectral X-ray dark-field in the realm of medical diagnostics is in its nascent stages. The goal of our work is to validate the applicability of this technology and eventually to screen and diagnose COPD via spectral dark-field radiology.

Method: This work focuses on grating-based X-ray dark-field imaging with a projective fringe system[3]. In order to simulate the dark-field signal of human lungs in different pathologies, PMMA spheres with different sizes (200μm and 400μm) were selected as samples[4].

Spectral dark-field imaging can be implemented by kVp-switching, dual-layer flat panel detector or photon counting detector. Here we employed sequenced scans with varying tube voltages to acquire spectral dark-field signals. The linear diffusion model of dark-field is defined as[5],

Preliminary results: In the experiment, we selected three different positions， 6.5、21.5、35.5 corresponding position 1 to 3 in figure2(b). The experimental and fitting results are shown below.

As the result shown, the dark-field signal for all materials decreases for increasing kVp and the fitting curve indicates that approximating the line diffusion coefficient to a power-law is appropriate. Variations exist in the dark-field signals across different-sized spheres positioned at the same location. Additionally, at identical energy levels, the dark-field signal is influenced by the specific position, with a notable trend indicating that proximity to G1 intensifies the dark-field signal.

Discussion: In this study, we employed an approximate empirical formula to model the linear diffusion coefficient of the dark-field. Our findings affirm that samples can be differentiated based on variations in the linear diffusion coefficient of the substance at different energy levels, analogous to the principles observed in dual-energy absorption imaging. Subsequent investigations will employ dual-layer flat panel detectors or photon counting detectors to explore spectral X-ray dark-field imaging in experimental settings. A comprehensive examination will be undertaken to elucidate the quantitative relationships between material properties and dark-field signals.

JIncheng Lu[1,2],Peiyuan Guo[1,2],Wenjie Yu[1,2],Runtao Deng[1,2],Li Zhang[1,2],Yongshuai Ge[3],Zhentian Wang[1,2]
1. Tsinghua University
2. Key Laboratory of Particle & Radiation Imaging (Tsinghua University) of Ministry of Education, Beijing
3. Research Center for Medical Artificial Intelligence, Shenzhen Institute of Advanced Technology, Chinese Academy of Sciences, Shenzhen, Guangdong 518055, China

Chronic Obstructive Pulmonary Disease (COPD) claims the lives of 3 million people annually, ranking as the third leading global cause of death. Diagnosis and staging of COPD is crucial to public health. In this work, we utilize the X-ray dual-phase grating imaging system for COPD diagnosis in animal models. By measuring the dark-field signals of PMMA microspheres with specific diameters, we simulate the dark-field signals in the lungs of both normal and COPD mice. This approach aims to explore the potential applicability of this method in the diagnosis and staging of COPD.

Multi-scale imaging in reciprocal space based on X-ray diffraction and small-angle scattering

Wenjie Yu,Yuxiang Xing, Li Zhang, *Zhentian Wang
Department of Engineering Physics, Tsinghua University, China
Email: *wangzhentian@tsinghua.edu.cn*

Summary: This study proposes a methodology for multi-scale imaging in reciprocal space, integrating X-ray diffraction and X-ray small-angle scattering in one, table-top imaging modality. Customized coded apertures are applied to help obtain the diffraction signal precisely in tomographic imaging and the small-angle scattering information is extracted using the grating-based imaging method [1,2]. The methodology proposed in this article can extract both microscopic lattice information and mesoscopic information of the tested sample in radiographic and tomographic imaging, which has great potential in analyzing industrial materials and medical samples [3-7].

With the rapid development of advanced materials science and diagnostic radiology, new requirements have been put forward for imaging the interior of relevant samples, such as meta-material, aeronautical materials, medical samples of diseased tissue etc. Conventional X-ray tomography techniques include X-ray attenuation imaging, and even with advanced phase-contrast imaging and X-ray small-angle scattering imaging (dark-field imaging). It is not possible to obtain information about the crystal lattice structure inside a tested sample. This limitation poses significant challenges in certain application scenarios. For example, in the tomographic imaging of Lithium battery cells, the methods mentioned above are unable to accurately determine the crystal types within the sample.

X-ray diffraction imaging is the only technique capable of obtaining internal crystallographic information of a tested sample. However, this technique typically relies on photons scattered at large angles as diffraction signals, and the photons scattered at small angles are often not fully utilized. In this work, we integrate X-ray diffraction imaging with X-ray small-angle scattering imaging in one imaging system. This integration allows for the simultaneous acquisition of diffraction signals from large-angle scattering and dark-field signals from small-angle scattering [8]. As a result, it becomes possible to obtain crystallographic structure information of each layer inside a tested sample and mesoscopic information at the same time. Though such experimental design can be implemented on synchrotron radiation facilities, to the best of our knowledge it has not been implemented in laboratory conditions. It is noted that the two signals (diffraction signals and dark-field signals) are naturally registered in our configuration, which is of great advantage for imaging.

The schematic diagram of the experimental setup in this work is shown in Figure 1.The device is composed of two main parts: the diffraction imaging part and the small-angle scattering imaging part. A cone beam of X-rays emitted from the X-ray tube is transformed into a fan beam of X-rays after passing through a collimator slit, and it illuminates a cross-section of the object after passing through the grating G0. The tested object receiving the X-rays generates both diffraction signals and small-angle scattering signals.

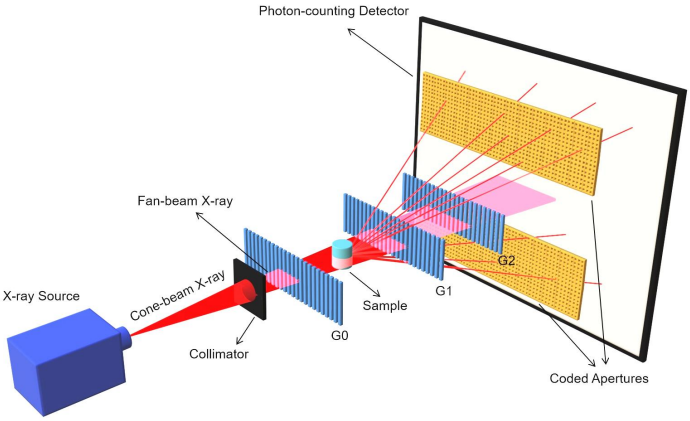

Figure 1: The schematic diagram of the system setup.

Specifically, the diffraction signals pass through two customized coded apertures and received by the detector. In this work, a photon-counting pixelated spectrometer is used, where each pixel can record the number of photons that hit the pixel during the exposure time, together with the energy of each photon. The coded apertures, which are made of gold, allow photons to pass through. Based on the principles of pinhole imaging, it can be accurately known to which object voxel the data collected by each detector pixel belongs, and further, the diffraction spectra of each voxel of the object can be obtained. Simultaneously, the small-angle scattering signals pass through the gratings G1 and G2, and through a phase-stepping approach, the dark-field information of the tested object is obtained [8-10]. Finally, by utilizing the diffraction spectra and dark-field information obtained for each cross-section voxel, the crystal information and mesoscopic information of each slice of the object can be reconstructed.

In order to enhance the reliability and efficiency of the proposed method, reconstruction algorithms will be designed and the system will be optimized. On the basis, the methodology will be tested with different samples, showing its potential in industrial inspection, scientific research, and medical diagnostics.

References

[1] S. Stryker, J. A. Greenberg, S. J. Mccall, et al, X-ray fan beam coded aperture transmission and diffraction imaging for fast material analysis, *Scientific Reports*, **11**(1), 10585, (2021)

[2] K. Liang , L. Zhang , Y. Xing, Method of sparse-view coded-aperture x-ray diffraction tomography, *Physics in Medicine & Biology*, **68**(6), 065008, (2023)

[3] G. Harding, M. Newton, J. Kosanetzky, Energy-dispersive X-ray diffraction tomography Physics in Medicine & Biology, **35**(1): 33 (1990)

[4] S. E. Bohndiek, G. J. Royle, R. D. Speller, An active pixel sensor X-ray diffraction (APXRD) system for breast cancer diagnosis, *Physics in Medicine & Biology*, **54**(11), 3513-27, (2009)

[5] C. Crespy, P. Duvauchelle, V. Kaftandjian, et al, Energy dispersive X-ray diffraction to identify explosive substances: Spectra analysis procedure optimization, *Nuclear Instruments Methods in Physics Research*, **623**(3), 1050-60, (2010)

[6] R. M. Moss, A. S. Amin, C. Crews, et al. Correlation of X-ray diffraction signatures of breast tissue and their histopathological classification, *Scientific Reports*, **7**(1), 12998, (2017)

[7] B. Ghammraoui, J. Tabary, S. Pouget, et al, New software to model energy dispersive X-ray diffraction in polycrystalline materials, *Nuclear Instruments Methods in Physics Research A*, **664**(1), 324-31 (2012)

[8] S. K. Lynch, V. Pai, J. Auxier, et al. Interpretation of dark-field contrast and particle-size selectivity in grating interferometers, *Applied Optics*, **50**(22), 4310-4319, (2011)

[9] M. Strobl, General solution for quantitative dark-field contrast imaging with grating interferometers, *Scientific Reports*, **4**(1), 1-6, (2014)

[10] K. Taphorn, F. De Marco, J. Andrejewski, et al. Grating-based spectral x-ray dark-field imaging for correlation with structural size measures, Scientific Reports, **10**(1), 1-9 (2020)

Phase contrast simulation study based on TTX and VIGAS

JIAYI SUN[1], HAO DING[1], ZHIJUN CHI[2], YINGCHAO DU[1], RENKAI LI[1], WENHUI HUANG[1], * CHUANXIANG TANG[1]

[1]*Department of Engineering Physics, Tsinghua University, China*

[2]*College of Nuclear Science and Technology, Beijing Normal University, China*

Email: *tang.xuh@tsinghua.edu.cn*

Summary: We demonstrate a simulation method of propagation-based phase-contrast imaging (PBI) which is applied to the inverse Compton scattering (ICS) sources. The properties of ICS X/γ-ray source implanted in this study are Tsinghua Thomson scattering X-ray source (TTX), and very compact ICS gamma-ray source (VIGAS) in Tsinghua university. Combining the Monte Carlo simulation and wave optics, we preliminarily explore the potential of gamma-ray PBI for metallic materials with consideration of the partial coherence effect.

The applications of PBI in manufacturing and industry, such as non-destructive testing (NDT), has received increasing attention. However, PBI has been mainly applied in the X-ray region, where the phantom contrast of low-Z material, especially organics, increases dramatically. As for the radiography in the γ-ray region, the spatial resolution is severely limited at the sub-millimeter level for traditional absorption-based imaging using a bremsstrahlung-based gamma-ray source. There is a strong demand for improving the gamma-ray source and corresponding PBI method for high-resolution imaging of metallic materials in NDT.

The rapid development of the compact ICS source during the last decade makes the on-site application possible due to the high spatial coherence and small footprint. Given to its spatial coherence, ICS source is able to extend the applicable energy region of PBI to gamma-ray region. Therefore, the sharp edge enhancement effect in the phantom of relatively high-Z metallic material could be achieved with soft-gamma-ray. Since the maximum cross-section ratio between the phase-shift and the absorption for metallic materials locates in ~100keV-~1MeV energy region, the PBI has the potential to discriminate the material interfaces, which can be used to identify the holes, cracks, etc.

For the above purpose, we developed a PBI simulation method which combined the Monte Carlo simulation and wave optics calculation [1]. With the consideration of finite focal spot, energy dispersion, and other physical properties of the ICS sources, the method can accurately simulate the effect of the source's imperfection on PBI. Our simulation is mainly based on the two ICS sources at Tsinghua University, the Tsinghua Thomson scattering X-ray source (TTX) [2] and the very compact ICS gamma-ray source (VIGAS, under construction) [3], which cover energy range 20-50 keV and 0.2-4.8 MeV respectively. A phantom of concentric tungsten–aluminum spheres is simulated demonstrating the feasibility of gamma-ray PCI for metal samples. Compared to conventional absorption imaging, clear edge enhancement is witnessed in the PCI image, which will facilitate the identification of the material interface.

Acknowledgments

This research is supported in part by the National Natural Science Foundation of China (No. 12027902 and No. 12305163).

References

[1] J.Y. Sun, Z.J. Chi, Y.C. Du, R.K. Li, W.H. Huang, C.X. Tang, A simulation method of gamma-ray phase contrast imaging for metal samples, *Nucl. Instrum. Methods Phys. Res. A*, **1053**, 168321, (2023)
[2] C.X. Tang, W.H. Huang, R.K. Li, Y.C. Du, L.X. Yan, J.R. Shi, Q. Du, P.C. Yu, H.B. Chen, T.B. Du, C. Cheng, Y.Z. Lin, Tsinghua Thomson Scattering X-Ray Source, *Nucl. Instrum. Methods Phys. Res. A*, **608(1)**, S70–74, (2009)
[3] Y.C. Du, H. Chen, H.Z. Zhang, Q. Gao, Q.L. Tian, Z.J. Chi, Z. Zhang, H. Zha, J.R. Shi, L.X. Yan, R. Qiu, C. Cheng, T.B. Du, R.K. Li, H.B. Chen, W.H. Huang, C.X. Tang, A very compact inverse Compton scattering gamma-ray source, *High Power Laser and Particle Beams*, **34**, 104010–104011, (2022)

An efficient ptychography reconstruction strategy through fine-tuning of large pre-trained deep learning model

Xinyu Pan[1,2,†] Shuo Wang[1,2,†] Zhongzheng Zhou[1,2] Liang Zhou[1,2] Peng Liu[1,2] Chun Li[1,3] Wenhui Wang[1,3] Chenglong Zhang[1,2,*] Yuhui Dong[1,2,*] , and Yi Zhang[1,2,4*]

SUMMARY

With pre-trained large models and their associated fine-tuning paradigms being constantly applied in deep learning, the performance of large models achieves a dramatic boost, mostly owing to the improvements on both data quantity and quality. Next-generation synchrotron light sources offer ultra-bright and highly coherent X-rays, which are becoming one of the largest data sources for scientific experiments. As one of the most data-intensive scanning-based imaging methodologies, ptychography produces an immense amount of data, making the adoption of large deep learning models possible. Here, we introduce and refine the architecture of a neural network model to improve the reconstruction performance, through fine-tuning large pre-trained model using a variety of datasets. The pre-trained model exhibits remarkable generalization capability, while the fine-tuning strategy enhances the reconstruction quality. We anticipate this work will contribute to the advancement of deep learning methods in ptychography, as well as in broader coherent diffraction imaging methodologies in future.

Keyword: ptychography, artificial intelligence, imaging techniques, phase reconstruction, neural networks, fine-tuning

INTRODUCTION

X-ray ptychography, a synchrotron coherent imaging technique that is theoretically capable of achieving diffraction-limited resolution, has been widely used in materials[1–3], life sciences[4,5], and other scientific fields[6–8]. Benefiting from the high brightness and excellent coherence nature of next-generation synchrotron sources, ptychography is reaching new levels of application scenarios. For example, the emergence of new ptychography based imaging technologies, including resonant ptychography[9,10], ptycho-tomography[11–13], and in situ ptychography[14,15], allows for multi-dimensional analysis, fine structure study and functional characterization of large-volume samples with improved temporal resolution. Despite the potential of these new ptychography methods, significant challenges remain in the algorithmic and software domain to address their online data analysis requirements[16].

Phase retrieval and ptychographic sample reconstruction are inherently one of the most difficult tasks in synchrotron radiation methodologies. As a relatively time-consuming scanning imaging technique, one of the main goals of ptychography is to achieve real-time analysis. Although the traditional physical reconstruction process is maturely developed[17–23], it is currently difficult to achieve highly precise reconstruction for new high-throughput multidimensional characterizations. Besides, the reconstruction algorithms are limited by numerous deficiencies, such as weak tolerance to interference, sensitivity to initial guesses, and the tendency to fall into local optima which may prevent obtaining a relatively accurate reconstruction. In recent years, Convolutional Neural Networks (CNNs) have achieved remarkable success in the field of image processing, such as image noise reduction[24] , image restoration[25] , image super-resolution[26] and object detection[27] , etc. Due to its efficiency and accuracy, CNN has been gradually adopted in the field of ptychography. Since 2017, CNNs

have obtained good results on ptychography reconstruction[28,29] . Later, PtychoNet[30] and PtychoNN[31] further improved the network architecture and achieved decent results under low overlap rates. In 2022, Welker[32] and others constructed Deep Iterative Projections

[1]Beijing Synchrotron Radiation Facility, Institute of High Energy Physics, Chinese Academy of Sciences, Beijing 100049, China

[2]University of Chinese Academy of Sciences, Beijing 100049, China

[3]Spallation Neutron Source Science Center, Dongguan, Guangdong, 523803, China

[4]Lead Contact

[†]These authors contributed equally to this work: X. P. and S. W.

[*] Correspondence and requests for materials should be addressed to:

C. Z. (zhangcl@ihep.ac.cn), Y. D. (dongyh@ihep.ac.cn), or Y. Z. (zhangyi88@ihep.ac.cn)

(DIP) neural network after analyzing the similarities between the speech signal processing domain and Ptychography, which better reconstructed the simulated objects. Recently, deep learning has also made significant progress in Ptycho-Tomography and dose reduction[33,34].

The aforementioned approaches focus on network architecture and methods optimization, aiming to obtain better reconstruction quality and effectiveness. In the realm of deep learning, significant advancements have been made in natural language processing (NLP) and computer vision (CV) through the utilization of data-driven large-scale models. These models leverage vast amounts of high-quality data to enable neural networks to learn the underlying data logics, accelerating the development of pre-trained models. Notably, pre-trained models have demonstrated remarkable performance across diverse downstream tasks, as evidenced by the success of models like ChatGPT and other language-based architectures[35,36]. In addition, for different downstream tasks, the fine-tuning approach leads to targeted tuning of the pre-trained model to obtain better performance. For example, the fine-tuning based on LLaMA pre-training model leads to increased performance in cross-language applications involving Chinese[37]. Looking ahead, the advent of fourth-generation synchrotron light sources would generate enormous volume of data for coherent diffraction imaging[38], which provides a unique opportunity to explore the application of large-scale models in the field of coherent diffraction, particularly when tackling challenges related to reconstruction. By leveraging the potential of training big models in this field, we can harness the power of data-driven approaches to enhance the effectiveness of coherent diffraction imaging techniques.

While deep learning algorithms have made significant progress in the field of coherent diffraction imaging, existing neural networks still require continuous optimization and improvement to achieve better performance in Ptychography as data volume continue to scale up. In this paper, to enhance the performance of neural networks in Ptychography, we first propose a lightweight and efficient network model (PtyNet-S). This model serves as a foundation that can be further improved to larger model (PtyNet-B) to accommodate larger-scale data training, thereby providing more accurate and robust reconstructions. Then, we introduce a novel fine-tuning method based on the pre-trained neural network model. This fine-tuning approach leads to better reconstruction quality and yields favorable results across different overlap rates. By leveraging the advantages of both pre-training and fine-tuning, our method presents a promising approach to the advancement of Ptychography.

RESULTS

Architectural improvements of small neural network

By using CNN to recover ptychography images, PtychoNN and PtychoNet has made substantial progress. Motivated by this, we designed a lightweight and effective convolutional network architecture named PtyNet-S. The main structure of the proposed PtyNet-S is shown in Fig. 1. In practice, we use group convolution instead of the two-branch decoder structure from PtychoNN. Group convolution allows different convolution kernels to extract information efficiently from different feature maps without affecting each other (see Architecture of neural networks in Methods for details). This approach avoids the excessive computational resources associated with double branching and also reduces the number of parameters in the model. The input to the model is a single diffraction pattern, and the output is the amplitude and phase of the reconstructed object corresponding to the diffraction pattern. When testing on the open-source dataset, PtyNet-S shows better phase reconstruction performance with only 320,000 parameters comparing to PtychoNN which has 1.2 million parameters (see Tab. 1 for details).

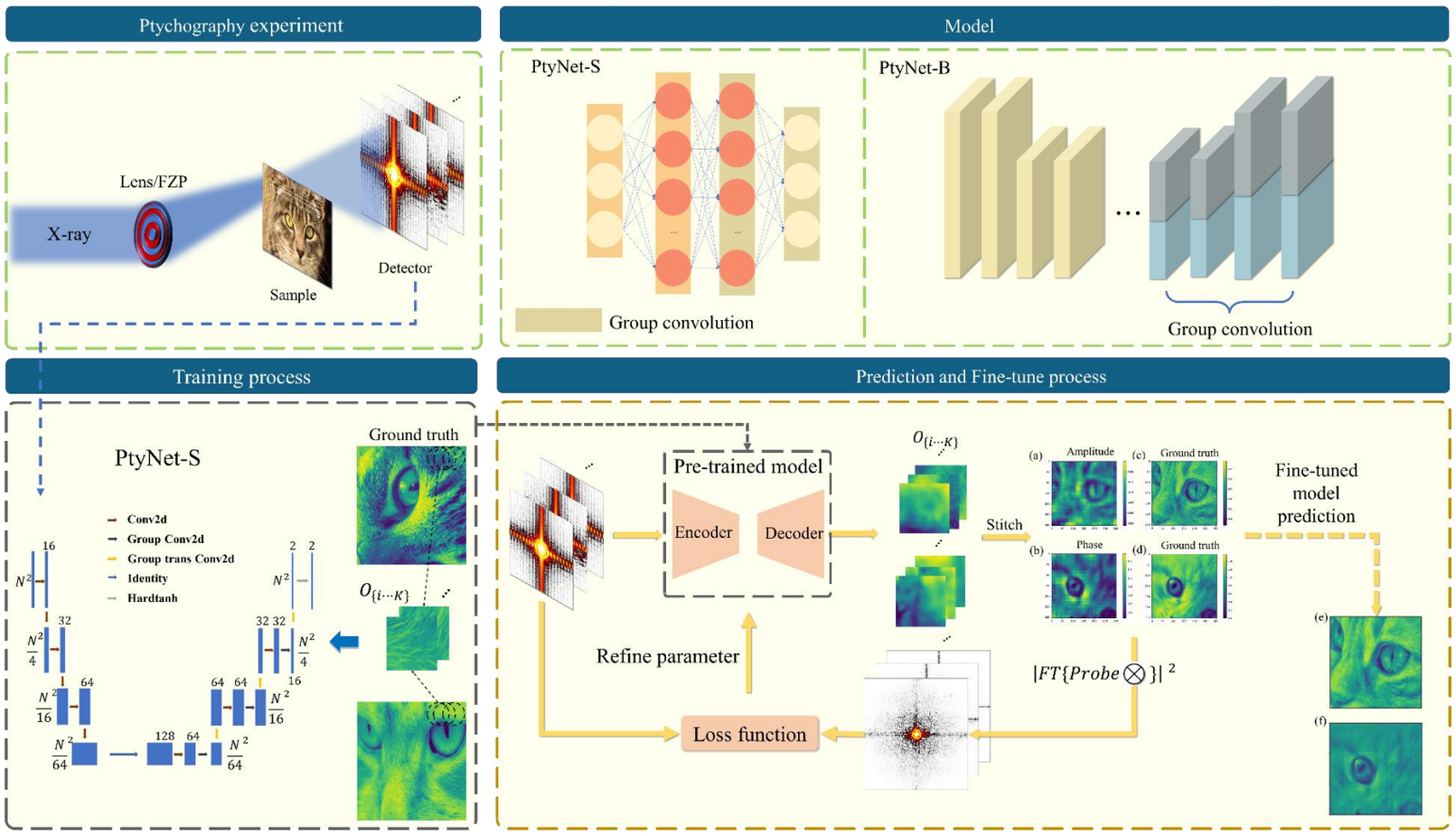

Fig. 1 This figure illustrates the essential stages in the PtyNet-S workflow, encompassing training, prediction, and fine-tuning. (a) and (b) in prediction and fine-tune process part depict the outcomes of PtyNet-S in reconstructing both amplitude and phase, while (c) and (d) showcase the distributions of simulated objects. PtyNet-S undergoes supervised training, relying on real object distributions as its foundation. After training, the model can predict corresponding amplitude and phase distributions for the input diffraction pattern at each scanning position. These predictions are subsequently stitched to generate the final distribution prediction. The fine-tuning process involves updating the neural network model using diffractograms obtained from known probes and get better reconstruction results.

We trained the PtyNet-S network using a small simulated training dataset (see Methods for details on training) and then put the cat face data from the test dataset into PtyNet-S for inference prediction after data preprocessing. The obtained experimental results are shown in Fig. 1. The neural network learns the mapping relationship F_θ from the diffraction domain to the real data domain, and the real-time online processing of the Ptychography experiment can be performed due to the lightweight design of the network.

It can be seen from Fig. 1 that the neural network can learn the mapping process from the diffraction to the real object. During the convolution process, the high frequency information of the data is lost and the low frequency information is retained which is thus recovered by the decoder. The artifacts showing pixelated effects are caused by the network's limitations when predicting final results with absolute accuracy, and by the stitching process(see Supplementary Information Fig. S7). This is mainly because that the detailed texture of the cat face data is too complex, and for scans of similar regions, the results predicted by the network will behave differently in the distribution of high frequency regions, while with little difference in the distribution of low frequency regions. This will lead to inconsistency in the overlapping regions of the scans predicted by the neural network, and the grid artifacts will appear after the stitching process.

Benchmark with previous models*:* to compare the difference between PtyNet-S, PtychoNet, and PtychoNN, we use the same training strategy and testing dataset to measure the effectiveness and accuracy of both models. The public experimental dataset[31] measured on tungsten sample which has been published in the PtychoNN paper. As shown in Fig. 2. Meanwhile, we compared the deviation of the three models on the experimental data, the number of model parameters, the computational resource utilization ratio, and the amount of the graphics memory occupied by the models, are shown in Tab. 1, which shows that PtyNet-S yields better results. In addition we also compared the ROI of the simulated data reconstruction results, as detailed in the Supplementary Information.

Tab. 1 Performance comparison of the three models on the same dataset.

	Parameters/Thousand	MSE(Phase)	Computational resource ratio (A100)/%	GPU memory/GB
PtychoNN	5512	0.0885	86%	2.7
PtychoNet	1247	0.1633	80%	2.3
PtyNet-S	**325**	**0.0852**	**46%**	**2.0**

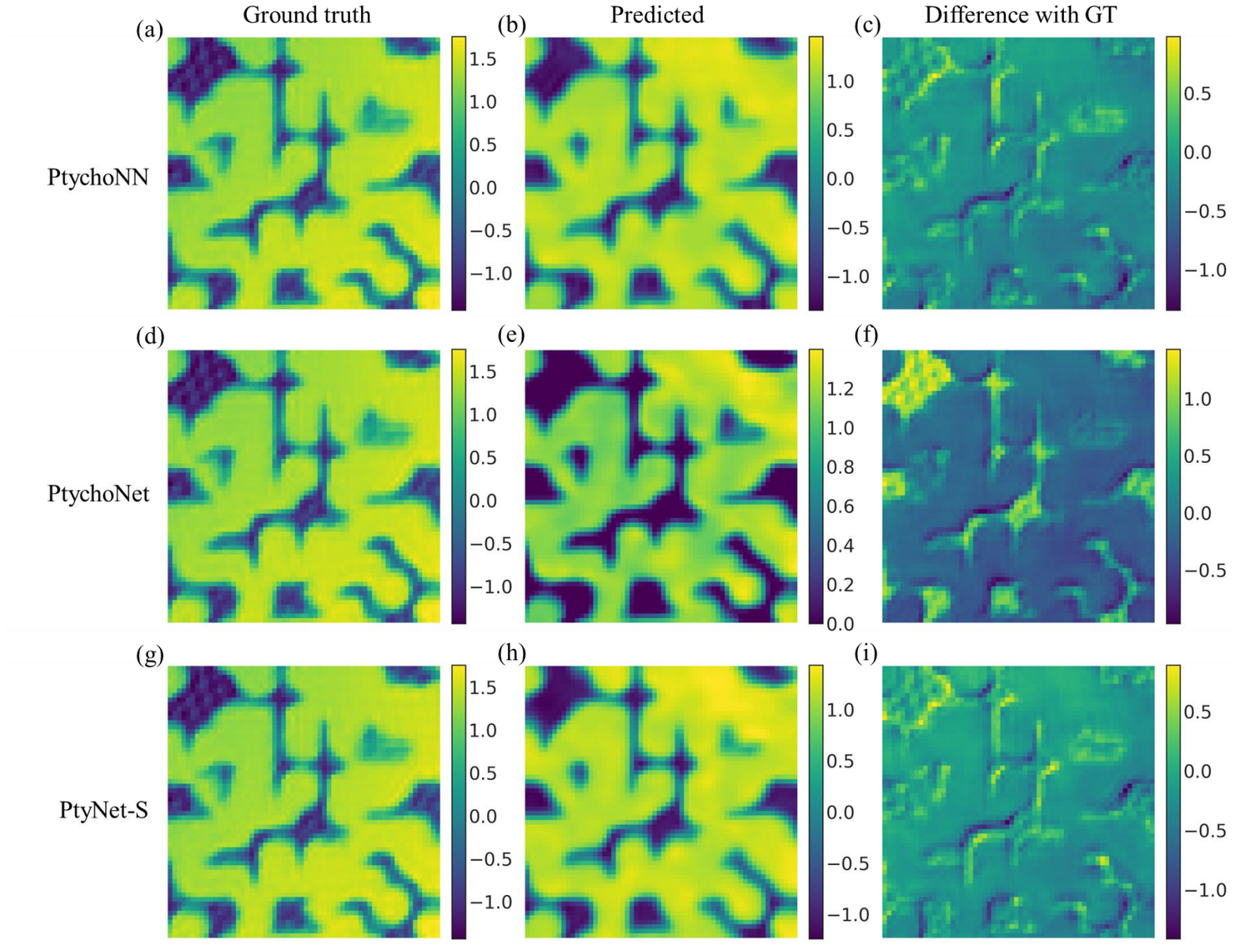

Fig. 2 Phase reconstruction results of the three models in tungsten test pattern. PtyNet-S and PtychoNN have similar performance, and both predict better than PtychoNet, while the PtychoNet predicts better on the sample profile.

Pre-trained models and generalization capabilities

As shown in Fig. 1 and Fig. 2, the model has good generalization ability even with a small dataset, which has the potential to build a pre-trained model with large dataset in the field of ptychography and even extent to general coherent X-ray diffraction methods. In recent years, the excellent performance of neural networks in the image processing domain highly depends on the growth of scale of the network parameters, as well as the amount and quality of data. For example, the SAM[39] introduced by Meta AI uses data comprising as much as 1.1 billion images and have 10 billion parameters(base model), showing excellent segmentation results. The results of SAM demonstrate that pre-trained networks by using large dataset have strong representational capacity. The improvement on quality and quantity of the data also requires the neural network be able to extract to the feature of more input data, and an increase of model size is an effective way to improve the performance. Therefore, further improved the architecture of PtyNet-S and build a larger pre-trained PtyNet-B using simulated data to achieve better reconstruction results. To accommodate the large amount of data (about 60000 diffractions), we modified the convolutional, downsampling and upsampling layers of PtyNet-B (Fig.S5). Besides, we investigated the reconstruction performance of PtyNet-B by varying the overlap rates (75%, 50%, 25%, 0%) in the production of the simulated data .

With the improved network architecture, the PtyNet-B has more parameters and can learn more of the intrinsic logic of the data. As shown in Fig. 3 and Tab.2, the performance of the PtyNet-B is improved compared to the previous PtyNet-S in all overlap rates. However,

during the convolution process, there are still some extents of loss in high frequency information even use PtyNet-B, while the low frequency information is retained and can be recovered subsequently by the decoder (see Supplementary Information Fig. S8 for visualisation).

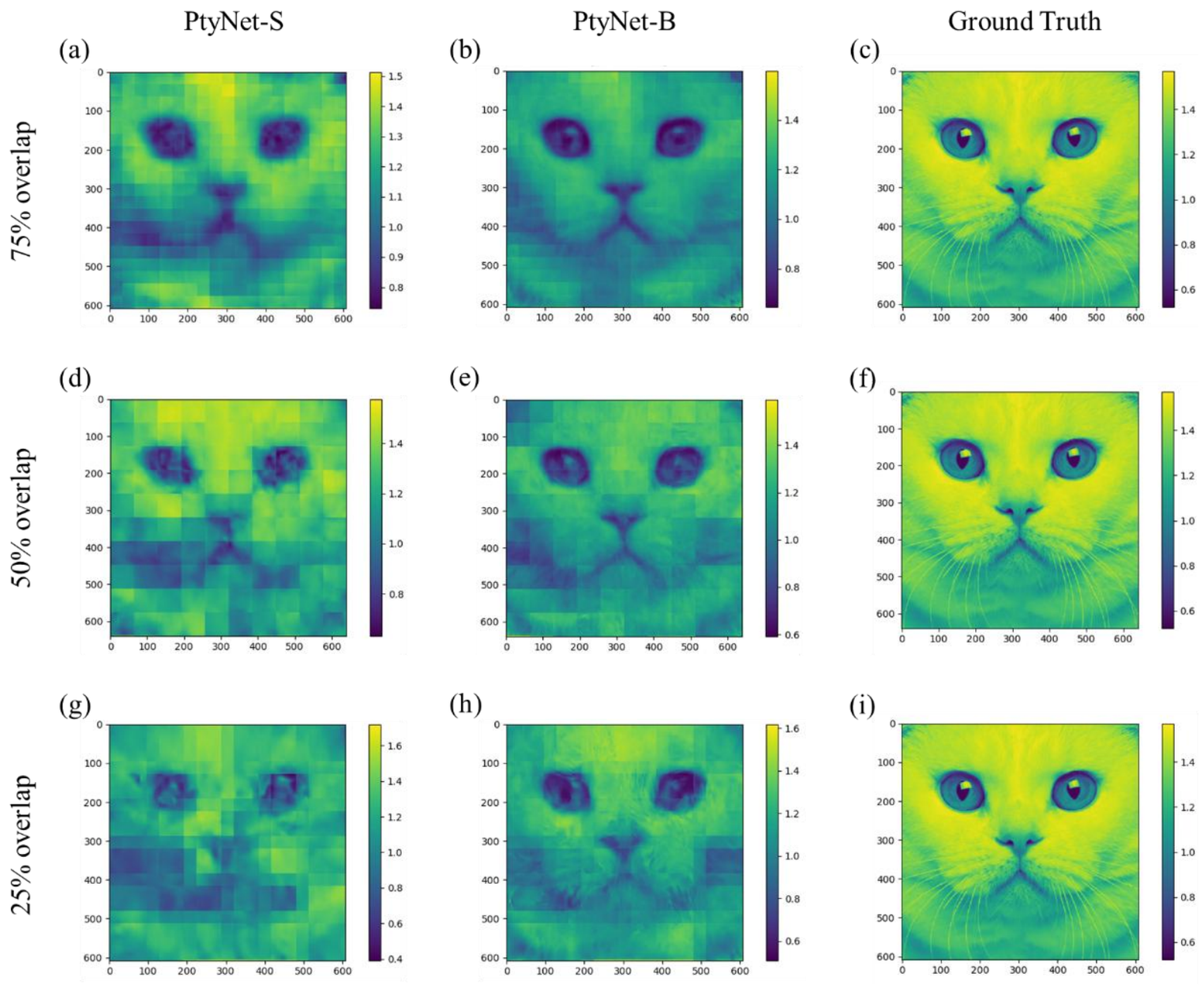

Fig. 3 Results of the prediction of the phases in the testing set using the PtyNet-S and PtyNet-B with different overlap rates. A-C, D-F, and G-I are the results of stitched results after PtyNet-S prediction, the results of stitched results after PtyNet-B prediction, and ground truth, respectively.

Tab. 2 Performance comparison of PtyNet-S and PtyNet-B

Model	% Overlap								
	75			50			25		
	PSNR	SSIM	MSE	PSNR	SSIM	MSE	PSNR	SSIM	MSE
PtyNet-S	**12.919**	0.793	0.010	**14.349**	**0.816**	**0.011**	12.353	0.791	0.041
PtyNet-B	12.419	**0.802**	**0.009**	12.434	0.799	0.021	**12.933**	**0.797**	**0.025**

Fine-tuning results

In the field of deep learning, specific downstream tasks such as medical image segmentation can be tackled by leveraging fine-tuning techniques that pre-train the model. The pre-training allows the model to acquire generalized knowledge, which can then be adapted to boost performance on the target task during fine-tuning. Through this transfer learning approach, the model's capabilities on specialized downstream applications can be significantly improved, yielding higher accuracy compared to training from scratch.

We use the pre-trained PtyNet-B as the initialization for fine-tuning. The image quality is optimized by fine-tuning for different

objects (see Methods for details of the fine-tuning process). We randomly select a cat face image in the testing dataset as the amplitude and phase (the reason for not using two randomly selected images is that the distribution of amplitude and phase of the samples is consistent in the experiment), and the results obtained by fine-tuning the scanned data with different overlap rates are shown in Fig. 4.

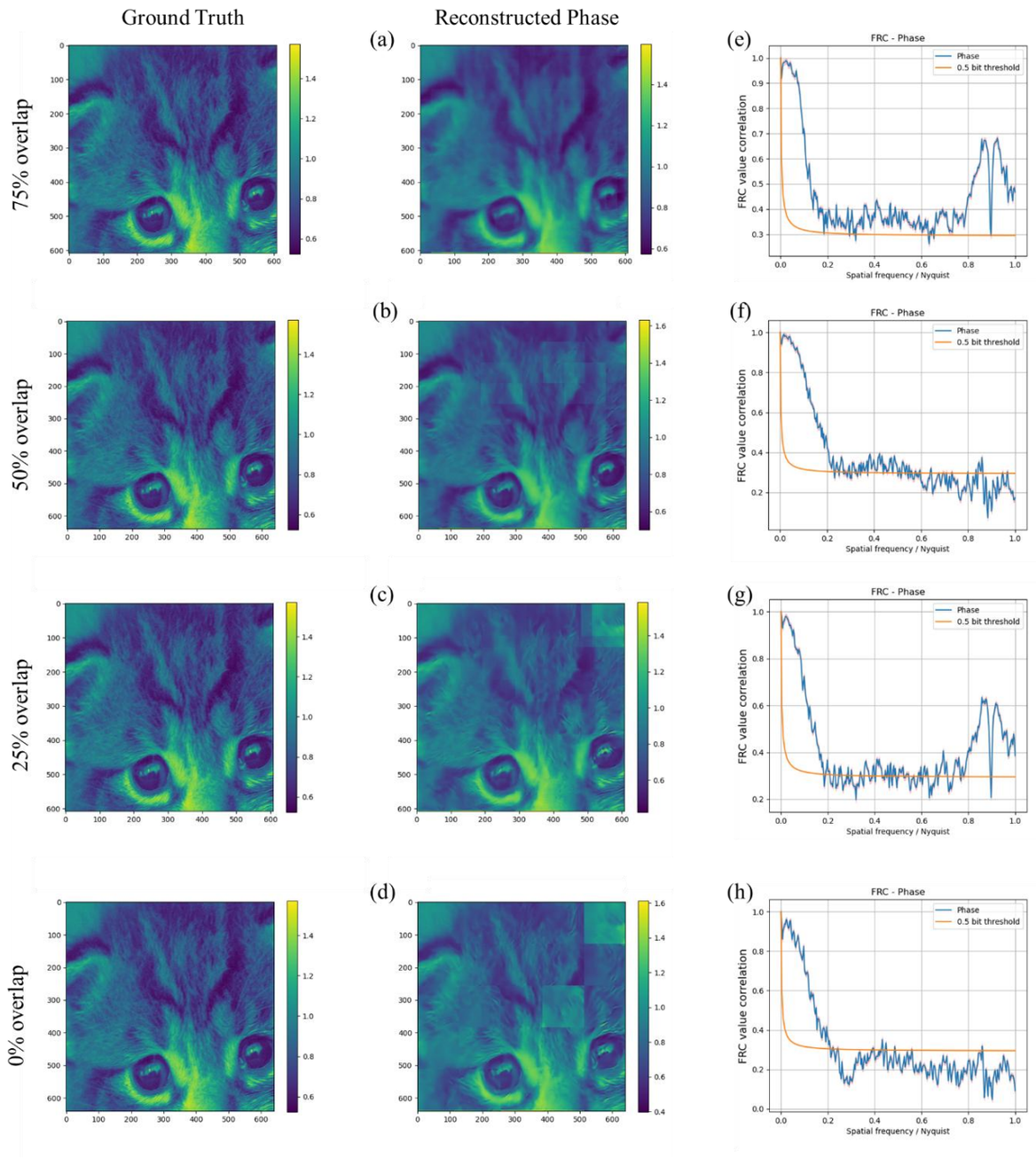

Fig. 4 Results of fine-tuning phase for different overlap rates. (a)-(d) show the results of fine-tuning the neural network with different overlap rates. (e)-(h) show the corresponding Fourier ring correlation (FRC) curves.

As illustrated in Fig. 4, the fine-tuning method can improve better prediction of the neural network for different samples and it also has good prediction results at low overlap rates. In the FRC curves in (e)-(g) of Fig. 4, there are peaks in the high frequency region. We believe this is due to various factors affecting the accuracy of the neural network reconstruction, such as those caused by the stitching method. As a result, the final object obtained presents tile-shaped artifacts locally, which may cause the peak in the FRC curves. In addition, at the highest overlap rate of 75%, the input diffraction pattern is 256×128×128, and it took about less than 90 s to fine-tune all the parameters of the neural network (with a single Nvidia A100 GPU). In order to verify the capability of the fine-tuning method on different types of data, we used both simulated data (human face) and experimental data[40] (fluid catalytic cracking catalyst particle, FCC)for testing. Using a 50% scanning overlap rate and regular raster scan method, a total number of 81 diffraction patterns (256×256 pixels) are acquired from the simulated human face. Using a 51% scanning overlap rate and Fermat spiral trajectory scan method, a total number of 2347 diffraction patterns (512×512 pixels) are acquired in the experiment.

It is worth noting that when using the FCC particle data for fine-tuning, we only used the initial guess probes in the fine-tuning process because the real probes are not given in the public dataset (only the initial guess probes) and the probes reconstructed by rPIE are not ideal. The results in Fig. 5 show that the fine-tuning method can still obtain good reconstruction results for datasets of different types and sizes. We noted that the results reconstructed after fine-tuning all the data are worse than those reconstructed after fine-tuning half the data. We believe this is because for the same number of fine-tuning epochs, reducing the amount of data by half allows the neural network to fit to the features of the samples faster thus allowing for a reduction in the overlap rate limitation. Also less data allows the

network to learn higher frequency information in more epochs to recover the details of the sample. The training using large amount of data can give the model good generalization ability and initialization, while the fine-tuning method allows the model to learn in detail for different data types, and improves the generalization ability even further.

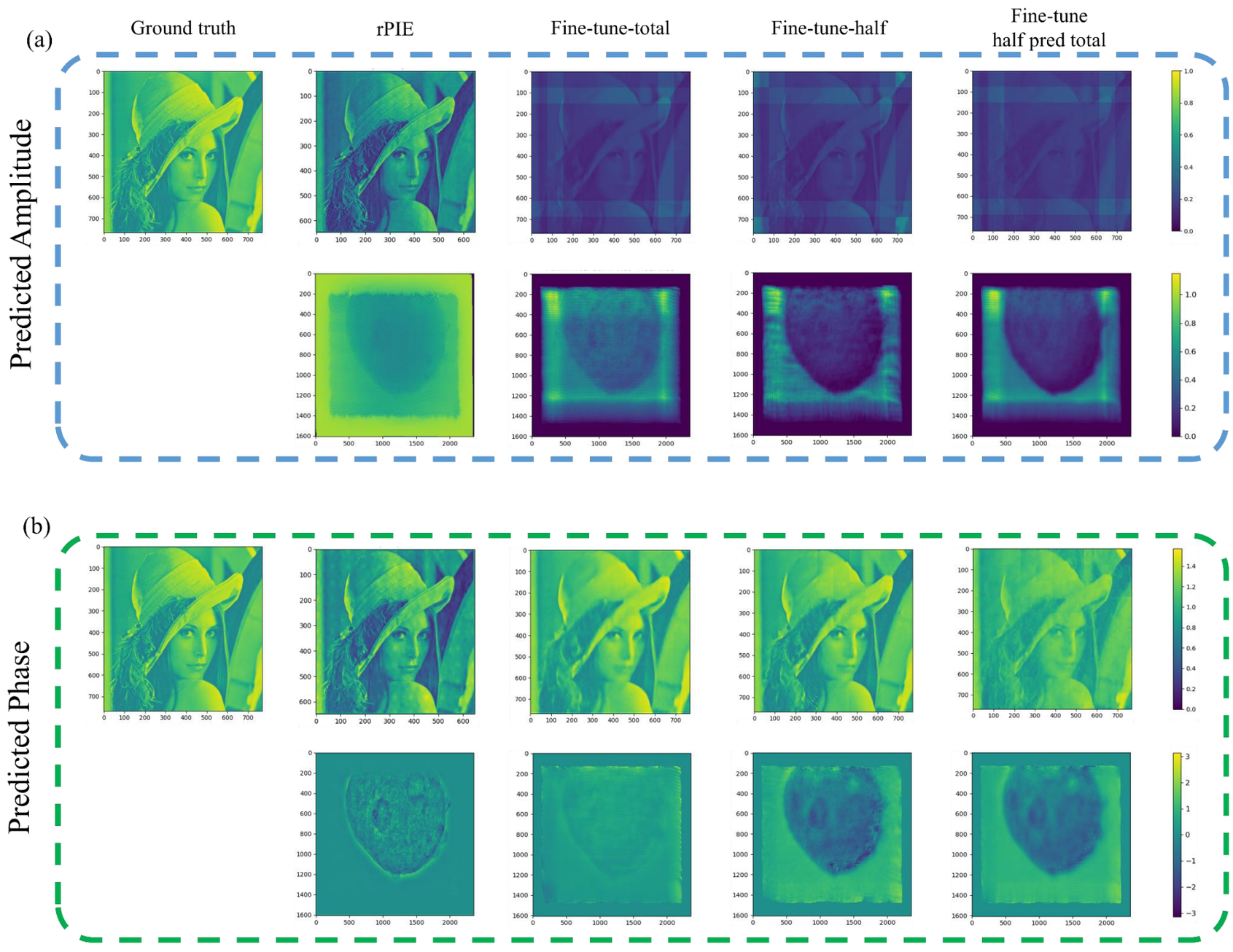

Fig. 5 Results of 400 epochs of fine-tuning using neural networks for different data types. (a) shows the amplitude results predicted by the model after fine-tuning. (b) shows the phase results predicted by the model after fine-tuning. Fine-tune-total indicates that all the data were fine-tuned. Fine-tune-half indicates that half of the data were fine-tuned to further reduce the overlap. Fine-tune half pred total indicates that the model with half of the data fine-tuned was used to predict the entire dataset.

DISCUSSION

Noise interference. In ptychography experiments, due to the small focusing probe size and large photon counts on the detector, the Gaussian noise in the detector background does not have a significant impact on the signal, while the effect of Poisson noise cannot be ignored. Since the self-encoder of the convolutional neural network has a natural tolerance to high frequency noise, we added Poisson noise to the data. We also considered the probe with a focus shift of about 5 μm in the object plane to better emulate real experimental scenarios. The results are shown in Fig. 6.

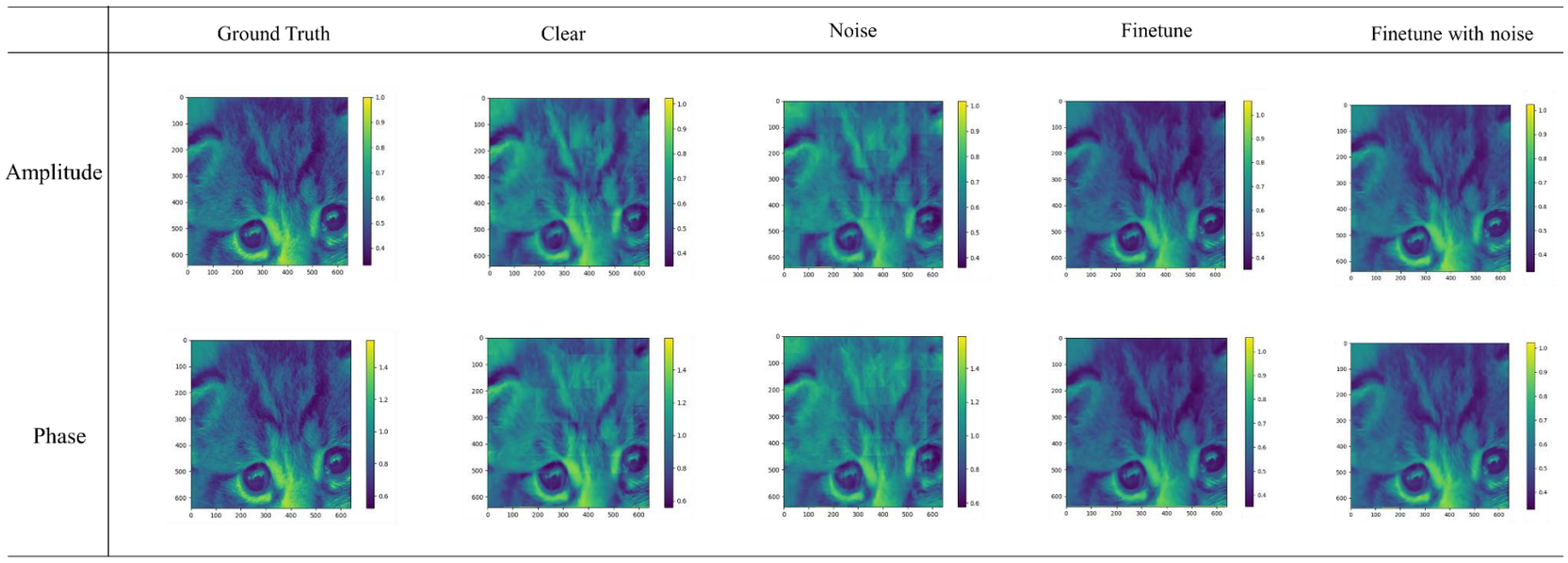

Fig. 6 Reconstruction results of PtyNet-B in noiseless and noisy conditions.

Tab. 3 Noise influence without and with fine-tuning on model performance

Poisson Noise	Ground Truth			Clear			Noise			Finetune with clear			Finetune with noise		
	PSNR	SSIM	MSE	PSNR	SSIM	MSE	PSNR	SSIM	MSE	PSNR	SSIM	MSE	PSNR	SSIM	MSE
Amplitude	\	1	0	**19.603**	**0.714**	**0.005**	17.710	0.689	0.009	22.714	0.753	0.002	**25.312**	**0.756**	**0.001**
Phase	\	1	0	**17.694**	**0.691**	**0.009**	16.384	0.670	0.013	22.713	0.748	0.002	**25.314**	**0.764**	**0.001**

The test results show that the neural network has strong robustness under the influence of noise. However, the fine-tuning results in Tab.3 with noise are better than the results without noise. This is because the neural network mainly recovers low and medium frequency information, and the high frequency information is largely lost under the effect of convolution after mixing with noise. And in the result with noise, the high frequency information corresponds to most of the distortion.

The noise can destroy the high frequency signal and make traditional algorithms fail to reconstruct the high-resolution components. Neural networks can reconstruct the low and medium frequency information better, while the deficiency in high frequency information reconstruction is still not resolved sufficiently. In the future, the solution of noise is one of the key factors to obtain high quality reconstruction in ptychography. The influence of noise in neural networks and how optimization can be done in noise presence is a focus of our future endeavor.

Probe issues. In Results section, fine-tuning improves the quality of the final neural network reconstruction. However, during the fine-tuning process (shown in the Fig. 7), the neural network requires known probes as input, which is only available in simulation. In real experimental situations, the probes are usually not readily available. Therefore, the fine-tuning technique needs to obtain the distribution of probes in advance. Unfortunately, the size and shape of the probe may change during the experiment due to instrumentation instabilities, position errors, and other unpredictable factors. The fine-tuning strategy can be applied if it is possible to use a standard sample to measure the probe in advance of the experiment, and it is assumed that the probe will not change after changing the sample to be measured. In the future, we will explore how to add adaptively tunable probes to the neural network and how to update the probes based on the results of the model.

设置格式[新宇 潘]: 字体颜色: 背景 2

High-dimensional ptychography expansion. All the experiments and methods discussed above are for the reconstruction of two-dimensional objects. However, the thickness of samples for ptychography often cannot be ignored. To obtain a higher resolution, multi-slice reconstruction is required. Although some multi-slice reconstruction methods are already available[41–43], there still remain concerns. For example, there are no definitive criteria on the number of slices and the thickness of the slices needed for multi-slice model reconstruction. The existing Ptycho-Tomography and Resonant Ptychography techniques face problems such as low-resolution projection reconstruction and expensive computational cost. Although our deep learning method has good extensibility, the extension to high-dimensional ptychography is another research direction.

Conclusions

We proposed two neural network architectures: PtyNet-S and PtyNet-B. PtyNet-S reduces memory usage and calculations through optimized design with better performance. It demonstrates good in reconstructing phase information. Building on PtyNet-S, PtyNet-B further expands the model scale and enhances the architecture. By increasing training data five times, PtyNet-B significantly improves final reconstruction quality across varying overlap rates. Finally, we use a fine-tuning approach to further improve the reconstruction quality, achieving satisfactory resolution. We also discuss the influence of noise on the neural network and the effect of probes in the fine-tuning methods. In the proposed reconstruction method, no prior knowledge of overlap is added. Compared with traditional algorithms, deep learning methods can reconstruct relatively better results even at low overlap rates. If it is used as a prior process to support the initial guessing of traditional algorithms, even higher efficiency and accuracy can be obtained. We believe a better applicable pre-training model can be obtained by supervised learning method using high quality reconstructed experiment data. The fine-tuning strategy is then applied to further increase the reconstruction resolution of data collected at various experimental scenarios (varied sample and probes). In the future, the fast prediction of neural networks can greatly improve the experimental efficiency in the data processing of Ptychography experiments where a huge amount of data are present. In combination with existing software packages such as PyNX[44], Ptypy[45], etc., it is also applicable to accelerate the computation process for these traditional algorithms to achieve real-time online analysis on Ptychography experimental results.

Limitation of the study

In this study, we propose a strategy for pre-training and fine-tuning ptychography data, aiming to enhance the efficiency and quality of ptychography reconstruction. We introduce an improved neural network model, PtyNet-S, which demonstrates the potential to achieve these improvements. Moreover, by expanding the model parameters, PtyNet-B can serve as a reliable pre-training model, offering a robust initialization for the subsequent fine-tuning process. The pre-training model also exhibits some degree of generalization ability. The limitation of the current study mainly lies in the fact that relying on single probe and distribution of similar pictures for training data restricts network generalization ability. For instance, the pre-training process is limited to cat faces as the training dataset, and the probes are constrained to a specific parameter setting. This may result in a weaker ability of the pre-trained model to generalize and learn mappings, which can be addressed by incorporating greater data diversity. Additionally, our fine-tuning strategy necessitates the use of known probes, which can lead to potentially significant different of diffraction data between the fine-tuned and pre-trained probes. This disparity in data may result in a resolution degradation(e.g., FCC data). However, we recommend customizing the training model to the specific beamline station and incorporating data from different probes during training. Furthermore, automating the loading of different probes for fine-tuning can help alleviate the aforementioned challenges.

STAR★METHODS

Detailed methods are provided in the online version of this paper and include the following:

- **KEY RESOURCES TABLE**
- **RESOURCE AVAILABILITY**
  - **Lead contact**
  - **Materials availability**
  - **Data and code availability**
- **METHOD DETAILS**
  - **Reconstruction principle of ptychography by neural network**
  - **Data simulation**
  - **Architecture of neural networks**
  - **Network training**

- **Fine-tuning method**
- **Integration with traditional algorithms**

SUPPLEMENTAL INFORMATION

Supplemental information can be found online at XXX

ACKNOWLEDGEMENTS

This work was funded by the National Science Foundation for Young Scientists of China (Grant No. 12005253; No. 12205328), the Strategic Priority Research Program of Chinese Academy of Sciences (XDB 37000000), and the Innovation Program of the Institute of High Energy Physics, CAS (No. E25455U210).

AUTHOR CONTRIBUTIONS

Y. Z., Y. D. initiated the idea and supervised the whole project. X. P. proposes deep learning methods and strategies. S. W. is responsible for comparing traditional algorithms with deep learning methods. C. Z accelerates the whole algorithmic process. Z. Z. proposes optimization strategies for the algorithms. L. Z, C. L, P. L., W. W. are responsible for proofreading and revising the article.

DECLARATION OF INTERESTS

The authors declare no competing interests.

INCLUUSION AND DIVERSUTY

We support inclusive, diverse, and equitable conduct of research.

References

1. Baier, S., Damsgaard, C.D., Scholz, M., Benzi, F., Rochet, A., Hoppe, R., Scherer, T., Shi, J., Wittstock, A., and Weinhausen, B. (2016). In situ ptychography of heterogeneous catalysts using hard X-rays: high resolution imaging at ambient pressure and elevated temperature. Microscopy and Microanalysis *22*, 178–188.

2. Ihli, J., Levenstein, M.A., Kim, Y.-Y., Wakonig, K., Ning, Y., Tatani, A., Kulak, A.N., Green, D.C., Holler, M., and Armes, S.P. (2020). Ptychographic X-ray tomography reveals additive zoning in nanocomposite single crystals. Chemical science *11*, 355–363.

3. Xu, H., Xu, W., Wang, S., and Wu, S. (2018). Semi-symmetric cryptosystem for complex-valued object via single-shot ptychography and random modulus decomposition. Journal of Optics *20*, 095702.

4. Bhartiya, A., Batey, D., Cipiccia, S., Shi, X., Rau, C., Botchway, S., Yusuf, M., and Robinson, I.K. (2021). X-ray ptychography imaging of human chromosomes after low-dose irradiation. Chromosome Research *29*, 107–126.

5. Zhou, L., Song, J., Kim, J.S., Pei, X., Huang, C., Boyce, M., Mendonça, L., Clare, D., Siebert, A., and Allen, C.S. (2020). Low-dose phase retrieval of biological specimens using cryo-electron ptychography. Nature communications *11*, 1–9.

6. Jiang, Y., Chen, Z., Han, Y., Deb, P., Gao, H., Xie, S., Purohit, P., Tate, M.W., Park, J., and Gruner, S.M. (2018). Electron ptychography of 2D materials to deep sub-ångström resolution. Nature *559*, 343–349.

7. Chen, Z., Odstrcil, M., Jiang, Y., Han, Y., Chiu, M.-H., Li, L.-J., and Muller, D.A. (2020). Mixed-state electron ptychography enables sub-angstrom resolution imaging with picometer precision at low dose. Nature communications *11*, 1–10.

8. Chang, C., Pan, X., Tao, H., Liu, C., Veetil, S.P., and Zhu, J. (2021). 3D single-shot ptychography with highly tilted illuminations. Optics Express *29*, 30878–30891.

9. Ihli, J., Diaz, A., Shu, Y., Guizar-Sicairos, M., Holler, M., Wakonig, K., Odstrcil, M., Li, T., Krumeich, F., and Müller, E. (2018). Resonant ptychographic tomography facilitates three-dimensional quantitative colocalization of catalyst components and chemical elements. The Journal of Physical Chemistry C *122*, 22920–22929.

10. Fevola, G., Jørgensen, P.S., Verezhak, M., Slyamov, A., Crovetto, A., Balogh, Z.I., Rein, C., Canulescu, S., and Andreasen, J.W. (2020). Resonant x-ray ptychographic nanotomography of kesterite solar cells. Phys. Rev. Research *2*, 013378. 10.1103/PhysRevResearch.2.013378.

11. Chang, H., Enfedaque, P., and Marchesini, S. (2019). Iterative Joint Ptychography-Tomography with Total Variation Regularization. In 2019 IEEE International Conference on Image Processing (ICIP) (IEEE), pp. 2931–2935. 10.1109/ICIP.2019.8803022.

12. Venkatakrishnan, S.V., Farmand, M., Yu, Y.-S., Majidi, H., van Benthem, K., Marchesini, S., Shapiro, D.A., and Hexemer, A. (2016). Robust X-Ray Phase Ptycho-Tomography. IEEE Signal Process. Lett. *23*, 944–948. 10.1109/LSP.2016.2562504.

13. Shirani, S., Cuesta, A., Morales-Cantero, A., Santacruz, I., Diaz, A., Trtik, P., Holler, M., Rack, A., Lukic, B., Brun, E., et al. (2023). 4D nanoimaging of early age cement hydration. Nat Commun *14*, 2652. 10.1038/s41467-023-38380-1.

14. Grote, L., Seyrich, M., Döhrmann, R., Harouna-Mayer, S.Y., Mancini, F., Kaziukenas, E., Fernandez-Cuesta, I., A. Zito, C., Vasylieva, O., Wittwer, F., et al. (2022). Imaging Cu2O nanocube hollowing in solution by quantitative in situ X-ray ptychography. Nat Commun *13*, 4971. 10.1038/s41467-022-32373-2.

15. Grote, L., Hussak, S.-A., Albers, L., Stachnik, K., Mancini, F., Seyrich, M., Vasylieva, O., Brückner, D., Lyubomirskiy, M., Schroer, C.G., et al. (2023). Multimodal imaging of cubic Cu2O@Au nanocage formation via galvanic replacement using X-ray ptychography and nano diffraction. Sci Rep *13*, 318. 10.1038/s41598-022-26877-6.

16. Xinyu Pan, Xiaoxue Bi, Dong Zheng, Geng Zhi, Han Xu, Yi Zhang, Yuhui Dong, and Chenglong Zhang (2023). Review of development for ptychography algorithm. Acta Physica Sinica *72*, 114–134. 10.7498/aps.72.20221889.

17. Rodenburg, J.M., and Faulkner, H.M.L. (2004). A phase retrieval algorithm for shifting illumination. Appl. Phys. Lett. *85*, 4795–4797. 10.1063/1.1823034.

18. Maiden, A.M., Humphry, M.J., Sarahan, M.C., Kraus, B., and Rodenburg, J.M. (2012). An annealing algorithm to correct positioning errors in ptychography. Ultramicroscopy *120*, 64–72. 10.1016/j.ultramic.2012.06.001.

19. Maiden, A.M., and Rodenburg, J.M. (2009). An improved ptychographical phase retrieval algorithm for diffractive imaging. Ultramicroscopy *109*, 1256–1262. 10.1016/j.ultramic.2009.05.012.

20. de Beurs, A., Loetgering, L., Herczog, M., Du, M., Eikema, K.S.E., and Witte, S. (2022). aPIE: an angle calibration algorithm for reflection ptychography. Opt. Lett. *47*, 1949–1952. 10.1364/OL.453655.

21. Maiden, A., Johnson, D., and Li, P. (2017). Further improvements to the ptychographical iterative engine. Optica *4*, 736. 10.1364/OPTICA.4.000736.

22. Rong, L., Tan, F., Wang, D., Zhang, Y., Li, K., Zhao, J., and Wang, Y. (2021). High-resolution terahertz ptychography using divergent illumination and extrapolation algorithm. Optics and Lasers in Engineering *147*, 106729. 10.1016/j.optlaseng.2021.106729.

23. Thibault, P., Dierolf, M., Bunk, O., Menzel, A., and Pfeiffer, F. (2009). Probe retrieval in ptychographic coherent diffractive imaging. Ultramicroscopy *109*, 338–343. 10.1016/j.ultramic.2008.12.011.

24. Lehtinen, J., Munkberg, J., Hasselgren, J., Laine, S., Karras, T., Aittala, M., and Aila, T. (2018). Noise2Noise: Learning Image Restoration without Clean Data. Preprint at arXiv, https://doi.org/10.48550/arXiv.2304.02643 https://doi.org/10.48550/arXiv.2304.02643.

25. Pathak, D., Krahenbuhl, P., Donahue, J., Darrell, T., and Efros, A.A. (2016). Context encoders: Feature learning by inpainting. In Proceedings of the IEEE conference on computer vision and pattern recognition, pp. 2536–2544.

26. Kalluvila, A., Koonjoo, N., Bhutto, D., Rockenbach, M., and Rosen, M.S. (2022). Synthetic Low-Field MRI Super-Resolution Via Nested U-Net Architecture. arXiv preprint arXiv:2211.15047.

27. Redmon, J., and Farhadi, A. (2017). YOLO9000: better, faster, stronger. In Proceedings of the IEEE conference on computer vision and pattern recognition, pp. 7263–7271.

28. Metzler, C.A., Schniter, P., Veeraraghavan, A., and Baraniuk, R.G. (2018). prDeep: Robust Phase Retrieval with a Flexible Deep Network. Preprint at arXiv, https://doi.org/10.48550/arXiv.1803.00212 https://doi.org/10.48550/arXiv.1803.00212.

29. Kappeler, A., Ghosh, S., Holloway, J., Cossairt, O., and Katsaggelos, A. (2017). Ptychnet: CNN based fourier ptychography. In 2017 IEEE International Conference on Image Processing (ICIP) (IEEE), pp. 1712–1716. 10.1109/ICIP.2017.8296574.

30. Guan, Z., Tsai, E., Huang, X., Yager, K., and Qin, H. (2019). PtychoNet: Fast and High Quality Phase Retrieval for Ptychography 10.2172/1599580.

31. Cherukara, M.J., Zhou, T., Nashed, Y., Enfedaque, P., Hexemer, A., Harder, R.J., and Holt, M.V. (2020). AI-enabled high-resolution scanning coherent diffraction imaging. Appl. Phys. Lett. *117*, 044103. 10.1063/5.0013065.

32. Welker, S., Peer, T., Chapman, H.N., and Gerkmann, T. (2022). Deep Iterative Phase Retrieval for Ptychography. In ICASSP 2022 - 2022 IEEE International Conference on Acoustics, Speech and Signal Processing (ICASSP) (IEEE), pp. 1591–1595. 10.1109/ICASSP43922.2022.9746811.

33. Wu, Z., Kang, I., Yao, Y., Jiang, Y., Deng, J., Klug, J., Vogt, S., and Barbastathis, G. (2023). Three-dimensional nanoscale reduced-angle ptycho-tomographic imaging with deep learning (RAPID). eLight *3*, 7. 10.1186/s43593-022-00037-9.

34. Schloz, M., Müller, J., Pekin, T.C., Van den Broek, W., Madsen, J., Susi, T., and Koch, C.T. (2023). Deep reinforcement learning for data-driven adaptive scanning in ptychography. Scientific Reports *13*, 8732. 10.1038/s41598-023-35740-1.

35. Thoppilan, R., De Freitas, D., Hall, J., Shazeer, N., Kulshreshtha, A., Cheng, H.-T., Jin, A., Bos, T., Baker, L., Du, Y., et al. (2022). LaMDA: Language Models for Dialog Applications. Preprint at arXiv. https://doi.org/10.48550/arXiv.2201.08239.

36. Brown, T., Mann, B., Ryder, N., Subbiah, M., Kaplan, J.D., Dhariwal, P., Neelakantan, A., Shyam, P., Sastry, G., Askell, A., et al. (2020). Language Models are Few-Shot Learners. In Advances in Neural Information Processing Systems, H. Larochelle, M. Ranzato, R. Hadsell, M. F. Balcan, and H. Lin, eds. (Curran Associates, Inc.), pp. 1877–1901. https://doi.org/10.48550/arXiv.2005.1416.

37. Cui, Y., Yang, Z., and Yao, X. (2023). Efficient and Effective Text Encoding for Chinese LLaMA and Alpaca. Preprint at arXiv. https://doi.org/10.48550/arXiv.2304.08177.

38. Dong, Y., Li, C., Zhang, Y., Li, P., and Qi, F. (2022). Exascale image processing for next-generation beamlines in advanced light sources. Nat Rev Phys *4*, 427–428. 10.1038/s42254-022-00465-z.

39. Kirillov, A., Mintun, E., Ravi, N., Mao, H., Rolland, C., Gustafson, L., Xiao, T., Whitehead, S., Berg, A.C., Lo, W.-Y., et al. (2023). Segment Anything. Preprint at arXiv. https://doi.org/10.48550/arXiv.2304.02643.

40. Odstrčil, M., Lebugle, M., Guizar-Sicairos, M., David, C., and Holler, M. (2019). Towards optimized illumination for high-resolution ptychography. Opt. Express *27*, 14981–14997. 10.1364/OE.27.014981.

41. Maiden, A.M., Humphry, M.J., and Rodenburg, J.M. (2012). Ptychographic transmission microscopy in three dimensions using a multi-slice approach. J. Opt. Soc. Am. A *29*, 1606. 10.1364/JOSAA.29.001606.

42. Chan, H., Nashed, Y.S.G., Kandel, S., Hruszkewycz, S.O., Sankaranarayanan, S.K.R.S., Harder, R.J., and Cherukara, M.J. (2021). Rapid 3D nanoscale coherent imaging via physics-aware deep learning. Applied Physics Reviews *8*, 021407. 10.1063/5.0031486.

43. Barutcu, S., Ruiz, P., Schiffers, F., Aslan, S., Gursoy, D., Cossairt, O., and Katsaggelos, A.K. (2020). SIMULTANEOUS 3D X-RAY PTYCHO-TOMOGRAPHY WITH GRADIENT DESCENT. In 2020 IEEE International Conference on Image Processing (ICIP) (IEEE), pp. 96–100. 10.1109/ICIP40778.2020.9190775.

44. Favre-Nicolin, V., Girard, G., Leake, S., Carnis, J., Chushkin, Y., Kieffer, J., Paleo, P., and Richard, M.-I. (2020). *PyNX*: high-performance computing toolkit for coherent X-ray imaging based on operators. J Appl Crystallogr *53*, 1404–1413. 10.1107/S1600576720010985.

45. Enders, B., and Thibault, P. (2016). A computational framework for ptychographic reconstructions. Proc. R. Soc. A. *472*, 20160640. 10.1098/rspa.2016.0640.

46. Ronneberger, O., Fischer, P., and Brox, T. (2015). U-net: Convolutional networks for biomedical image segmentation. In Medical Image Computing and Computer-Assisted Intervention–MICCAI 2015: 18th International Conference, Munich, Germany, October 5-9, 2015, Proceedings, Part III 18 (Springer), pp. 234–241.

47. Krizhevsky, A., Sutskever, I., and Hinton, G.E. (2017). Imagenet classification with deep convolutional neural networks. Communications of the ACM *60*, 84–90.

48. Kingma, D.P., and Ba, J. (2017). Adam: A Method for Stochastic Optimization. Preprint at arXiv. https://doi.org/10.48550/arXiv.1412.6980.

49. Goyal, P., Dollár, P., Girshick, R., Noordhuis, P., Wesolowski, L., Kyrola, A., Tulloch, A., Jia, Y., and He, K. (2018). Accurate, Large Minibatch SGD: Training ImageNet in 1 Hour. Preprint at arXiv. https://doi.org/10.48550/arXiv.1706.02677.

50. Bunk, O., Dierolf, M., Kynde, S., Johnson, I., Marti, O., and Pfeiffer, F. (2008). Influence of the overlap parameter on the convergence of the ptychographical iterative engine. Ultramicroscopy *108*, 481–487.

STAR★METHODS

KEY RESOURCES TABLE

RESOURCE AVAILABILITY

Lead contact

Further information and requests for resources and reagents should be directed to and will be fulfilled by the lead contact, Yi Zhang(zhangyi88@ihep.ac.cn)

Materials availability

This study did not generate new unique reagents.

Data and code availability

- The Python code used for network reconstruction in this paper is available at: https://github.com/paidaxinbao/PtyNet.
- The publicly available data can be found at https://zenodo.org/records/10068181. The link contains the trained and fine-tuned model.
- Any additional information required to reanalyze the data reported in this paper is available from the lead contact upon request.

EXPERIMENTAL MODEL AND STUDY PARTICIPANT DETAILS

Our study does not use experimental models.

METHOD DETAILS

Reconstruction principle of ptychography by neural network

The reconstruction of the sample at each scanning position of Ptychography can be described as an inverse problem by Fourier transform.

In the sample plane, the coherent light interacts with the sample and the wavefront is:

$$\psi_i(r) = P(r) * O_i(r)$$

Under the far-field approximation, the wavefront in the detector plane can be described as the Fourier transform of the sample plane as follows:

$$\psi_i(k) = \mathcal{F}[P(r) * O_i(r)] = A_i(k)e^{i\phi(k)}$$

where r denotes the real domain and k represents the frequency domain.

The reconstruction process of the sample can be described as:

$$O_i(r) = \frac{1}{P(r)}\mathcal{F}^{-1}\left[A_i(k)e^{i\phi(k)}\right] = \mathcal{F}^{-1}[\frac{A_i(k)}{P(r)}e^{i\phi(k)}]$$

However, due to the missing phase of the detector, the acquired signal is only $|A_i(k)|^2$. We expect that the neural network can learn a transformation process that allows the corresponding sample distribution to be reconstructed at each scanning position:

$$\widehat{O}_i(r) = F(A_i(k); \theta)$$

where θ is the parameter to be learned by the network. The parameters of the neural network are updated by back propagation :

$$\theta_{New} = \theta - \eta \times \frac{\partial L}{\partial \theta}$$

$$\theta \leftarrow \frac{\partial L}{\partial \theta} = \frac{\partial L}{\partial \widehat{O}_i(r)} \times \frac{\partial \widehat{O}_i(r)}{\partial \theta}$$

where L is the loss function and η is the learning rate. While updating the parameters of the neural network, the output will be close to the target so that the neural network learns the mapping relationship.

Data simulation

For the data used in the reconstruction training, we generated them by simulating real physical processes. We followed coherence experiments conducted at synchrotron light sources and simulated highly focused small spots for the experiments. A highly focused spot has a more complex structure, which implies a higher frequency component in the frequency domain and helps to reconstruct the object image with higher resolution. We used the spot out of focus at a certain position, thus reducing the number of scans. The probe is simulated by Fresnel propagation of a 100 nm-focused and by intercepting a 1 μm size probe at $5mm$ out of focus. The wavelength used for the spot simulation was $0.1\,nm$ (see Supplementary Information Fig. S9 for visualisation). To generate images with more similar

structures, we cropped the pictures of cats and used only the part containing the cat's face to generate data. The size of the diffraction pattern by generating is 128×128. We used raster scanning to generate diffraction pattern data with overlaps of 75%, 50%, 25%, and 0%, and added about 1% positional error to the scanning process, with scanning steps of 250 nm (32 pixel), 500 nm (64 pixel), 750 nm (96 pixel), and 1 μm (128 pixel), respectively.

The sample simulated consists of two cat faces, one as the amplitude and one as the phase. The transmittance function of the object is expressed as the following equation:

$$O_n(r) = f_i(r)e^{if_j(r)}$$

Considering the absorption of X-rays by the real object, we set the amplitude range of the object to [0, 1]. The phase range of the object is set to [0, $\frac{\pi}{2}$]. For the diffraction generation, we generate the diffraction intensity at the detector plane by Fraunhofer diffraction and use the raster scanning.

$$I = |\mathcal{F}[P(r)O(r - R_n)]|^2$$

Subsequently, the target reconstructed by traditional algorithms in this paper is carried out using ePIE[19] and rPIE[21], respectively.

Architecture of neural networks

The structure of the PtyNet-S is similar to the U-Net[46] with a 3-layer encoder block used in the encoder module. The encoder block consists of two 3x3 convolutional layer (the second convolution has a step size of 2), followed by a LeakyReLU activation function after each convolutional layer. The decoder part uses a 3-layer decoder block, where each block is composed of two 3x3 convolutional kernels and one deconvolutional layer with 4x4 kernel size and step size of 2. The convolution operation in the decoder part is performed using group convolution[47], where the input tensor is divided into two groups according to the batch, and each group is convolved separately without overlapping, which is more consistent with the physical process of recovering amplitude and phase separately through the neural network (see Supplementary Information Fig. S5). The LeakyReLU activation function is used after the convolutional layer of the decoder. PtyNet-B consists of 4 coding and 4 decoding layers and uses residual connections for effect enhancement.The specific architecture of PtyNet-B is detailed in Supplementary Information Fig. S6. The PtyNet-S and PtyNet-B does not use skip-connections, which are commonly used to enhance data transfer from the decoder to the encoder. As we believe that ptychography aims to recover the amplitude and phase distribution of the sample from the diffraction pattern, and the network should learn a mapping relationship rather than relying on skip-connections. Following the network outputs, we will perform a zero assignment operation on the predicted objects to satisfy the oversampling condition.

Network training

We choose 110 images of cat faces to generate diffraction patterns as our dataset, 100 of which are used as the training dataset and 10 as the testing dataset. Cat faces have clear contours and hair features existing as texture details and high frequency information, which are suitable for training and testing the network performance. The simulated physical probe is used for Fresnel diffraction to obtain 12800 diffraction patterns of the corresponding scanning positions of each cat face as the input of PtyNet-S. We set the batch size to 16, applied the Adam optimizer [48] , and used a cyclic learning rate (starting learning rate of 2e-4)[49] . We used the MSE as the loss function for back propagation to update the parameter of network. 1000 epochs were performed on an Nvidia A100 (80G), and it took approximately 3.2 hours.

For the dataset of PtyNet-B, we use the same method as above to produce the dataset. We chose different cat face images for which a ptychography simulation process with 75%, 50%, 25%, and 0% overlap was randomly performed to generate diffraction patterns. Then, we balance the data according to different overlap rates, and added a limit on the number of probes randomly jittering, as well as on the number of photons in order to more closely match the experimental scenarios. We set the batch size to 64, applied the Adam optimizer, and used a cyclic learning rate. 1000 epochs were performed on an Nvidia A100 (80G), taking approximately 23.4 hours.

Fine-tuning method

In this work, we propose a fine-tuning strategy that allows the neural network to reconstruct different objects in high quality. The workflow of fine-tuning is shown in Fig.7. First, we input the data which need to be fine-tuned into the neural network. Then, the exit wavefront is obtained by interacting with the probe and predicted object. Probes are required to be known. The exit wavefront is forward propagated to obtain the diffraction signal in the diffraction plane. The predicted diffraction signal is input to the loss function:

$$\widehat{\psi}_i = P_{known} \times F_\theta(\sqrt{I_{real}})$$

$$L = \frac{1}{N^2}\left|\left|FFT(\widehat{\psi}_i)\right|^2 - I_{real}\right|$$

with the input real diffraction signal updating some parameters of the neural network. The reason for choosing L1 loss as the loss function is that it is the same as the R-factor. For the fine-tuning part, we use the Adam optimizer with a stepped learning rate (learning rate decays by half every 20% epoch, starting with a learning rate of 1e-4). The number of rounds of fine-tuning can be adjusted. In this article, for the simulated data, fine-tuning 300 epochs can get good reconstruction results and for the experimental data we fine-tuned 400 to 500 epochs.

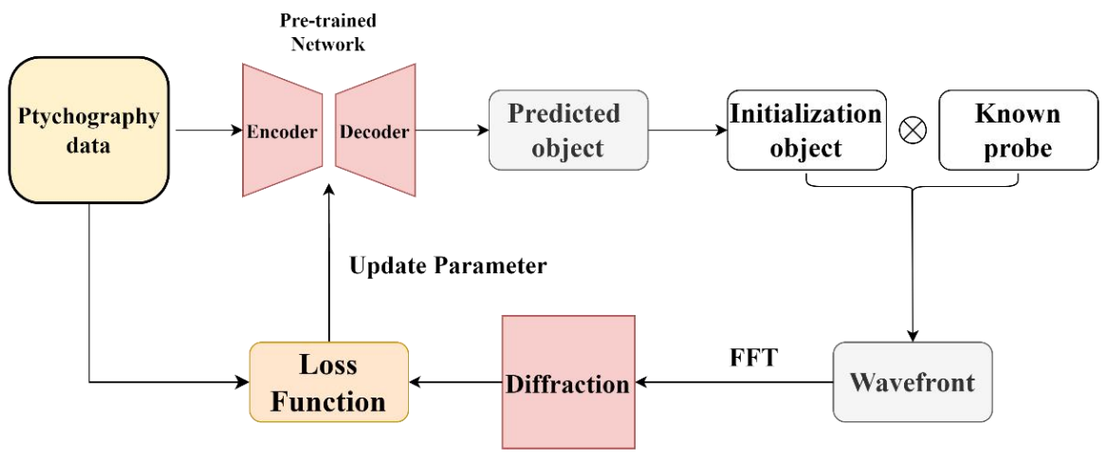

Fig. 7 Schematic diagram of the fine-tuning workflow. The predicted object is obtained from the ptychography data after pre-trained network prediction. Then, the wavefront is obtained by interaction with the probe, and then the diffraction pattern is obtained by forward propagation. The fine-tuned network can make the predicted diffraction pattern as close as possible to the real diffraction pattern.

Integration with traditional algorithms

In traditional algorithms, different scanning overlap rates can have a critical impact on the reconstruction quality of the object[50]. Generally, more than 50% overlap is required to obtain better results. Also, iterative algorithms rely on the selection of initial guesses when reconstructing objects. A more accurate initial guess can speed up the convergence process. When computational resources are not available for training or fine-tuning larger models, a combination of PtyNet-S and traditional algorithms can be used to improve the reconstruction efficiency and reconstruction quality.

As shown in Fig. 8, we reconstructed the results of the neural network PtyNet-S with different overlap rates as initial guesses after 50 rounds using rPIE and ePIE algorithms. For complex objects, good initial guesses yield better reconstruction results under the conditions of a few iterative rounds and low overlap rates. As shown by the curves in Figure 9, a better initial guess allows the algorithm to converge faster. This indicates that the combination of neural networks and traditional algorithms can greatly improve the efficiency and accuracy of the results. Moreover, the traditional algorithms do not easily fall into local optimal solutions. The fast prediction ability of the neural network and the accuracy of the traditional algorithm combined are ideal to save the experimental time and obtain the imaging information in real time.

设置格式[新宇 潘]: 字体颜色: 背景 2

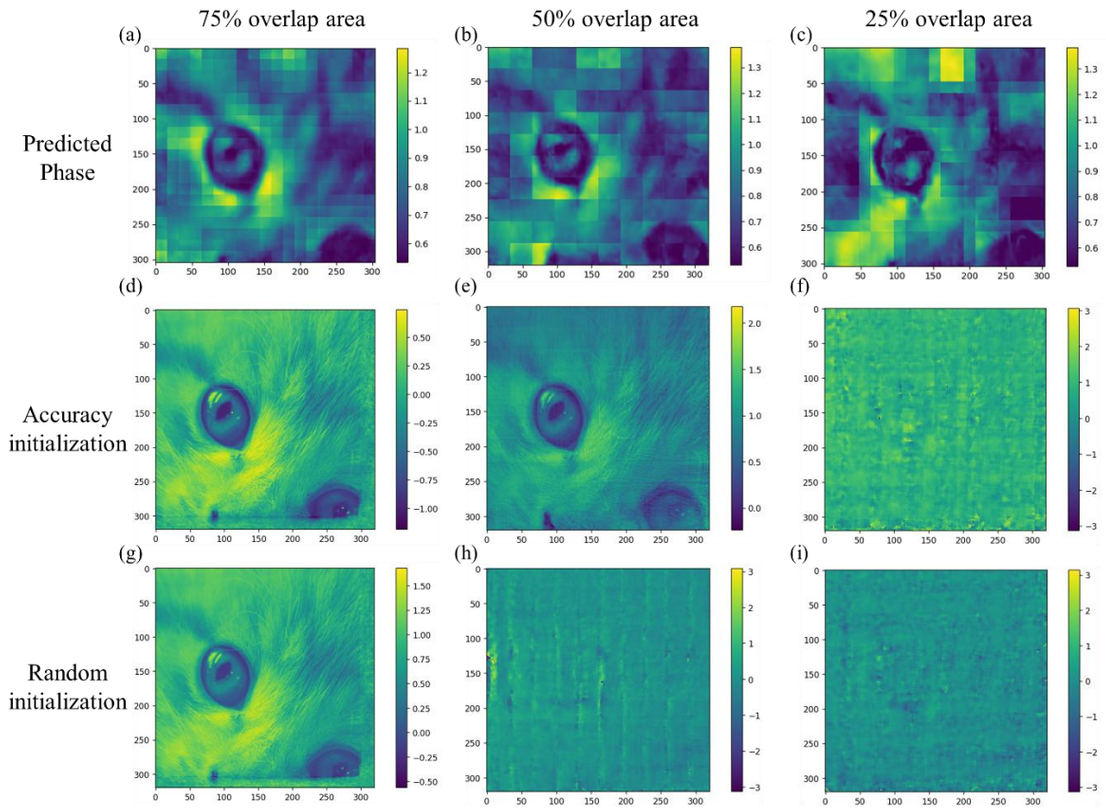

Fig. 8 The output of the neural network is used as an initial guess for the iterative algorithm. (a)-(c) show the phase values of the network predictions at different overlap rates as initial guesses for rPIE and ePIE. (d)-(f) are the results of reconstructing 50 rounds of phases from the network predictions as initial guesses at different overlap rates. (g)-(i) are the results of reconstructing 50 rounds of phases with random initial guesses at different overlap rates.

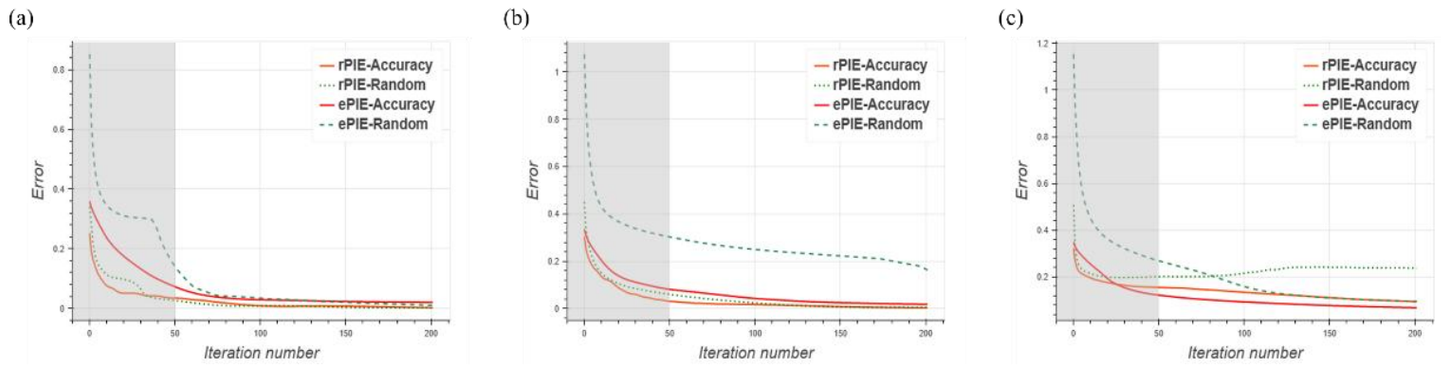

Fig. 9 (a)-(c) shows the error curves of the reconstructed objects using different algorithms. From the error curves, it can be seen that the accuracy variant of the initial guesses converges faster.

Based on Generative Adversarial Networks for Blurred X-Ray Imaging Restoration

JIACHENG ZENG, MINGHUI ZHU, *JIANHENG HUANG, JIAQI LI, YAOHU LEI, XIN LIU, JI LI

Key Laboratory of Optoelectronic Devices and Systems of Ministry of Education and Guangdong Province, College of Physics and Optoelectronic Engineering, Shenzhen University, China

Email: *xianhuangjianheng@163.com*

Summary: In X-ray phase-contrast imaging, to obtain multi-contrast images, researchers use phase-stepping or Fourier-transform methods. However, these methods inevitably introduce artefacts or blurring effects in the images. To achieve high-quality image restoration, this paper introduces deep learning algorithms for the high-quality reconstruction and restoration of low-quality phase-contrast image.

Unlike traditional X-ray absorption imaging that predominantly captures absorption features, X-ray phase-contrast imaging delves into the analysis of X-ray refraction angles post-object passage. This method leverages these angles to discern phase alterations within the object. Among the diverse methodologies for X-ray phase-contrast imaging, grating-based techniques [1] are at the forefront of contemporary research. The Talbot-Lau principle, serving as the foundation of these approaches, is exemplified in its fundamental structure [2], as shown in Figure 1.

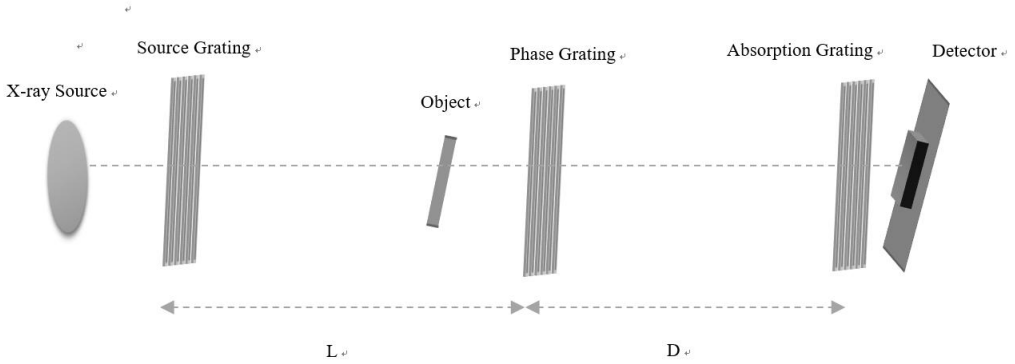

Figure 1: Talbot-Lau Grating Imaging

To decipher absorption, refraction, and scattering information from detector data, the most prevalent techniques are the phase-stepping method [3] and the Fourier-transform algorithm [4]. While the phase-stepping method offers detailed insights, its prolonged imaging duration and susceptibility to errors from inconsistent step sizes pose challenges. Further, grating inhomogeneities can introduce additional phase inaccuracies, and the size of the X-ray source's focal point may result in image blurring. Conversely, the Fourier-transform algorithm, characterized by its shorter imaging time and requirement for only a single exposure, faces limitations due to the choice of window function. This method's dependence on the zero-order and first-order spectra significantly affects image quality, and the selection of the window function can cause edge blurring and spectral overlap, potentially leading to artefacts. However, the advent of deep learning, renowned for its exceptional image restoration and learning capabilities, now paves the way for achieving flawless X-ray images

Generative Adversarial Networks (GANs) [5], a form of advanced deep learning model, consist of two interlinked neural networks engaged in a competitive process. These networks are trained to process noisy images and subsequently generate high-quality, low-

noise counterparts. This capability is particularly crucial in the realm of X-ray phase-contrast imaging, where GANs can reconstruct clearer and more precise images from low-quality phase-contrast data. The architecture of GANs is bifurcated into a generator and a discriminator. The generator's objective is to fabricate images indistinguishable from authentic ones, thereby fooling the discriminator. Conversely, the discriminator is trained to differentiate between real and artificially generated images. The operational steps and the model's framework are depicted in Figure 2

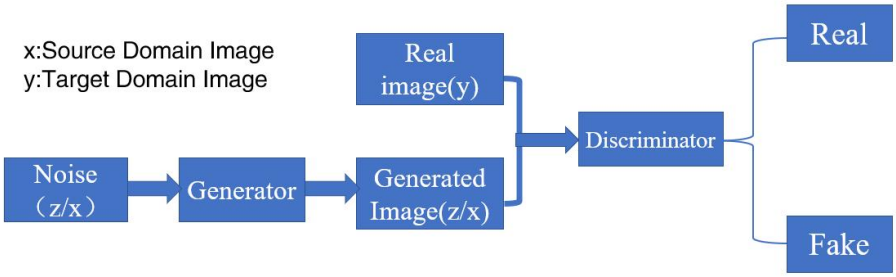

Figure 2: Generative Adversarial Network Model

In this study, the hardware employed is the RTX3090, with TensorFlow serving as the computational framework. The dataset comprises 1000 image sets, partitioned into 800 sets for training and 200 sets for validation. Each set consists of a training image and a corresponding label image. The training images are blurred phase-contrast images obtained from the simulation using the phase-stepping algorithm, while the label images are clear phase-contrast images. The process unfolds in two primary stages. Initially, the model undergoes pre-training with the 800 image sets, aiming to familiarize it with the mapping from training to label images. Following pre-training, the model enters the fine-tuning stage, where it focuses on enhancing the resemblance of the generated images to the label images by analyzing their similarity and adjusting hyperparameters accordingly. Post these stages, the validation set is employed to assess the model's generalization ability and image restoration prowess. The simulations are conducted under specific conditions: a Gaussian source size of 4*4m², system distances of L=63.2mm and D=93.62mm, and the maximum phase information of each image is randomly set between 1.2 and 1.8. Figure 3 illustrates the training image, label image, and the generated image of a simulated leaf.

(a) (b) (c)

Figure 3: (a)Training Image. (b)Label Image. (c) Generated Image

To visually illustrate the results, we employ image quality metrics, notably PSNR (Peak Signal-to-Noise Ratio) and SSIM (Structural Similarity Index Measure), to quantify the differences between the training and label images, as well as between the generated and label images. These comparative results are depicted in Figure 4

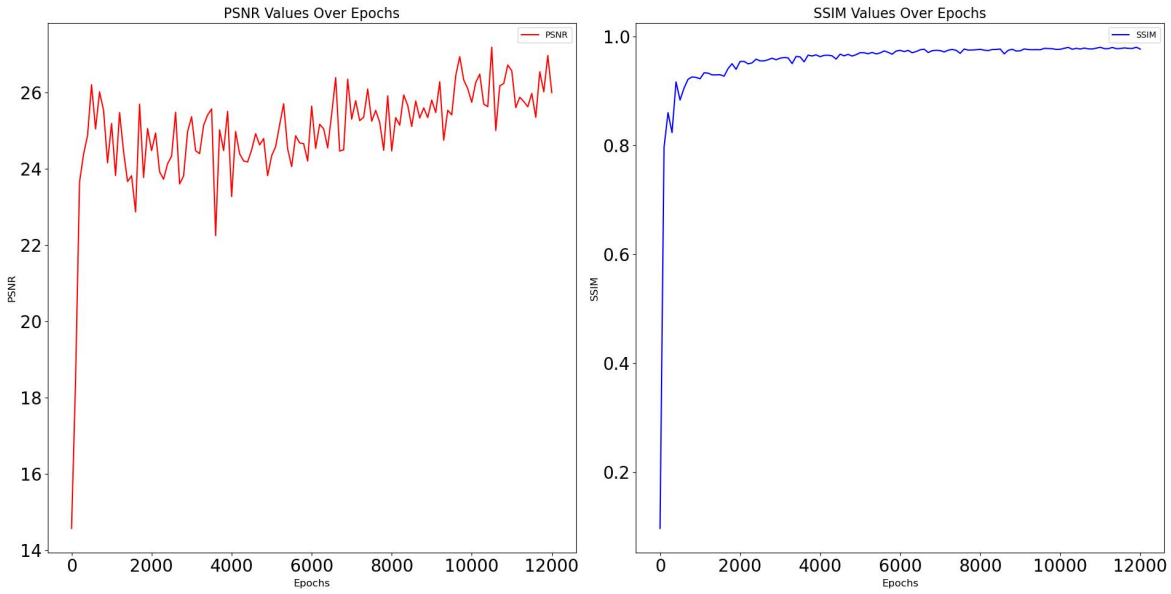

Figure 4: Generated Image versus Label Image

Prior to initiating training, PSNR (Peak Signal-to-Noise Ratio) and SSIM (Structural Similarity Index) evaluations were conducted on the training and label images. The initial test results indicated a PSNR value of 23.71 and an SSIM value of 0.71, setting a baseline for our model's performance. As training advanced and the iteration count increased, a notable upward trajectory in PSNR values was observed, signaling substantial improvements in the model's image reconstruction quality and an ongoing enhancement in image clarity. Particularly in the advanced stages of training, a significant reduction in PSNR fluctuations was noted, suggesting the stabilization and convergence of model parameters and a more precise mapping from the training to the target image. Simultaneously, the SSIM values commenced at a high level, nearing 1, denoting a strong initial structural resemblance between the training and label images. This metric consistently increased throughout the training process, ultimately nearing the optimal value of 1, further corroborating the high structural fidelity of the generated images. In summary, these outcomes underscore our model's formidable proficiency in image reconstruction. The elevated PSNR and SSIM scores not only attest to the model's efficacy in visually and structurally replicating the target image but also underscore its adeptness in deblurring and image restoration tasks.

In this deblurring endeavor, Generative Adversarial Networks have exhibited remarkable capabilities in image reconstruction and recovery. The line graphs presented in the study depict a direct correlation between the number of training iterations and the enhanced quality of the generated image; a greater number of iterations corresponds to improved image quality. Theoretically, given an unlimited number of training iterations, the model could produce an image virtually indistinguishable from the label image, achieving a degree of realism that might be mistaken for the original. This underscores the potential of this model to restore images of high quality, even when faced with low-quality phase-contrast images in experimental settings.

Acknowledgments:

This work was supported in part by the National Natural Science Foundation of China (62075141,12375299), and Natural Science Foundation of Guangdong Province (2021A1515010051).

References:

[1] David C, Nöhammer B, Solak H H, et al. Differential x-ray phase contrast imaging using a shearing interferometer[J]. Applied physics letters, 2002, 81(17): 3287-3289.
[2] Pfeiffer F, Weitkamp T, Bunk O, et al. Phase retrieval and differential phase-contrast imaging with low-brilliance X-ray sources[J]. Nature physics, 2006, 2(4): 258-261.
[3] Momose A, Kawamoto S, Koyama I, et al. Demonstration of X-ray Talbot interferometry[J]. Japanese journal of applied physics, 2003, 42(7B): L866.
[4] Bevins N, Zambelli J, Li K, et al. Multicontrast x-ray computed tomography imaging using Talbot-Lau interferometry without phase stepping[J]. Medical physics, 2012, 39(1): 424-428.
[5] Goodfellow I, Pouget-Abadie J, Mirza M, et al. Generative adversarial networks[J]. Communications of the ACM, 2020, 63(11): 139-144.

Two mass density images in X-ray grating-based phase tomography and their density resolutions

Dongliang Guo[1],Qisi Lin[1],Zhao Wu[1],Meng Huang[1,2],Yong Guan[1],Gang Liu[1],Yalin Lu[1],Yangchao Tian[1]

1. University of Science and Technology of China

2. The First Affliated Hospital of Anhui Medical University

Grating-based X-ray phase imaging is a multi-mode imaging technology. Various criterions, including angular sensitivity, have been adopted to assess the performance of phase-sensitive imaging. However, due to differences in physical quantities, these criterions cannot be compared with attenuation-based imaging directly. Thanks to the versatility and energy independence of mass density, it may serve as a benchmark for comparing various imaging methods. In this work, we retrieve two mass density images in X-ray grating-based phase tomography and define the mass density resolution as a general criterion to compare attenuation-based imaging and phase contrast imaging.

Investigations on the melt pool boundaries in a 3D printed Al-Fe alloy using Talbot interferometry

*SHAN LIN[1], TOSHIHIRO OKAJIMA[1], YUE CHENG[2], NAOKI TAKATA[2], TAKUYA SHIRAMOMO[3], RYOSUKE UEDA[4], ATSUSHI MOMOSE[4]

[1]*Beam Line Division, Aichi Synchrotron Radiation Center, Japan*

[2]*Department of Materials Science and Engineering, Nagoya University, Japan*

[3] *DENSO Corporation, Japan*

[4] *Institute of Multidisciplinary Research for Advanced Materials, Tohoku University, Japan*

Email: *shan.lin@aichisr.jp*

Summary: Investigations of additively manufactured Al-15wt%Fe were conducted using Talbot interferometry and Small-Angle X-ray Scattering (SAXS) method. Results from Talbot interferometry revealed contrasts around the melt pool boundary, as well as in the cracks and voids, across all imaging types—transmission, phase, and visibility. The 2D SAXS profiles exhibited isotropy in both interlayer and planar directions. This study demonstrates that Talbot interferometry is an effective method for detecting the microstructure in metallic materials.

Metal components produced by 3D printers such as L-PBF [1] method consist of melt pools. Due to this, the microstructures of these melt pools are complexly distributed both within and between the layers of the material. In a material like this, it is necessary to investigate small structural details over a large area. This is particularly important in precipitation-strengthened materials where the distribution of nanostructures determines the strength of the material, necessitating an investigation of the distribution of these nanostructures. In this study, we used an Al alloy produced by a 3D printer, attempted to observe the microstructure using Talbot interferometer, which is Vector Radiography [2], and Tomography. The anisotropy of scattering images was investigated beforehand using Small-Angle X-ray Scattering (SAXS).

Al-15wt%Fe alloy was used by L-PBF method. The manufacturing process has been reported by Wang et al. [3]. Plates of approximately 40 μm and 90 μm thick was prepared for the X-Y (two laser scanning directions) and Z (stacking direction)-X surface. A square pillar witch 500 μm thick was cut for the Talbot tomography measurement.

SAXS experiments were carried out at the Aichi Synchrotron's BL8S3, using an incident X-ray beam with an energy of 13.5 keV and a beam size of approximately 0.1 mm × 0.5 mm. Investigations with the Talbot interferometer were conducted at BL11S3, using the white X-rays that can be considered plane waves as the incident X-rays. For the G1G2 diffraction gratings, 1D diffraction gratings with a period of 4.8 μm were used for both, and the distance between G1 and G2 was set to about 12 cm to achieve a design energy of 12.4 keV. The measurements with the Talbot interferometer were carried out using the fringe scanning method6), with the number of scanning steps set to 5. Vector radiography was performed on the XZ surface plates of the two alloys, conducting fringe scanning at intervals of 30° in the 0-180° angle range, and transmission images were measured. Talbot tomography was carried out on the Al-15wt%Fe pillar, rotating it in increments of 0.2° over a range of 0-185°. Fringe scanning was conducted at each angle.

One of the results of the Talbot interferometer, the transmission images of Vector radiography are shown on the left in Fig. 1. This is the overlayed images of which rotated 0-150° in the vector radiography, and the dark, scale-like pattern with low transmission is thought to be due to the formation of the stable phase $Al_{13}Fe_4$ with a width of about 3 μm at the melt pool boundaries [3]. In the right image of Figure 1, an optic microscopy image on the same sample location is shown. The scale-like pattern corresponds partially in some of the dark pattern with each other. When the longitudinal direction of a melt pool is aligned to the direction of the incident X-ray (for this case, perpendicular to the paper surface), the cross section shows a scale-like pattern, and the contrast between the melt pool boundary and the interior is directly projected; when they are perpendicular (in the up and down direction of the paper surface), the contrast between the two is effectively reduced. Internal defects such as cracks and voids were also observed in these images.

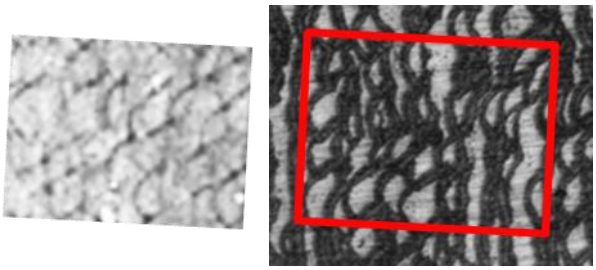

Figure 1: The images of a thin film of Al-15wt%Fe alloy on the plane XZ by (left) vector radiography and (right) optical microscopy. Left image is the pile upped image comprised of 6 transmission images rotated 0-150° by a step of 30°. The red square is the position of the pile upped image.

Similar scale-like patterns were observed in both the phase images and the visibility images, indicating that the boundaries of the melt pools in the Al alloy and internal defects were observed in all images of transmission, phase, and visibility.

2D SAXS pattern showed no anisotropy either within or between the stacking layers, and even when radially averaged, no differences were observed in the scattering vector region of about 0.04-1.5 nm^{-1}. This can be interpreted by the metastable phase Al_6Fe having spherical and lamellar in shape coexisting within the melt pool [3]. This result indicates that the scale-like pattern in the visibility was due to the scattered intensity by the micro-meter ordered $Al_{13}Fe_4$.

The melt pool boundaries, cracks, and voids were observed in 3D for the reconstructed X-ray attenuation coefficient via Talbot tomography. Cracks and voids were confirmed in the reconstructed visibility values. The visibility contrast around the melt pools was believed to be obscured by artifacts from the reconstruction process.

This research is a part of the C6 Project Core Industry of the Aichi Science & Technology Foundation.

References

[1] T. DebRoy, H.L. Wei, J.S. Zuback, T. Mukherjee, J.W. Elmer, J.O. Milewski, A.M. Beese, A. Wilson-Heid, A. De and W. Zhang, *Prog. Mater. Sci*., **92**, 112, (2018).

[2] F. Pfeiffer, M. Bech, O. Bunk, P. Kraft, E. F. Eikenberry, CH. Brönnimann, C. Grünzweig and C. David, *Nature Mater.,* **7**, 134, (2008).

[3] W. Wang, N. Takata, A. Suzuki, M. Kobayashi and M. Kato, *Intermetallics*, **125**, 106892, (2020).